Development of New Self-Assembly Driven Chemo-Sensors for Various Important Analytes

by

Bapan Pramanik

Department of Chemistry

Indian Institute of Technology Guwahati

Guwahati, Assam, 781039

India

A Thesis Submitted in Partial Fulfillment of the

Requirements for the degree of

Doctor of Philosophy

In

Chemistry

IIT Guwahati, March 2019

Dedicatied

To

My Parents and Sister…

Declaration

I hereby declare that the matter embodied in this thesis is result of investigations carried out by me in the Department of Chemistry, Indian Institute of Technology Guwahati, India, under the guidance of Dr. Debapratim Das. In keeping with the general practice of reporting scientific observations, due acknowledgements have been made wherever the work described is based on the findings of other investigators.

(Bapan Pramanik)

भारतीय प्रौद्योगिकी संस्थान गुवाहाटी
INDIAN INSTITUTE OF TECHNOLOGY GUWAHATI

Dr. Debapratim Das
Associate Professor
Department of Chemistry
Ph: + 91 361 258 3301
Fax: + 91 361 258 2349
E-mail: ddas@iitg.ac.in

05th March, 2019

To whom it may concern.

This is to certify that the thesis entitled **"Development of New Self-Assembly Driven Chemo-Sensors for Various Important Analytes"** submitted by Bapan Pramanik (Roll No. 146122005) for the award of PhD degree to IIT Guwahati, is absolutely based on his own research work and that neither this thesis nor any part of it has been submitted for any degree/diploma or any academic award anywhere before.

(Dr. Debapratim Das)

Contents

Abstract

The thesis **"Development of New Self-Assembly Driven Chemo-Sensors for Various Important Analytes"** deals with the development of new fluorescent chemo-sensors based on the aggregation dis-aggregation phenomenon.

Chapter 1 is a brief introduction of aggregation dis-aggregation based chemo-sensors with up to date literature review.

Chapter 2 describes the efficacy of a viologen perylene diimide conjugate towards base in solution phase and solid crystalline phase. Also, this bola-amphiphilic viologen-**PDI** conjugate showed solvatochromism with generation of distinguishable colors in different solvents.

Chapter 3 deals with the tandem sensing of Pd^{2+} and CN^- ions utilizing a perylenediimide-peptide conjugate based on aggregation dis-aggregation phenomenon.

Chapter 4 describes the sensing of histone, a DNA binding protein. A series of Naphthalenediimide (**NDI**) derivatives are subjected to DNA binding studies for the sensing of histone. The strong binding affinity of histone toward DNA lead to release of the **NDI** molecules from the **NDI**-DNA complex resulting in enhancement of the fluorescence intensity and used as an efficient "turn-on" sensor for histone.

Chapter 5 describes the sensing of picric acid (PA), a well-known explosive based on a pyrene based short peptide gelator. The gelator molecule shows its efficacy and selectivity towards PA in solution phase, gel phase as well as in paper based systems with high sensitivity. In addition to that, the test strips can detect PA vapors in sub ppb level and are effective for detection of PA contamination in ground water.

Acknowledgements

This thesis is the last milestone of my journey in acquiring my Ph.D. and has been kept on track which is also governed by the support and encouragement of numerous people including my labmates, well wishers, friends, and various institutions. I would like to thank all those people who made this thesis successful and a remarkable experience for me. Also, it is a great opportunity to express my gratitude to all those who contributed in several ways to the victory of this study.

Prior to all I would like to express my sincere gratefulness to my supervisor Dr. Debapratim Das. This work would not have been accomplished in the absence of his guidance, scholary inputs, consistent encouragement and unconditional support that I received throughout the research work. I am truly honoured and blessed to have been a part of his research team and I fruitfully overcame many obstacles which assisted me to learn a lot from his research expertise. His unflinching courage and conviction always inspires me, and I anticipate to continue further research with his gallant thoughts. He has been by my side always whenever and wherever I needed. He is known for his amicablity and positive disposition. Thank you Sir, for all your immense support, enthusiasm, and dedication.

Besides my supervisor, I would like to give special thanks to my doctoral committee members: Dr. Debasis Manna, Dr. Sunanda Chatterjee and Dr. Dipankar Srimani for their encouragement, insightful comments, and suggestions.

I am grateful to the collaborators for deploying me their expertise and instinct to my scientific and technical problems: Prof. Jyotirmayee Mohanty (BARC, India), Prof. Oren Scherman (University of Cambridge, UK).

I would like to thank Department of Chemistry, IIT Guwahati for availing me the innumerable facilities. Also, I am thankful to IIT Guwahati for financial support.

I would also like to extend huge, warm thanks to to my past and present lab mates Dr. Julfikar Hassan Mondal, Dr. Sahnawaz Ahmed, Dr. Tanur Sinha, Dr. Subhajit Ghosh, Payel, Basab, Sumit, Supriya for providing an amusing and fun filled environment. I am especially greatful to Dr. Julfikar Hassan Mondal and Dr. Sahnawaz Ahmed who have made me familiar with the lab environment and for their support and motivation during the initial days in the lab. My heartfelt thanks to Payel, Basab, and Sumit for their constant support and cooperation during the course of my work.

I would like to express my special thanks to Nilotpal and Ananta for showing their unbreakable friendship, moral support and understanding. And of course, I would like to show my adoration to Saurav for showing his love, carefulness, words of inspiration and motivation, and finally for his brother like behaviour. I would like to thank Dr. Antara Dasgupta for her support and her generous care.

My special acknowledgements goes to Ayan, Rajat, Utsab, Mostakim, Rana, Subhas, Suresh, Pinaki, Sourav, Gourab, Sayanta, Santanu, and Ashalata for their support during my research endeavor. I am indebted to Tousif, Arpita, Minati, Abhishek, and Baishaki for their valuable help. My special thanks to Rupam, Sambit, Varsha, Reshma, Sohini, Sarupa, Plabita and Ujjal.

I sincerely thank all the research scholars of Department of Chemistry, Bioscience and Bioengineering for their help and friendship. I would like to express my gratitude to all others who are associated with my work directly or indirectly at IIT Guwahati.

Last but not the least, I would like to share this moment of happiness with my loving, supportive, encouraging family members who are the pillars of my life. They boost me up whenever I have to cross the hurdles of my career. The support of my parents and sister has remained constant all these years. Without their encouragement, prayers and understanding it would have been an impossible task for me to finish this valuable piece of work. I would like to show my affection to my fondly grandmother for her incomparable love, delicious food, and wonderful bedtime stories.

List of Abbreviations

Abbreviations

ADI	Arylene Diimide
NDI	Naphthalene Diimide
PDI	Perylene Diimide
NMR	Nuclear Magnetic Resonance
ESI-Ms	Electrospray Ionization
UV-Vis	Ultraviolet–Visible Spectroscopy
FL	Fluorescence
λ_{max}	The wavelength in the absorption spectrum where the absorbance is maximum
λ_{em}	The wavelength in the emission spectrum where the emission is maximum
Δ_{abs}	Change in Absorbance
Δ_{em}	Change in Emission
NIR	Near-infrared
MAC	Minimum Aggregation Concentration
MeOH	Methanol
EtOH	Ethanol
ACN	Acetonitrile
DMSO	Dimethyl Sulfoxide
DMF	N,N-Dimethylformamide
DIPEA	N,N-Diisopropylethylamine
TEA	Triethylamine
TPA	Tripropylamine
DMAP	4-Dimethylaminopyridine
NaOH	Sodium Hydroxide
Φ	Quantum Yield
EPR	Electron Paramagnetic Resonance
FESEM	Field Emission Scanning Electron Microscopy
FETEM	Field Emission Transmission Electron Microscopy
AFM	Atomic force microscopy
FTIR	Fourier-transform Infrared Spectroscopy
DLS	Dyanamic Light Scattering

ζ	Zeta potential
TCSPC	Time-correlated Single Photon Counting
Pd	Palladium
CN	Cyanide
α_{agg}	Mole fraction of aggregate
B-H	Benesi–Hildebrand
FP	Filter paper
TLC	Thin Layer Chromatography
EDA	Ethylenediamine
DETA	Diethylenetriamine
TETA	Triethylenetetramine
PBS	Phosphate Buffer
HEPES	4-(2-hydroxyethyl)-1-piperazineethanesulfonic acid
Tris	Tris(hydroxymethyl) aminomethane
TAE	Tris-acetate-ethylenediaminetetraacetic acid
MOPS	3-(N-morpholino)propanesulfonic acid
Ct-DNA	Calf-thymus Deoxyribonucleic Acid
ITC	Isothermal Titration Calorimetry
K_a	Binding constant
ΔH	Change in Enthalpy
ΔS	Change in Entropy
ΔG	Change in Gibbs Free Energy
T_m	Melting Temperature of DNA
EtBr	Ethidium Bromide
DAPI	4′,6-Diamidino-2-Phenylindole
S-V	Stern-Volmer
K_{sv}	Stern Colmer Constant
CD	Circular Dichroism
ICD	Induced circular Dichroism
BSA	Bovine Serum Albumin
HRP	Horseradish Peroxidase
Alk. Phos.	Alkaline Phosphatase

PA	Picric Acid
DNP	2,4-Dinitrophenol
PNP	p-Nitrophenol
2,4-DNT	2,4-Dinitrotoluene
2,6-DNT	2,6-Dinitrotoluene
4-NT	4-Nitrotoluene
1,3-DNB	1,3-Dinitrobenzene
NB	Nitrobenzene
4-NBA	4-Nitrobenzoic acid
BA	Benzoic acid
Phe	Phenylalanine
G′	Storage Modulus
G″	Loss Modulus
CGC	Critical Gelation Concentration
Tg	Gel Melting Temperature
$CDCl_3$	Deuterated Chloroform
D_2O	Deuterium Oxide
d_6-DMSO	Deuterated Dimethyl Sulfoxide
CD_3CN	Deuterated Acetonitrile
DL	Detection Limit
nM	Nanomolar
μM	Micromolar
mM	Milimolar
ppb	Parts Per Billion
ppm	Parts Per Million
ppt	Parts Per Trillion
μg/mL	Microgram Per Mililitre
Pg cm^{-2}	Picogram Per cm^2

Chapter 1

Introduction

1.1 INTRODUCTION

A chemo-sensor is a chemical system that is used for the sensing of an analyte to produce some easily detectable responses, such as change in emission intensity, color or conducting property, *etc.*[1] In recent years, the development of chemo-sensors has gained much attention in the field of chemistry, biology and material sciences.[2] Among the different chemo-sensors, fluorescent active sensors have emerged as an attractive domain because of their high sensitivity, ease of operation, applicability in different material state, real-time detection, non-destructive determination and low-cost instrumentation.[2,3] Fluorescent chemo-sensors showed potential in a variety of fields like biological probes, environmental sensors, molecular devices, volatile gas sensing, food safety, process control, medical diagnosis, and fluorescence imaging, *etc.* and it has the advantage over others sensors because fluorescence signals offer high selectivityas well as sensitivity.[4,5] A fluorogenic chemo-sensor is a molecule or it's aggregate which undergoes changes in the photophysical properties upon binding with an analyte species to give a detectable signal.

Self-aggregation of small molecules can be of tremendous help while designing and constructing new fluorescent chemo-sensors.[6] Aggregation of small fluorescent molecules leads to a modest to significant change in the emission behaviour of the probe. Decrease in the emission intensity of a fluorophore as a result of aggregation is a common phenomenon. The decrease accompanies a fall in their life time. In certain cases, the aggregates generates a new emission band in the form of excimer or exciplex.[7,8] Aggregation induced emission is another phenomenon which gained tremendous attention owing to their wide applicability in imaging and sensor development. [9, 10] However, all the systems can be restored with their original photophysical properties once the aggregation in destroyed so that the fluorophore molecules come back to monomeric state. The process is reversible as the self-assembly involves only some weak physical forces and no covalent bonding is involved. The assembly and disassembly processes thus result in reversible changes in the emission property of a fluorophore which can be used as a signal for chemo-sensing processes.

We envisioned that proper design of fluorogenic molecules which can assemble/dis-assemble in presence of the targeted analyte molecule can lead to new selective and highly sensitive chemo-sensors (**Scheme 1.1**). The key behind the success here is the attachment of proper ligand for the analyte under scanner and the effect of the analyte binding on the self-assembly/dis-assembly of the sensor molecule.[11]

Below is an overview of the present literature status of self-assembly based chemo-sensors. In this process, a discussion on different fluorophores capable of self-assembly and their self-aggregation

processes are discussed. Different biologically and environmentally important species for which development of new chemo-sensors are essential is also discussed in the later section.

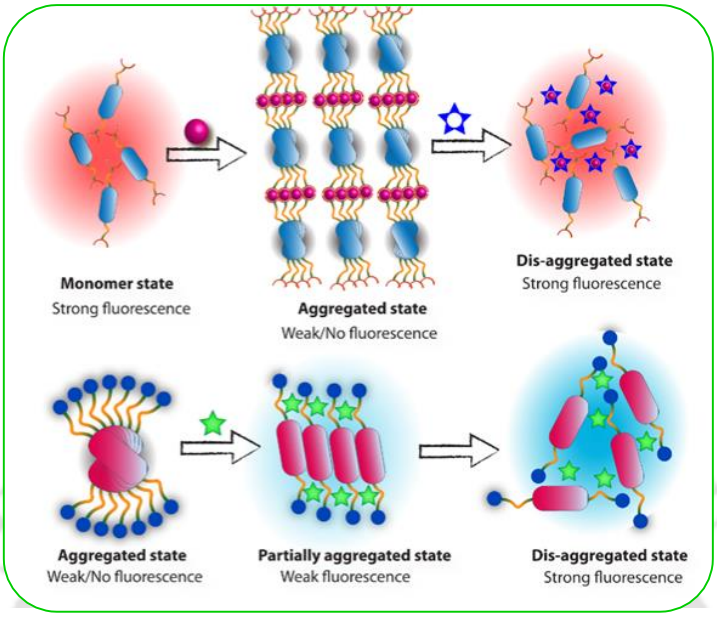

Scheme 1.1 Pictorial representation of aggregation/dis-aggregation based chemo-sensors.

Organic fluorophores, in general possess fused π-ring systems. When they self-assemble in solution or at the solid-liquid interface, they often form H-type or J-type aggregates, depending on the relative alignment of the transition dipole moments on adjacent molecules.[12]

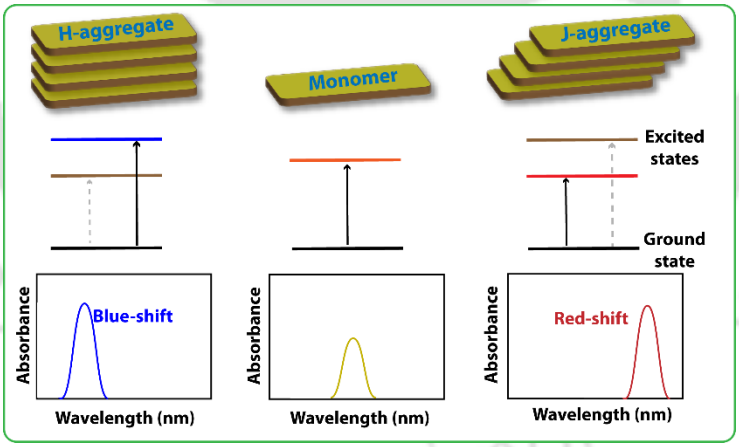

Figure 1.1 Pictorial representation of J- and H- aggregate.

J-aggregation is defined as the aggregation pattern where the absorption band is shifted to higher wavelength (bathochromic shift) *i.e.*, red shifted compared to monomer absorption band in which the molecules arrange themselves in such a way to align in head to tail fashion as can be seen in **Figure1.1**. When the absorption band is shifted to lower wavelength (hypsochromic shift) *i.e.*, blue shifted compared to monomer absorption band in which the molecules arrange themselves in such a way to align in side-by-side fashion, it is denoted as J-aggregation and exhibit in most cases low or no fluorescence.[13]

1.2 ARYLENE DIIMIDES (ADI)

Arylenediimdes are the inherently electron deficient molecules with π-scaffold.[14] It has gained enormous attention towards academic as well as in industry due to their wide range of application including industrial pigments,[15] models for biological systems,[16-21] and n-type semiconductors for photovoltaic and organic electronics semiconductors,[22-25] radical ion-based sensor probes, charge transporting materials, solar cell, energy storage and in catalysis of reactions.[14] Out of the arylenediimides, naphthalenediimides (**NDI**)[26-27] and perylenediimides (**PDI**)[28-30] have been established as promising electronic materials because of their large electron deficient π- surfaces and ability to form self-assembled structures. Also, the synthesis of **NDIs** and **PDIs** are relatively easier compared to other arylenediimides and they are easily soluble in organic non-polar or polar solvents. **NDIs** and **PDIs** can be solubilized in aqueous media by incorporating hydrophilic substituents at imide positions of **NDI** and **PDI** respectively. The chemical structure of **NDI**, **PDI** and their corresponding normalized absorption and emission spectra are shown in **Figure 1.2**.

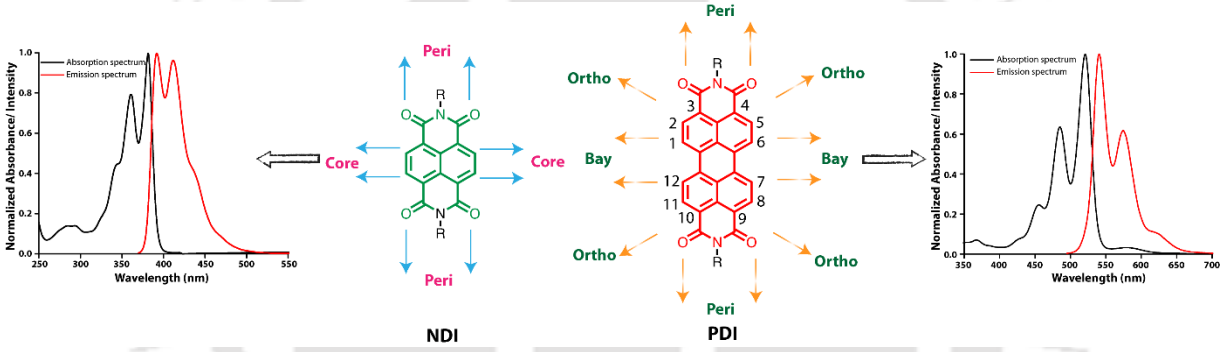

Figure 1.2 Chemical structures of **NDI**, **PDI** and their corresponding ansorption and emission spectra.

1.2.1 Naphthalenediimides (NDI)

NDIs are neutral, planar, chemically robust, redox-active, electron-deficient class of aromatic compounds, and they have been used for a variety of applications, ranging from biomedicine to electronics.[26] The structure of the parent **NDI** compound is composed of a naphthalene core that bears at its four α–positions two electron-withdrawing imide groups, whose nitrogen atom can further be substituted with a variety of alkyl or aryl residues[27] which are displayed in **Figure 1.2**. Naphthalene diimide (**NDI**) chromophores have drawn considerable attention due to their unique optical and electronic properties, which have led to various applications in sensors, semiconductor devices, organic phtovoltaic devices, and artificial photosynthesis, as well as biological applications.[31] **NDIs** are the most fascinating and versatile class of organic n-type semiconductors in the field of designing of electronic conducting functional materials due to their high electron affinity, good charge carrier mobility, and excellent thermal and oxidative stability that enable applications such as organic field effect transistors (OFETs), photovoltaic devices and flexible

displays.[26] The **NDIs** make desirable chemo-sensors, as they are small, easy to functionalize, soluble in a broad range of solvents, and they have tuneable fluorescent properties.

1.2.2 Perylene Diimides (PDI)

Perylene diimides (**PDI**) are well-known for their chemical inertness, bright photoluminescence with quantum yield up to unity, [15, 32-34] and excellent n-type semiconductivity.[35-37] The **PDIs** are extensively used as industrial pigments, laser dyes, photovoltaic cells, fluorescence switches, molecular wires, molecular transistors, sensors[38-39], probes for single molecule spectroscopy, [40-41] organic thin film transistors, [42] and solar cells.[43-45] However, most **PDIs** are not water-soluble, and those which are soluble show a strong tendency to aggregate extensively in aqueous solution leading to fluorescence quenching. As a result, **PDI** derivatives have seldom been used as fluorescent labels for bio-sensing applications.[46] **PDIs** have a large core aromatic chromophore of 11.52 × 4.88 °A (length × width), and as a result **PDIs** exhibit coherent π- π stack. The π- π stacks may be attributed for the strong solvophilic and π- π forces.[47] **PDI** has twelve functionalizable positions out of which 3, 4,9,10 positions are called peri positions; 1, 6,7,12 positions are called bay positions and 2, 5,8,11 are termed as ortho positions as shown in **Figure 1.2**. In general, **PDIs** display an absorption band in the visible range particularly from 400 nm to 800 nm. Despite different substituents at the imide nitrogen, the shape and position of the absorption and emission bands of these dyes are almost identical in their non-aggregated state.[48] The UV-Vis absorption spectrum of **PDIs** in different solvents show three fine vibronic bands which arise from the 0→0, 0→1, and 0→2 electronic transitions respectively.[38,48] To describe the behaviour of **PDI** derivatives in solution phase, the intensity and the pattern of absorption bands have been used.[49-51] It is reported that an electronic transition is coupled to a single vibration and the intensities of the transitions within the progression follow the order $S_{0\rightarrow0} > S_{0\rightarrow1} > S_{0\rightarrow2}$ for non-aggregated monomeric form.[52-54] But as the monomer starts to self-aggregate, the peak intensities start to follow the reverse order *i.e.*, $S_{0\rightarrow1}$ or $S_{0\rightarrow2} > S_{0\rightarrow}0$.[50,55-56] The emission spectra of **PDIs** look like the mirror image of the absorption spectra.[57]

1.2.3 NDI Based Chemo-sensors

Out of the different applications of **NDI** derivatives, the development of chemo-sensors using these arylenediimides gained much popularity amongst the chemists and biologists. There are several research groups who are involved in designing **NDI** based fluorescent sensors. Yoon *et al.* reported a fluorescent chemo-sensor (**1.1**) for pyrophosphates (PPi) with high selectivity over adenosine triphosphate (ATP), adenosine diphosphate (ADP), adenosine monophosphate (AMP) or Pi in aqueous medium based on **NDI** derivative.[58] In presence of PPi, compound **1.1** shows a unique dimeric system which can induce an excimer band through π–π stacking between the **NDI** cores.

Tian and co-workers described two near-IR fluorescent chemo-sensor for Zn^{2+} ions based on core-substituted **NDI** (**cNDI**) as a novel NIR fluorophore (**1.2** and **1.3**). Water-compatible and membrane-permeable chelators, N, N-di (pyridin-2-ylmethyl) - ethane-1, 2-diamine (DPEA) and N, N, N′-tri (pyridin-2-ylmethyl) ethane-1, 2-diamine (TPEA), were incorporated into the core position of **NDI** for the sensing of zinc ions over other metal ions under physiological conditions. [59] Upon addition of Zn^{2+}, the fluorescence enhancement was observed for both the cases but in case of **1.2**, the enhancement was observed due to photoinduced electron transfer (PET) process but in case of **1.3**, the enhancement is a combination of PET and intramolecular charge transfer (ICT) process. Both of the **NDI** derivatives were used successfully to image intracellular Zn^{2+} ions in living human nasopharyngeal epidermal carcinoma cells. In 2012, George *et al.* designed two **NDI** amphiphiles (**1.4** and **1.5**) functionalized with dipicolylethylenediamine motifs for sensing of ADP.[60] These motifs form dipicolylethylenediamine–zinc (DPA–Zn) complex in presence of zinc salts and these amphiphiles self-assemble into one-dimensional helical assemblies in presence of different adenosine phosphates and competitive guest binding leads to the dynamic helix reversal of these assemblies. In presence of adenosine di phosphate, the absorption band gets broadened along with reversal of peak and the fluorescence is decreased which is the characteristic feature of the **NDI** self-assembly.

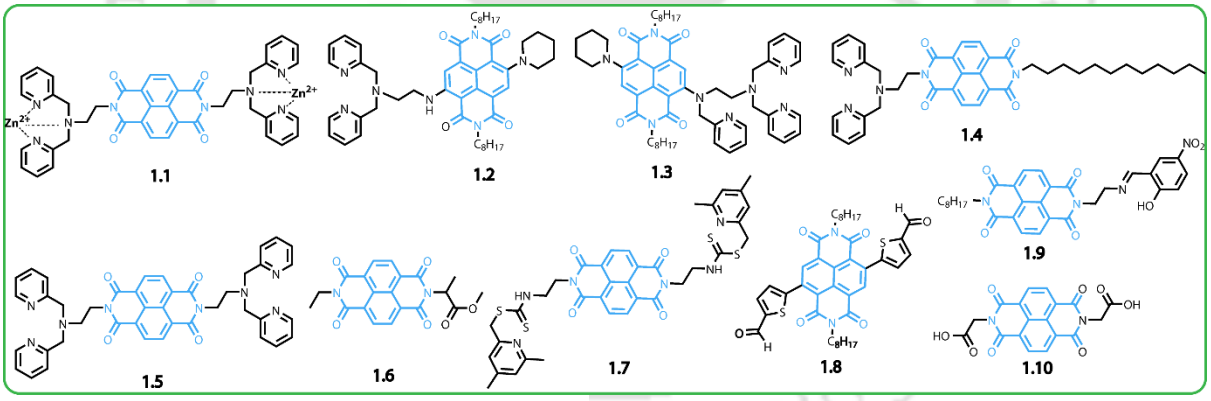

Figure 1.3 Some reported **NDI** based chemo-sensors.

Govindaraju *et al.* reported an asymmetric **NDI** based chemo-sensor (**1.5**) for sensing of aromatic solvents.[61] The derivative showed multicolour emission properties in the visible spectrum, changing from blue to greenish yellow (λ_{max} = 450, 487 and 523 nm for benzene, toluene and xylene respectively) with large Stokes shifts in aromatic solvent due to the excited state specific solvent–fluorophore interactions (or excited state exciplex formation). Bandyopadhyay *et al.* reported a highly selective fluorescence probe for Hg^{2+} ions, based on dithiocarbamate-**NDI** (**1.7**) in aqueous-ethanol (4:1, v/v) media.[62] In presence of Hg^{2+}, weakly fluorescent dithiocarbamate-**NDI** (Φ = 0.03) converted into a highly fluorescent isothiocyanate (Φ = 0.11). This conversion can be easily detected by a distinct blue-shift (43 nm) with the detection limit of 2.1×10^{-7} M. Bhosale *et al.* reported core

substituted **NDI** probe (**1.7**) for detection of cysteine in HEPES buffer based on the photo-induced electron transfer (PET) mechanism.[63] The derivative forms a thiazolidine with Cys through a formyl-Cys reaction. The same group have developed another **NDI** based probe (**1.8**) for selective detection of Cu^{2+} and Fe^{3+} ions as compared to other metal ions.[64] Wei's group have developed a novel water soluble chemo-sensor (**1.10**) for selective detection of mercury ion based on **NDI** derivative.[65] The probe does not emit any fluorescence but upon addition of Hg^{2+}, the probe emitted bright blue colour emission. So, the probe acts as a "turn-on" fluorescence sensor for Hg^{2+} in water with high selectivity and sensitivity.

1.2.4 PDI based chemo-sensors

The excellent fluorescence properties of **PDIs** have been utilized to develop fluorescent probes for analytes. For example, Jingsong and co-workers employed a **PDI** derivative (**1.11**) functionalized with a dipicolylethylenediamine (DPEN) moiety as a colorimetric and fluorometric dual-channel sensor to specifically detect the presence of Cu^{2+} over a wide range of other cations in THF-water mixture.[66] The probe **1.11** displayed a relatively strong emission. Upon addition of Cu^{2+}, the fluorescence intensity was decreased due to the photoinduced electron transfer from the fluorophore to protonated pyridine unit. When the dipicolylamine units coordinate to a metal ion, the electron density of the DPEN moiety might be decreased, and lower the electron-donating ability of the fluorophore accordingly. Yu's group reported a fluorescence "turn-on" approach for the selective and sensitive detection of proteins based on a nucleic acid aptamer and **PDI** probe (**1.12**).[46] In water, **1.12** showed both monomeric and aggregated forms, therefore strong fluorescence was observed. In presence of a negatively charged nucleic acid aptamer, **PDI** probe (**1.12**) undergoes instantaneous binding with the aptamer through strong electrostatic interactions between the dye monomer/aggregates and the aptamer. As **PDI** probe (**1.12**) is prone to self-assemble via $\pi-\pi$ stacking between themselves, decrease in the fluorescence intensity was observed. Upon addition of lysozyme, the recovery of fluorescence was observed as the monomer of **PDI** probe (**1.12**) becomes free due to the strong affinity of lysozyme toward the aptamer. Jiang *et al.* reported a fluorescent sensor based on **PDI** derivative (**1.13**) for detection of mercury through aggregation dis-aggregation process.[67] They have observed the imide groups of the derivative are similar to the binding site of thymine (T) for Hg^{2+} for the well-known "T–Hg^{2+}–T" structure which can be used as a sensor material for Hg^{2+}. In presence of Hg^{2+}, the modestly fluorescent derivative form linear complex via the "T–Hg^{2+}–T" binding mode which further extend to form H-type aggregate, leading to decrease of fluorescence intensity. Upon addition of Cys or other thiol species, the Hg–imide interaction is replaced by that of Hg–S, resulting in the dissociation of "**PDI**–Hg" aggregates and recovery of fluorescence was observed. The same **PDI** probe (**1.11**) was reported for detection

of ATP in aqueous media with high selectivity by Zhang *et al.* [68] Here, they have first prepared Zn-complex with Zn^{2+} ion and this complex was used for the sensing purpose. The complex exhibited a moderately strong fluorescence emission. A remarkable enhancement of fluorescent intensity was observed only for ATP upon addition of different anions. Shi and co-workers prepared a symmetric

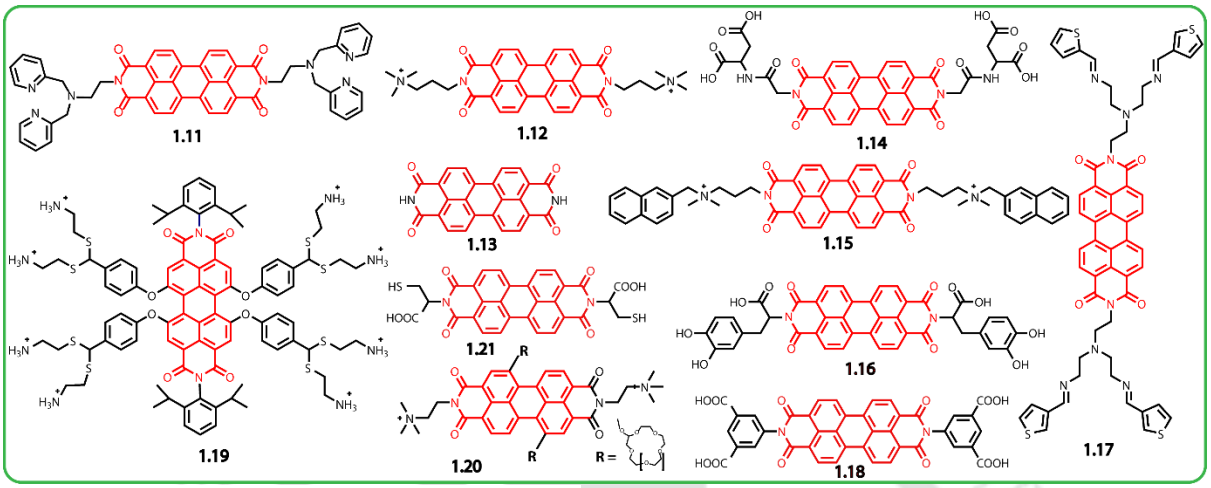

Figure 1.4 Some reported **PDI** based chemo-sensors.

PDI derivative (**1.14**) in which the imide position of the **PDI** core is substituted by the dipeptide unit Asp-Glu, shows a "turn-on" sensor for pyrophosphate. In presence of cupric ion, **PDI** derivative (**1.14**) undergoes assembly to form **1.14**/Cu^{2+} and as a result fluorescence intensity get quenched. Upon addition of PPi into the aggregates, the aggregates break down due to the disassembly of the aggregates as the Cu^{2+} acts as a competitive binder towards pyrophosphate compared to **1.14** and simultaneously the fluorescence enhancement was observed.[69]

Zhang *et al.* synthesized a **PDI** derivative (**1.15**), tethered by naphthyl linker and investigated the sensing properties towards spermine in aqueous media through host-guest chemistry.[70] In presence of host, cucurbit[7]uril (CB[7]), **PDI** derivative (**1.15**) undergoes dis-aggregation because of the binary complexation between the naphthyl group of the probe and the host CB[7], so the fluorescence get enhanced. Upon addition of spermine, the dissociation of the complex was observed as spermine has affinity towards CB[7] owing to the presence of multiple charges and long alkyl chains and thus leading to the fluorescence quenching. Later, Shaangguan *et al.* investigated fluorescence response of the same derivative **1.11** to Zn^{2+} and Cd^{2+} at different pH values. [71] They have observed that the derivative **1.11** shows low fluorescence at pH above 6.0 due to the photo-induced electron transfer (PET) process from 2-pyridylmethyl-amine (DPA) to **PDI** unit. In presence of Zn^{2+} and Cd^{2+}, DPA undergoes chelation with Zn^{2+} and Cd^{2+}, rapidly the PET is inhibited which results in the fluorescence recovery of **1.11**. It shows good selectivity and sensitivity for Zn^{2+} at pH 6.0 and for Cd^{2+} at pH 9.0. Govindaraju *et al.* reported an amphiphilic **PDI** derivative (**1.16**) connected with a L-DOPA derivative as a reversible fluorescence switching probe for the detection and sensing of cationic surfactants and Fe^{3+}/Cu^{2+} in an aqueous media through host–guest

interactions driven assembly and disassembly of the derivative.[39] In presence of cationic surfactant, **1.16** undergoes disassembly, as a result the fluorescence intensity is increased. As L-DOPA has binding ability with metal ions, in presence of Fe^{3+}/Cu^{2+}, **1.16** undergoes self-assembly again and the fluorescence intensity is decreased. The Erdemir group developed a fluorescent probe (**1.17**) for the selective detection of mercury ion in Water-DMF mixture solvent.[72] In presence of Hg^{2+} ion, it exhibits a remarkable fluorescence enhancement with respect to other competing metal ions because of photoinduced electron transfer (PET) from di (2-thiopheneylimino) ethylamine unit to the **PDI** core. Wurthner *et al.* reported a fluorescent sensor (**1.18**) for Ba^{2+} ion, in which 1, 7-position of the aromatic core is functionalized with crown ether receptor.[73] The derivative **1.18** exhibited a high fluorescence intensity. In presence of Ba^{2+}, it undergoes H-type self-assembly and as a result fluorescence intensity decreased. Shen *et al.* prepared a multifunctional dithioacetal-modified perylenediimide (**1.19**) for the sensing of Hg^{2+} and as an effective DNA carrier.[74] The probe showed higher emission intensity but upon addition of the Hg^{2+}, the fluorescence quenching was observed because **1.19** underwent a fast Hg^{2+}-promoted hydrolysis. Malik *et al.* reported a water-soluble fluorescent probe consisting of a **PDI** derivative (**1.20**) and melamine, for the detection of L-Cys and L-Hcy.[75] In presence of melamine, **PDI** derivative generates very bright yellow luminescence and the emission spectra showed characteristic emission bands in 550-600 spectral range, which indicates lack of $\pi-\pi$ interactions. With a gradual addition of Hg^{2+} to the complex solution, the quenching of the emission bands is instantaneously observed due to complex formation between the carboxylic groups in **PDI** derivative with Hg^{2+} ion. In presence of Hg^{+2} ions, the –COOH groups of the complex become deprotonated and the resulting perylene moieties get aggregated. As a result, the fluorescence quenching of monomeric emission was observed along with a weak excimer band at a higher wavelength. Then they have used this non-fluorescent probe for the sensing of amino acids or peptides. They have found among all the amino acids, only the two thiol containing amino acids (L-Cys and L-Hcy) recovered the intensity of fluorescence in the solution. Also they have used the fluorescence technique to quantity Cys or Hcy in human blood plasma and urine in presence of other biothiols. Galeotti and co-workers developed a cysteine based **PDI** derivative (**1.21**) for sensing of Hg^{2+} ions in water with high selectivity and sensitivity.[76] The probe has tendency to self-aggregate in aqueous medium even at low concentration which results in a dramatic fluorescence emission quenching. In presence of Hg^{2+} ion, cysteine unit of the probe get complexed with mercury ion, creating steric hindrance which leads to the partial dis-aggregation of the probe. As a result, the fluorescence intensity is recovered.

1.3 Pyrene

Compounds containing polyaromatic hydrocarbons (PAHs) have drawn particular attention due to their extended π-conjugation that provides them with unique photophysical and charge transport properties. Pyrene belongs to the family of PAHs, and its use in the design of optical devices has increased due to the ability to tune its electrochemical and photophysical properties as a result of strong π-electron delocalization over the four fused benzene rings.

1.3.1 Photophysical properties of Pyrene derivatives

Pyrene is a well-known organic fluorescent compound with environment-responsive vibrational fluorescence structures, exceptionally long fluorescence lifetime and the ability to form excimers.[77-78] As a simple aromatic fluorophore, pyrene has a large extinction coefficient,[79] pure blue fluorescence with high quantum yield.[80] The fluorescence emission spectrum of pyrene is characterized by major vibronic bands I, II, III, IV, and V, with well-defined peaks at ~375, 379, 385, 395, and 410 nm, respectively and presence of these peaks are referred as the monomer band. Another interesting feature of pyrene fluorescence emission is the appearance of a broad, structureless band at longer wavelengths (ranging from 425 to 550 nm, centered on 460 nm) when two pyrene rings are ~10 Å from each other. It arises due to formation of an excited state dimer or 'excimer' and involves interaction between two pyrenes. The unusually long lifetime of pyrene emission (>100 ns) allows this excited state reaction to occur. The monomer/excimer (*m/e*) ratio, calculated by comparing the fluorescence intensity (or quantum yield) of the first monomer peak (typically ~375 nm) with respect to the excimer band (generally~460 nm), is a relative indicator of the extent of excimer formation, and therefore the spatial proximity between two pyrene moieties.[81]

1.3.2 Pyrene Based Chemo-sensors

Pyrene as an important fluorophore, has been widely used to build fluorescence chemo-sensors due to its high sensitivity for detection through excimer formation.[82] More importantly, a ratiometric fluorescence may be achieved when pyrene is introduced into chemo-sensors, which can effectively eliminate most interferences from the environment by built-in correction of two emission bands. Ratiometric fluorescence is defined as the ratio of the excimer to monomer emission of the pyrene units. Therefore, it has been widely used to evaluate the concentration of the analyte.

Yam *et al.* reported a positively charged pyrene probe (**1.22**) for sensing of nucleic acid in an aqueous buffer solution.[83] In presence of oligonuecleotide, the probe exhibited a remarkable change in the fluorescence and UV-Vis absorption spectra. In case of fluorescence, the probe showed a significant decrease in emission from the monomeric form of pyrene probe and the concomitant appearance of a red-shifted, broad pyrene emission band which was assigned to

excimer emission of pyrene unit. In that year, they developed another synthetic polymer connected with a boronic acid group and a pyrene derivative containing a quaternary ammonium group (**1.22**).[84] The addition of glucose to an aqueous buffer solution containing both the boronic acid-containing polymer and the pyrene derivative, caused the formation of a very broad, red-shifted, new structureless band which can be assigned as the excimer band of the pyrene derivative. In the presence of glucose, the polymer containing multiple boronic acid functional groups is converted into a polyanion and as pyrene contains positive charge, it undergoes electrostatic interaction. As a result, the concentration of the probe molecule are increased in the vicinity of the polymer. So, the hydrophobic π–π interaction between the pyrene moieties increases and an enhanced excimer band is observed. Cao *et al.* reported a fluorescent sensor (**1.23**) for detection of mercury based on pyrene derivative with high selectivity in aqueous medium.[85] The probe showed typical monomeric emission when excited at the excitation wavelength. Upon addition of mercury salt, a significant fluorescence quenching was observed due to the chelation enhanced quenching (CHEQ). Later, the same group developed another pyrene containing fluorescent sensor (**1.24**) for lead detection.[86] The probe exhibited characteristic spectral features of pyrene monomer in the 365–425 nm spectral region but in presence of lead salt, the fluorescence emission spectrum of **1.24** also displayed an excimer band at 469 nm together with a decrease of the emission intensity of monomeric band. Das

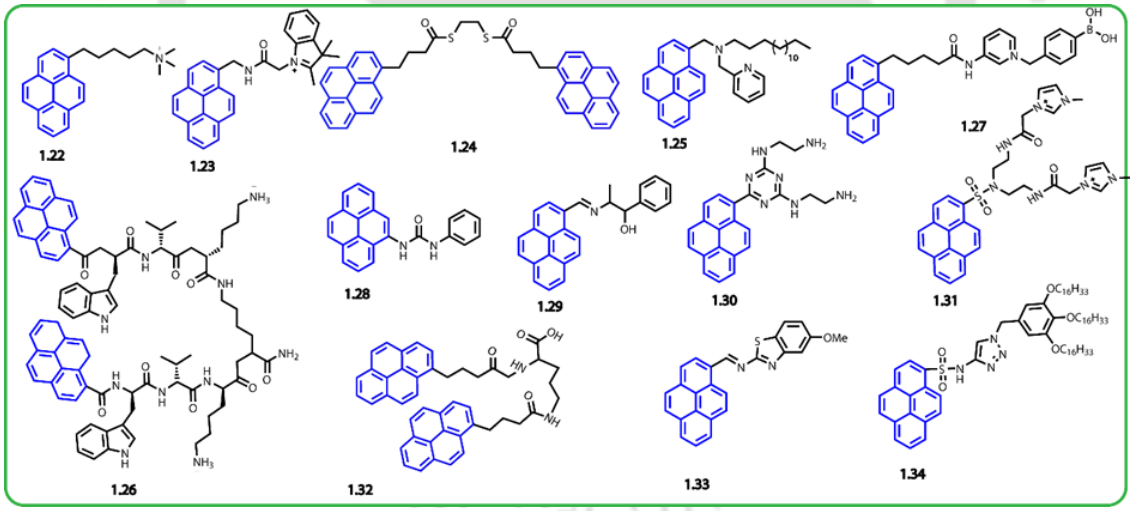

Figure 1.5 Some reported Pyrene based chemo-sensors.

et al. prepared a new fluorogenic compound (**1.25**) for Hg^{2+} detection.[87] The derivative **1.25** showed an excimer band with the monomeric emission of the pyrene unit. In presence of Hg^{2+}, the intensity of the excimer band decreases along with enhancement of the monomeric band. Schmuck and co-workers reported a pyrene-based peptide beacon (**1.26**) which is capable of intercalating with DNA.[88] The beacon exhibited a typical excimer band in solution state due to its folded nature. In presence of DNA, the beacon undergoes a conformational change from folded state to unfolded state and as a result it showed monomeric emission pattern rather than excimer emission.

An aggregation-based glucose sensor (**1.27**) has been developed by Jiang's group for sensing of glucose.[89] The probe consists of a pyrene unit and a phenyl boronic acid derivative. In an alkaline (pH 10) medium, **1.27** exhibited small aggregates which showed only the pyrene monomer emission. Upon binding with glucose, **1.27** formed more ordered aggregates because one glucose molecule binds two boronic acid groups and the complex obtained are hydrophobic in nature, leading to the pyrene excimer emission. Fabbrizzi and Amendola group reported a fluorescent chemo-sensor (**1.28**), consisting of a pyrene unit and a urea binding group for sensing of F^- ion.[90] The probe showed pyrene monomeric emission but upon addition of F^- ion, the fluorescence intensity decreases (off) because of the electron transfer process occurring in the locally excited complex and the conversion of locally excited complex to poorly emissive excited tautomer. Interestingly, upon further addition of F^- ion, a new emission band was observed with a yellow fluorescence which can be attributed to a charge transfer emission by the deprotonated receptor. Das *et al.* prepared a pyrene based schiff base (**1.29**) probe for sensing of lysine.[91] The probe **1.29** showed typical emission bands at 404 and 505 nm, attributed to pyrene monomer and excimer emissions respectively. Upon addition of Lys to **1.29**, the intensity of monomer emission band significantly decreases whereas a gradual increase of excimer band was observed.

Anzenbacher Jr. and Co-workers developed three pyrene based fluorescent chemo-sensors for sensing RDX out of which **1.30** showed higher selectivity over others.[92] The fluorescence intensity is increased in presence of RDX because of the imine formation. Fang's group designed a pyrene based fluorescent sensor (**1.31**) for sensing of heparin and then they have used this complex (pyrene with heparin) for detection of protamine in water.[93] The probe showed monomer emission in aqueous medium. In presence of heparin, the monomer emission is significantly reduced along with gradual enhanced excimer emission with a color change of the solution from dark blue to bright green. When protamine was added to this complex solution, the monomer intensity is significantly enhanced, at the same time the excimer emission is gradually reduced due to strong heparin binding affinity. The higher binding constant of protamine is able to compete with the cationic probe and thus releasing the probe from the complex. As a result, the probe emits monomer emission. Another pyrene based fluorescent sensor (**1.32**) was developed by Ma's group for detection and removal of Fe^{3+} and Pb^{2+} from aqueous solution.[94] The probe exhibits an intense excimer band and a weak monomer emission around 370–400 nm in Water-ACN (v/v = 3:2). Upon addition of Fe^{3+}, the emission bands of the probe decreased dramatically with decrease in fluorescence intensity. Under UV light, the color of the solution changed from green to colorless. Bhosle *et al.* prepared a pyrene-based chemo-sensors (**1.33**) connected with a benzothiazole ionophore for the "turn-on" sensing of Fe^{3+} and Fe^{2+} ions.[95] The chemo-sensor showed optical as well

as colorimetric changes towards Fe^{3+} and Fe^{2+} ions along with a remarkable enhancement in fluorescence emission. Cao *et al.* prepared an amphiphilic probe (**1.34**) consisting of a pyrene fluorophore and a hydrophobic cetyl chain for the sensing of Hg^{2+}. The probe showed monomer emission and in presence of Hg^{2+}, the fluorescence intensity decreases.[96]

1.3.3 Peptide Self-assembly

One of the characteristic properties of a peptide is the self-assembly which leads to different secondary structure. The secondary structures are regulated by different non-covalent interactions like hydrogen-bonding, salt-bridge, $\pi-\pi$ stacking, hydrophobic interactions *etc.* The common secondary structures are α-helix, β-sheet, β-hairpin, β -turn.[97]

1.3.4 Chemo-sensors Based on Peptide Self-assemblies

Peptide based soft materials are gaining increasing attention in the context of sensor field. Some of the peptide based sensors are summarized below. Lee *et al.* prepared a new peptidyl fluorescent chemo-sensor (**1.35**) for selective detection of mercury ions in which two pyrene (Py) fluorophores are attached to a tetra peptide using sulfonamide group.[98] The peptide **1.35** showed both monomer emission and excimer emission band in buffer solution. Upon addition of Hg^{2+}, the intensities of monomer and excimer emissions decreased significantly due to the quenching effect of Hg^{2+}. Lee *et al.* have prepared three pyrene based short peptides (**1.36**, **1.37**, and **1.38**) consisting of arginine units for monitoring heparin in serum samples.[99] Among these three peptides, **1.37** and **1.38** showed typical pyrene monomeric emission band with an excimer band. When heparin is added to the **1.37**, there is a decrease in the pyrene monomer emission band as well as increase of the pyrene excimer band with a clear iso-emission point. Similar change was observed in case of **1.38** but the fluorescence response is higher compared to **1.37** due to the electrostatic interaction between the positively charged arginine group and negatively charged heparin.

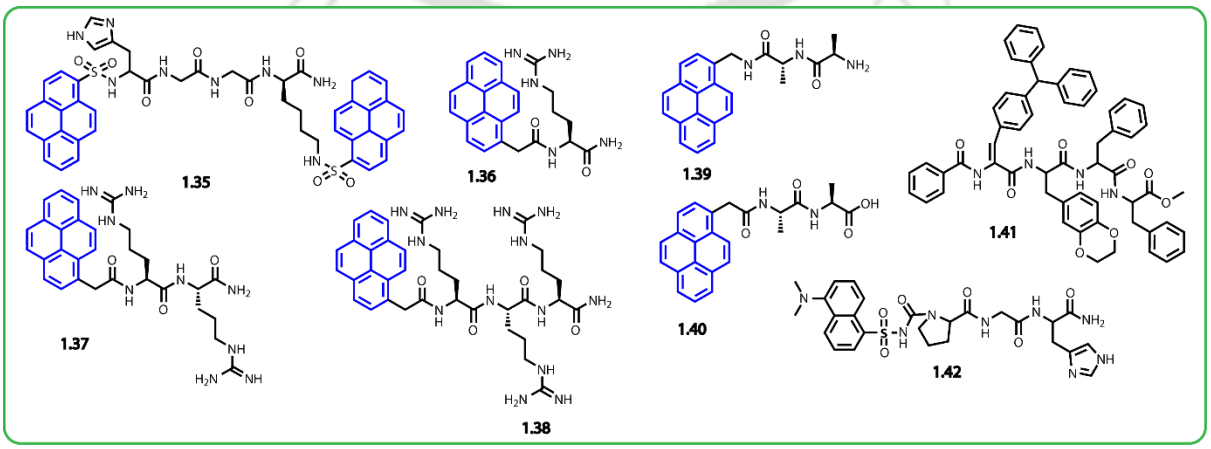

Figure 1.6 Some reported peptide based chemo-sensors.

Recently, Govindaraju *et al.* reported two anti- parallel β-sheet forming peptides (**1.39** and **1.40**) in which the N-terminus are connected with pyrene.[100] These two peptides form hydrogel when mixed into 1:1 molar ratio and the gel can be used as a fluorescence sensor for nitro explosives. The 1:1 mixture of **1.39** and **1.40** exhibited an excimer band which could be due to the effective cofacial π–π stacking between the pyrene chromophores in the bicomponent assembly state. In presence of nitro explosives, the excimer band intensity get quenched due to the PET from an excited pyrene to the electron deficient nitro-aromatic compounds. Ramanathan *et al.* designed a tetrapeptide (**1.41**) for self-assembly and its application as a mercury sensor.[101] The emission spectra of ligand have a weak emission but in presence of Hg^{2+}, the enhancement in fluorescence intensity of peptide was observed with a blue shift and it gave rise to a colour emission change from light yellowish to cyan under UV light. Liu *et al.* prepared a peptide-based fluorescent chemo-sensor (**1.42**) for sensing of Zn^{2+} in aqueous media.[102] The peptide showed moderate fluorescence intensity but in presence of Zn^{2+}, the fluorescence intensity increases due to the binding with the imidazole moiety of the peptide.

1.4 Some Important Analytes and their Reported Chemo-sensors

In recent years, the recognition and detection of environmentally and biologically important analytes has become an essential research topic in chemistry, biology as well as in material chemistry. So, we attempt to describe the recent development of chemo-sensors based on **NDI**, **PDI** and pyrene derivatives in a systematic and inclusive manner.

1.4.1 Base Sensors

Detection of amines is important for monitoring industrial and environmental pollution, checking the quality of food products and medical diagnosis of certain diseases.[103] Zang *et al.* prepared fluorescent ultrathin nanofibers from perylene monoanhydride imide (**1.43**) for sensing of amine

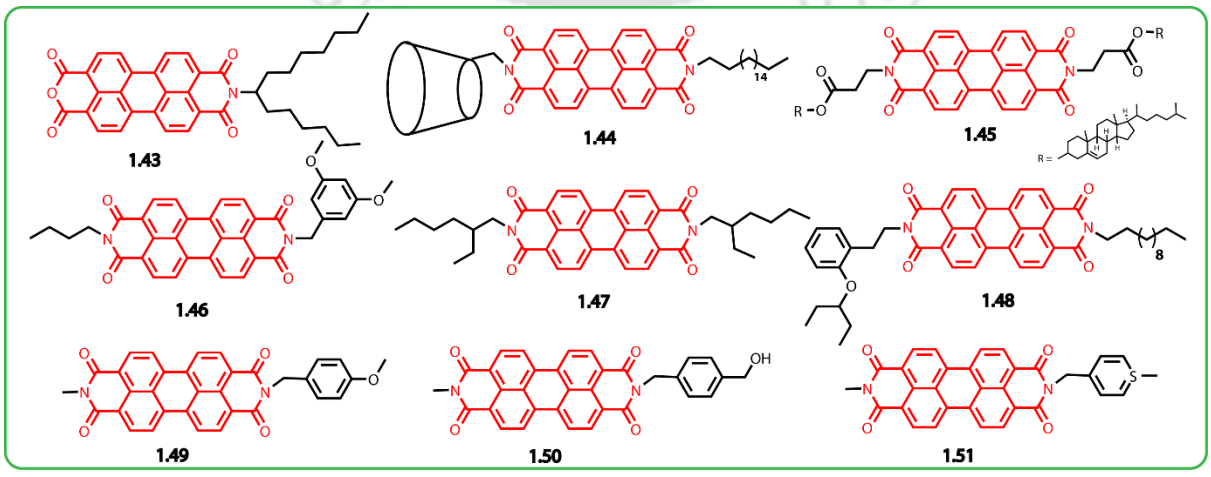

Figure 1.7 Some reported base sensors.

vapours.[104] In presence of amine vapours, the fluorescence gets quenched due to the increased surface area and the enhanced exciton diffusion along the long axis of nanofiber. Liu *et al.* designed an asymmetric amphiphilic **PDI** derivative (**1.44**) by grafting permethyl-β-cyclodextrin at one side and an octadecyl chain at the other side.[105] They have checked the aggregation study of **1.44** in pure methanol and Water-MeOH binary solvent mixture and the resulting aggregate was used for the sensing of amines. As the aggregates of **1.44** showed solid-state emission, it can act as fluorescent sensory material for amine vapour detection. In presence of amine vapour, the fluorescence get quenched due to two reasons: one is photoinduced electron transfer from analytes to **1.44** and the other is the inclusion of analytes into the cyclodextrin cavity which disturbs the well-ordered π-π stacking of **PDI** backbones.

In another example, Fang *et al.* prepared a nanofilm from a symmetric **PDI** derivative (**1.45**) connected with cholesterol units at both the N-terminus of the **PDI** core.[106] The fluorescence of the nanofilm gets quenched in presence of organic amine vapors. The nanofilm exhibited moderate higher fluorescence but in presence of amine vapours the fluorescence decreases because of the electron transfer between the electron rich amine to electron deficient **PDI** core. Later Zhao *et al.* reported fluorescent bilayer nanocoils assembled from an asymmetric perylene diimide molecule (**1.46**) which is very sensitive to amine vapours.[107] The nanocoil formed is highly emissive with a fluorescence quantum yield of 25%. When the nanocoil is deposited onto a glass substrate, it exhibited ultra-sensitivity to trace amines. Valiyaveettil *et al.* designed and prepared a perylene dimide based probe (**1.47**) for sensing of organic amines in solution phase. Upon addition of a series of aliphatic primary, secondary, tertiary and aromatic amines to the solution of **1.47** in THF, instantly the fluorescence quenching was observed which could be due to photoinduced electron transfer from HOMO of electron donor amines to HOMO of **PDI**. [108]

Zhao *et al.* reported an asymmetric perylene diimide derivative (**1.48**), exhibiting high sensitivity and selectivity to amines in the vapour phase, which renders them capable of monitoring and assessing the deterioration of meat.[109]The asymmetric **PDI** derivatives are prone to assemble into a fluorescent nanotube which shows "turn-off" emission in presence of amine vapours. Sillanpää *et al.* prepared a series of structurally analogous PDIs (**1.49, 1.50** and**1.51**) and used as fluorescent sensor arrays. [110]These arrays displayed high sensitivity to amine vapours and allowed the fingerprint differentiation of different species.

For easy reference, a table containing prominent chemo-sensors for bases are tabulated in **Table 1.1** with their sensitivity and medium of function.

SL. No.	Material	Medium	Detection Limit
01	**PDI** derivative[104]	Solid state	5 ppt
02	**PDI** derivative[105]	Solid state	44 ppm
03	**PDI** derivative[106]	Solid state	150 ppt
04	**PDI** derivative[107]	Chloroform	0.8 ppt
05	**PDI** derivative[108]	THF	Not reported
06	**PDI** derivative[109]	Solid state	1.2 ppb
07	**PDI** derivative[110]	Solid state	6.67× 10^{-7} ppm

Table 1.1 A comparative chart of the detection limits for bases.

1.4.2 Palladium Sensors

Palladium is one of the important elements used in various industries, such as automobile, fuel cells, dental crowns and catalysts in drug synthesis. Its extensive use and thereby the produced waste has raised pollution in water bodies and soil. This in turn severely effects plants, animals and humans. Palladium influences our health and environment in an adverse way because it can bind to thiol-containing amino acids, proteins, DNA, and other biomolecules and thereby may disrupt variety of cellular processes.[111] Detection of palladium in aqueous medium is thus an important challenge for chemists. Below is brief description of reported chemo-sensors for palladium.

Liu *et al.* reported a water soluble colorimetric and fluorescent sensor for the detection of palladium based on a naphthalimde derivative (**1.52**) with high selectivity and sensitivity.[112] In presence of Pd^{2+}, it undergoes Pd^{0}-catalyzed cleavage of an allyoxy carbonyl group of amines and as a result **1.52** exhibited a visual colour change from colourless to jade-green as well as the fluorescence change was observed from blue to green through internal charge transfer (ICT) process. Furthermore, the probe was successfully used for ratiometric fluorescence imaging of Pd^{2+} in living cells. Wang *et al.* designed two novel NIR fluorescence probe (**1.53** and **1.54**) for selective detection

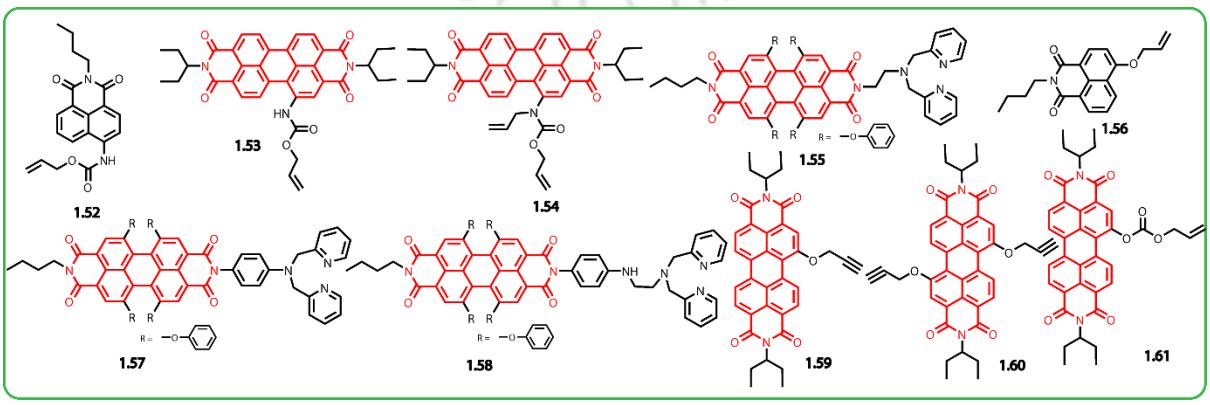

Figure 1.8 Some reported palladium sensors.

of palladium based on a perylene diimide based allyl carbonate derivative.[113] In presence of Pd^{2+}, deallylation of **PDI** occurs and as a result fluorescence quenching was observed along with a red shift Li *et al.* developed a series of **PDI** derivatives (**1.55**, **1.57**, and **1.58**) for sensing of Pd^{2+} ions in mixed aqueous media.[114] Out of these derivatives, **1.58** showed negligible fluorescence due to quick and efficient PET process from nitrogen lone pair of DPA to **PDI** fluorophore but in presence of Pd^{2+} ions, the fluorescence intensity is enhanced due to chelation of the DPA moiety with the Pd^{2+} ions. Zhang *et al.* reported a highly sensitive fluorescent chemo-sensor (**1.56**) for the intracellular Pd^{2+} imaging based on triphenylphosphine supported Pd-catalyzed deallylation. [115] In presence of Pd^{2+}, the probe undergoes Pd-catalyzed deallylation reaction and as a result, the emission spectrum got shifted to higher wavelength with a decrease of fluorescence.

In another example, Singh *et al.* prepared a new **PDI** based mono-propargyloxy derivative, **1.59** having N-(ethylpropyl) and N-cyclohexyl groups, respectively at imide positions and bis-propargyloxy derivative **1.60** substituted with N-(ethylpropyl) group at imide positions.[116] On addition of Pd^0, the fluorescence intensity of **1.59** gradually decreased due to photo induced electron transfer (PET) process**.** The cause of change in colour or fluorescence intensity of the solution of **1.59** on addition of Pd^0 could be attributed to de-propargylation. Singh *et al.* reported another allylcarbonate-functionalized perylene diimide (**1.61**) for sensing of palladium in solution as well as in solid state. [117] In presence of Pd^0, the alloc group cleaves and the fluorescence intensity gets diminished to provide **PDI**-OH.

For easy reference, a table containing prominent chemo-sensors for palladium are tabulated in **Table 1.2** with their sensitivity and medium of function.

SL. No.	Material	Medium	Detection Limit
01	**NMI** derivative[112]	Water : ACN (1:4, v/v)	6.1 nM
02	**PDI** derivative[113]	Water:THF (1:4, v/v)	Not reported
03	**PDI** derivative[114]	Water:DMF (1:7, v/v,)	7.32×10^{-9} M
04	**NMI** derivative[115]	PBS buffer (10 mM, pH 7.4)	1 nM
05	**PDI** derivative[116]	1. THF- HEPES buffer (1: 1, v/v, pH 7.3) 2. Water:DMSO (9:1, v/v)	1. 6.6×10^{-9} M 2. 2.1×10^{-8} M
06	**PDI** derivative[117]	Water:ACN (1:1, v/v)	39 nM (UV), 45 nM (FL), 0.58 pg cm^2 (solid state)

Table 1.2 A comparative chart of the detection limits for palladium ions.

1.4.3 Cyanide Sensors

Cyanide (CN) is one of the highly toxic anions that can affect many biological functions such as vascular, visual, central nervous, cardiac, endocrine and metabolic systems.[118] On the other hand, cyanide ions are widely used in numerous chemical processes, such as electroplating, plastic

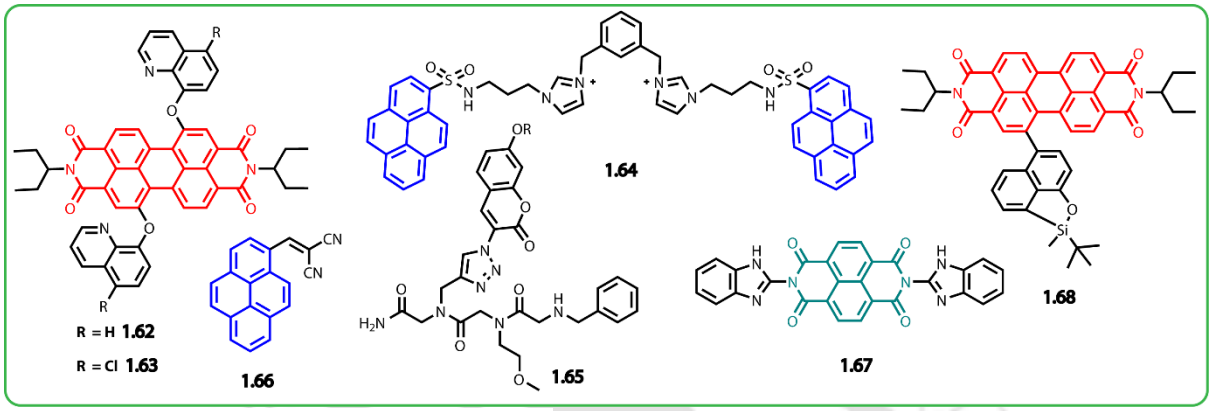

Figure 1.9 Some reported cyanide ion sensors.

manufacturing, gold and silver extraction, tanning and metallurgy. Therefore, trouble-free, inexpensive and easy-to-prepare colorimetric or fluorometric chemo-sensors with high selectivity and sensitivity could be a good option.[119] Kumar *et al.* reported **PDI** based chemo-sensors (**1.62** and **1.63**) for detection of cyanide ion in which the 8-hydroxy quinoline group is connected at the bay position of perylene core.[120] At first, it undergoes chelation with Cu^{2+} ion to form chelate complex and as a result, the fluorescence of **PDI** core gets quenched. When cyanide ion is added to the complex solution, the fluorescence is again enhanced due to strong complex formation between Cu^{2+} and cyanide ion and **PDI** molecule becomes free. Kim *et al.* prepared a pyrene based chemo-sensor (**1.64**) for detection of cyanide ion in a PBS–EtOH solution.[121] The probe **1.64** exhibited an excimer band with green fluorescence with the typical monomeric emission in the fluorescence profile and the excimer band is attributed due to strong π–π stacking between pyrene moieties. Upon addition of cyanide ion to the probe solution, the intensity of pyrene monomer as well as the excimer band decrease and the excimer band was completely diminished due to the synergistic effects of π–π interaction, ionic interaction, and hydrogen bonding.

Lee *et al.* reported a peptoid-based fluorescent probe (**1.65**) in which coumarin moiety was incorporated for the sensing of cyanide ion. The peptide undergoes dramatic quenching of fluorescence in presence of Cu^{2+} ion owing to the photo induced electron transfer, and the resulting peptoid-Cu^{2+} complex exhibited enhanced emission in presence of cyanide ion.[122] The enhanced emission is attributed to the complex formation between CN^- and Cu^{2+} ion to form $[Cu(CN)_x]_n$ complex which released the peptide from the peptoid-Cu^{2+} complex. As a result, the enhanced emission was observed. Velmathi *et al.* prepared a pyrene based fluorescent sensor (**1.66**) for

sensing of CN^- in aqueous media.[123] When CN^- was added to **1.66**, the fluorescence is decreased due to the Michael addition of cyanide to dicyanovinyl group of the probe. Wei *et al.* have prepared a fluorescent chemo-sensor (**1.67**) via a simple one step reaction through rationally combining benzimidazole and naphthalene diimide (**NDI**) moieties together.[124] Upon the addition of aqueous solution of cyanide salt into the DMSO solution of **1.67**, it shows an instant fluorescence enhancement and other anions couldn't interfere in the CN^- detection process. Singh *et al.* designed a perylene diimide based probe (**1.68**) in which the bay postion is functinalized with an O-silylated-8-hydroxyquinoline group.[125] The derivative **1.68** is capable of differentiating CN^- from F^- over other anions. When the CN^- ion is added, three is an electron transfer from cyanide ions to **1.68** which leads to the emergence of panchromatic and NIR absorption bands due to the formation of a radical anion. As a result, the fluorescence gets quenched.

For easy reference, a table containing prominent chemo-sensors for CN^- ions are tabulated in **Table 1.3** with their sensitivity and medium of function.

SL. No.	Material	Medium	Detection Limit
01	**PDI** derivative[120]	Chloroform	8×10^{-6} M
02	Pyrene derivative[121]	PBS–EtOH (5 : 95), pH = 7.4	13 ppb
03	Peptide[122]	DMSO	Not reported
04	Pyrene derivative[123]	ACN	1.76 nM
05	**PDI** derivative[125]	THF	Not reported
06	**NDI** derivative[124]	DMSO	8.32×10^{-7} M

Table 1.3 A comparative chart of the detection limits for cyanide ions.

1.4.4 Histone Sensors

Histone, the DNA-binding protein, has been gaining notable significance in clinical diagnostics. Abnormal epigenetic patterns have been found in many diseases like cancer, diabetes, microbial infections, HIV and others. In the case of a fatal mosquito-borne viral disease, dengue, the capsid protein of the virus binds with nuclear histone in liver cells and results in the inhibition of nucleosome formation and overexpression of histone. So, the need for a reliable, fast histone sensing method is gravely required.[126]

Hayashida *et al.* developed fluorescent rotaxanes (**1.69** and **1.70**) receptor composed of cyclophane as the wheel for histone-binding site and a 2,6-disubstituted naphthalene derivative having two fluorophore moieties, such as fluorescein and rhodamine residues, as the axle for fluorescence spectral changes upon complexation with histone.[127] In presence of histone, receptor **1.69** forms a

complex with histone in a 3: 1 molar ratio and as a result fluorescence intensity coming from fluorescein groups of **1.69** increased. A similar binding characteristic toward histone was observed for receptor **1.70**. The receptors show high selectivity compared to other acidic and neutral proteins. In addition, the pair of rotaxanes **1.69** and **1.70** exhibited FRET detection of histones. That is, upon addition of **1.70** to an aqueous solution containing histone and **1.69**, the fluorescence intensity originating from **1.69** at 518 nm decreased along with a concomitant increase in fluorescence intensity of **1.70** bound to histone at 576 nm by excitation at 430 nm of the fluorescein residues of

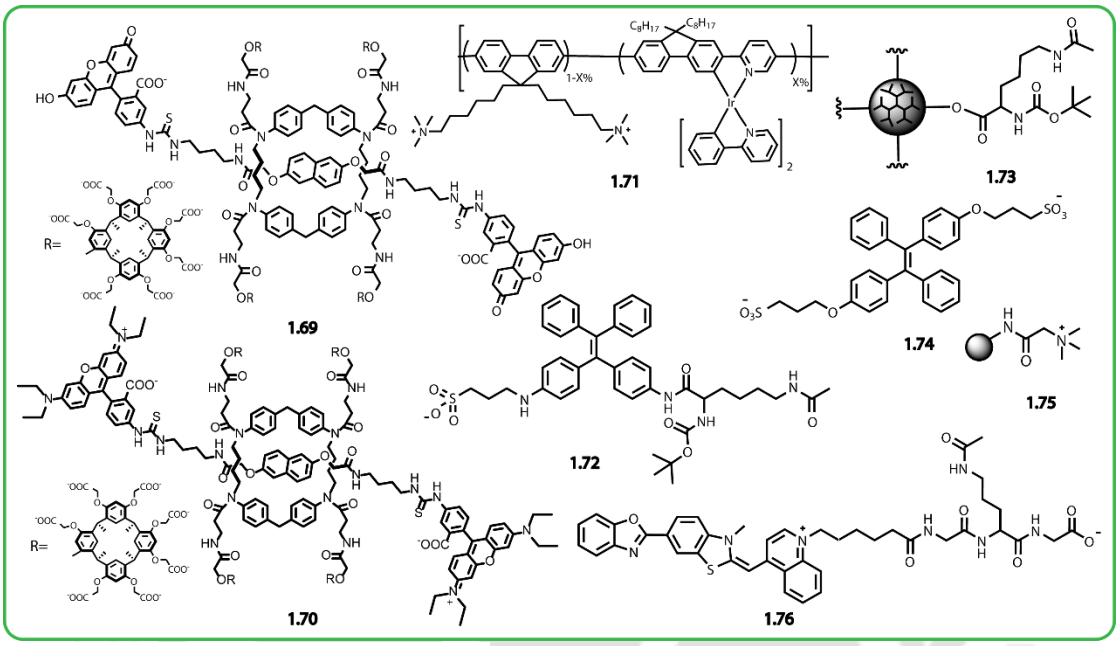

Figure 1.10 Some reported histone sensors.

1.69. Huang *et al.* designed and prepared iridium (III) complex containing cationic conjugated polyelectrolytes (CPEs) (**1.71**) with energy donor–acceptor architecture for detection of histone.[128] Investigation of emission responses of **1.71** toward proteins reveals a unique weakened FRET process from the main segments (donor) to the $(ppy)_2Ir(FlPy)$ units (acceptor) in presence of histone. Zhang and co-workers reported a novel approach for detection of histone proteins with high selectivity based on the recognition of a specific aptamer.[129] They have modified the aptamer with biotin, followed by attachment to streptavidin agarose beads. The beads selectively interact with histone and in addition this work might be highly attractive for chromatin histone marker identification in epigenetic research. Kikuchi *et al.* reported a fluorescent probe (**1.72**) based on tetraphenylethylene unit for detection of histone deacetylases (HDAC). [130] In the acetylated state, the probe exhibits weak fluorescence due to lack of aggregation of the probe. In presence of HDAC, the deacetylation of the probe occurs which helps in electrostatic interaction among the sulphonate unit and the cationic N-ε-ammonium ion which eventually leads to fluorescence enhancement based on aggregation-induced emission (AIE).

Wu's group reported a hyper branched polyester (**1.73**) based one-step fluorescent assay for HDAC.[131] This assay system consists of two water-soluble components: the hyperbranched polyester coupled with the acetylated lysine groups (H40-Lys(Ac)) and negatively charged tetraphenylethylene (TPE) derivative (**1.74**) bearing two sulfonic acid groups (TPE-2SO_3^-) HDAC triggers the deacetylation of H40-Lys (Ac), thereby turning the electroneutral polymer into positively charged one. Consequently, complexation occurs between the positively charged polymer and negatively charged **1.74**, thereby leading to the formation of nanoaggregates. Eventually, the fluorescence enhancement as a result of AIE effect is achieved. Das *et al.* prepared a quaternized carbon dot–DNA nanobiohybrid (**1.75**) which is used for the detection of histone.[126] The quaternized carbon dot forms complex with DNA and as a result the fluorescence gets quenched. Upon addition of histone, the fluorescence enhancement of the complex was observed due to strong binding between DNA and histone. Kikuchi *et al* designed and prepared a fluorogenic probe which is a DNA staining dye–peptide conjugate (**1.76**) containing an acetylated lysine, used for the detection of activity of histone deacetylases (HDACs), which are key enzymes involved in epigenetic gene regulation.[132] BOXTO is a DNA staining dye derived from thiazole orange (TO) that binds to the minor groove of DNA with high specificity and shows a strong increase in fluorescence upon binding to double-stranded DNA. The DNA-dependent fluorescence of BOXTO-GK (Ac) G was greatly enhanced upon deacetylation of the acetylated lysine moiety, owing to the increased DNA binding ability of the probe. Li *et al.* presented an effective approach to improve the fluorescence intensity and stability of DNA-templated CuNCs through histone–DNA interactions.[133]

For easy reference, a table containing prominent chemo-sensors for histone are tabulated in **Table 1.4** with their sensitivity and medium of function.

SL. No.	Material	Medium	Detection Limit
01	Resorcinarene tetramers[127]	HEPES buffer (0.01 M, pH 7.4)	Not reported
02	Conjugated polyelectrolytes (CPEs)[128]	PBS buffer(2 mM, pH = 7.4)	0.06 µM
03	DNA aptamer[129]	Water	Not reported
04	Cu nanoclusters[133]	MOPS buffer (10 mM, pH 7.6).	8.3 nM
05	Hyperbranched Polyester[131]	HEPES buffer (20 mM, pH 8.0)	0.025 µg mL^{-1}
06	Carbon –dot[126]	PB buffer (10 mM, pH 7.0)	0.2 ng mL^{-1}
07	Peptide Conjugate[132]	Tris buffer (20 mM, pH =8.0)	Not reported

Table 1.4 A comparative chart of the detection limits for histones.

1.4.5 Picric acid Sensors

Picric acid (PA) is highly explosive and toxic in nature. It can pollute ground water due to its higher solubility in water and causes severe poisoning, including skin and eye irritations, headache, nausea, vomiting, liver malfunction and chronic diseases such as destruction of erythrocytes, cyanosis, and cancer.[134] So, more attention needs to be paid for the rapid detection of PA with high selectivity and sensitivity.

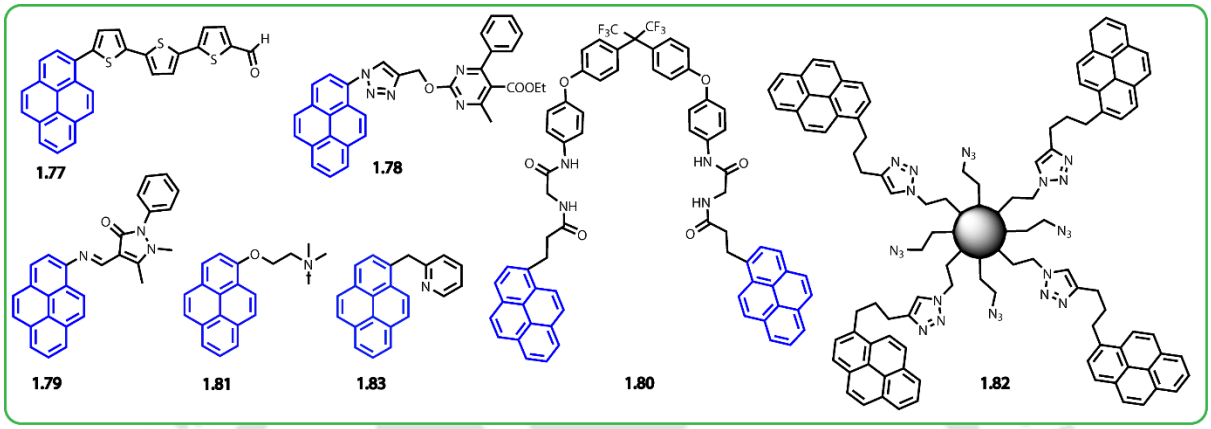

Figure 1.11 Some reported picric acid sensors.

Fang *et al.* prepared a pyrene derivative (**1.77**) connected with terthiophene group and the derivative can be chemically immobilized onto a glass wafer surface via a flexible spacer by employing a single-layer chemistry technique.[135] The film prepared from the derivative shows fluorescence due to presence of the fluorophore but upon addition of PA, the fluorescence intensity of the film was quenched due to possible proton transfer from quencher to the film surface. It is also true in case of vapour phase sensing. Singh *et al.* reported another pyrene probe (**1.78**) for sensing of PA in mixed aqueous media *i.e.*, in THF–HEPES buffer solvent mixture.[136] In pure THF, the probe showed a typical monomeric emission spectrum, but at higher percentage of HEPES buffer, the probe tends to aggregate due to overlapping of pyrene unit to form an excimer band and as a result, the emission intensity gets enhanced. Upon gradual addition of PA solution, the intensity band of the probe decreases.

Misra *et al.* prepared a pyrene based schiff base (**1.79**) connected with anti-pyrene group for sensing of PA in aqueous media.[137] The probe **1.79** showed an aggregation induced emission enhancement at higher percentage of water. The fluorescence intensity of the hydrosol prepared at higher percentage of water decreased with the addition of PA along with a red shift, signifying a charge-transfer interaction between them. Chae *et al.* designed and prepared a pyrene-based dipodal probe (**1.80**) with a range of molecular flexibility for PA detection.[134] Due to the presence of dipodal character, these probes show an excimer band and aggregation induced emission phenomenon. The emission of the probe gets quenched upon addition of PA due to the formation of probe-PA

complexes via π–π interactions between the pyrene ring and PA in an aqueous solution. This complex formation enabled energy transfer from electron-rich pyrene to electron-poor PA upon excitation, leading to fluorescence quenching. Wu *et al.* reported a pyrene based fluorescent sensor (**1.81**) functionalized with a quaternized ammonium group for rapid detection of PA in aqueous media.[138] When PA was added to the probe solution, there is a possibility of electrostatic interaction between positively charged probe and PA. Simultaneously, there are π–π stacking and charge transfer interactions which cooperate with electrostatic interactions, thereby leading to efficient fluorescence quenching of the probe. This approach affords a rapid detection of PA in 100% aqueous solution with high selectivity and sensitivity. Bicak *et al.* prepared a pyrene tethered microsphere (**1.82**) by anchoring of 1-[(2-Propynyloxy) methyl] pyrene] onto the surface of the microspheres via alkyne-azide click chemistry for the sensing of PA in aqueous media.[139] The pyrene-linked microspheres showed an intense green-blue excimer emission with a maxima at 480 nm, implying π–π stacking between pyrene moieties on the microsphere surfaces. This fluorescence emission is extremely sensitive to the aromatic nitro compounds. As a result, the green-blue light fades immediately upon addition of trace amounts of 2, 4, 6-trinitrotoluene (TNT), 2, 4-dinitrotoluene (DNT) and PA in 100% aqueous media. Laskar *et al.* reported a pyrene based schiff base (**1.83**) for detection of PA in aqueous media.[140] The compound exhibits aggregation induced phenomenon that means at higher water percentage the molecule shows higher fluorescence intensity. Upon addition of PA to aqueous solution of the probe, fluorescence intensity gets diminished. This is because of the acidic nature of PA which causes protonation of pyrene probe to change the fluorescence signal.

For easy reference, a table containing prominent chemo-sensors for PA are tabulated in **Table 1.5** with their sensitivity and medium of function.

SL. No.	Material	Medium	Detection Limit
01	Pyrene derivative[135]	Water	2.08×10^{-7} M
02	Pyrene derivative[136]	THF:HEFES buffer (10:90 v/v)	1.93 ppb 0.46 attogram (contact mode)
03	Pyrene derivative[138]	HEPES buffer (10 mM, pH 7.4)	23.2 nM
04	Pyrene derivative[137]	Water:ACN mixture (7:3, v/v)	16.51 nM
05	Pyrene derivative[134]	Water	0.13 pM
06	Pyrene derivative[140]	Methanol	56 nM

Table 1.5 A comparative chart of the detection limits for PA.

1.5 The Present Thesis

In the previous section, a detailed analysis of various fluorphores, their aggregation properties as well as uses toward development of new chemo-sensors is provided. Along with that, a brief description of various important analytes and the present status of their chemo-sensors is also given. In the present thesis, we were focused on developing chemo-sensors based on the self-aggregation and analyte induced dis-aggregation of the system. For that purpose, we have used **PDI**, **NDI** as well as Pyrene as the fluorogenic unit and rationally designed various self-aggregating molecules. These molecules were used for efficient and selective sensing of bases, histone, palladium, cyanide as well as PA. The entire work is divided into four chapters as given below,

Chapter 2. Solvochromism and Efficient Base Sensing by a Viologen-Perylenediimide Conjugate

In this chapter, a viologen- perylenediimide conjugate is prepared. This bola-amphiphilic viologen--**PDI** conjugate showed solvatochromism with generation of distinguishable colors in different solvents. Also, the probe exhibited its efficacy towards base in solution phase and solid crystalline phase.

Chapter 3. A Perylenediimide-Peptide Conjugate for Self-Assembly Assisted Tandem Sensing of Pd^{2+} and CN^-

Here, a tandem sensor for Pd^{2+} and CN^- ions based on perylenediimide-peptide conjugate is reported. Binding with Pd^{2+} leads to aggregation of the ligand and consequently results in quenching of its emission. The quenched emission can be turned on in presence of CN^- ions as the cyanides form stronger complex with Pd^{2+} leading to dis-aggregation of the aggregated system.

Chapter 4. Efficient Detection of Histone by a DNA –Naphthalenediimide Hybrid

In this report, a series of Naphthalenediimide (**NDI**) derivatieves are subjected to DNA binding studies for the sensing of histone, a DNA binding protein. The strong binding affinity of histone toward DNA lead to release of the **NDI** molecules from the **NDI**-DNA complex resulting in enhancement of the fluorescence intensity and used as an efficient "turn-on" sensor for histone.

Chapter 5. Picric Acid Detection at Femtogram Level by a Short Peptide Gelator

This chapter describes the sensing of picric acid (PA), a well-known explosive based on a pyrene based short peptide gelator. The gelator molecule shows its efficacy and selectivity towards PA in solution phase as well as gel phase even in paper based systems with high sensitivity. In addition to that, the test strips can detect PA vapors in sub ppb level and are effective for detection of PA contamination in ground water.

Chapter 2

Solvochromism and Efficient Base Sensing by a Viologen-Perylenediimide Conjugate

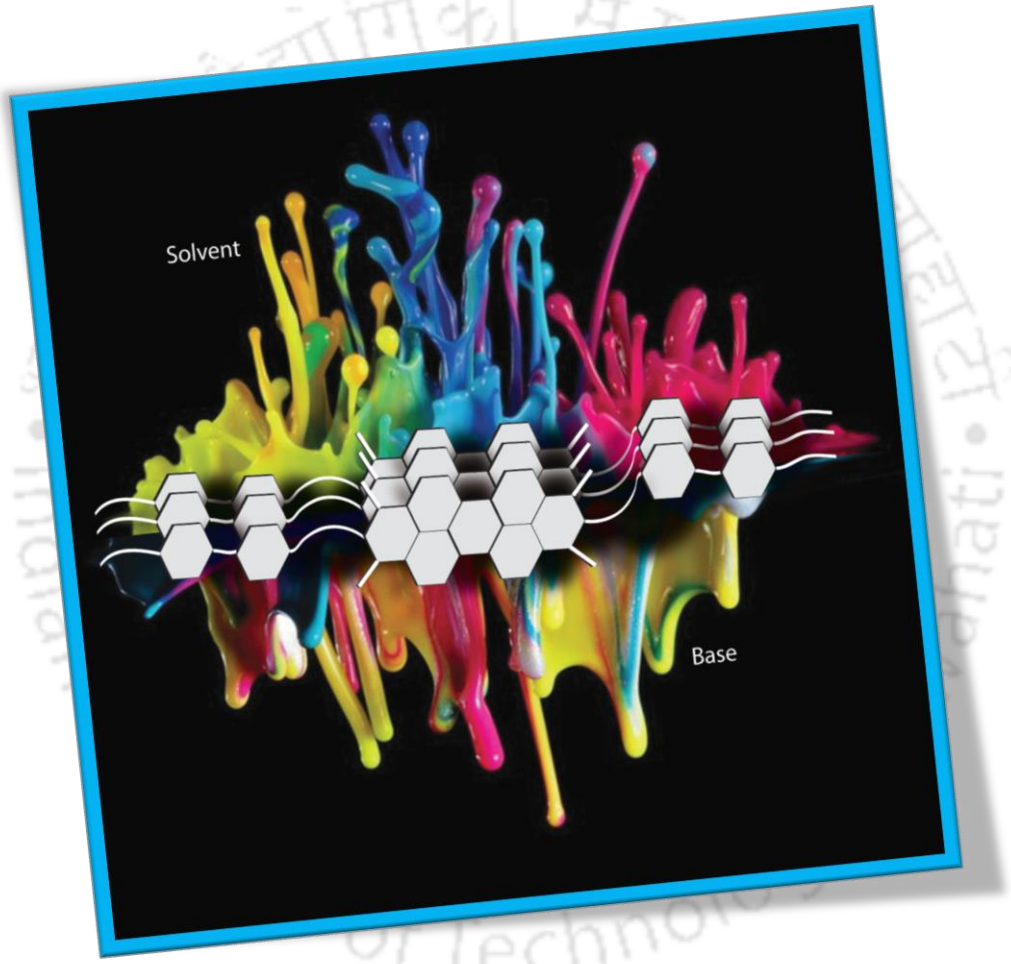

2.1 Introduction

Solvents and bases are two important constituents of the modern chemical industry and are produced and used in huge quantities. However, the inherent cytotoxicity and volatility of these chemicals have an adverse impact on the environment and effective ways to sense these toxic chemicals are essential. [141-142] Detectors allowing efficient visual sensing of solvent polarity and bases are therefore of great importance.

The sensitivity of viologen towards bases can be amplified by conjugating viologen units with a suitable fluorophore that can also act as an alternative to common solvatochromic probes. As discussed in chapter 1, perylenediimides (**PDIs**) are a well-studied class of fluorophores with excellent electronic, optical, and redox properties. [143-144] **PDIs** have recently emerged as very efficient moieties for the preparation of fluorescent sensors for a variety of species, especially because of their outstanding photochemical stability and high quantum yields.[143-144] In addition, the **PDI** chromophores have an added advantage in the design of sensors because of their inclination towards self-assembly through π--π stacking, electrostatic, and solvation interactions. [17, 46, 69] The presence of a planar π-conjugated core leads to the formation of both J- and H-type aggregates, depending on the functionalization at the imide positions and the medium (solvent).[50, 145-147] Aggregation of **PDIs** is associated with drastic effects on their photophysical properties.[17, 46, 50, 69, 143-147] The aggregation of **PDIs** and consequently the changes in their photophysical properties are highly influenced by the medium, and thus **PDIs** with appropriate conjugation can be solubilized in solvents with a wide range of polarity and used as solvatochromic agents.[148-149]

In this chapter, we have selected **PDI** as the emissive component of our sensor and prepared a viologen-**PDI** conjugate (**2.1**, **Scheme 2.1**). This bola-amphiphilic viologen-**PDI** conjugate showed solvatochromism with generation of distinguishable colors in different solvents. As expected, the presence of viologen units at the two termini of **PDI** make this compound an effective sensor for bases. Incorporation of the fluorophore significantly enhanced the base-sensing efficiency (sensitivity ≈1—77 ppb for various bases) compared to those of the previously reported viologen-based base sensors in the solution phase (sensitivity ≈130—1880 ppb for various bases) [150] and solid crystalline phase.

2.2 Results and Discussion

Viologens (**Scheme 2.1**) have found use as base sensors owing to their redox-controlled color change induced by charge-transfer complexation.[150-151] An important feature of viologens is their electron-deficient nature, which makes them very good electron acceptors.[152-154] Viologens undergo a fast and reversible two-step redox process and are capable of forming three different species:

dication, radical cation, and the neutral species (**Scheme 2.1**).[155-157] The charge transfer between N^+ and $N^{\cdot}$ of the radical cation makes them intensely colored.[155-157]

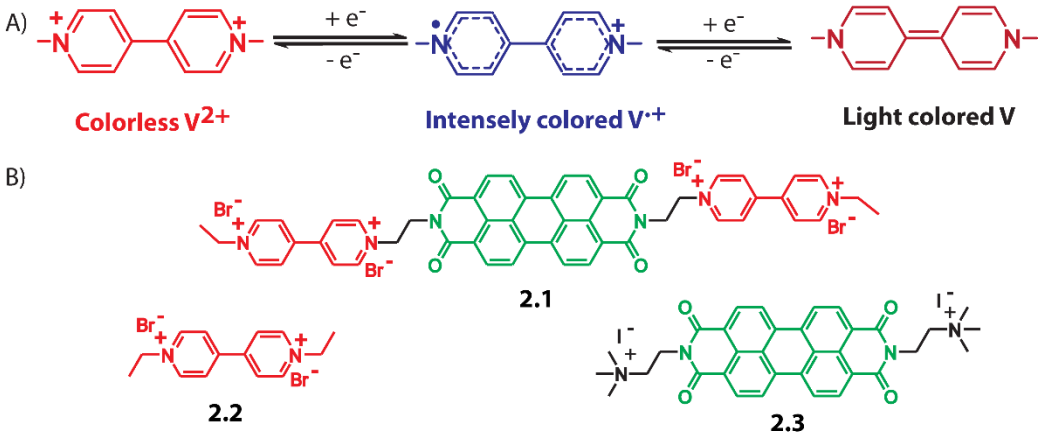

Scheme 2.1 A) Redox induced chromic process of viologens; B) Chemical structures of the compounds synthesized and used in this study.

The absorption spectra of **2.1** exhibited several absorption bands in the range between 200 nm - 800 nm which are arising from the viologen unit and **PDI** chromophore in aqueous medium. As the **PDI** core is predominantly responsible for the aggregation and emission, the absorption region corresponding to the **PDI** core (400—800 nm) is shown throughout this chapter. The compound **2.1** showed two prominent vibronic bands at 534, 494 and a shoulder at 464 nm which are attributed to the 0-0, 0-1, and 0-2 vibrational transitions.[48, 158] To check the aggregation behavior of the **2.1**, concentration dependent UV-Vis spectra was measured and it was observed that up to 2.6 x 10^{-5} (M) concentration, the absorbance value increases gradually with the progression 0-0> 0-1> 0-2 but after this concentration, the intensity order changes from 0-0>0-1 to 0-1>0-0, and this order reversal is characteristic of aggregation of the **PDI** core. In this process, the $A_{0\text{-}0}/A_{0\text{-}1}$ ratio decreased from 1.54 (0.1×10^{-6} M) to 0.85 ($\geq 2.6 \times 10^{-5}$ M). Thus, 2.6×10^{-5} M can be considered to be the minimum aggregation concentration (MAC, **Table2.1**).

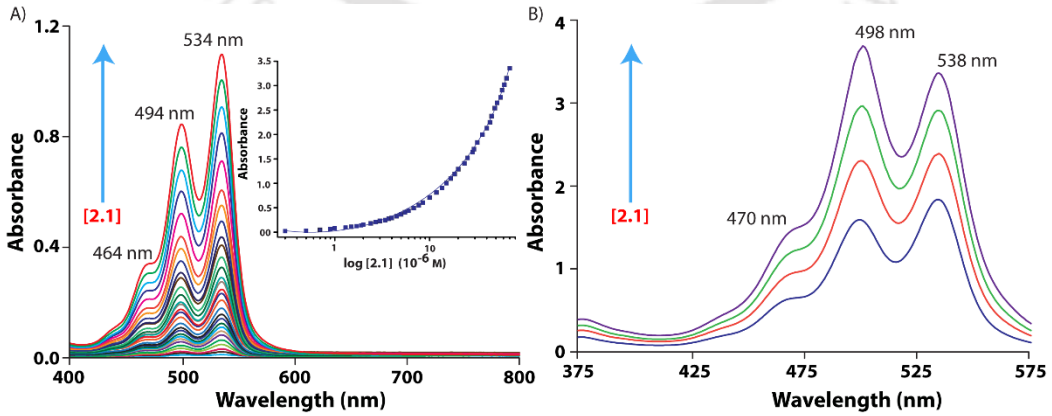

Figure 2.1 Absorption spectra of **2.1** in water with varying concentrations. A) up to 2.6×10^{-5} M, and B) above 2.6×10^{-5} M showing the reversal of order of 0-0, 0-1 transitions above this concentration. Inset of A) plot of absorbance at 534 nm versus log [**2.1**] showing the inflection point.

The emission spectrum of **2.1** in water is the mirror image of the absorption spectrum with a Stokes shift of 12 nm. The fluorescence spectra showed three emission peaks at 549, 588, and 639 nm.[56] Notably, the concentration-dependent emission pattern also showed a drastic change at 2.6×10^{-5} M. The initial linear enhancement of the intensities with increasing **2.1** concentration suddenly took on a negative slope above 2.6×10^{-5} M. Above a concentration of 1×10^{-4} M, no measurable emission intensity was observed. The decrease in the emission intensity and complete loss of emission can presumably be explained in terms of self-quenching by stacked arrangements of molecules. The inflection point at 2.6×10^{-5} M is very similar to the MAC obtained from absorption spectra and can be regarded as the concentration above which all the molecules remain in aggregated form.

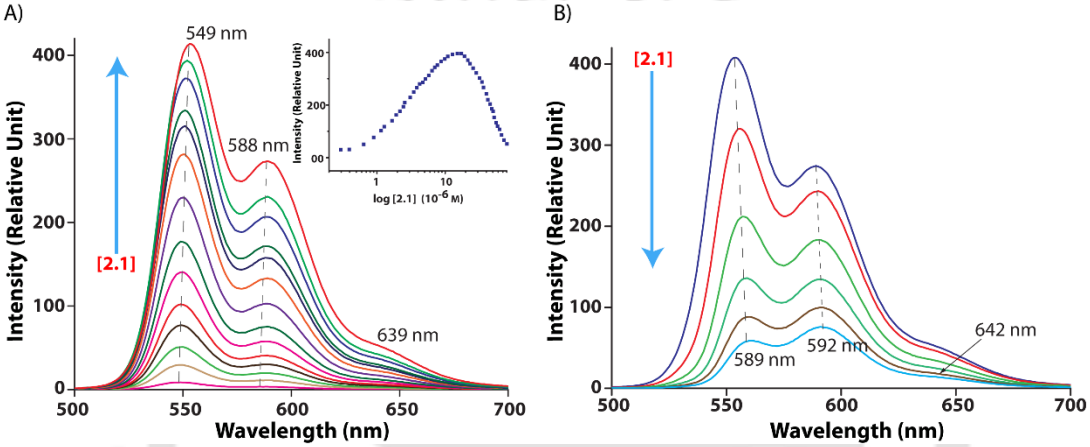

Figure 2.2 Emission spectra of **2.1** in water with varying concentration A) up to 2.6×10^{-5} M, and B) above 2.6×10^{-5} M showing the decrease in emission intensities after this concentration. Inset of A) plot of absorbance at 534 nm versus log [**2.1**] showing the inflection point.

Solvents	$E_T(30)$/ kcal mol^{-1}	E_T^N	λ_{abs} (nm)	$\bar{\nu}_{abs}$ (cm^{-1})	λ_{em} (nm)	$\bar{\nu}_{em}$ (cm^{-1})	$\Delta\bar{\nu}$ (cm^{-1})	Φ_f	MAC ($\times 10^{-6}$ M)
Water	63.1	1	534	18727	549, 588	18215	512	0.06	**26**
MeOH	55.4	0.762	530	18868	536, 574	18656	212	0.04	**32**
EtOH	51.9	0.654	528	18939	537, 575	18622	317	0.08	**12**
ACN	45.6	0.46	526	19011	533, 572	18762	249	0.06	**12**
DMSO	45.1	0.444	524	19084	539, 577	18553	531	0.06	**20**
DMF	43.2	0.386	523	19120	542, 581	18450	670	0.08	**8.2**
Acetone	42.2	0.355	522	19157	523, 562	19120	37	0.03	**5.2**

Table 2.1 Photophysical parameters of **2.1** in different solvents.

2.1 has fairly high solubility in water, DMF, DMSO, methanol (MeOH), ethanol (EtOH), acetonitrile (ACN), and acetone. The concentration-dependent studies in these solvents exhibited similar behavior as in case of water as shown in **Figure 2.3**. However, a sudden change in the absorption in all these solvents was observed above a particular concentration but no peak reversal was observed in any of these organic solvents.

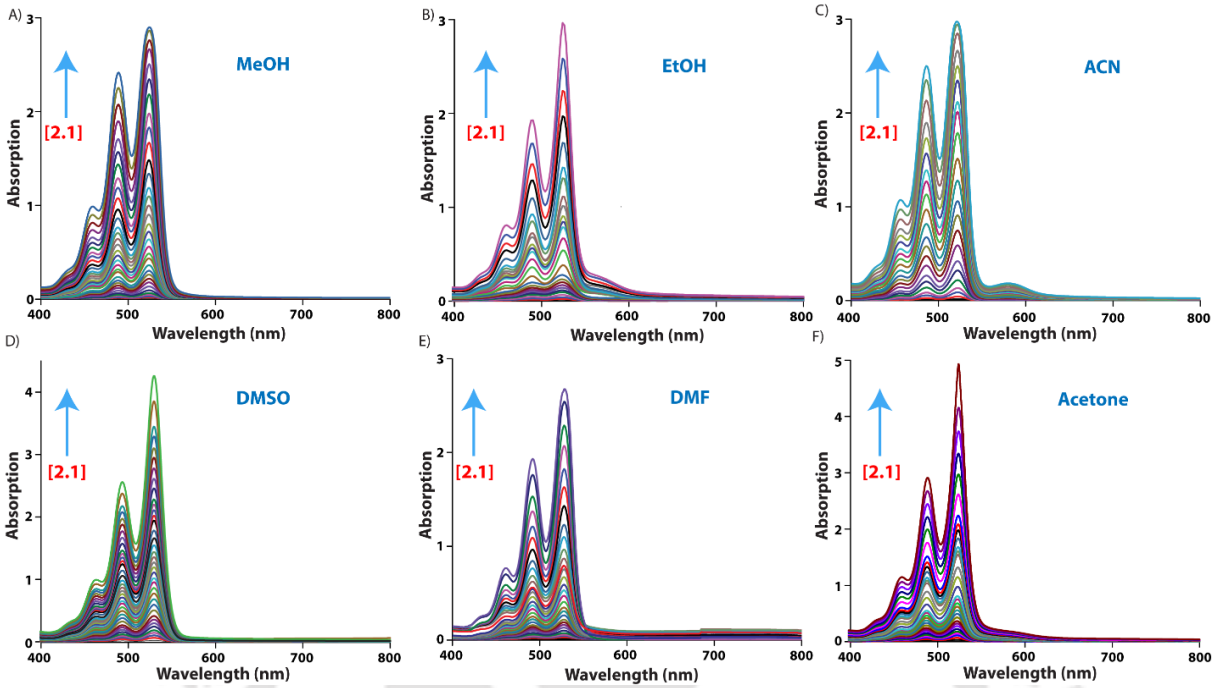

Figure 2.3 Concentration dependent absorption spectra of **2.1** in A) MeOH, B) EtOH, C) ACN, D) DMSO E) DMF, and F) Acetone at room temperature.

As in the case of water, the fluorescence intensities increased with increasing concentration, and a sharp decrease was observed above a certain concentration. The inflection points in both absorption and emission spectra were obtained at very similar concentrations for a particular solvent.

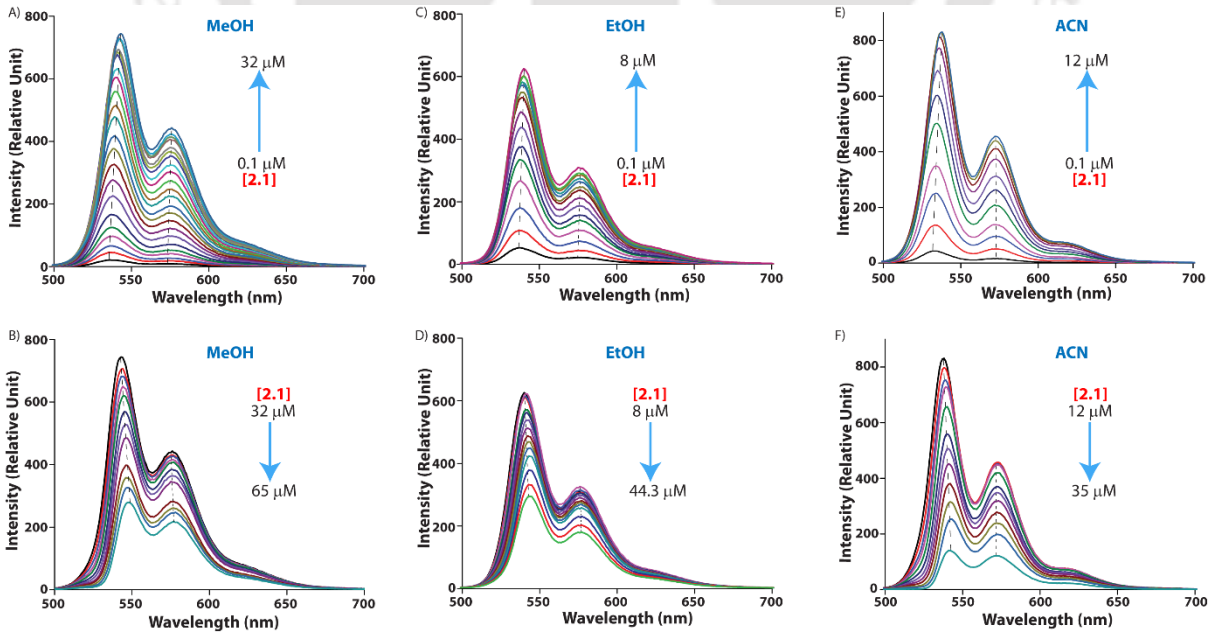

Figure 2.4 Concentration dependent emission spectra of **2.1** in A, B) MeOH, C, D) EtOH, E, F) ACN at room temperature.

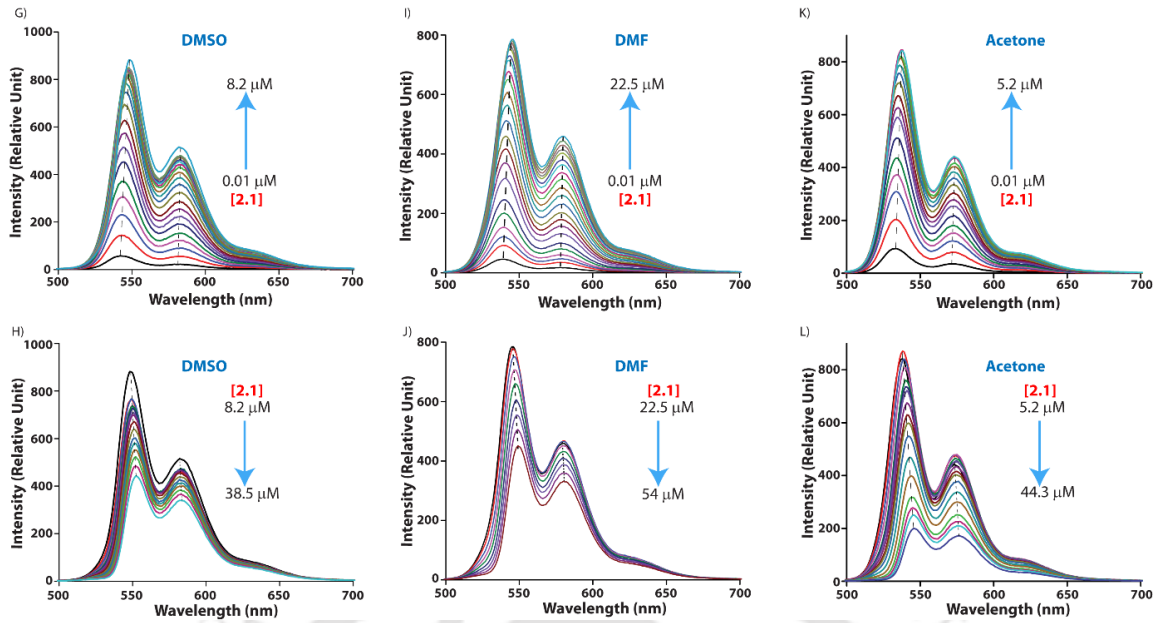

Figure 2.5 Concentration dependent emission spectra of **2.1** in G, H) DMSO, I, J) DMF, K, L) Acetone at room temperature.

Then at low concentration where the **2.1** molecule remains as a monomer, the UV-Vis and fluorescence spectra of **2.1** in different solvents was measured (1×10^{-6} M) and it was observed that there is a clear bathochromic shift in the peaks generated from 0-0, 0-1, and 0-2 vibrational transitions with increasing solvent polarity as shown in **Figure 2.5**. The absorption maxima of **2.1** show good linear correlation with the $E_T(30)$ values (parameter indicative of solvent polarity and hydrogen-bond donating ability) of the solvents and shift to lower energies with increasing $E_T(30)$ value. This can probably due to the presence of dicationic viologen units at both ends of **2.1**, which stabilize the excited states with increasing solvent polarity.[17]

The emission of **2.1** in these solvents, except DMF and DMSO (hydrogen-bond-accepting solvents), also show similar changes in the emission-band positions. A red shift was observed for all the peaks on moving from nonpolar to polar solvents as shown in **Figure 2.6**.[29,54] However, the quantum yields Φ of **2.1** in these solvents, determined by using rhodamine 6G as standard, did not reveal any correlation with solvent polarity (**Table 2.1**). Interestingly, **2.1** exhibited different colours in these solvents which indicates the solvatochromic property. (**Figure 2 .6**) The aqueous solution of **2.1** was reddish orange in color, while the color changes to pale straw yellow to dark straw yellow in ACN and DMSO respectively. Under UV light (365 nm), the same solutions fluoresce differently, as can be expected from the emission studies. On moving from water to the less polar acetone, the color of the emitted light changes from dark orange (water) to fluorescent yellow (ACN) to fluorescent greenish yellow (acetone).

Then the effect of pH on the spectroscopic behavior of **2.1** was tested by varying the pH of the solution using various buffer solutions. The UV-visible spectra of **2.1** in different pH are shown in

Figure 2.7. The three absorption peak pattern is clearly seen for the entire pH range of 1-13. Notably, the absorption corresponding to the 0-1 transition was observed to be higher than that of the 0-0 transition suggesting the aggregated state even at this low concentration (1×10^{-6} M) which is much lower than the observed MAC in water.

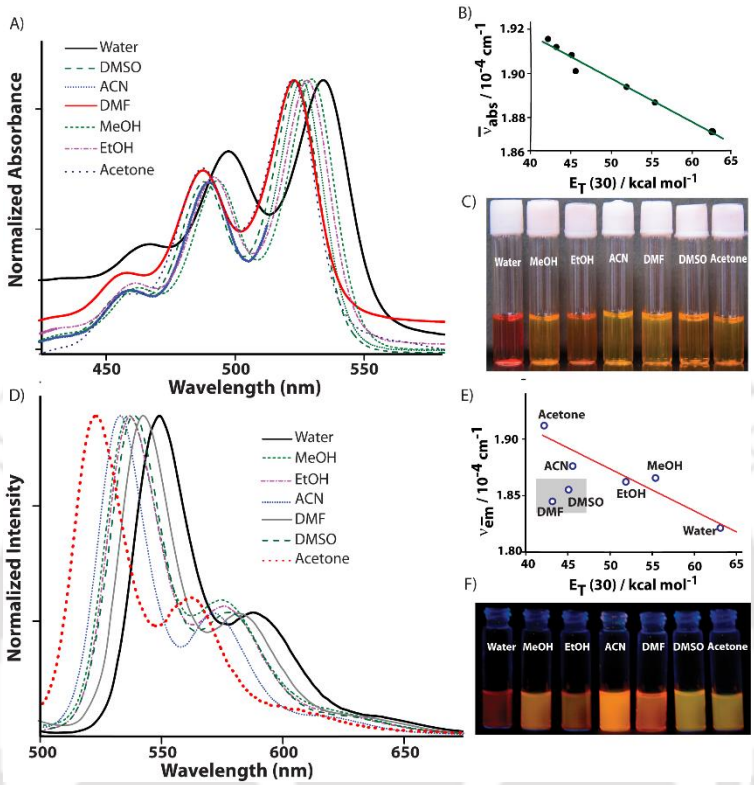

Figure 2.6 A) Normalized absorption and C) normalized emission spectra of **2.1** in different solvents. B) $\bar{\nu}_{abs}$ vs $E_T(30)$ of solvents, E) $\bar{\nu}_{em}$ vs $E_T(30)$ of solvents plots. Photographic images of **2.1** in different solvents, C) under normal light, and F) under UV light (λ = 365 nm). [**2.1**] = 1×10^{-6} M.

With increase in pH, the absorption corresponding to all three transitions decreased while the ratio between signals arising from 0-1 and 0-0 transitions enhanced consistently. At extremely high pH (pH 13), all the peaks showed significant hypsochromic shifts (~ 35 nm) as well as a significant decrease in the absorption from 0-0 transition observed. The change in the **PDI** core related absorption at higher pH was also associated with the appearance of new bands in the near infrared (NIR, 700-1000 nm) region. The new peaks in the NIR region at pH 13 can be attributed to the reduced species generated from **2.1** at this highly basic condition. The new bands in the NIR region is characteristic of the viologen radical cations (**Scheme 2.1**). The generation of the viologen radical cation is associated with a prominent change in the absorption spectra with three new bands (the positions of the bands depend on the substitution on the viologen units as well as on solvent).[144] In the present case, at pH 13, the new absorption profile can presumably be attributed to the overlapping of the radical cation absorption and the **PDI** absorption in the 400-500 nm range. Another broad absorption band can be seen at ~ 750 nm arising from the radical cation. The third

band in the NIR region is the most prominent signature of the formation of the viologen radical cation in the present case as shown in inset of **Figure 2.7A**. Though no visible change in the color of the solutions was observed up to pH 11, the solution turned slightly bluish at pH 13. The generation of the blue color is also a well-studied phenomenon of viologen radical cations. The formation of the radical cations on both terminals certainly affect the electronic transitions in the **PDI** core which results in the observed blue shifts.

The fluorescence spectra of **2.1** at various pH also showed a clear dependence of the emission property of **2.1** with pH of the system. Increasing the pH, caused a prominent decrease in the luminescence intensity as shown in **Figure 2.7B**. At pH 13, a sudden change in the emission pattern was also observed as the emission intensity dropped significantly and the fine emission structure is no longer visible. The change in the emission behavior at higher pH can also be attributed to the effect of the radical cations formed on the viologen units.

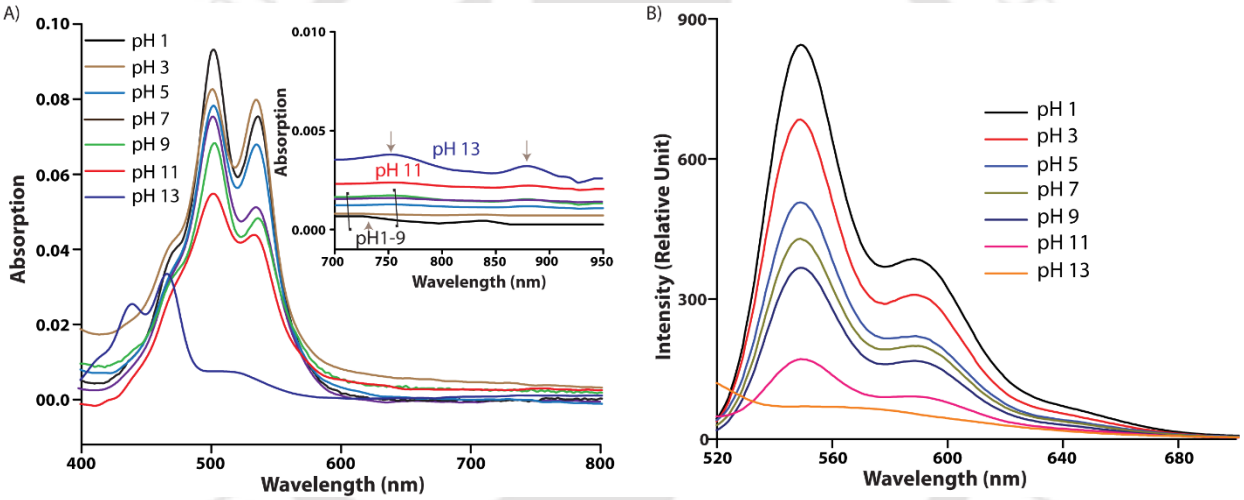

Figure 2.7 A) Absorption and B) emission spectra of **2.1** at different pHs. [**2.1**] = 1×10^{-6} M. [Buffer] = 2.0×10^{-2} M. Inset of A) Higher wavelength region of the absorption spectra.

The base sensitivity of **2.1** was checked in presence of six different amines [diisopropylethylamine (DIPEA), N, N-dimethyl-4-aminopyridine (DMAP), pyridine, piperidine, triethylamine (TEA), and triisopropylamine (TPA)] and NaOH. Addition of base to the **2.1** solution, the colour of **2.1** changed dramatically as shown in **Figure 2.8**. Compound **2.1** can act as a fast detector of amines for the naked eye. These prominent changes in color can be detected even at a concentration of 5×10^{-6} M in the presence of 1-2 equiv of base, which makes **2.1** a far superior and efficient visual base sensor to other viologen-based sensors.[10-11] Under the influence of UV light (365 nm), these solutions emit differently, and notably the visual detection limit further dropped to 5×10^{-7} M of **2.1**, which is the lowest ever reported to the best of our knowledge.

To gain insight into the possible reason behind such changes in color, we examined the absorption and emission behavior of **2.1** in the presence of various bases. When titrated with NaOH, the absorption profile of 2.1 showed a decrease in intensity up to an equimolar amount of NaOH as shown in **Figure 2.8**. Above this concentration, the absorption corresponding to the 0-1 transition becomes stronger than that of the 0-0 transition, owing to aggregation. With further increase in NaOH concentration (>2 equiv.), the absorption bands are blue shifted significantly and broadened. A similar absorption profile was observed at high pH as well (**Figure 2.7**). Along with these changes in the UV/Vis region, new bands started appearing in the NIR region at higher molar ratios (3-4 equiv.) as shown in **Figure 2.8**. The new bands in the NIR region and deep blue color suggest radical-cation formation.[155-156] Above this concentration, the material precipitated.

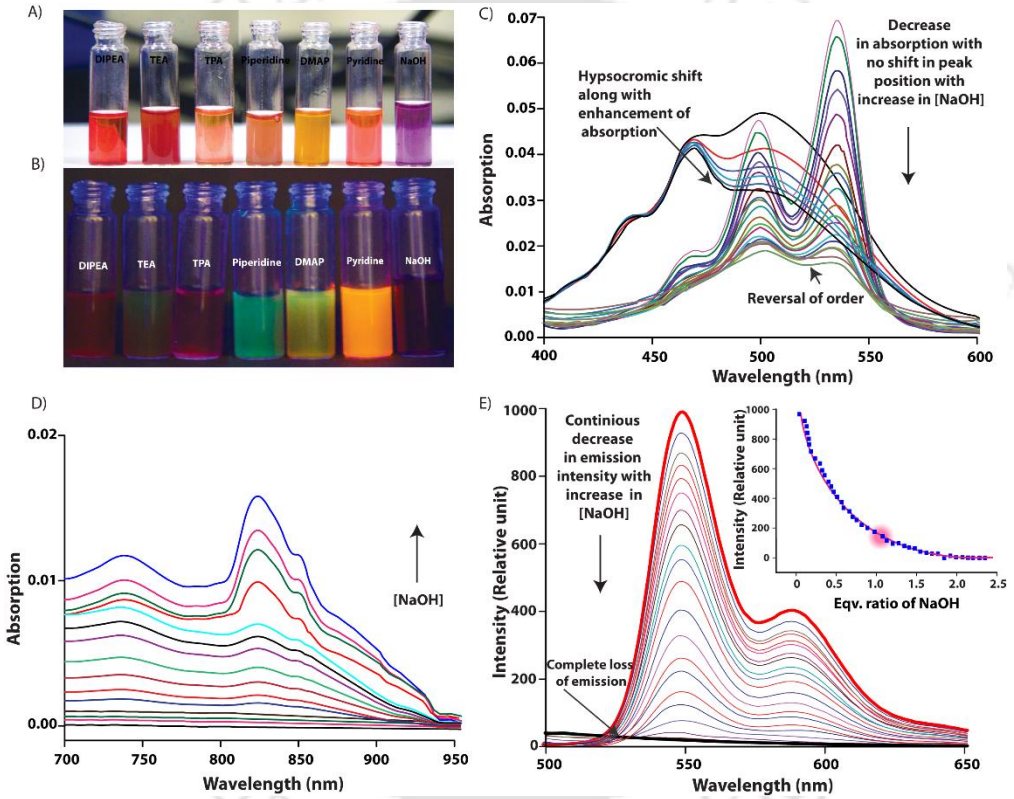

Figure 2.8 Photographic images of **2.1** in presence of different bases, A) under normal light [**2.1**] = 5×10^{-6} M and B) under UV light (λ = 365 nm), [**2.1**] = 5×10^{-7} M. Photographs were taken two minutes after the addition of aqueous (inorganic bases) or ACN (amines) solutions to an aqueous solution of **2.1** and mixing.C) Absorption spectra of **2.1** in water with increase in concentration of NaOH, D) same in the higher wavelength region showing the appearance of the viologen radical cation peaks, E) emission spectra of **2.1** in water with increase in concentration of NaOH. Inset of E) Intensity vs molar ratio of NaOH/[**2.1**] plot. F) under UV light (λ = 365 nm). [**2.1**] = 1×10^{-6} M.

SEM image of the precipitate showed extremely ordered flowerlike arrangements as shown in **Figure 2.9**. Aqueous solutions of **2.1** at concentrations below the MAC showed no prominent morphology, whereas above the MAC a highly ordered arrangement of bricklike structures was found. As expected, the fluorescence intensity decreased with increasing NaOH concentration without any significant change in the emission pattern as shown in **Figure 2.8**. The intensity versus concentration plot showed an inflection point when one equivalent of NaOH was added. At higher

concentrations of NaOH (>2 equiv.), the emission property vanishes completely. The blue shift of the absorption bands and complete loss of emission suggests H-type aggregation of the **PDI** core.[29]

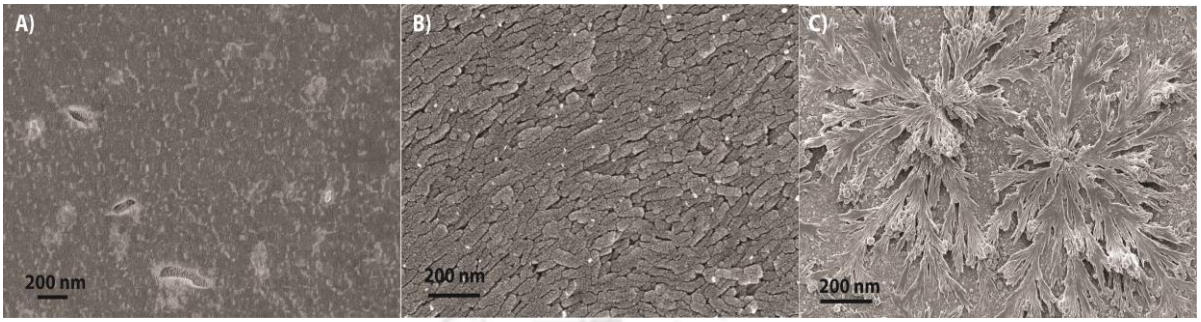

Figure 2.9. FESEM images of dried samples of A) 1 μM, and B) 50 μM aqueous solution of **2.1** and C) of the precipitate obtained from the 1 μM aqueous solution of **2.1** treated with 3 equiv. of NaOH. Image A shows no particular feature whereas image B indicates well-ordered brick arrangement of aggregated **2.1** molecules. Upon treatment with NaOH, a flower like growth is observed as can be seen in C.

Excitation spectra of the **2.1**/NaOH (1:2) solution collected at 575 nm showed a broad, structureless band centered at 535 nm suggesting the formation of H-type aggregates as shown in **Figure 2.10**.

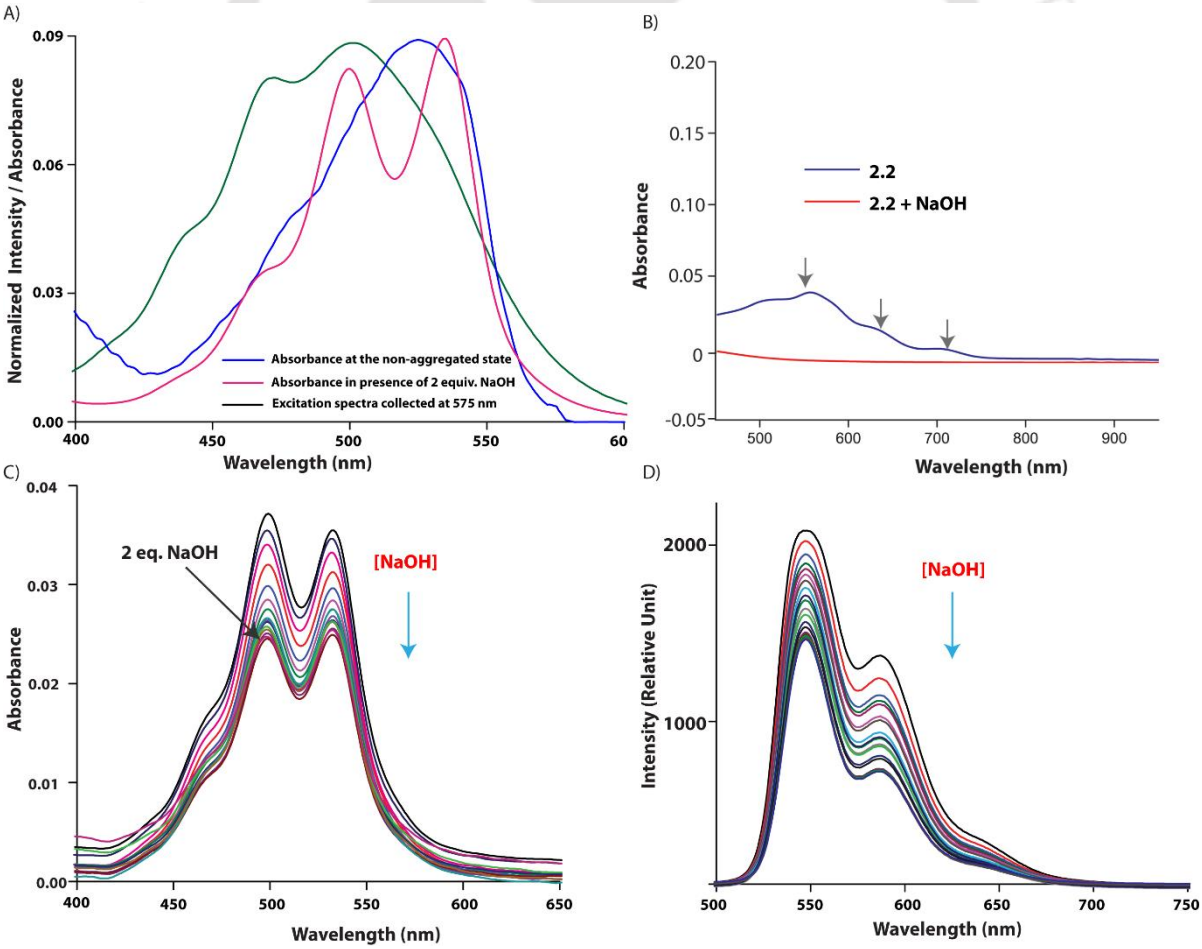

Figure 2.10 A) Normalized fluorescence excitation spectra of 1:2 [**2.1**]-NaOH collected at 575 nm and Absorption spectra of **2.1** and 1:2 [**2.1**]-NaOH; [**2.1**] = 1 × 10^{-6} M, B) absorption spectra of **2.2** in absence and presence of NaOH showing the generation of absorption peaks associated with the of titration of **2.3** formation of viologen radical cations; [**2.3**] = 1 × 10^{-6} M. C) Absorption and D) emission spectra of **2.3** with NaOH. [**2.3**] = 1 × 10^{-6} M.

Notably, for **2.3** under similar conditions, only about 25 % decrease in emission intensity was detected with no change in the color of the solution as shown in **Figure 2.10**. The absorption spectra of **2.3** in the presence of NaOH also did not show the appearance of any new peak in the NIR region. Additionally, treatment of **2.2** with NaOH produces a strong blue color and peaks corresponding to viologen radical cations in the NIR region as shown in **Figure 2.10**. These results conclusively indicate the effect of the viologen units in **2.1**. In a strongly basic medium, the formation of viologen radical cations leads to aggregation and consequently affects the emission of the **PDI** core.

In the case of the organic bases, for solubility reasons, ACN solutions of the amines were used for titration. In all cases, the absorption corresponding to all three transitions decreased with increasing base concentration, but no reversal of the peak intensities was detected in any case as shown in **Figure 2.11**.

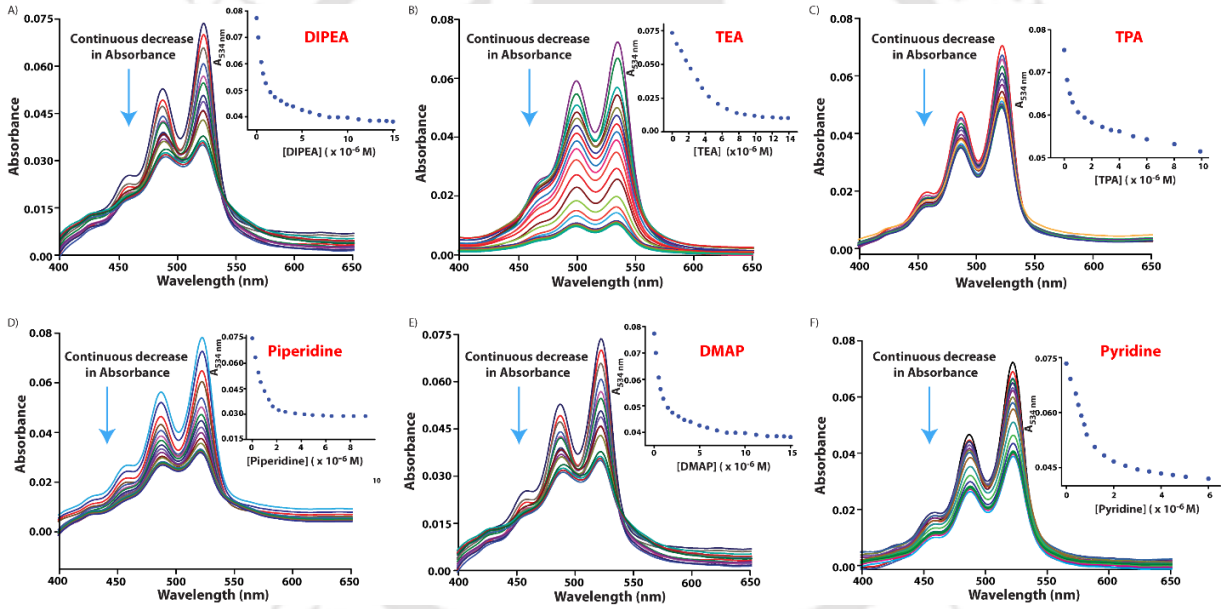

Figure 2.11 A) Absorption spectra of titration of **2.1** with A) DIPEA, B) TEA, C) TPA, D) Piperidine, E) DMAP, and F) Pyridine. Inset Absorbance at λmax vs. concentration of respective bases. [**2.1**] = 1 × 10^{-6} M.

Also in the emission spectra, a continuous decrease in the emission intensity was noted with increasing base concentration (**Figure 2.12**). Owing to the weak nature of the organic bases, no noticeable absorption band in the NIR region was detected.

The EPR spectra of **2.1**, **2.2**, and **2.3** showed no measurable signal as shown in **Figure 2.13**. When treated with NaOH, intense signals were observed only in the cases of **2.1** and **2.2**. As a standard, the EPR Spectrum of **2.1** in the presence of a strong reducing agent (sodium hyposulfite) was monitored for comparison purposes. Though the signal position remained the same, the intensity was found to be much higher than those of the other samples at similar **2.1** concentration. These

observations, along with the appearance of absorption bands in the NIR region in case of NaOH-treated **2.1** samples, clearly indicate the formation of viologen radical cations.[156] However, the presence of various amines resulted in extremely weak signals indicating a minor population of the radical cation in these cases as shown in **Figure 2.13**.

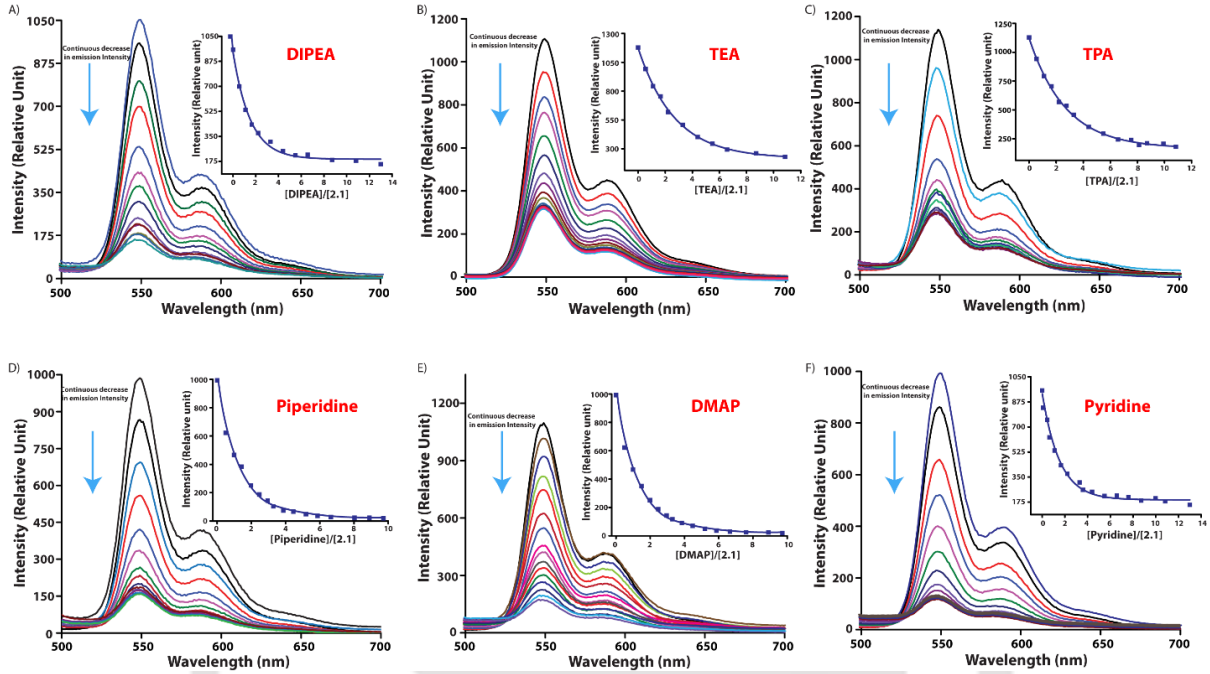

Figure 2.12 Fluorescence spectra of titration of **2.1** with A) DIPEA, B) TEA, C) TPA, D) Piperidine, E) DMAP, and F) Pyridine. Inset of A: Inset: Emission intensity at 549 nm vs. molar ratio of respective bases. [**2.1**] = 1×10^{-6} M.

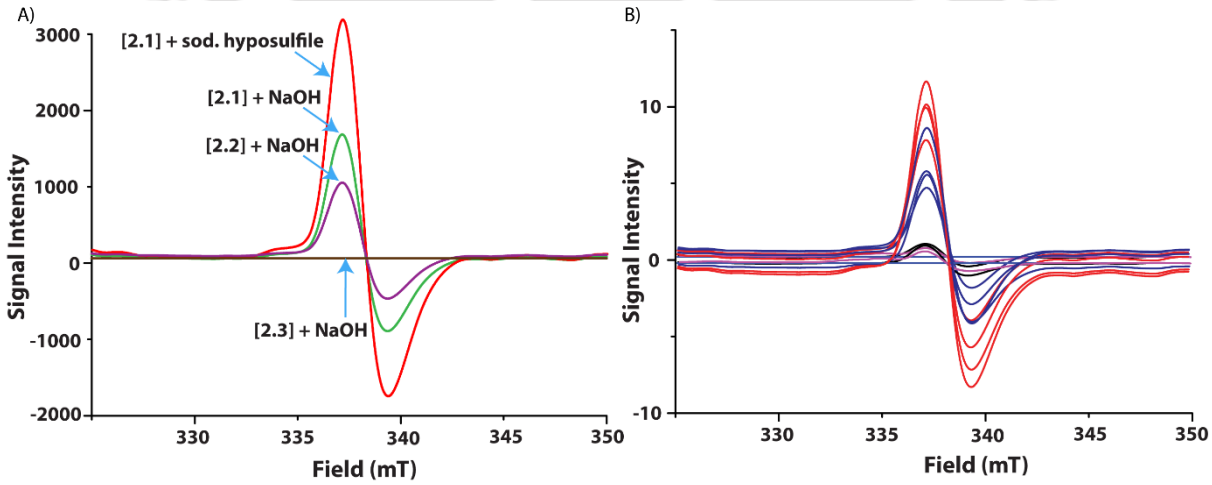

Figure 2.13 A) EPR spectra of **2.1**, **2.2** and **2.3** in presence of various inorganic bases, B) same in presence of various amines.

Base sensitivity of **2.1** in the solution phase was quantified in terms of both absorbance and fluorescence. Only the absorbance and fluorescence changes of the **PDI** core were considered, as it is not directly affected by the bases. Plots of the changes in absorption and emission intensities versus the equivalents of bases in all cases follow a linear trend up to 2 equiv. of base. These linear

plots can be regarded as calibration curves for quantitatively estimating the amount of base present. However, concentrations of bases required to change the absorbance by 0.01 (Δ_{abs}=0.01) and emission intensity by 10 % (Δ_{em}=10 %) in the initial linear part of these calibration plots were considered to calculate the sensitivity (Table 2.2). Remarkably, the sensitivities were at or below the ppb level. The sensitivity observed in the present case was in the range of 1-77ppb, whereas the previously reported best viologen-containing sensor showed sensitivity on the order of 130-1880 ppb.[150] Overall, the sensitivity is observed to be three orders of magnitude lower than those of the previously reported viologen-based sensors. To the best of our knowledge, these results suggest that **2.1** is the most sensitive base sensor both qualitatively and quantitatively.

Base	λ_{abs} (nm)	Base Sensitivity (ppb)	
		Δ_{abs} = 0.01	Δ_{em} = 10%
NaOH	535		1.89
DIPEA	533	19.95	12.27
DMAP	522	29.10	14.68
Piperidine	524	17.78	3.69
Pyridine	523	36.76	17.45
TEA	533	77.41	41.01
TPA	521	40.84	18.91

Table 2.2. Absorption maxima of [**2.1**] in presence of various bases, Base sensitivity at Δ_{abs} = 0.01 and Δ_{em} = 10% of a 1.0 × 10^{-6} M Aqueous Solution of **2.1** Measured at Absorbance and Emission Maxima.

Besides solution-based detection, for practical colorimetric detection, it would be preferred if the compound showed color changes in solid state on exposure to amines. To this end, the tetrafluoroborate salt of **2.1** was prepared and crystallized from acetonitrile. On exposure to amine vapors, the dark red crystals immediately changed to purple as shown in **Figure 2.14**. When kept under ambient conditions, the color of the crystals slowly returned to the original dark red color. Unfortunately, the obtained crystals could not be analyzed by X-ray crystallography owing to poor diffraction.

For another practical application, a paper-based sensor was developed for in situ on-site detection of both solvents and bases. A strip of filter paper was immersed in a methanolic (for base sensing) or aqueous (for solvents) solution of **2.1** and air-dried. Papers from the aqueous solution do not fluoresce under UV light (365 nm), whereas those from methanolic solution emit strongly as shown in **Figure 2.14**. On exposure to various solvents, the test papers from the aqueous medium showed different colors (**Figure 2.14**). Spraying dilute solutions of different bases on the test papers from

methanolic solution quenched the emission completely (**Figure2.14**). These results show that **2.1** can be used to prepare efficient and easy paper-based sensors for both solvents and bases.

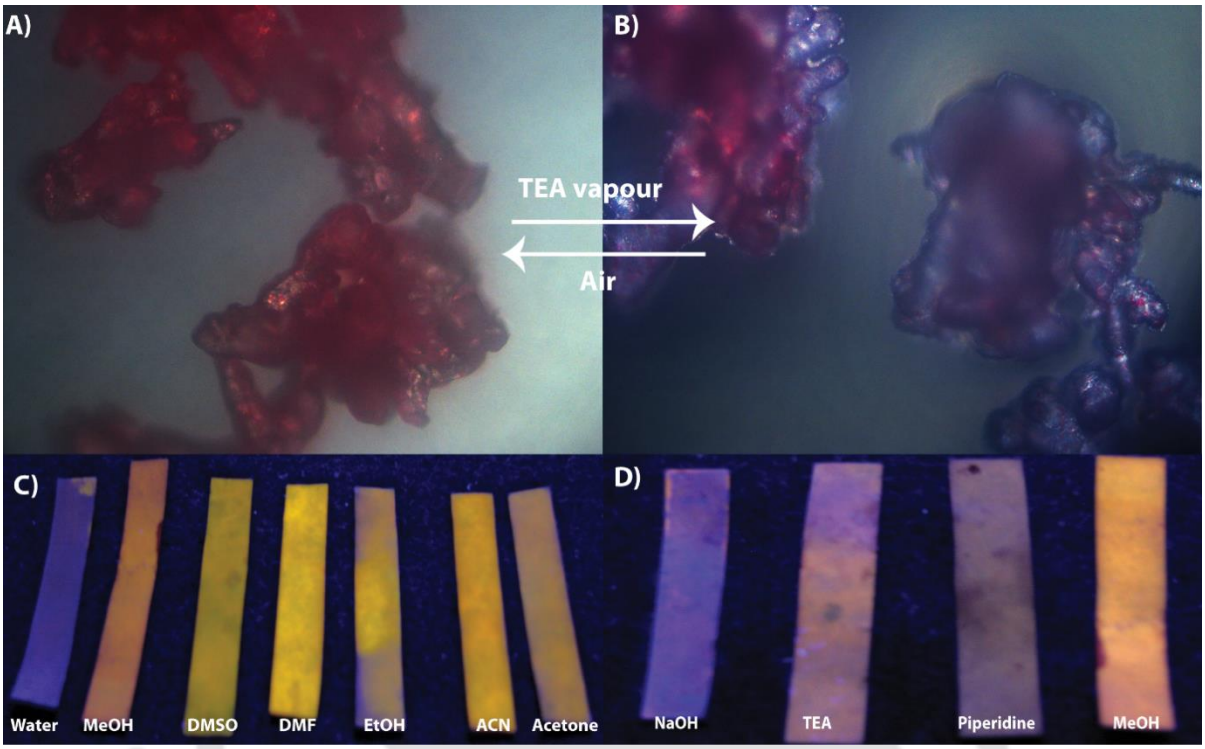

Figure 2.14 A-B)Photographs of **2.1** crystals A) before and B) after exposure to amine vapor, C-D) photographs of test papers soaked in **2.1** solution and then exposed to different C) solvents and D) bases. C-D) images were taken under UV light (365 nm).

2.3 Conclusions

Conjugation of **PDI** with viologen allowed us to prepare an efficient base sensor and solvatochromic probe. **2.1** shows linear dependence of its photophysical properties on solvent polarity and generates distinguishable colors in different solvents. In the presence of bases, viologen radical cations are produced, which affect the photophysical behavior of the **PDI** core and thus allow optical sensing of bases. Bases can be detected by **2.1** at the ppb level in solutions and in the crystalline state. For practical application, a paper-strip-based technique was developed to detect bases and solvents through color changes. These findings open up the possibility to create new base and solvent sensors with higher efficacy.

2.4 Experimental section

2.4.1 General Information and Materials: All the chemicals and reagents used were obtained from Sigma-Aldrich (USA) and used without further purification. All solvents were procured from Merck, India and Spectrochem, India. Amberlite IR 400 anion exchange resin was obtained from Merck, India. To prepare samples, Milli-Q water with a conductivity of less than 2 $\mu S \cdot cm^{-1}$ was used. ^{1}H NMR

and ^{13}C NMR were recorded either on a Bruker Ascend 600 MHz (Bruker, Coventry, UK) or on an Oxford AS400 (Varian) spectrometer and referenced to deuterated solvents. ESI-MS was measured using a Q-tof-Micro Quadrupole mass spectrophotometer (Micromass). UV visible data was recorded using a PerkinElmer Lambda 750 spectrometer. Fluorescence measurements were obtained using a Carry Eclipse spectrophotometer (Agilent). All emission spectra were recorded by exciting the sample at 485 nm. Unless otherwise mentioned, all studies were performed at room temperature. Standard 10 mm path quartz cuvettes were used for all spectroscopic measurements.

2.4.2 Synthesis: All the compounds were synthesized following the routes shown in **Scheme 2.2**.

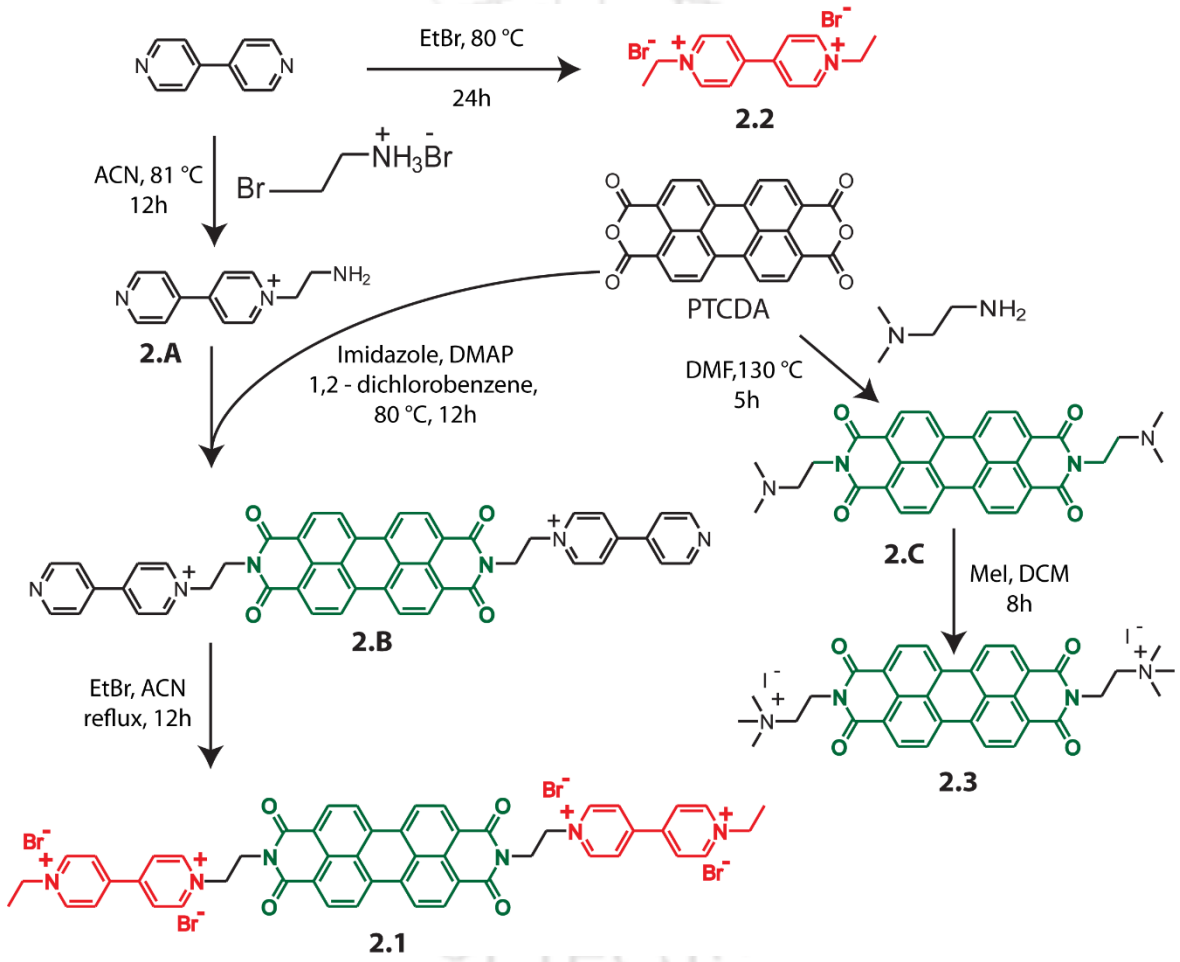

Scheme 2.2 Synthetic route for synthesis of the compounds **2.1**, **2.2** and **2.3**.

Compound 2.A: To a stirring solution of 4, 4-bipyridyl (1 g, 6.4 mmol) in acetonitrile (10 mL), 2-bromoethylamine hydrobromide (262 mg, 1.28 mmol) was added and was refluxed. After 12 h, the reaction mixture was cooled to room temperature and volatiles were removed under reduced pressure. The crude product was then washed several times with ether to get the white solid. Yield: 83%. ^1H NMR (600 MHz, D_2O) δ = 9.09 (d, J = 6.6 Hz, 2H), 8.80 (d, J = 4.8 Hz, 2H), 8.53 (d, J = 6.6 Hz, 2H), 7.96 (d, J = 4.8 Hz, 2H), 5.07 (t, J = 6.6 Hz, 2H), 3.79 (t, J = 3.6 Hz, 2H) ppm; Mass (ESI-MS): *m/z* calcd. for $C_{12}H_{14}N_3^+[M]^+$, 200.1184; found, 200.1174.

Compound 2.B: Perylene-3, 4, 9, 10-tetracarboxylic anhydride (PTCDA, 100 mg, 0.255 mmol), compound **2.A** (184 mg, 0.501 mmol), and imidazole (68 mg, 1 mmol) were taken in 1, 2-dichlorobenzene (8 mL), 4-N, N-dimethylaminopyridine (56 mg, 0.5 mmol), and was heated at 80 °C with stirring for 12 h. The reaction mixture was then cooled to room temperature and the precipitate was collected by centrifugation. The collected red solid was dissolved in water (50 mL) and washed with dichloromethane (DCM) to remove water insoluble residues. The volume of the aqueous layer was lowered by removing water on a rotory evaporator and to it was added a portion of saturated aqueous ammonium hexafluorophosphate (NH_4PF_6) solution (10 mL). The resulting red precipitate was collected by filtration and dried under vacuum. Yield: 62%. ^{1}H NMR (400 MHz, DMSOd_6): δ = 9.37 (d, J = 5.6 Hz, 4H), 8.87 (d, J = 4.4 Hz, 4H), 8.72 (d, J = 8 Hz, 4H), 8.63 (d, J = 6 Hz, 4H), 8.35 (d, J = 8 Hz, 4H), 8.04 (d, J = 4 Hz, 4H), 5.0 (s, 4H), 4.70 (s, 4H) ppm. Mass (ESI-MS): *m/z* calcd. for $C_{48}H_{32}N_6O_4^{2+}[M]^{2+}$, 378.1237; found 378.1227.

Compound 2.1: A mixture of **2.B** (100 mg, 0.09 mmol) and ethyl bromide (104 mg, 0.9 mmol) in acetonitrile was refluxed for 12 h. After cooling to room temperature, the resulting precipitates were collected by centrifugation and washed with acetonitrile several times before drying it under reduced pressure. The material was then taken in water and subjected to ion exchange by passing the solution through a column of bromide functionalized amberlite IR 400 anion exchange resin. The fractions containing the compound was freeze dried and crystalized from methanol-diethyl ether solvent mixture to get the desired compound. Yield: 63 %. ^{1}HNMR (600 MHz, DMSOd_6): δ = 9.58 (d, J = 5.4 Hz, 4H), 9.44 (d, J = 5.4 Hz, 4H), 8.92 (d, J = 7.2 Hz, 4H), 8.85 (q, J = 5.4, 6.0 Hz, 8H), 8.47 (d, J = 7.2 Hz, 4H), 5.10 (s, 4H), 4.74 (t, J = 7.8 Hz, 8H), 1.61 (t, J = 7.2 Hz, 6H) ppm; ^{13}C NMR (100 MHz, DMSO*d6*) δ = 163.17, 162.91, 148.79, 148.13, 146.68, 145.68, 134.18, 131.08, 126.54, 126.18, 125.61, 124.28, 122.63, 56.53, 40.95, 16.33 ppm. Mass (MALDI-TOF, DHB matrix): *m/z* calcd. for $C_{52}H_{42}N_6O_4^{4+}$ $[M]^{4+}$, 814.3246; found 814.3510.

Compound 2.C: A suspension of PTCDA (500 mg, 1.27 mmol) and N, N-dimethylaminoethylamine (1.5 mL, 13.7 mmol) in dimethyl formamide (10 mL) was heated at 130 °C under stirring for 5 h. After cooling to room temperature, 25 mL tetrahydrofuran (THF) was added and the resulting precipitate was collected by suction filtration and washed with 3 ×10 mL THF. Drying the residue in vacuum oven at 40 °C overnight yielded the title compound as a dark purple solid. Yield: 90 %. ^{1}H NMR (400 MHz, $CDCl_3$) δ = 8.67(d, J = 8.0 Hz, 4H), 8.62 (d, J = 8.0 Hz, 4H) 4.37(t, J = 8.0 Hz, 4H), 2.70 (t, J = 8.0 Hz, 4H), 2.38 (s, 12H).ppm. Mass (ESI-MS): *m/z* calcd. for $C_{32}H_{29}N_4O_4$ $[M + H]^+$, 533.2183; found 533.2183.

Compound 2.2: Compound **2.C** (50 mg, 0.094 mmol), iodomethane (58 µL, 0.94 mmol) were taken in DCM and the mixture was stirred for 8 h. The reaction mixture was centrifuged and the precipitate was washed with DCM, finally with THF. The resulting red precipitates were dried under vacuum.

Yield: 84 %. 1H NMR (600 MHz, DMSO-d_6) δ = 9.02 (d, J = 7.8, 4H), 8.64 (d, J = 7.8 Hz, 4H), 4.51(t, J = 7.2 Hz, 4H), 3.67 (t, J = 7.2 Hz, 4H), 3.24 (s, 12H) ppm; 13C NMR (125 MHz, DMSOd_6) δ = 162.69, 133.93, 130.92, 128.36, 125.26, 124.21, 122.36, 61.89, 52.56, 33.76 ppm. Mass (ESI-MS): *m/z* calcd. for $C_{34}H_{34}N_4O_{42}^{2+}$ $[M]^{2+}$, 281.1284; found 281.1280.

Compound 2.3: Compound **2.3** was prepared following a previously reported protocol.[36] In brief, excess (10 equivalent) ethyl bromide was mixed with 4, 4′-dipyridyl in a glass tube and the mouth of the tube was sealed. The tube was heated to 80 °C for 24 h. After being cooled to room temperature, the seal was broken and the material was concentrated on a rotory evaporator, and the residue was crystallized three times from methanol-diethyl ether to get a yellow solid. Yield: 35%. ^{1}H NMR (400 MHz, D_2O) δ = 9.15 (d, J = 7.2 Hz, 4H), 8.56 (d, J = 7.2 Hz, 4H), 4.77 (m, 4H), 1.73 (t, J = 8.0 Hz, 6H) ppm; ^{13}C NMR (100 MHz, D_2O) δ = 150.17, 146.12, 129.21, 57.92, 15.91 ppm; Mass (ESI-MS): *m/z* calcd. for $C_{14}H_{18}N_2$ $[M]^{2+}$, 214.1459; found 214.150.

2.4.3 Method

Sample Preparation: The stock solutions of **2.1**, **2.2**, and **2.3** were prepared in a 10 mL of volumetric flasks in different solvents. These stock solutions were diluted to desired concentration as required for the experiments. For amine sensitivity, the organic bases were dissolved in acetonitrile at high concentration and appropriate amounts from these stocks were added to the aqueous solutions of **2.1**. In order to avoid any effect from added acetonitrile, only 0.1% v/v of the base solutions were added. An appropriate control experiment carried out by adding exactly the same amount of acetonitrile in aqueous solution of **2.1** resulted in no observable change in the absorption as well as emission spectra.

Field Emission Electron Scanning Microscopy (FESEM): FESEM samples were prepared by casting a drop of the solution on a silicon wafer and dried under ambient conditions. FESEM images were taken using a SIGMA ZEISS Microscope.

Electron paramagnetic resonance (EPR): For EPR measurements, prior to the addition of the bases, all the samples were degassed by purging argon gas for 10 mins. After the addition of bases, Argon was flushed thoroughly and the sample tubes were sealed properly to prevent any areal oxidation. All measurements were carried out with 1 × 10^{-6} M samples (**2.1**, **2.2** and **2.3**) with 2 equivalents of bases/reducing agent on a JES-FA200 instrument from JEOL.

Quantum Yield Measurements: The fluorescence quantum yields of **2.1** in different solvents were determined by using Rhoamine-6G as a standard fluorophore following equation (2.1),

$$\Phi_u = (A_s F_u n_u^2)/ (A_u F_s n_s^2) \Phi_s \qquad (2.1)$$

where, Φ_s is the quantum yield of the reference (Rhodamine, 0.95) in ethanol, Φ_u is the quantum yield of **2.1**, A_s and A_u are the absorbance of Rhodamine and **2.1** at the excitation wavelength, F_s and F_u are the area of integrated fluorescence intensity of the Rhodamine and **2.1** sample when excited at the same excitation wavelength. The refractive indices of the solvents for the **2.1** and Rhodamine are denoted by n_u and n_s respectively. To minimize the reabsorption of the fluorescence light passing through the samples their absorption maximum was kept 0.1.

Calculation: The initial linear parts of the absorption (at absorption maximum) or emission intensity (at 588 nm) vs concentration of added bases are considered. The concentration of base required ([base conc.]) to change the absorbance by 0.01 ($\Delta_{Abs} = 0.01$) or initial emission intensity by 10% ($\Delta_{em} = 0.01$) used in equation 2.2 to calculate the base sensitivity.[10]

$$\text{Sensitivity (ppb)} = MW \times [\text{base conc.}] \times 1000000 \qquad (2.2)$$

Chapter 3

A Perylenediimide-Peptide Conjugate for Self-Assembly Assisted Tandem Sensing of Pd^{2+} and CN^-

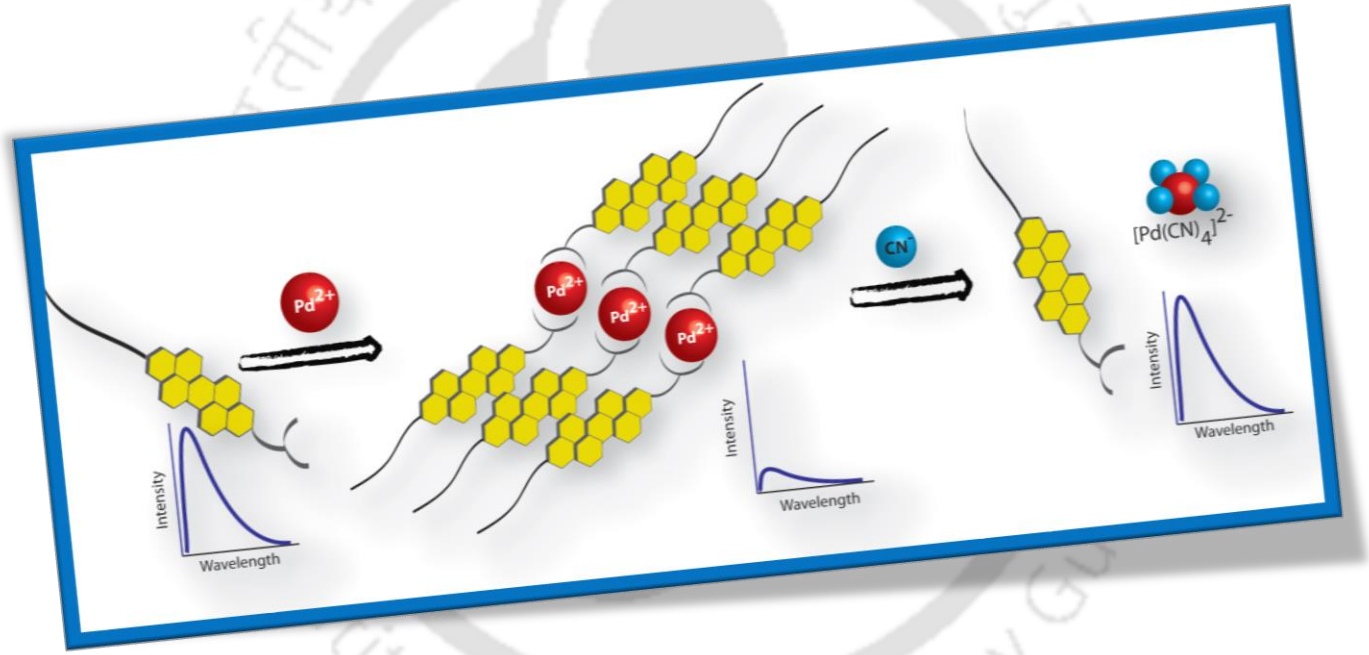

3.1 Introduction

Palladium (Pd) compounds are widely used as catalysts for numerous chemical conversions in the fine chemical, pharmaceutical and polymer industries.[159-160] Palladium is also extensively found in various commercial materials such as jewellery, dental alloys, automobile catalytic converters, fuel cells, medical instruments, and electronics to name a few.[161] However, release of Palladium by these materials or the industrial wastes has raised great concern because of its adverse effect on human health and environment.[162] Palladium is cytotoxic and causes considerable damage and degradation of DNA.[163-164] It is also known to damage mitochondria as well as inhibits various enzyme activities.[163-164] The threshold level of palladium in pharmaceutical products is thus stringently limited to be less than 10 ppm.[165-166] Monitoring these low levels thus require efficient and easy methods.

Among the common anionic species, cyanide (CN^-) is in particular, highly toxic. Cyanide inhibits the enzyme, cytochrome-C oxidase, by attaching with iron of this protein which consequently disrupts the electron transport chain.[167] Though certain bacteria, fungi and algae produces cyanides, majority of cyanide existence in environment is primarily due to metal finishing and mining industries.[168-169] Consequently, efficient methods for monitoring these low levels of cyanides in industrial as well as in environmental samples, are highly desirable.

Several chemo-sensors have separately been reported for sensing either Pd^{2+} or CN^-.[116, 170-178] A tandem sensing system could be extremely useful to detect both species present or generated from the same source, for example, processes involved with Palladium catalysed cyanation reaction or medicines or other consumable supplies. Therefore, designing of new and effective chemo-sensor for sequential sensing of palladium and cyanide with high selectivity and sensitivity under mild conditions is required for further developments. In order to design such a sensor molecule, perylenediimide (**PDI**) was chosen as the fluorophore unit. In recent years **PDI**s have emerged as efficient fluorescent sensors for a variety of species especially because of their outstanding photochemical stability and high quantum yields.[143-144] Moreover, the emission property of these fused π-ring systems can easily be fine-tuned through their aggregation behavior.[17, 46, 69, 179-180] The aggregation dis-aggregation of these arylenediimides and consequent changes in their emission behavior has been utilized to develop several arylenediimides of analytes.[29, 69, 76, 181-184] We envisioned that a proper ligand for Pd^{2+} attached to **PDI** core can lead to such aggregation induced quenching in presence of Pd^{2+} and subsequent addition of CN^- will be able to break the aggregation and lead to "turn-on" the fluorescence.

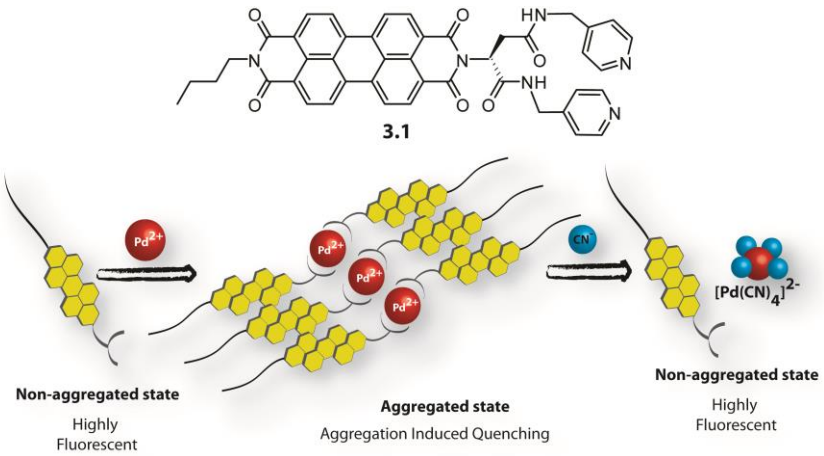

Scheme 3.1 Chemical structure of the ligand and pictorial presentation of the sensing mechanism.

3.2 Results and Discussion

Compound **3.1** (**Scheme 3.1**) was designed and synthesized where two pyridine groups are attached to the **PDI** core through peptide linkages in order to bind metal ions efficiently.[114] Notably, the asymmetric positioning of the pyridine groups are achieved by incorporating aspartic acid residue in order to gain selectivity toward Pd^{2+} over other metal ions as palladium is capable of forming distorted square planar structures. In order to find a suitable mixed solvent system for the study, the effect of water on the aggregation and consequently on the spectroscopic properties of **3.1** in DMF was tested. The absorption spectra of **3.1** in different volume ratio of Water-DMF showed two prominent vibronic bands as shown in **Figure 3.1** at 531, 494 and a shoulder at 463 nm which are attributed to the 0-0, 0-1, and 0-2 vibrational transitions generated by the **PDI** core.[158 185] The absorption decreases along with a red shift in the absorption bands with increasing amount of water and at higher water content, a broad band appeared. However, the absorption ratio of 0-0 and 0-1 bands ($A_{0\text{-}0}/A_{0\text{-}1}$) remained constant at ~1.54 up to 50% water content but decreases dramatically to reach a saturation value of 0.65 with more water. It is worth mentioning here that the $A_{0\text{-}0}/A_{0\text{-}1}$ ratio is commonly considered as a tool to monitor the aggregation. For perylene chromophores in aggregated state, typical values for the absorption ratio A_{0-0}/A_{0-1} are <0.7 while monomerically solubilized **PDIs** show Franck–Condon progression with a ratio A_{0-0}/A_{0-1} of ~ 1.6.[55, 180, 186] When excited at 490 nm, compound **3.1** showed an intense emission at 545 nm in 1:1 Water-DMF as shown in **Figure 3.1.** Interestingly, only a small decrease in the emission intensity was observed up to 50% water content (**Figure 3.1**). However, with more water, the emission quenched drastically. These results signify that at higher water content, the **PDI** cores stack to form J-type aggregates whereas up to 1:1 Water-DMF, the major population of the molecules remain in non-aggregated state.

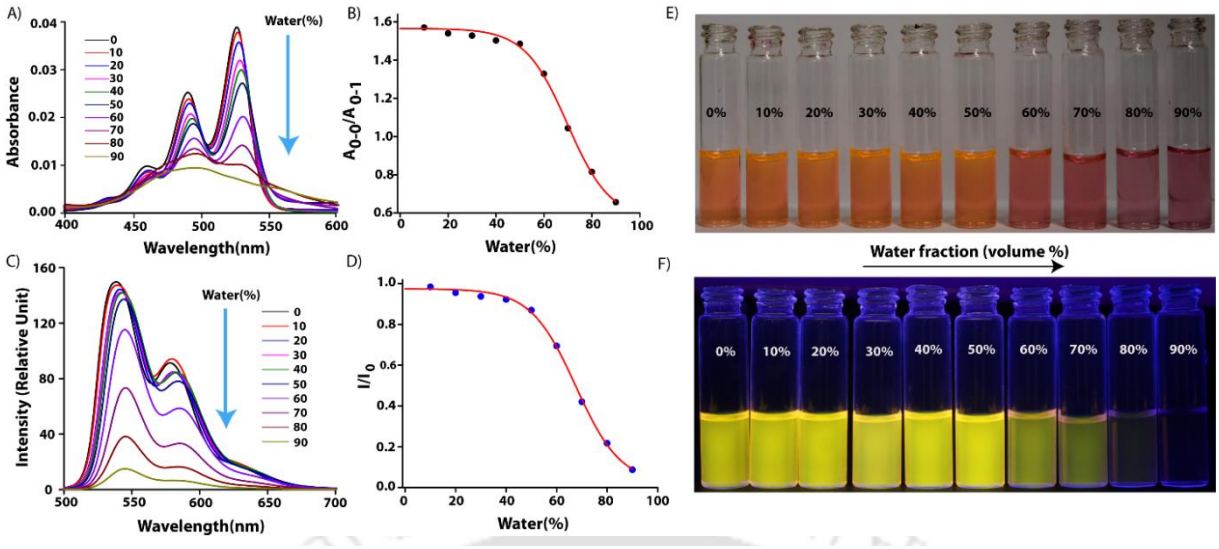

Figure 3.1 A) UV-Visible spectra of **3.1** (1μM) in different volume ratio of DMF-Water under ambient condition, B) absorption ratio of the 0-0 and 0-1 transitions at different water content, C) emission spectra of 1 (1μM) in different volume ratio of Water-DMF under ambient condition, D) the relative intensity of fluorescence with increase in water content. Photographs of **3.1** in different Water-DMF compositions, E) under normal light, and F) under UV light. [**3.1**] =1 X 10^{-6} M.

Further, to confirm the aggregation, FESEM images were taken from 1:1 and 2:1 Water-DMF samples. While no clear morphology can be found after careful investigation in case of 1:1 Water-DMF, the 1:2 DMF-water system showed uniform spherical aggregates of ~ 50 nm (**Figure 3.2**). The aggregate size was further confirmed by DLS measurement (**Figure 3.2**). In accordance with these results, 1:1 DMF-water system was chosen as the medium for testing the sensing ability of **3.1**.

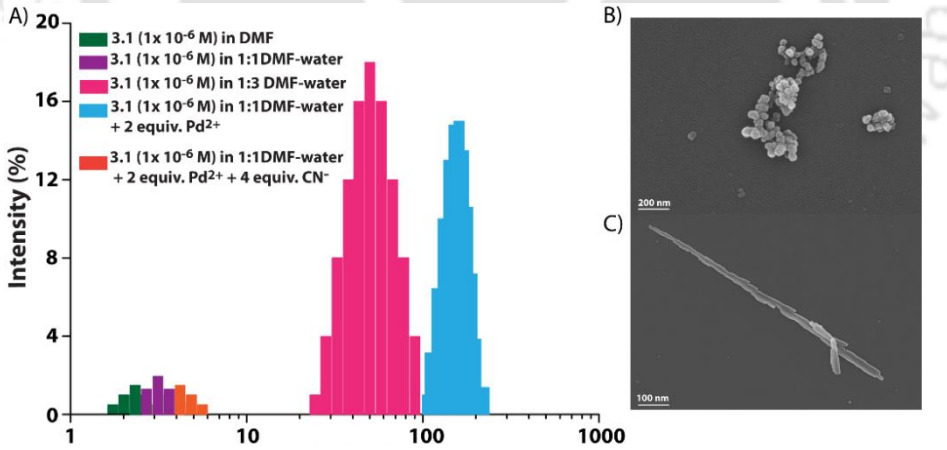

Figure 3.2 A) Intensity weighted distribution of particle sizes from different compositions of **3.1**, Pd^{2+} and CN^-, B) FESEM images of samples of compound **3.1** in 2:1 Water-DMF, and C) FESEM images of a Pd^{2+}(1 equiv.) sample of **3.1** in 1:1 Water-DMF. [**3.1**] = 1 μM.

To check the response of compound **3.1** toward Pd^{2+} ions, absorption and fluorescence spectra were recorded in 1:1 Water-DMF in presence of Pd^{2+} ions. Addition of $PdCl_2$ resulted in continuous decrease in absorption for all three transitions as can be seen in **Figure 3.3**. Along with decrease in absorbance, the absorption order changes from 0-0 > 0-1 to 0-1 > 0-0. The reversal of the order is a characteristic of the aggregation of **PDI** molecules. [158, 185] In this process, the $A_{0\text{-}0}/A_{0\text{-}1}$ ratio decreased

from 1.54 (without Pd^{2+}) to 0.3 (with 1.8 equivalents of Pd^{2+}) suggesting fully aggregated state. Further, the presence of Pd^{2+} created flake like morphology with dimension of 20 × 150 nm and similar size distribution was also observed in DLS measurement as can be seen in **Figure3.2**. These observation further confirm the aggregation due to the presence of Pd^{2+}. Further, the mole fraction in aggregated state (α_{agg}, considering the absorbance at 530 nm) are calculated and correlated with the equivalence of Pd^{2+} which fits perfectly with the trend observed from $A_{0\text{-}0}/A_{0\text{-}1}$ ratio (**Figure 3.3**).[51]

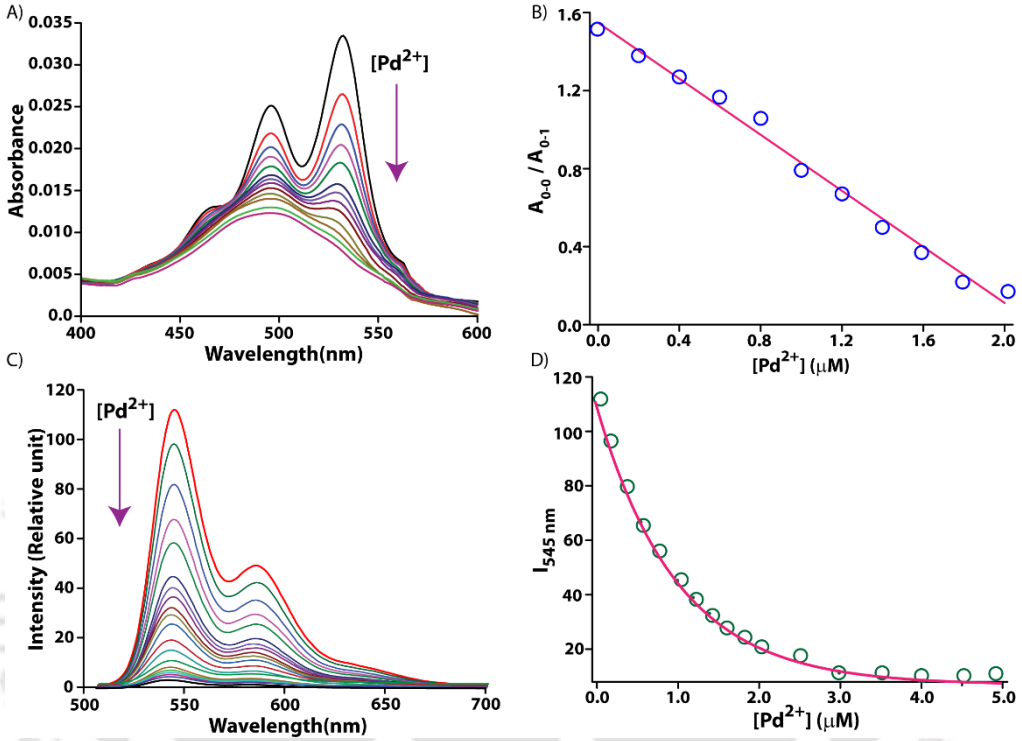

Figure 3.3 Absorption A) and fluorescence C) spectra (λ_{ex} = 490 nm) of **3.1** (1.0 μM) in Water-DMF (1:1, v/v) in presence of various amounts of Pd^{2+}, B) absorption ratio of the 0-0 and 0-1 transitions at different concentrations of Pd^{2+}, and D) fluorescence intensity (λ_{max} = 545 nm) vs. [Pd^{2+}] (μM).

Interestingly, a dramatic change in the appearance of the solution is also observed as it changed from yellowish orange to pink (**Figure 3.4**). The highly fluorescent solution becomes almost non-fluorescent after treatment with Pd^{2+}. As observed in **Figure 3.4**, the emission property of **3.1** is significantly affected by the presence of Pd^{2+} salt. When excited at 490 nm, compound **3.1** showed an intense emission at 545 nm. With increase in Pd^{2+}, the emission quenched drastically and above 4 equivalents of Pd^{2+}, it becomes negligible. Compound **3.1** showed a high quantum yield of 0.63 in 1:1 Water-DMF. With the addition of Pd^{2+} (1 equivalent), the quantum yield dropped to 0.07.

In order to check the selectivity of the ligand, quenching ("turn-off") of the emission was monitored for several other metal ions (Mg^{2+}, Sr^{2+}, Al^{3+}, Cr^{3+}, Pb^{2+}, Mn^{2+}, Fe^{3+}, Co^{2+}, Ni^{2+}, Zn^{2+}, Cd^{2+}, Hg^{2+} and Cu^{2+}). The fluorophore shows high selectivity toward Pd^{2+} over other metal ions, which is evident from the negligible fluorescence changes in presence of other metal ions as shown in **Figure 3.4**. The

competitive experiment in presence of other metal ions, also suggest the high selectivity toward Pd^{2+} as the background metal ions showed no effect to the detection of Pd^{2+} (**Figure 3.4C**). The detection limit for Pd^{2+} was measured using fluorescence titration and found to be 0.55 ppb (**Figure 3.8**). The detection limit observed for Pd^{2+} is at per with other reported sensors for this metal ions.

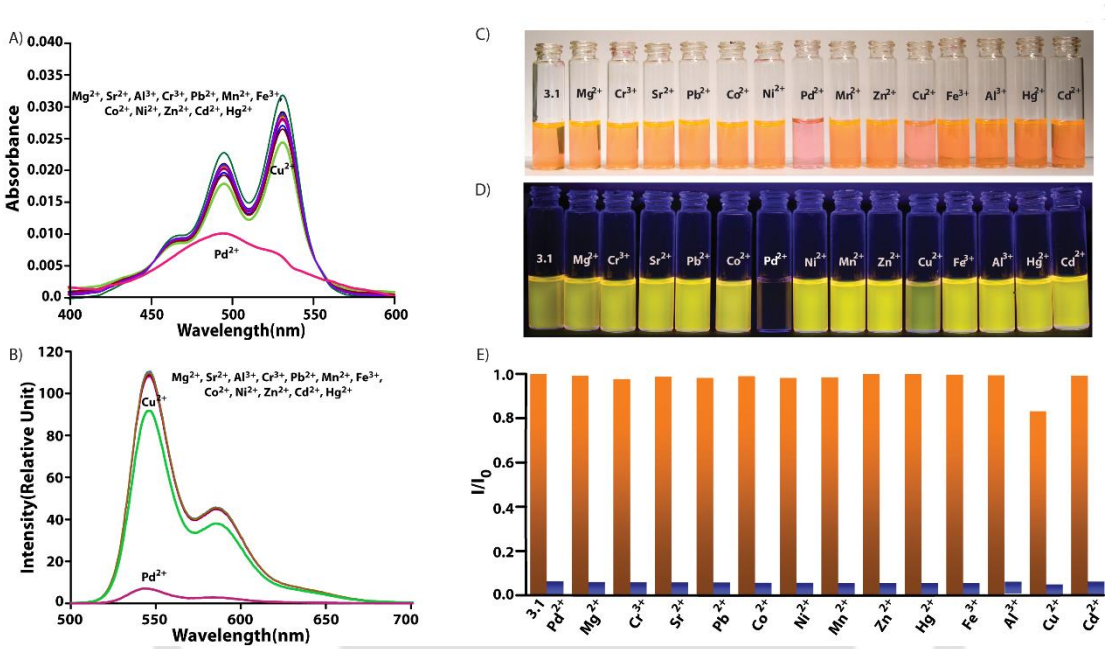

Figure 3.4 A) UV-Visible spectra of **3.1** (1 μM) in presence of different metal ions in Water-DMF (1:1, v/v) under ambient condition, B) emission spectra of **3.1** (1μM) in presence of different metal ions in Water-DMF (1:1,v/v) under ambient condition. Photographs of solutions of **3.1** in presence of different metal ions, C) under normal light and D) under UV light, [**3.1**] = 1μM, and E) relative Fluorescence response of **3.1** toward Pd^{2+} over miscellaneous competitive metal ions upon excitation at 490 nm. Orange bars represent the decrease in the intensity of **3.1** in presence of Mg^{2+}, Sr^{2+}, Al^{3+}, Cr^{3+}, Pb^{2+}, Mn^{2+}, Fe^{3+}, Co^{2+}, Ni^{2+}, Zn^{2+}, Cd^{2+}, Hg^{2+} and Cu^{2+}. Blue bars represent the subsequent addition of Pd^{2+} to the solution.

To understand the mechanism behind such changes in spectroscopic properties of **3.1** upon addition of Pd^{2+} salt, Job's plot experiment was carried out which results in a 2:1 binding between **3.1** and Pd^{2+} as can be seen in **Figure 3.5**. Further, the binding constant was measured using both UV and fluorescence titration employing Benesi–Hildebrand equations and in both cases very strong binding (10^5 M^{-1}) was observed.[188-189] To confirm the actual quenching mechanism, fluorescence lifetime of **3.1** was measured as a function of concentration of Pd^{2+}. The lifetime remained constant throughout the titration, confirming static quenching.

Analysis of IR spectra of the free ligand and 2:1 complex of 3.1-Pd^{2+} showed the involvement of pyridine groups in the complex formation. The stretching frequency generated by pyridine groups of the free ligand merged with the imide signals of **PDI**. Whereas, the same stretching in the Pd^{2+} treated sample shifted to lower wavenumber and appeared as a new band at 1620 cm^{-1} as can be shown in **Figure 3.5**. Based on these data it can be postulated that Pd^{2+} binds with two molecules of **3.1** as shown in Scheme 3.1. This complexation is accompanied with π–π stacking of the **PDI** core

leading to the aggregation induced quenching of emission and thus creates a "turn-off" sensing for Pd^{2+}.

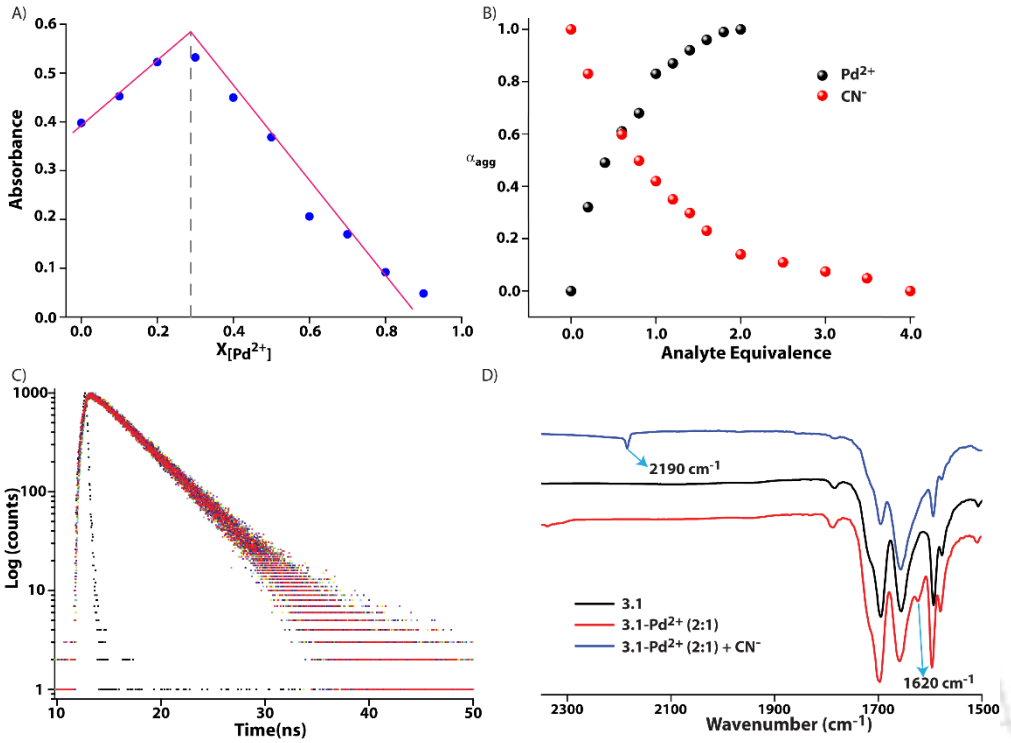

Figure 3.5 A) Job's plot for Pd^{2+} indicating 1:2 chelation from conventional Job's plot experiment, B) variation of α_{agg} with equivalence of analyte added to the sensor solution. For Pd^{2+}, a 1μM solution of **3.1** was titrated with Pd^{2+}. For CN^-, a 2:1 solution of **3.1**-Pd^{2+} was titrated with CN^-. α_{agg} were calculated by considering the absorbance value at 530 nm.C) Fluorescence life time of **3.1** in presence of varying amount of Pd^{2+} ions measured in 1:1 Water-DMF at room temperature., and D) IR spectra of **3.1** (Black), **3.1**-Pd^{2+} (2:1) complex (Red) and **3.1**-Pd^{2+} (2:1) treated with 4 equivalents of CN^- (Blue).

The 2:1 complex of **3.1** and Pd^{2+} was then employed for the sensing of cyanide ions. UV-Visible and fluorescence spectra were recorded with the incremental addition of tetrabutylammonium cyanide (TBACN). Upon addition of aqueous solution of CN^-, a continuous increase in absorption peaks were observed as shown in **Figure 3.6A**. After addition of 0.4 equivalents of CN^-, the $A_{0\text{-}0}$ transition becomes higher than $A_{0\text{-}1}$ transition and at 4 equivalents, the $A_{0\text{-}0}/A_{0\text{-}1}$ value goes back to 1.54 indicating complete dis-aggregation of the **PDI** chromophore. Correlation between α_{agg} and concentration of CN^- also showed similar trend. The emission spectra of the complex in presence of CN^- showed a drastic enhancement in fluorescence emission intensity as observed in **Figure 3.6C**. Interestingly, the emission intensity reaches the value of free ligand above 4 equivalents of CN^- and no further change was observed. Moreover, the color of the solution reverts back to yellowish orange (**Figure 3.7**). Interestingly, the FESEM image of CN^- sample showed no particular morphology which is also supported by the disappearance of any prominent particle size distribution in the DLS measurement (**Figure 3.2**).

To evaluate the selectivity of the sensor toward CN^- ions, the emission spectra were recorded in presence of other common anions, including OAC^-, ClO_4^-, HSO_4^-, $H_2PO_4^-$, SCN^-, BF_4^-, PF_6^-, NO_3^-, OH^-, F^-, Cl^-, Br^-, I^-, SO_4^{2-}, and PO_4^{3-} as can be seen in **Figure 3.7**. None of these anions caused any change to the fluorescence intensity under the same condition. Unlike the case of CN^-, no change in the color of these solutions were observed upon addition of these anions (**Figure 4A**). Further, the competitive experiment was performed and the results showed that **3.1**-Pd^{2+} (2:1) is highly specific toward CN^- even in presence of other anions (**Figure 4B**).

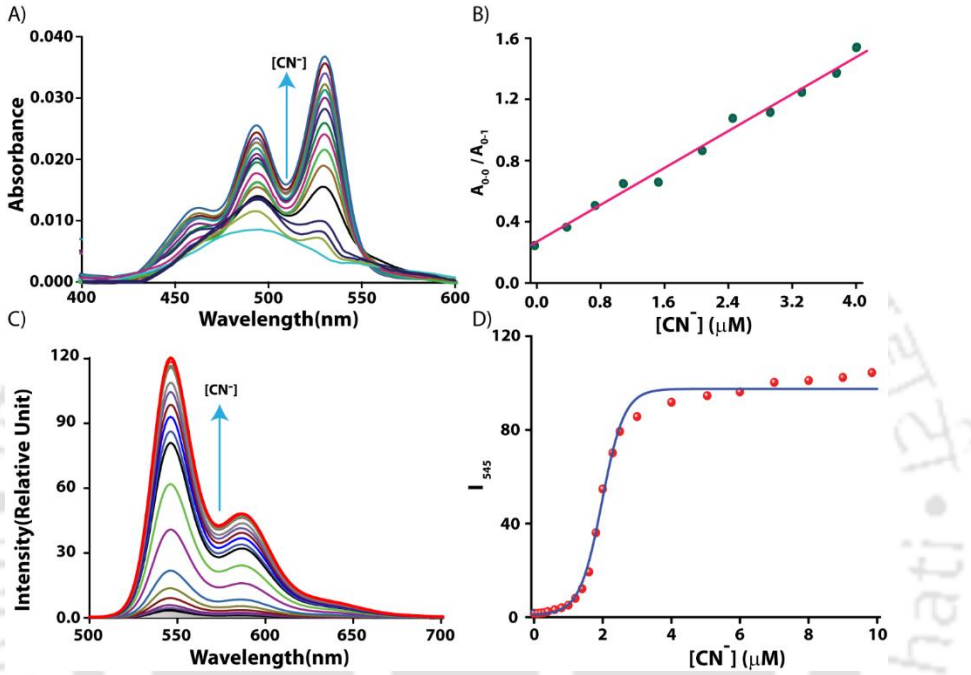

Figure 3.6 A) Absorption spectra of **3.1**-Pd^{2+} (2:1,[**3.1**] = 1.0 μM) complex in Water-DMF (1:1, v/v) in presence of various concentrations of CN-, B) absorption ratio of the 0-0 and 0-1 transitions at different concentrations of CN^-, C) fluorescence (λ_{ex} = 490 nm) spectra of **3.1**-Pd^{2+}(2:1,[**3.1**] = 1.0 μM) complex in Water-DMF (1:1, v/v) in presence of various concentrations of CN^-, and D) fluorescence intensity (λ_{max} = 545 nm) vs. [CN^-] (μM).

IR spectra of the CN^- treated samples showed the disappearance of the pyridine stretching frequency back to its original position which suggests that the ligand is no longer in complex with Pd^{2+} (**Figure 3.5**). Notably, addition of a DMF solution of $Pd(CN)_2$ to a 1:1 Water-DMF solution of **3.1** resulted in no change in the spectroscopic property of **3.1**. Cyanide, being a strong field ligand as well as softer than pyridine (HSAB principle),[191] presumably replaces pyridines to form a stable $[Pd(CN)_4]^{2-}$ coordination polymer.[192] The high stability constant of $[Pd(CN)_4]^{2-}$ (log $\beta 4 > 60$)[193] as reported by Hancock as well as the appearance of the CN stretching frequency (~2190 cm-1, **Figure 3.5**, typical of bridging cyanide ions)[191] in the IR spectra of cyanide treated **3.1**-Pd^{2+} complex support this hypothesis. In the present case, due to the formation of $[Pd(CN)_4]^{2-}$, the complex between **3.1** and Pd^{2+} is destroyed leading to dis-aggregation of the ligand. This, in turn results in the enhancement of emission and the "turn-on" sensing of Cyanide ions (**Scheme 3.1**).

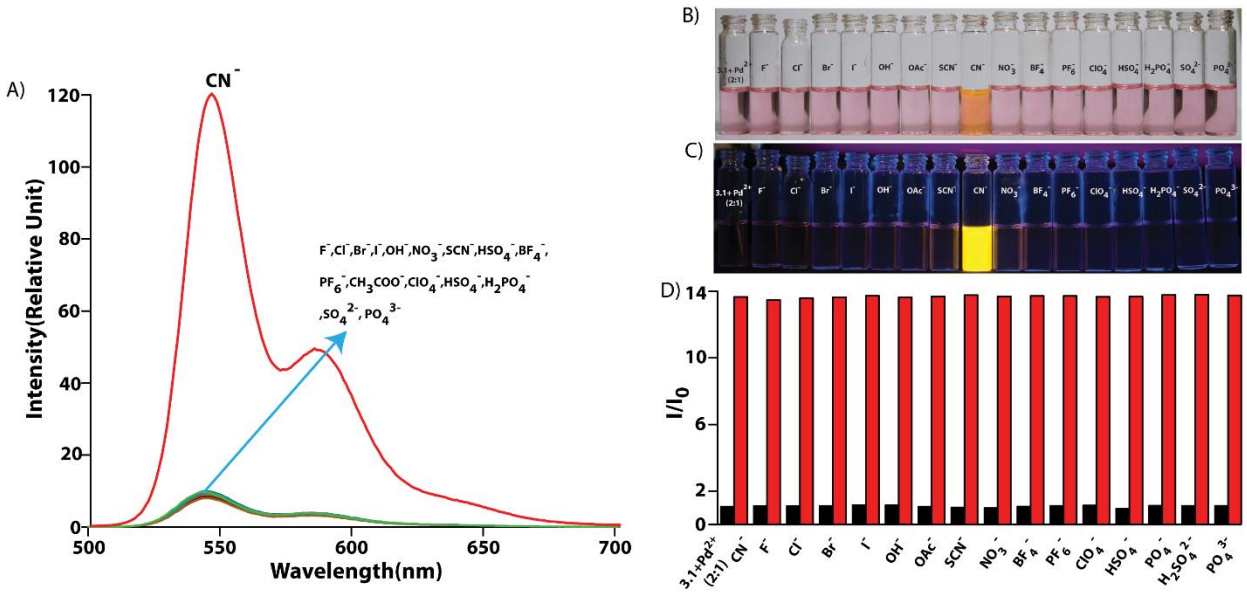

Figure 3.7. A) Emission spectra of **3.1**-Pd^{2+} (2:1) complex in presence of different anions in Water-DMF (1:1,v/v) under ambient condition ([**3.1**] = 1.0 μM). Photographs of solutions of 2:1 complex of **3.1** and Pd^{2+} in presence of different anions, B) under normal light and C) under UV light, [**3.1**] = 1.0 μM. D) Relative Fluorescence response of **3.1**-Pd^{2+} (2:1) toward CN^- over miscellaneous competitive anions upon excitation at 490 nm. Black bars represent the addition of the intensity of **3.1**-Pd^{2+} (2:1) in presence of OAc^-, ClO_4^-, HSO_4^-, $H_2PO_4^-$, SCN^-, BF_4^-, PF_6^-, NO_3^-, OH^-, F^-, Cl^-, Br^-, I^-, SO_4^{2-}, and PO_4^{3-}; Red bars represent the subsequent addition of CN^- to the solution.

The detection limit for the CN- ion was calculated to be 0.26 ppb which is much lower than the highest permissible limit in drinking water (0.07 ppm) recommended by World Health Organization (WHO).[193] The mechanism of the tandem sensing process can be summarized in terms of the aggregation/dis-aggregation of the **PDI** moiety. In 1:1 Water-DMF, compound **3.1** (1×10^{-6} M) remained in monomeric state as can be observed from the $A_{0\text{-}0}/A_{0\text{-}1}$ ratio, high emission, no clear morphology as well as the absence of any particular particle size distribution in DLS measurement. Upon addition of Pd^{2+} to this solution a 2:1 complex was formed between **3.1** and Pd^{2+} as can be seen from Jobs plot. The metal complexation lead to aggregation of the **PDI** core which was confirmed by the appearance of a broad peak in UV-vis absorption spectra along with a sharp decrease in $A_{0\text{-}0}/A_{0\text{-}1}$ ratio (0.3). Moreover, flake like morphology in the FESEM and a distribution centered at 150 nm in the DLS also suggested the aggregation in this case. The aggregation was further confirmed by the aggregation induced quenching of the emission. In presence of CN^-, the same solution resulted in reappearance of the emission. In this case, CN^- being a stronger ligand displaces the pyridine groups and forms $[Pd(CN)_4]^{2-}$. As the **3.1**-Pd^{2+} complex breaks down, compound **3.1** also returns to its original non-aggregated form which was confirmed from the reappearance of the structured absorption profile, increase in the $A_{0\text{-}0}/A_{0\text{-}1}$ ratio to 1.54, re-appearance of emission, dis-appearance of any particle distribution in DLS. Further evidences were obtained from the FESEM images.

The selectivity as well as high sensitivity of the developed sensor can thus be used for practical purposes. To test its practical use, a solution of **3.1** (1 x 10^{-6} M) was casted on a pre-coated thin layer chromatography (TLC) plate with a syringe as shown in **Figure 3.8**. After drying, the casted portion of the plate showed strong fluorescence under UV-light irradiation. The plate was then dipped in a solution containing Pd^{2+} (5 x 10^{-6} M) and taken out after two minutes. The solvent was removed under reduced pressure. In this case, no fluorescence could be detected under UV-light as the metal ions are now complexed with the ligand and thereby quenched the emission property of the ligand. The plate was further dipped in a solution containing CN^- (5 x 10^{-6} M) and taken out of the solution after two minutes before drying the solvent. Under UV light, as expected, the fluorescence re-appeared as can be seen in **Figure 3.8**. Thus, the developed chemo-sensor can be used for an easy and effective sequential sensing of Pd^{2+} and CN^- ions at this concentration range. Naked eye detection showed a detection limit of 5 x 10^{-6} M for both Pd^{2+} and CN^- when a 1 x 10^{-6} M solution of **3.1** was used. Below this concentration of **3.1**, no emissive spot was observed.

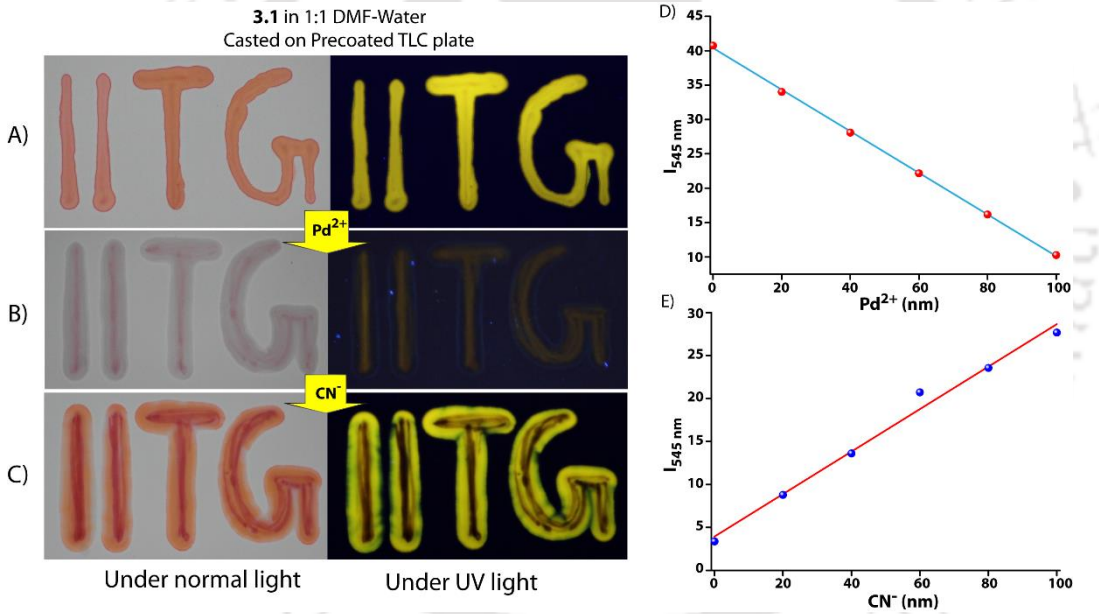

Figure 3.8 Photographs of a TLC plate casted with a solution of **3.1** (A) and consequently treated with a solution of Pd^{2+} (B) and finally with a solution of CN^- (C), D) intensity vs. concentration of Pd^{2+} plot for determination of detection limit, and e) intensity vs. concentration of CN^- plot for determination of detection limit.

Analyses of Pd^{2+} and CN^- in environmental samples such as tap water and pond water collected from different sources were also carried out. Different samples were spiked with various concentrations of Pd^{2+} and CN^- ions.[116] The concentrations thus determined by both absorbance and emission spectroscopy agreed with actual concentrations with a relative error of ~ 2% or better for both Pd^{2+} and CN^- as shown in **Table 3.1**.

Sample	Added (1×10^{-6} M)	Conc. ± SD (μM)[a]/ (relative error) (UV@530 nm)	Added (1×10^{-6} M)	Conc. ± SD (μM)[a]/ (relative error) (FL@545 nm)
Tap water (Pd^{2+})	0.2	0.2 ± 0.0003 (0.66)	0.2	0.2 ± 1.73 (3.50)
	0.2	0.4 ± 0.0001 (0.70)	0.2	0.4 ± 1.56 (2.30)
	0.4	0.6 ± 0.0004 (0.57)	0.4	0.6 ± 0.58 (9.00)
	0.8	0.8 ± 0.0005 (0.71)	0.8	0.8 ± 1.21 (11.80)
Pond water (Pd^{2+})	0.2	0.2 ± 0.0005 (6.50)	0.2	0.2 ± 0.64 (9.50)
	0.2	0.4 ± 0.0003 (7.30)	0.2	0.4 ± 1.32 (9.50)
	0.4	0.6 ± 0.0002 (6.40)	0.4	0.6 ± 0.92 (14.90)
	0.8	0.8 ± 0.0005 (7.40)	0.8	0.8 ± 1.11 (15.50)
Tap water (CN^-)	0.4	0.4 ± 0.003 (7.10)	0.1	0.1 ± 1.50 (4.80)
	0.8	0.8 ± 0.0002 (8.00)	0.2	0.2 ± 1.45 (3.70)
	1.2	1.2 ± 0.0004 (7.10)	0.3	0.3 ± 1.89 (4.10)
	1.6	1.6 ± 0.0006 (8.00)	0.4	0.4 ± 1.05 (2.50)
Pond water (CN^-)	0.4	0.4 ± 0.0005 (6.10)	0.1	0.1 ± 1.43 (11.0)
	0.8	0.8 ± 0.0001 (9.20)	0.2	0.2 ± 1.76 (10.30)
	1.2	1.2 ± 0.0004 (3.50)	0.3	0.3 ± 1.57 (10.40)
	1.6	1.6 ± 0.0008 (1.80)	0.4	0.4 ± 1.09 (9.70)

[a]Average ± standard deviation of three determinations.

Table 3.1. Application of **3.1** for the determination of Pd^{2+} and CN^- in various environmental samples.

3.3 Conclusion

In conclusion, we have developed an efficient and highly selective chemo-sensor for both, Pd^{2+} and CN^- ions. The detection limits observed in this case for both the ions are significantly lower to those reported earlier.[9] Moreover, the tandem detection of these ions is the first of its kind. The 2:1 binding of the ligand with Pd^{2+} leads to the formation of π–π stacking between the **PDI** cores. The aggregation essentially quenches the emission property of the dye. In presence of CN^- ions, the coordination between pyridine groups of the ligand and Pd^{2+} ions are disrupted which causes dis-aggregation of the **PDI**-cores and brings the ligand molecules to non-associated state leading to "turn-on" emission. The ligand can be used for environmental samples and was employed to create a TLC plate based efficient and easy sequential sensing tool for Pd^{2+} and CN^- ions.

3.4 Experimental section

3.4.1 General Information and Materials: All chemicals and reagents were purchased from Sigma-Aldrich (USA) and used without further purification. All solvents were procured from commercial suppliers. To prepare samples, Milli-Q water with a conductivity of less than 2 μS cm^{-1} was used. UV-Visible spectra were recorded on a PerkinElmer Lambda 750 spectrometer, while fluorescence measurements were performed on a FluoroMax-4 (Horiba). All emission spectra were recorded by exciting the sample at 490 nm. Standard 10 mm-path quartz cuvettes were used for all spectroscopic measurements. ^{1}H NMR and ^{13}C NMR were recorded with a Bruker Ascend 600 MHz (Bruker, Coventry, UK) spectrometer and referenced to deuterated solvents. ESI-MS was performed with a Q-tof-Micro Quadrupole mass spectrophotometer (Micromass).

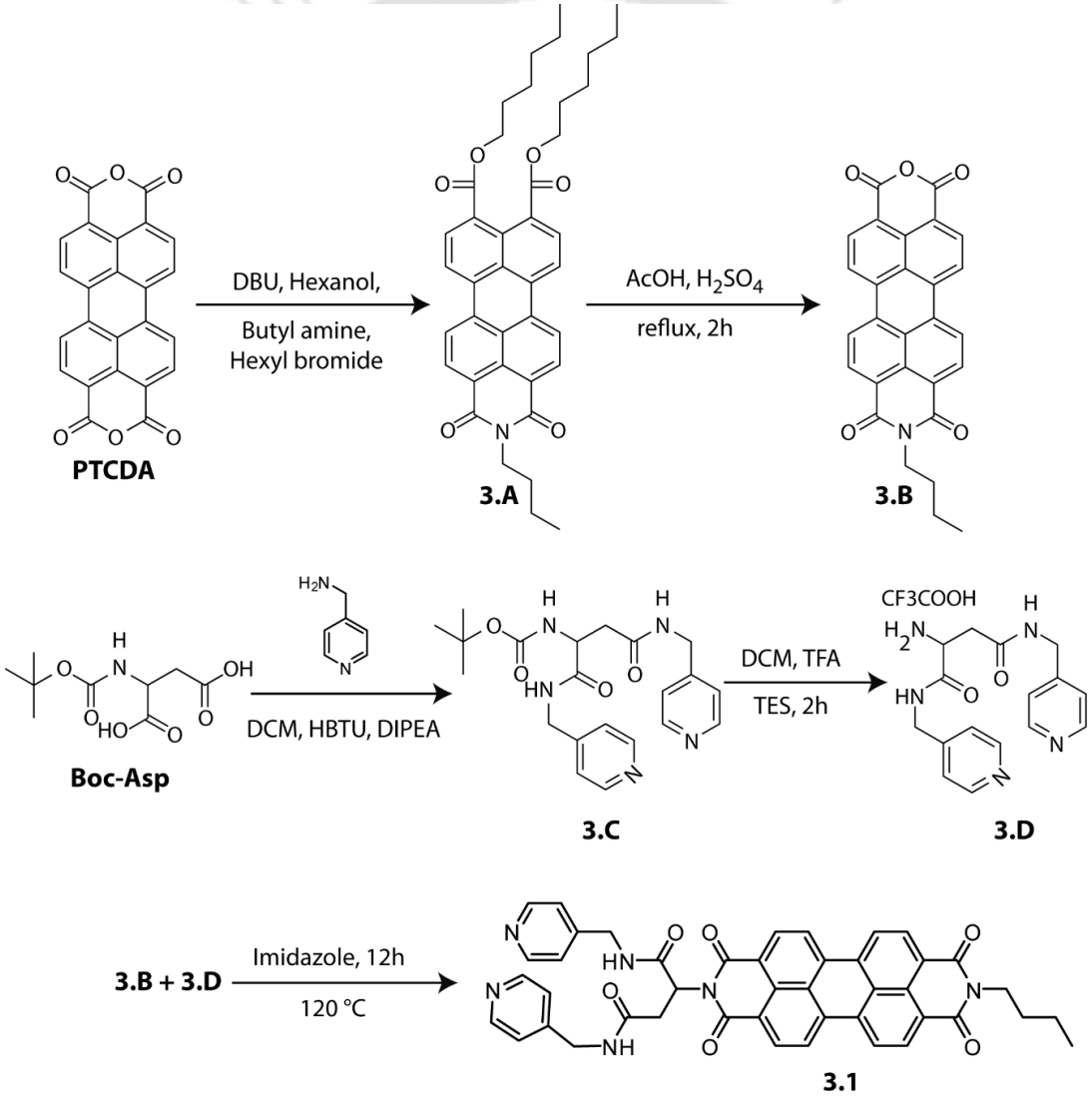

Scheme 3.2: Synthetic Scheme for compound **3.1**.

3.4.2 Synthesis and Characterization of Compounds

Compound **3.1** was synthesized according to **Scheme 3.2**.

Synthesis of compound 3.A: Perylene-3,4,9,10-tetracarboxylic dianhydride (PTCDA, 2.0 g, 5.10 mmol) was suspended in 20 mL DMF and to it 1,8-diazabicycloundec-7-ene (DBU, 3.09 g, 20.3 mmol) and 1-hexanol (4.17 g, 40.8 mmol) were added. After stirring for one hour at room temperature a homogeneous red solution was obtained. After 24 hours, butyl amine (186.5 mg, 2.55 mmol) was added and the solution was stirred for 3 days. 1-butyl bromide (5.59 g, 41.4 mmol) was added and the mixture was stirred for further 24 hours. The mixture was poured into 100 mL of deionized water and neutralized with HCl (2N), and subsequently extracted four times with dichloromethane (250 mL each time) and the organic phase was dried with sodium sulfate. After purification by column chromatography (silicagel 60-120 mesh, DCM), the product was obtained as a red solid. Yield = 75%. ^{1}H NMR (600 MHz, $CDCl_3$): δ = 8.46(d, J = 7.9 Hz, 1H), 8.28-8.21 (m, 2H), 8.12-8.07 (m, 2H), 8.01 (d, J = 7.8 Hz, 2H), 7.93 (d, J = 7.8 Hz, 1H), 4.33 (t, J = 7.4 Hz, 4H), 4.20 (t, J = 7.4 Hz, 2H) 1.82 – 1.81 (m, 8H), 1.37 – 1.35 (m, 4H), 1.02 (m, 8H), 0.92 – 0.90 (t, J = 7.4 Hz, 9H) ppm. Mass (MALDI-TOF, DHB matrix): *m/z* calcd. for $C_{40}H_{43}NO_6$ $[M + H]^+$, 633.31; found 633.52.

Synthesis of compound 3.B: The di-ester **3.A** (1.28 g, 1.73 mmol) was suspended in a mixture of 30 g glacial acetic acid and 1.5 g concentrated sulfuric acid and refluxed for two hours. The mixture was cooled to room temperature and poured into 100 mL of deionized water. The precipitate was filtered and washed with water until the filtrate was neutral. After drying the red-brown solid at 80 °C for 12 hours under high vacuum the mono-anhydride **3.B** was obtained. Yield = 98%. The product was used without further purification and characterization due to insolubility in all common organic solvents. Mass (MALDI-TOF, DHB matrix): *m/z* calcd. for $C_{28}H_{17}NO_5$ $[M + H]^+$, 477.45; found 477.44.

Synthesis of Compound 3.C: To an ice-cooled solution of Boc-Asp (0.5 g, 2.14 mmol) in 10 mL of dry DCM and 0.3 mL DMF, was added N,N,N′,N′-Tetramethyl-*O*-(1*H*-benzotriazol-1-yl)uronium hexafluorophosphate (HBTU, 1.79 g, 4.72 mmol), N, N-diisopropylethyl amine (DIPEA, 1.22g, 9.43 mmol) and stirred for 10 min. To the reaction mixture, 4-aminomethyl pyridine (0.51 mL, 4.68 mmol) was added and stirred for 24 h at room temperature. The reaction mixture was filtered and the filtrate was diluted with 100 mL of DCM, washed with saturated $NaHCO_3$ solution and brine solution. The organic layer was dried over Na_2SO_4, and concentrated on a rotory evaporator. The crude product was chromatographed on a column of silica gel using DCM/MeOH as eluents to obtain the pure product **3.C** as white solid. Yield = 62%. ^{1}H NMR (600 MHz, $CDCl_3$): δ = 8.52(d, J = 7.5 Hz, 4H), 7.19 (d, J = 7.5 Hz, 4H), 4.99-5.03(m, 2H), 4.94-4.96 (m, 2H), 4.49-4.53 (m, 1H), 2.98 – 3.02 (m, 1H), 2.65-2.69 (m, 1H), 1.44 (s, 9H) ppm. Mass (ESI-MS): *m/z* calcd. for $C_{21}H_{27}N_5O_4$ $[M + H]^+$, 414.21; found 414.22.

Synthesis of Compound 3.D: Compound **3.C** (300 mg, 1.33 mmol) was taken in DCM (1 mL). To it, trifluoroacetic acid (1 mL) and few drops of triethylsilane (TES) were added and stirred for 2h. Then solvent was removed on a rotory evaporator and the residue was taken in MeOH and precipitated from diethyl ether to get the product as a white solid. It was then dried under vacuum and used for the next step. Yield = 84 % (400 mg). Mass (ESI-MS): *m/z* calcd. for $C_{16}H_{20}N_5O_2$ $[M + H]^+$, 314.16; found 314.16.

Synthesis of Compound 3.1: Monoanhydride **3.B** (200 mg, 0.44 mmol) and the amine **3.D** (470 mg, 0.72 mmol) were heated together with 8 g of imidazole for 6 hours at 130 °C under nitrogen atmosphere. The reaction mixture was then poured into 100 mL of deionized water and neutralized with HCl (2N, 60 mL). The mixture was extracted with DCM (3 x 30 mL). The organic phase was washed with 400 mL saturated potassium carbonate solution, dried with sodium sulfate and concentrated on a rotory evaporator. The crude product was purified by washing with acetonitrile to obtain the title compound **3.1** as a red solid. Yield: 40%. ^{1}H NMR (600 MHz, DMSO-d_6): δ = 8.63 (s, br,4H), 8.54 (s,br, 4H), 7.98-7.92 (m, 2H), 7.83-7.78 (m, 2H), 7.72 – 7.65 (m, 2H), 7.51-7.49 (m, 2H), 6.14 (s, 2H), 5.15-5.11 (m, 1H), 4.86-4.76 (m, 6H), 3.83 (t, J = 7.5 Hz, 2H), 1.60 (t, J = 7.5 Hz, 2H), 1.37-1.35 (m, 2H), 0.96 (t, J = 7.5 Hz, 3H) ppm. ^{13}C NMR (150 MHz, DMSO-d_6): δ = 174.6, 174.5, 162.2, 162.0, 149.5, 149.4, 145.0, 133.9, 131.1, 128.9, 125.6, 124.1, 123.3, 122.2, 122.1, 48.7, 40.8, 40.0, 33.5, 29.3, 19.8, 13.6 ppm. Mass (MALDI-TOF, DHB matrix): *m/z* calcd. for $C_{44}H_{34}N_6O_6Na$ $[M + Na]^+$, 765.24; found 765.28.

3.4.3 Method

Sample Preparation: Stock solution of compound **3.1** was prepared in a 10 mL of volumetric flask in DMF. The stock solution was then diluted to the concentrations with Water-DMF solvent mixtures for the experiments. Stock solutions of various metal ions and anions were prepared in mili-Q water. Chloride salts of various metal ions were chosen for the selectivity experiments of metal ion sensing whereas for the anion sensing tetrabutyl ammonium salts were used. Control experiment was carried out by adding exactly the same amount of water to the 1:1 solutions of Water-DMF but no observable change in the absorption and emission spectra were obtained.

Job's plot experiment: Ten sets of 3 mL Water-DMF (1:1, v/v) solution were prepared and labeled 1 to 10. Appropriate amounts of the ligand stock solutions were added to each set of solution so that the concentration of ligand in the solutions varies from 1 µM to 10 µM in these ten vials. Appropriate amounts of Pd^{2+} solution was added to each set of solution in a way to maintain the total concentration of the ligand and metal ion to 10 µM. The UV-Vis spectra of all these 10 sets were recorded and the absorbances at 530 nm were plotted against the mole fraction of Pd^{2+} to obtain Job's plot.

Binding constants using spectroscopic titration data: The binding constant for the formation of the complex was determined using the Benesi–Hildebrand (B–H) equation 3.1 and 3.2 for UV-Vis and fluorescence spectroscopy respectively.[1]

$$1/(A-A_0) = 1/(K(A_{max}-A_0)\,[Pd^{2+}]^{0.5}) + 1/(A_{max}-A_0) \quad (3.1)$$

$$1/(I-I_0) = 1/(K(I_{max}-I_0)\,[Pd^{2+}]^{0.5}) + 1/(I_{max}-I_0) \quad (3.2)$$

Here A_0 is the absorbance of the ligand in absence of analyte (Pd^{2+}), A is the observed absorbance in presence of added analyte, A_{max} is the maximum absorbance value that was obtained during titration with varying analyte concentrations. Similarly, I_0 is the emission of the ligand in absence of analyte, I is the observed emission in presence of added analyte, I_{max} is the maximum emission value that was obtained during titration with varying analyte concentrations. *K* is the binding constant, determined from the slope of the linear plot between $(A_{max}-A_0)/(A-A_0)$ vs $1/[Pd^{2+}]^{0.5}$ in case of absorbance and $(I_{max}-I_0)/(I-I_0)$ vs $1/[Pd^{2+}]^{0.5}$ in case of emission.

Fourier transformed infrared spectroscopy (FTIR): To get the complexes, concentrated samples in 1:1 Water-DMF were prepared and kept under high vacuum at 40 °C for several hours when precipitates were obtained. These precipitates were then centrifuged and collected before drying them for 48 h under high vacuum over dessicant silica gel. KBr pellets were prepared by mixing the samples with oven dried KBr. The spectra were recorded on a Nicolet is10 spectrometer. The baseline was subtracted from the obtained absorbance intensity in each case.

Dyanamic Light Scattering (DLS): The particle sizes of the samples were measured at 298 K on a Zetasizer Nano ZS90 from Malvern using a 632.8 nm He–Ne laser. Prior to measurements, the samples were filtered through appropriate filters to remove dust particles if any.

Calculation of α_{agg}: The mole fraction of aggregate (α_{agg}) was estimated by using Equation 3.3,

$$\alpha_{agg} \approx (A-A_{mon})/(A_{agg}-A_{mon}) \quad (3.3)$$

Where, α_{agg} is the mole fraction of aggregate at any stage, and A_{mon}, A, and A_{agg} are the absorbance at 530 nm for the monomer, the solution under question, and the pure aggregate solutions respectively.

Quantum Yield measurement: The fluorescence quantum yields of **PDI** ligand was determined by Parker-Rees method using Rhoamine-6G as a standard fluorophore. The Parker-Rees equation (2.1) is written as follows,

$$\phi_u = (A_s F_u n_u^2 / A_u F_s n_s^2)\,\phi_s$$

where, ϕ_s = Quantum Yield of standard fluorophore = 0.95 in EtOH, ϕ_u = Quantum Yield of unknown fluorophore, A_s = the absorbance of standard fluorophore at the excitation wavelength, A_u = the absorbance of unknown fluorophore at the excitation wavelength, F_s = the area of integrated fluorescence intensity of the reference sample when excited at the same excitation wavelength, F_u

= the total area of integrated fluorescence intensity for the unknown sample when excited at the same excitation wavelength, The refractive indices of the solvents for the unknown and the standard samples are denoted by n_u and n_s respectively. To minimize the reabsorption of the fluorescence light passing through the samples their absorption maximum was kept 0.1.

Time-resolved fluorescence lifetime measurements: Lifetime measurement was done using Eddinburg (FSP920) spectrophotometer.

Detection Limit: Detection limits were calculated from the fluorescence titration. The fluorescence emission spectra of **3.1** was measured 10 times, and the standard deviation of blank measurement was determined. To achieve the slope, the fluorescence emission at 545 nm was plotted as a function of the concentration of Pd^{2+} and CN^- individually. The detection limits were obtained using the following equation,

Detection limit = $3\sigma/k$ (3.4)

Where σ is the standard deviation of blank measurement, and k is the slope between the fluorescence emission intensity versus $[Pd^{2+}]$ or $[CN^-]$.

The calculated detection limits for Pd^{2+} and CN^- ions were 5.2 nM and 9.8 nM respectively. The conversion to ppb unit was done considering Mol. wt. of Pd^{2+} and CN^- as 106.42 and 26.01 respectively.

Preparation TLC Based Tool: To test its practical use, a solution of **3.1** (1×10^{-6} M) in 1:1 Water-DMF was casted on a pre-coated thin layer chromatography (TLC) plate using a syringe. After drying, the casted portion of the plate showed strong fluorescence under UV-light irradiation. The plate was then inserted in a solution containing Pd^{2+} (5×10^{-6} M in water) and taken out after two minutes. The solvent was removed under reduced pressure. In this case no fluorescence could be detected under UV-light. The plate was further dipped in a solution containing CN^- (5×10^{-6} M in water) and taken out of the solution after two minutes. The plate was dried under vacuum and irradiated with UV-light. To check the lower detection limit for this TLC based tools, different concentrations of **3.1** was used. However, it was observed that below 1×10^{-6} M, emission bands could not be observed.

Preparation of environmental samples: The measurements of optical properties of **3.1** towards Pd^{2+} and CN^- were performed in the environmental samples such as tap water, pond water. For preparation of solution of **3.1** (1×10^{-6} M) in these environmental samples, the de-ionized water in DMF-Water (1:1, v/v) was replaced by tap water, or pond water followed by addition of various concentration of Pd^{2+} and CN^- as per design of the experiment . The samples were equilibrated for 1h and then absorption and emission spectra were recorded. The absorption and emission spectra of **3.1** were measured in triplicate, and the standard deviation of each sample was determined. Relative error of each sample was also calculated.

SL. No.	System	Medium	Detection Limit	Reference
01	Small molecule	Water-DMF	0.552 ppb (5.2 nM)	This work
02	Small molecule	DMF-HEPES buffer	780 nM	195
03	Small molecule	EtOH-HEPES buffer	470 nM	196
04	Small molecule	Water-EtOH	191 nM	172
05	Small molecule	Water-EtOH	10 nM	197
06	Small molecule	Water-DMSO	85 nM	171
07	Purine Nucleoside	DMSO-Tris buffer	647 nM	198
08	Small molecule	EtOH	5 nM	199
09	Small molecule	Water-ACN	6.1 nM	113

Table 3.2. Comparison of detection limit between previously reported Palladium sensors and compound **3.1**.

SL. No.	System	Medium	Detection Limit	Reference
01	Small molecule	Water-DMF	0.26 ppb(8.69 nM)	This work
02	Quantum dots	NaOH-$NaHCO_3$ buffer	520 nM	200
03	Nanoparticles	Water	9.1 nM	201
04	Metal coefficient	ACN	1600 nM	202
05	Gold nanoclustures	Water	75 nM	203
06	Metal complex	Water	5770 nM	204
07	Peptide	HEPES buffer	24.9 nM	205
08	Metal complex	ACN	0.3 ppm	206
09	Small molecule	Water	320 nm	175

Table 3.3. Comparison of detection limit between previously reported CN^- sensors and compound **3.1**-Pd^{2+} complex.

Chapter 4

Efficient Detection of Histone by a DNA-Naphthalenediimide Hybrid

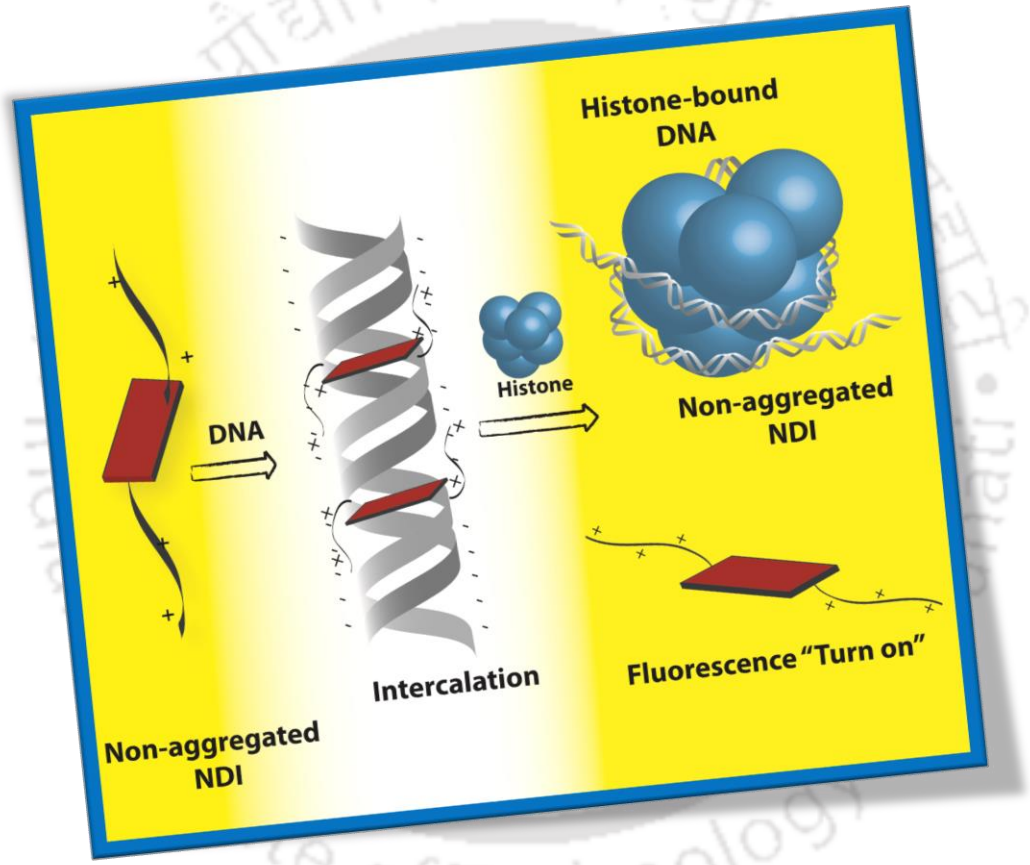

4.1 Introduction

Histone, a DNA-binding protein, governs the chromosomal organization and gene regulation in cells.[207-208] Anomalous epigenetic arrangements have been found in a plethora of diseases, such as cancers, schizophrenia, Alzheimer's and Huntington's diseases, heart failure, arthritis, diabetes, microbial infections, HIV *etc.*[127, 209-211] Dengue virus, a continuing global threat, works via binding with the nuclear histone in liver cells and inhibits the nucleosome formation and over-expression of histone.[207-208] A reliable, efficient histone sensing thus became essential. Unfortunately, methods capable of sensing histone are rare and the existing ones often has issues with the sensitivity and ease of use.[212-213] Nevertheless, the efficiency of sensing as well as that of the process need to be enhanced further.

In this regard, small molecules with the ability to recognize and bind with DNA have drawn considerable interest owing to their potential on imaging, diagnostics, and therapeutics.[214-215] Recognizing and binding with DNA by small molecules follow mainly intercalation through non-covalent interactions.[216] To this end, naphthalene diimides (**NDI**) with appropriate functionalization were found to be an excellent probe to intercalate with DNA double strands.[26, 217-218] Several detailed studies on **NDI**-DNA interaction have been reported by Iverson and Wilson.[219-224] A direct consequence of DNA-binding by all these **NDI** derivatives is the drastic fall in fluorescence quantum yield of **NDIs**.[219-222] We envisioned that this quenching of emission upon binding with DNA can be utilized to create new sensor for proteins capable of binding with DNA, such as histone. The strong binding affinity [225] of histone toward DNA will lead to release of the **NDI** molecules from the **NDI**-DNA complex resulting in enhancement of the fluorescence intensity (**Scheme 4.1**). This phenomenon can be quantified and used as an efficient "turn-on" sensor for histone.

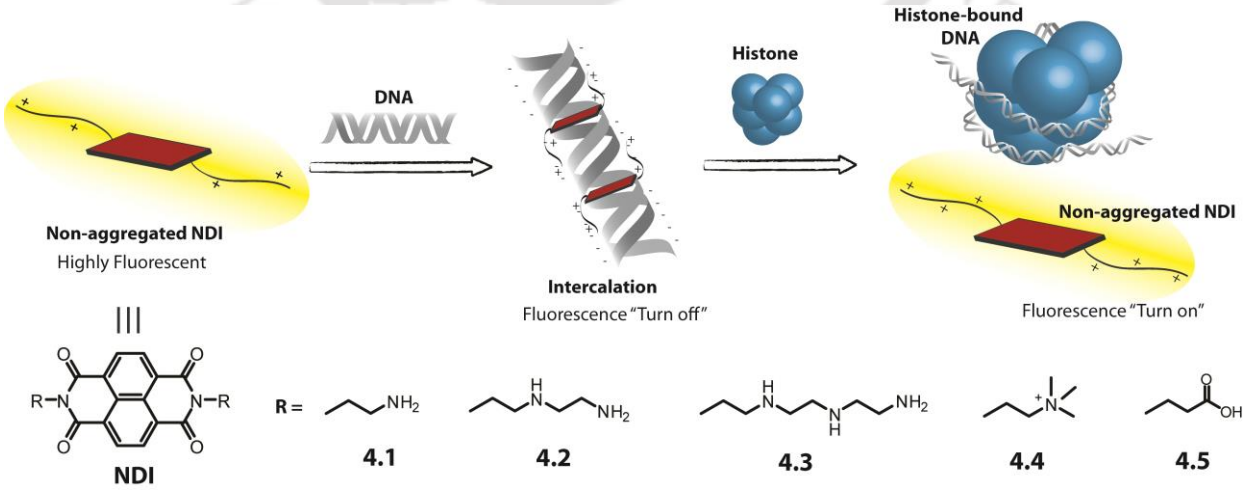

Scheme 4.1. Pictorial presentation of histone sensing mechanism and chemical structures of **NDIs**.

In this chapter, we have created a new **NDI**-DNA hybrid material for efficient and selective sensing of histone. To find a suitable **NDI** derivative toward creating the planned sensor, four amine functionalized **NDIs** having different numbers of amine groups (**4.1- 4.4**, **Scheme 4.1**) were prepared to find the effect of positive charges on their DNA binding ability. A control molecule (**4.5**) with acid functionality is also prepared for comparative studies.

4.2 Results and Discussion

The absorption spectra of all **NDI**s showed two prominent vibronic bands at ~ 380, 360 and a shoulder at 340 nm attributed to the 0-0, 0-1 and 0-2 vibrational transitions as seen in **Figure 4.1**. In each case, the absorption increases with increase in concentration. The minimum aggregation concentrations (MAC) measured from the inflection points in emission vs. concentration plots for all compounds were observed to be higher than 10 μg mL^{-1}. Similar trends were observed in their concentration dependent emission behavior as observed in **Figure 4.1**. Emission intensities for both the emission bands at ~393 and ~412 nm increased with concentration and after the critical value, decreased rapidly as shown in **Figure 4.1**.This is typical of arylenediimides.[179,185] Thus, for DNA binding studies, concentration of the **NDI** derivatives was kept at 1 μg mL^{-1} to avoid any self-aggregation induced changes. Concentration dependent DLS studies were performed for all these compounds and it was observed that the first sign of any aggregation was seen above 15 μg mL^{-1} concentration for all the samples. Further, to confirm that there is no aggregation at a concentration below 15 μg mL^{-1}, FESEM images of 1 and 10 μg mL^{-1} samples were checked and no sign of any aggregation was observed. Based on these observation, to avoid any effect from aggregation, we have carried out all studies below 15 μg mL^{-1} concentration for the DNA binding studies.

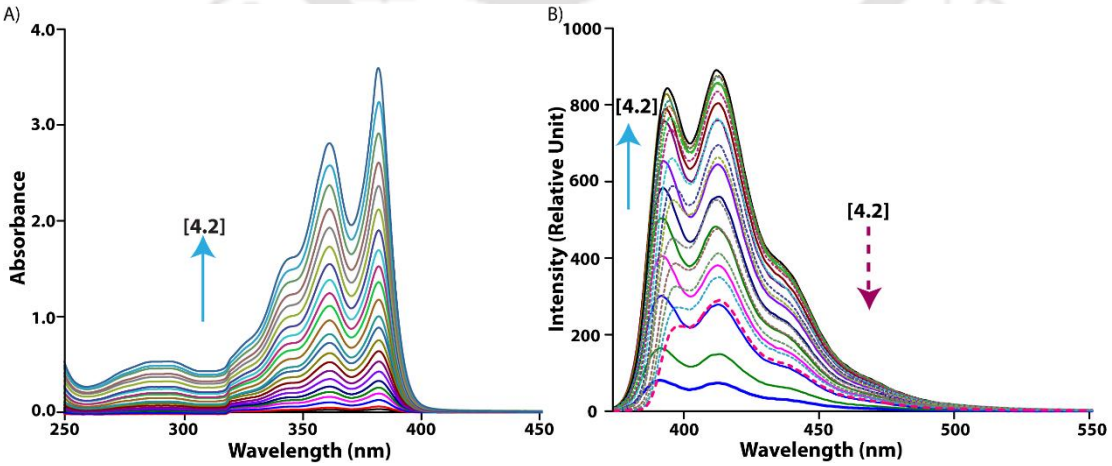

Figure 4.1 Concentration dependent changes in A) absorption, B) emission for **4.2** in phosphate buffer (10 mM, pH 7.4), (solid lines and dashed lines represent concentration up to 22 μg mL^{-1} and concentrations thereafter respectively).

All **NDI** derivatives were subjected to binding studies with double stranded calf thymus DNA (CT-DNA). Titrating 1 μg mL^{-1} solutions of **NDIs** with DNA solution resulted in hypochromicity and a small red-shift of the absorption maxima as shown in **Figure 4.2** and **4.3** except in case of compound **4.5**. The % hypochromism for 1 μg mL^{-1} **NDI** and 10 μg mL^{-1} DNA are listed in **Table 4.1**. The prominent hypochromism (32-45%) in case of cationic **NDI** signifies that the molecules are strongly intercalated with the DNA.[226] Among the cationic **NDIs**, compound **4.2** showed maximum hypochromism (45%) indicating the strongest binding among this series of molecules. Along with hypochromism, two clear isosbestic points were also observed. Both, hypochromicity and red-shifts are indications of intercalation of the molecules between the DNA strands.[220] The presence of isosbestic points indicated the equilibrium between the bound and free ligand. In case of the anionic analogue, **4.5**, no noticeable change was observed which presumably due to no binding in this case.

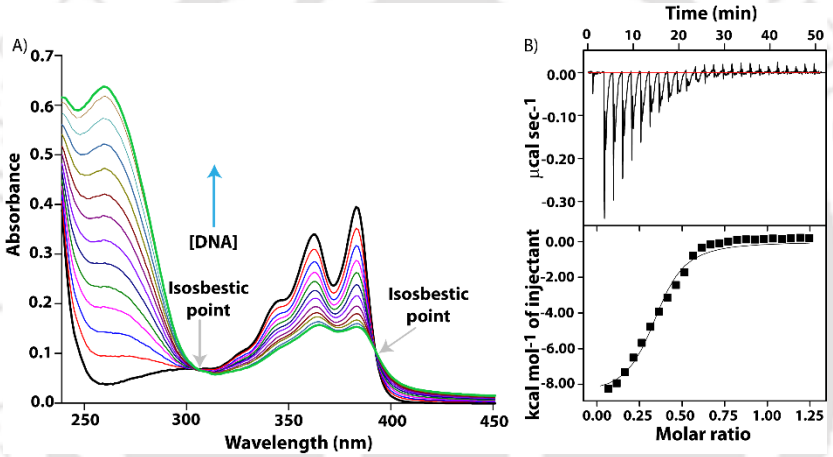

Figure 4.2 A) Changes in absorption of **4.2** upon titration with DNA, the arrows indicate isosbestic points, [**4.2**] = 10 μg mL^{-1}, B) thermogram (top) and binding isotherm (bottom) of **4.2** and DNA obtained from ITC measurement.

Further information about the binding affinity were obtained from Isothermal Titration Calorimetry (ITC) measurements as shown in **Figures 4.2B)** and **4.3E-H)**. **NDI** conjugates were titrated at room temperature into 10 mM phosphate buffer, pH 7. 4 containing DNA, and the heat change was measured over time. The binding isotherm of heat exchange versus the molar ratio was generated by fitting the raw data by nonlinear least-squares fitting with a one-site binding model. As expected, cationic **NDIs** (**4.1-4.4**) showed efficient binding with DNA ($K_a \sim 10^5\ M^{-1}$) while no proper isotherm obtained for the anionic analogue (**4.5**). The terminal acid groups of **4.5** interacted repulsively with the phosphate backbone of DNA which prevent any measurable binding. **4.2** resulted in significantly higher binding constant than the other analogues suggesting much stronger binding in this case. Other thermodynamic parameters like change in enthalpy and entropy (**Table 4.1**) were also found to favor stronger binding in case of **4.2** over other analogues and the exothermic binding process was found to be enthalpy driven.[227] The positively charged ammonium groups on each side of the **NDI** core of cationic **NDIs** interacted with the phosphate backbone of DNA to contribute to

the gain in enthalpy. These results clearly indicate toward the possible threading intercalation by these cationic derivatives of **NDI**. The entropy variations (**Table 4.1**) were observed due to the differential binding behavior of **NDI** derivatives with DNA.

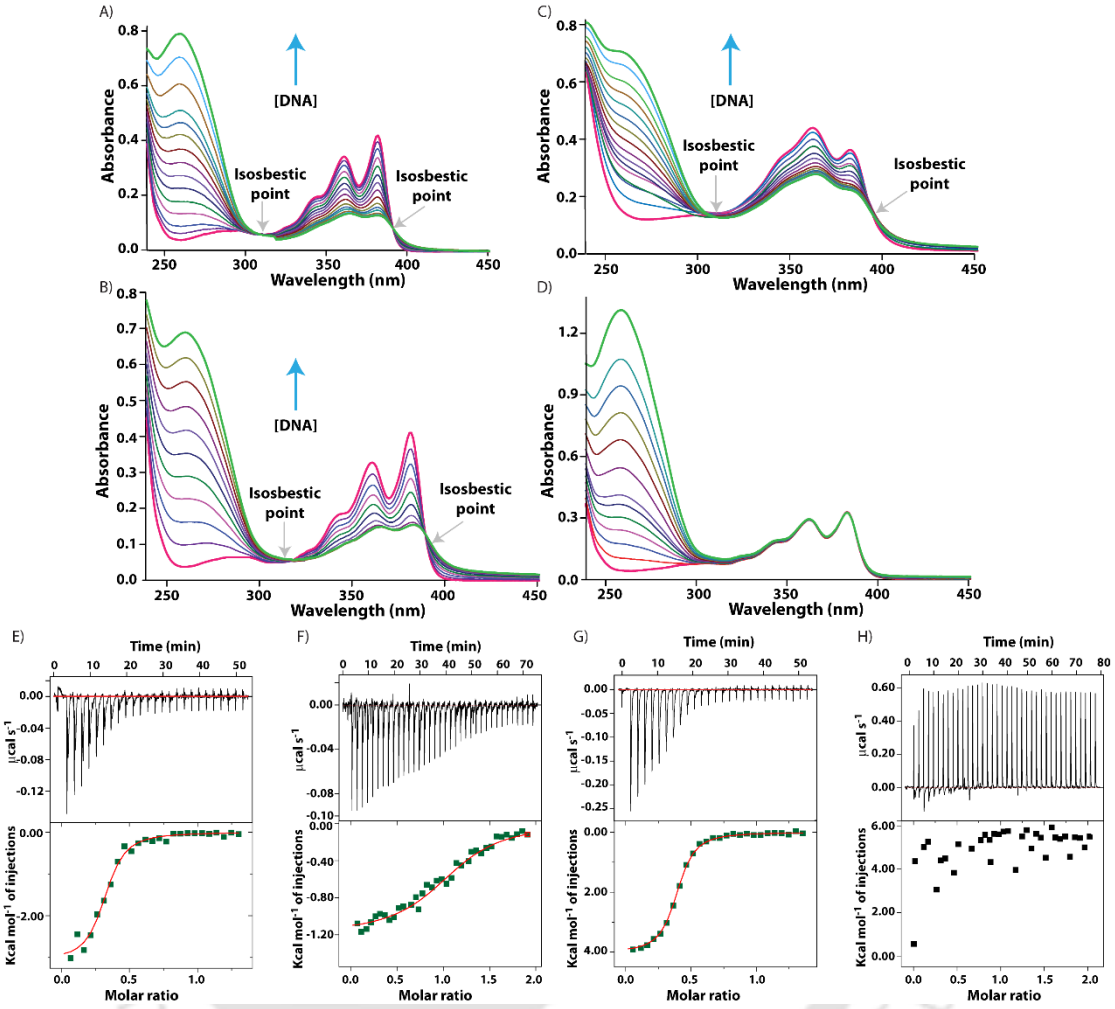

Figure 4.3 Changes in absorption of A) **4.1,** B) **4.3,** C) **4.4,** D) **4.5** upon titration with DNA, the arrows indicate isosbestic points, [**NDI**] = 10 µg mL^{-1}, and E-H) thermogram (top) and binding isotherm (bottom) of **4.1, 4.3, 4.4, 4.5** and DNA obtained from ITC measurement.

In order to identify the binding mechanism, competitive binding assays were performed. Binding of **NDI** molecules were studied using fluorescent dye displacement assays.[228] EtBr and DAPI were used as intercalating and groove binding dyes respectively. The fluorescence of EtBr and DAPI bound DNA was monitored upon addition of **4.1-4.5** as shown in **Figure 4.4**. The extent of quenching of emission for these two dyes in presence of **NDI** derivatives were then correlated with the binding affinity as shown in **Figure 4.4**. The cationic **NDIs** effectively displaced both dyes from their intercalation and groove binding. Maximum quenching was observed in case of **4.2** while **4.5** did not show any noticeable change in the fluorescence intensities.

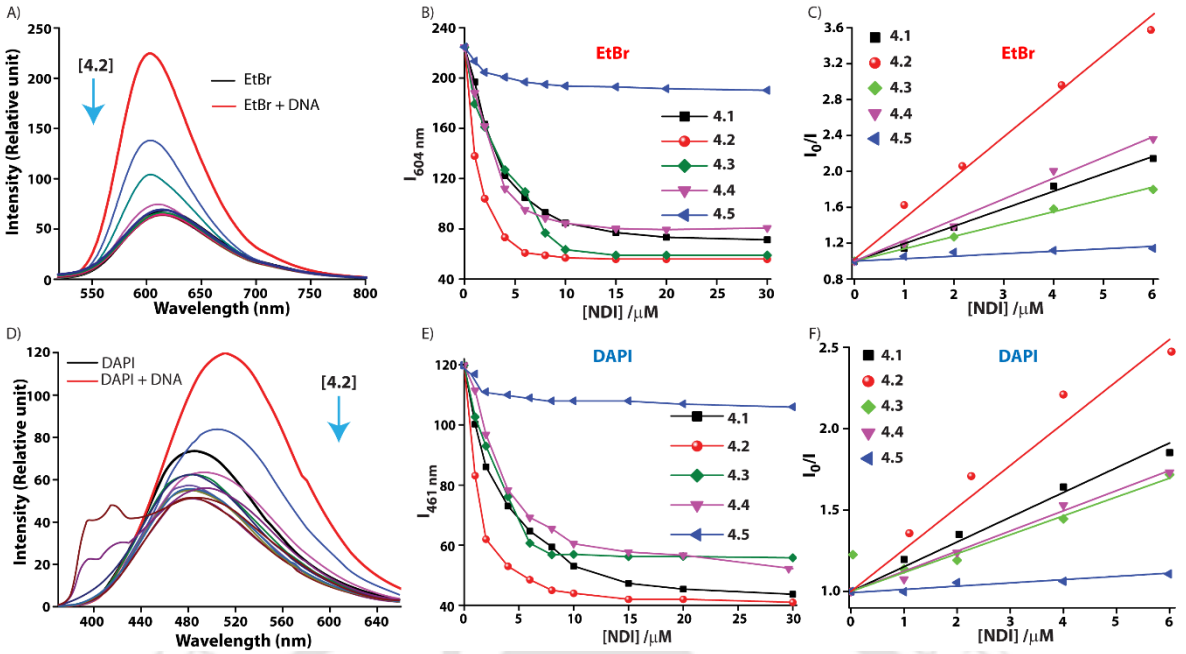

Figure 4.4 Decrease in emission intensity of EtBr (A) and DAPI (D) bound DNA with increase in **4.2** concentration. Decrease in emission intensity (B, E) and Stern-Volmer plots (C, F) for fluorescence quenching of EtBr and DAPI bound to DNA upon treatment with increasing concentration of different **NDIs**.

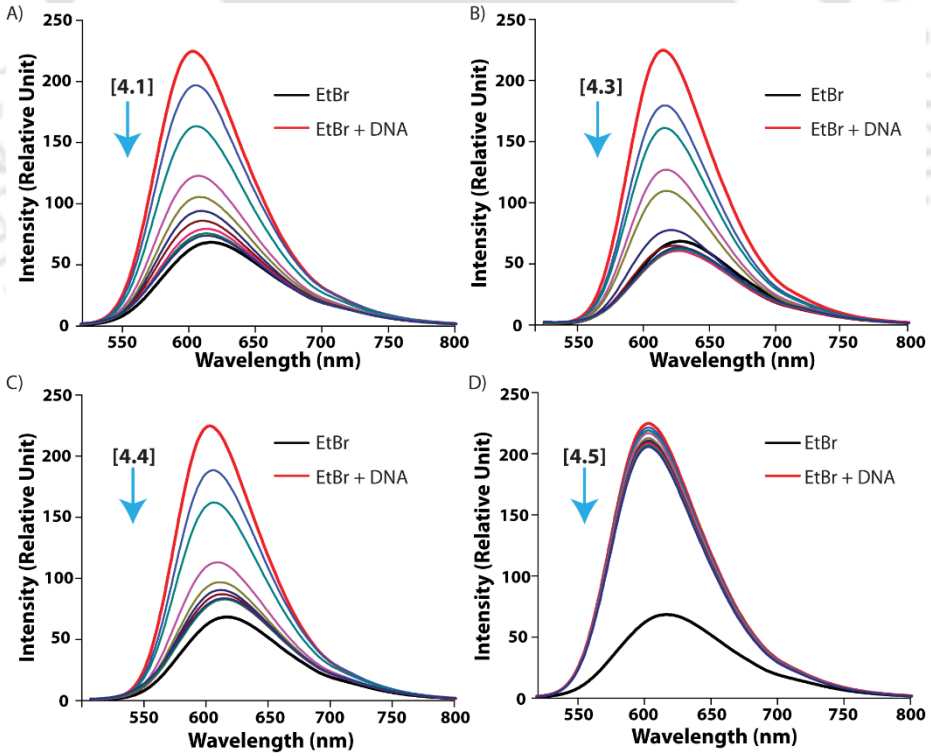

Figure 4.5 A)-D) Fluorescence quenching of EtBr (10 μM) bound to DNA (10 μM) upon titrating with A) **4.1**, B) **4.3**, C) **4.4**, D) **4.5** at room temperature in 10 mM phosphate buffer pH 7.4.

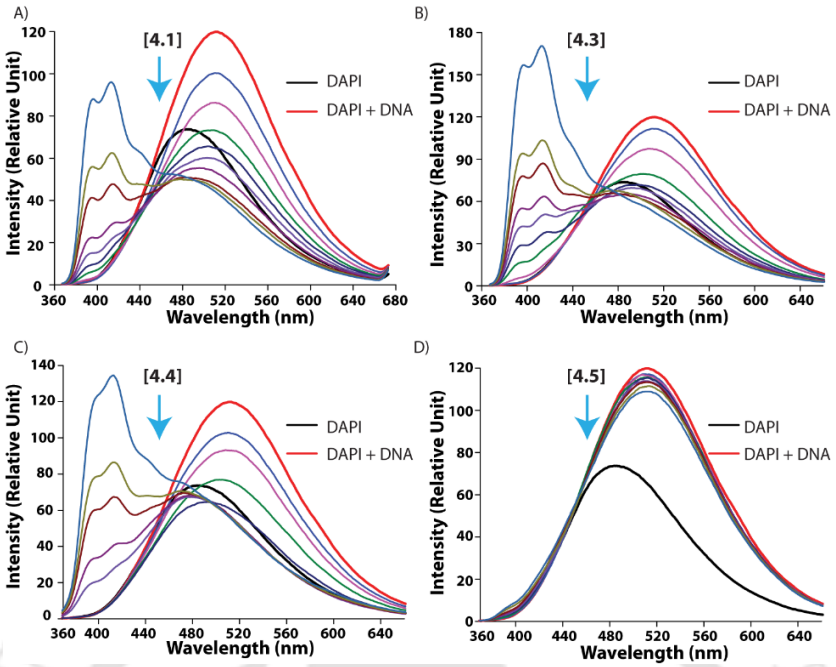

Figure 4.6 A)-D) Fluorescence quenching of DAPI (4 µg mL^{-1}) bound to DNA (14 µg mL^{-1}) upon titrating with A) **4.1**, B) **4.3**, C) **4.4**,D) **4.5** at room temperature in 10 mM phosphate buffer pH 7.4.

The plots of fluorescence quenching of DNA-bound EtBr and DAPI by **NDI**s are in good agreement with linear Stern-Volmer Equation.[229] K_{sv}, the Stern-Volmer quenching constant, a measure of the quenching efficiency, was found to be highest in case of **4.2** (for both EtBr and DAPI displacement, **Figure 2** and **Table 4.1**) indicating stronger intercalation and groove binding in this case.[228] Interestingly, the K_{sv} values obtained are in good agreement with the binding constants (~ 10^5 M^{-1}) obtained from the ITC measurements. Moreover, higher K_{sv} values for EtBr displacement than for DAPI, suggests that these **NDIs** (**4.1**-**4.4**) preferentially intercalate with DNA and then slowly binds in the grooves through ionic interaction between cationic side groups of **NDIs** and phosphates of DNA.[221] Thus, the molecules are binding in a threading intercalation mechanism.

The ΔT_m for all the **NDI**-DNA hybrids are given in **Table 4.1** and these values also follow similar trend to that of the binding affinity. Higher ΔT_m value indicates better stability of the complex and accordingly, the **4.2**-DNA hybrid was observed to be the most stable complex of the series. The stability of the **4.2**-DNA hybrid was further evaluated by its dissociation kinetic. Dissociation kinetic was measured by using the SDS sequestration method with time dependent UV monitoring as shown in **Figure 4.7**.[221, 222] Reasonably high half-life value 67 min was observed which not only support strong binding but also signifies intercalation as well as groove binding by the cationic **4.2**.[221, 222]

NDI	MAC (μg mL^{-1}) UV-Visible, Fluore-scence	% Hypo-chromism[a] Upon DNA Binding	Thermodynamic properties for DNA binding			Dye displacement K_{sv} (× 10^5 M^{-1})		ΔT_m[a] (° C)
			K_a (× 10^5 M^{-1})	ΔH Kcal/mol	ΔS cal/mol/deg	EtBr	DAPI	
4.1	20.5, 17.6	38	2.33 ± 1.09	-2.09 ± 0.1	9.8	1.9	1.5	4.2
4.2	22.2, 21.9	45	9.18 ± 0.88	-9.68 ± 0.3	23.40	4.6	2.6	12.5
4.3	34.1, 28.1	32	1.11 ± 0.51	-1.19 ± 0.1	12.5	1.4	1.1	1.9
4.4	19.6, 19.1	40	2.86 ± 1.05	-1.03±0.01	8.5	2.3	1.2	5.5
4.5	16.2, 15.2	-	-	-	-	0.28	0.25	0.2

[a]calculated for 1 μg mL^{-1} of **NDI** in presence of 10 μg mL^{-1} of DNA; [b]T_m of DNA = 64.5 °C

Table 4.1 Minimum aggregation concentrations, thermodynamic parameters of DNA binding, dye displacement data and melting temperatures data for **4.1-4.5**.

Interestingly, the binding ability was found to follow the order, **4.2** > **4.4** > **4.1** > **4.3**, from all these studies. The binding stability of the **NDI**-DNA hybrids can be expressed in terms of their melting temperature.[218] Melting temperatures (T_m) were determined using absorption spectroscopic method and the free DNA showed a T_m of 64.5 °C (**Figure 4.7**).

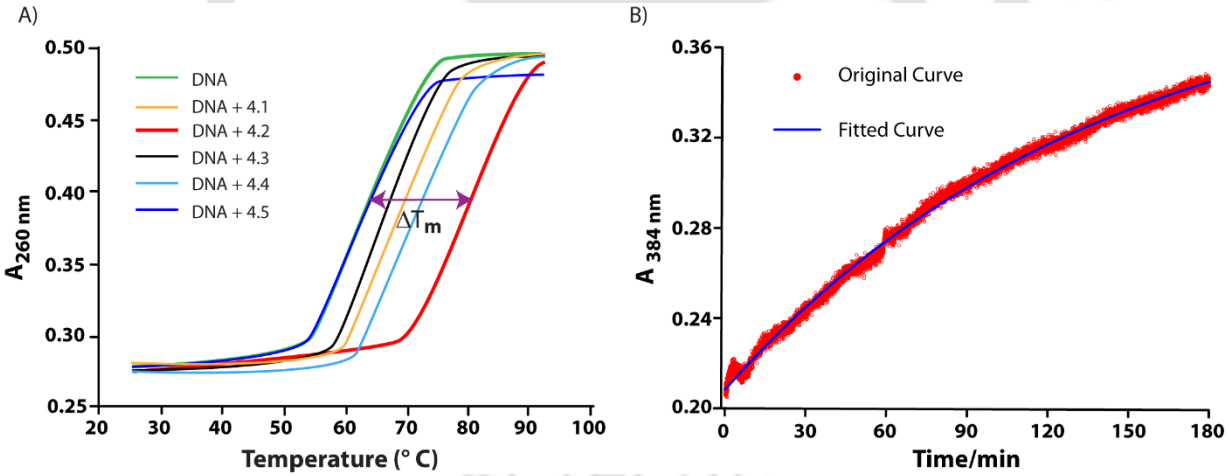

Figure 4.7 A) UV melting curves of DNA in the absence and presence of **4.1-4.5**; [**NDI**] = 50 μg mL^{-1}, [DNA] = 10 μg mL^{-1}, B) dissociation kinetic profile of **4.2** from DNA in 1%SDS; data are fitted to one-phase exponential decay.

Overall, all the results from DNA binding studies lead to the conclusion that the cationic **NDIs** are binding with DNA through threading intercalation mechanism. The **NDI** core binds between the strands of DNA via intercalation while the cationic side chains interact with the phosphate exteriors of the double stranded DNA through electrostatic interaction. The anionic analogue failed to bind phosphate groups of DNA which not only prevent any grove binding but also did not allow the planner **NDI** core to intercalate. The order of binding affinity was found to be **4.2** > **4.4** > **4.1** > **4.3**.

These results indicate that though the presence of positive charge is important, the overall binding efficiency depends on the optimal charge on the molecule. **4.2**, having two positive charges on each sides of the **NDI** group showed strongest affinity toward DNA.

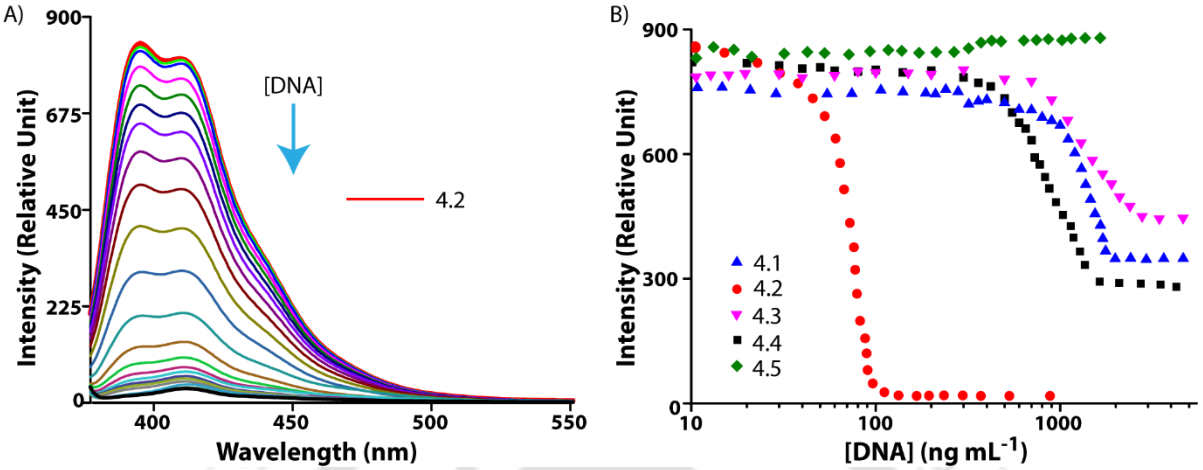

Figure 4.8 A) Emission spectra of **4.2** with increasing concentration of DNA, B) changes in emission intensity of **4.1-4.5** upon titration with DNA. [**NDI**] = 1 μg mL^{-1}

In order to utilize these threading intercalators as a probe for histone detection, the effect on their emission property upon binding with DNA was evaluated. As expected, binding with DNA resulted in significant quenching in the emission intensity for all cationic **NDIs** as shown in **Figure 4.8**.

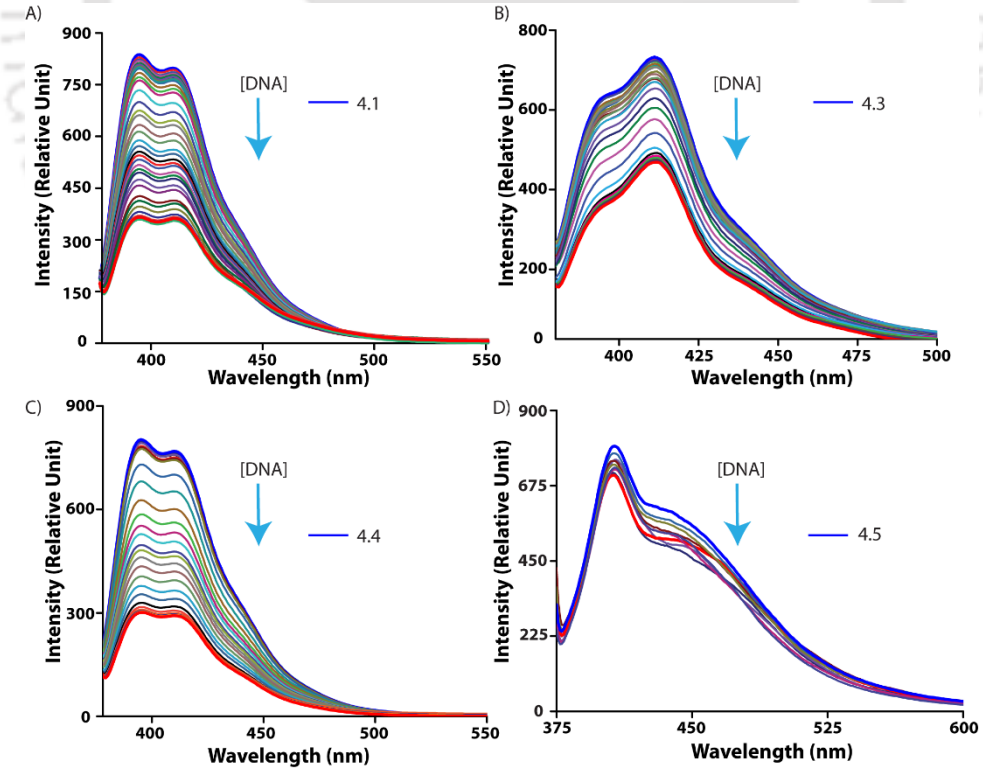

Figure 4.9 Emission spectra of A) **4.1**, B) **4.3**, C) **4.4**, D) **4.5** upon titrating with DNA, λ_{ex} = 360 nm, [**NDI**] = 1 μg mL^{-1} at room temperature in 10 mM phosphate buffer pH 7.4.

A saturation in the emission intensity is recorded in all cases after a certain concentration of DNA. However, the extent of quenching was found to be maximum (~97%) in case of **4.2**. Moreover, the concentration of DNA at which the emission reached its saturation was much lower for **4.2** (120 ng mL^{-1}) than the other analogues. This is presumably due to stronger affinity of **4.2** compared to the other **NDIs** as observed in the binding studies. Based on these results, **4.2** was selected as the probe for histone detection.

To verify our idea (Scheme 1), a mixture of **4.2** (1 μg mL^{-1}) and DNA (140 ng mL^{-1}) was prepared. Concentrations of the components were chosen in a way to achieve maximum binding and consequently the least possible emission arising from **4.2**. Varying amounts of histone (to reach the final concentrations of 0.1–1000 ng mL^{-1}) were added in this solution and the change in emission intensity was monitored as shown in **Figure 4.10**. A sharp increase in emission intensity was observed upon addition of 0.1–400 ng mL^{-1} of histone and thereafter no further change in fluorescence was noted up to 1000 ng mL^{-1} (**Figure 4.10**). Interestingly, with 400 ng mL^{-1} or higher histone, the system recovered ~95% of its original emission (**4.2** without DNA). As a control, a

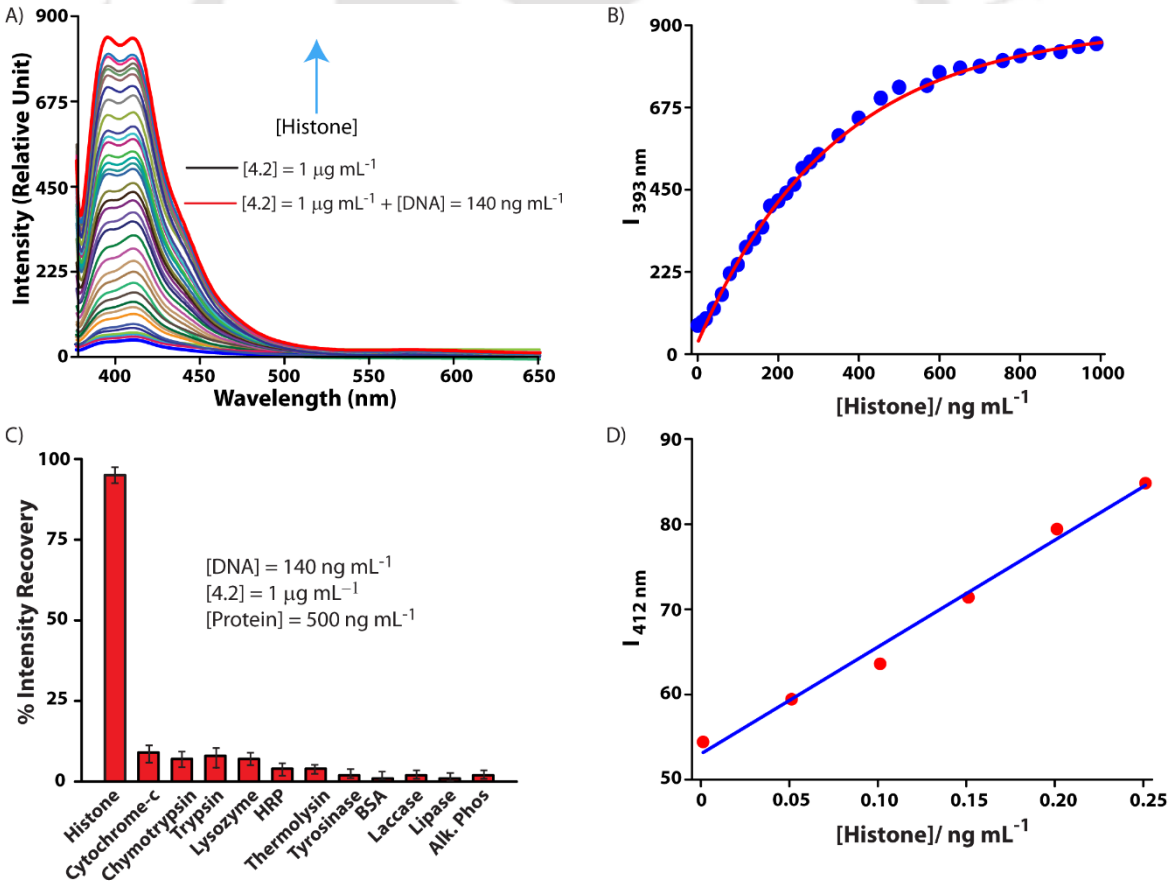

Figure 4.10 A) Enhancement of emission intensity of **4.2** upon titration of DNA-**4.2** hybrid with histone, B) plot for intensity (at 393 nm) vs concentration of histone, C) % emission intensity recovery of **4.2** of a DNA-**4.**2 hybrid upon addition of excess of various proteins. [**4.2**] = 1 μg mL^{-1}; [DNA] = 140 ng mL^{-1}, D) intensity versus concentration of histone plot for determination of detection limit.

solution of **4.2** (1 μg mL^{-1}) was titrated with histone and followed by fluorescence spectroscopy. Notably, no detectable change was monitored in the emission of **4.2** in this case. Additionally, when excited at 360 nm, a 1 μg mL^{-1} solution of histone produced no measurable emission which negate the possibility of any contribution arising from histone. Further, The detection limit of the system was calculated to be 0.052 ng mL^{-1} or 52 ppt (parts-per-trillion, as shown in **Figure 4.10** which is much lower compared to the previously reported histone sensors (previously reported lowest detection limit was 0.2 ng mL^{-1}).[126] Further, to check the effect of **4.2** concentration on the detection limit, another composition of 5 μg mL^{-1} **4.2** and 600 ng mL^{-1} of DNA was tested. The detection limit of the system was calculated to be 0.03 ng mL^{-1} or 30 ppt which is very similar to that of the original composition of 1 μg mL^{-1} **4.2** and 140 ng mL^{-1} of DNA. Lowering the **4.2** concentration to 0.1 μg mL^{-1} yielded in very low emission value which restricted us to use this concentration for sensing histone.

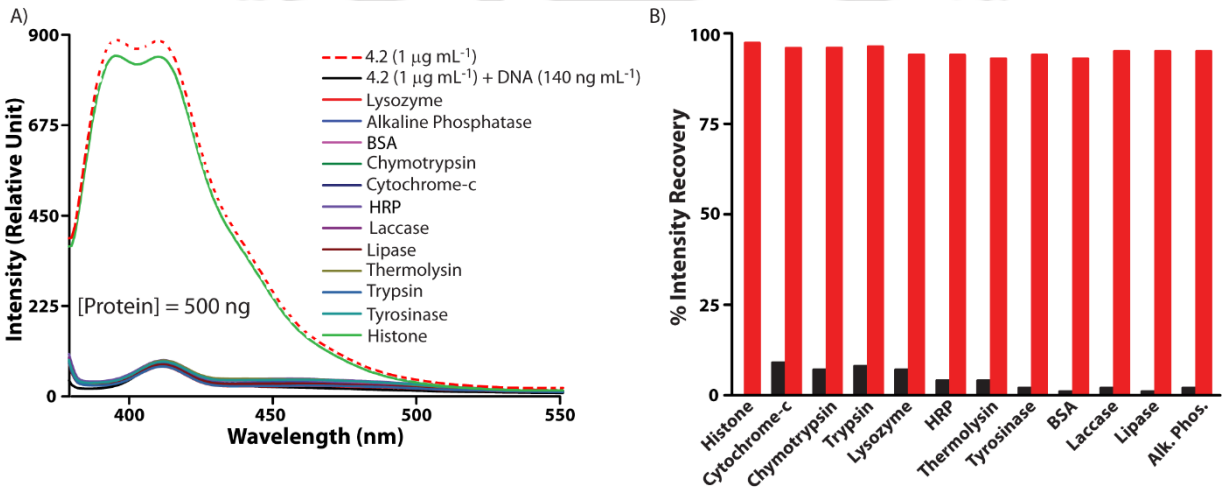

Figure 4.11 A) Emission spectra of **4.2**-DNA hybrid in presence of various proteins, B) comparative study of **4.2** toward histone over miscellaneous competitive proteins. Black bars represent the increase in the intensity of **4.2**-DNA in presence of proteins and red bars represent the enhancement with subsequent addition of histone to the solution. λ_{ex} = 360 nm, [**NDI**] = 1 μg mL^{-1}; [DNA] = 140 ng mL^{-1}, [protein] = 500 ng mL^{-1}. All samples in 10 mM phosphate buffer pH 7.4 and measurements were done at room temperature.

To establish that the method is specific to histone sensing, a number of other proteins were also examined. Four positively charged proteins (lysozyme (pI 10.8), trypsin (pI 10.5), chymotrypsin (pI 8.5) and cytochrome-c (pI 9.6)) with isoelectric points close to the pI of histone (10.8),[225] along with five anionic proteins (bovine serum albumin (BSA, pI 4.5), tyrosinase (pI 4.5), alkaline phosphatase (Alk. Phos, pI 4.4-5.8), lipase (pI 4.5) and laccase (pI 5.0)) were used for the study. As control, two neutral proteins (thermolysin and horseradish peroxidase (HRP)) were also subjected to similar experiments. In each case, a solution of 1 μg mL^{-1} of **4.2** and 140 ng mL^{-1} of DNA was treated with these proteins and the final concentration of the protein was maintained at 500 ng mL^{-1} to ensure maximum displacement of **4.2** from DNA upon protein binding. However, nominal changes in fluorescence intensity of **4.2** were detected in all cases. The percentage recovery of the fluorescence

is presented in **Figure 4.11** for all the proteins tested. Though nominal, higher recovery (5-9%) was detected in case of positively charged proteins compared to the neutral or anionic proteins and that may be due to similar pI values as well as positive surfaces of these proteins. To verify the effect of pH, further experiments in different other buffers (pH7-12) were carried out. However, no change in the trend was observed. To further determine the selectivity, histone (500 ng mL^{-1}) was added to **4.2**-DNA hybrid ([DNA] = 140 ng mL^{-1}, [**4.2**] = 1 μg mL^{-1}) containing one of these different proteins and the changes in the emission intensity were monitored. The competitive experiment in presence of other proteins also suggest the high selectivity of **4.2**-DNA hybrid toward histone as the background proteins showed no effect to the detection of histone as shown in **Figure 4.11**.

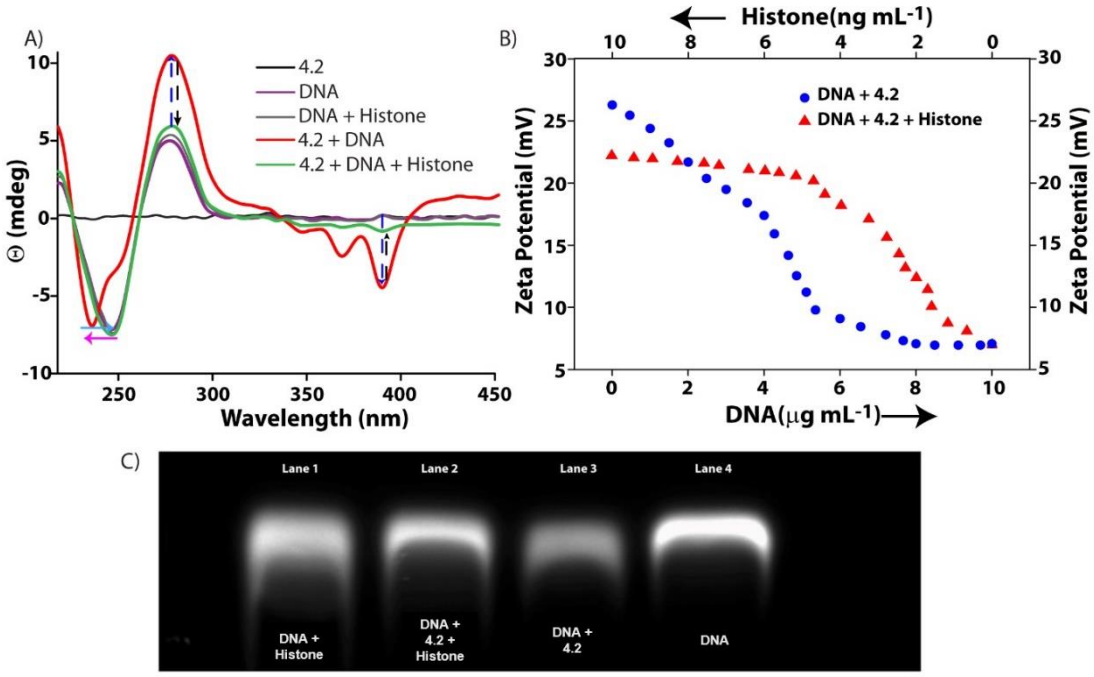

Figure 4.12 A) CD spectra of DNA under different compositions with **4.2** and histone, B) change in the zeta potential value of a **4.2** solution with increasing amount of DNA to reach a saturation value and subsequent addition of various amounts of histone to it, and c) Agarose gel electrophoresis of different compositions of DNA with **4.2** and histone.

To get insight into the structural changes in DNA upon binding with **4.2** followed by treatment with histone, circular dichroism (CD) spectra were recorded. The CD spectra of DNA alone presented in **Figure 4.12** exhibits two characteristic peaks, one positive band around 280 nm complemented to π–π stacking of the bases and a negative band around 245 nm for helicity.[218] Upon addition of **4.2**, DNA generates an induced CD (ICD) signal near 350-400 nm region along with increase in π–π stacking peak. In addition to that, the peak owing to the helicity is shifted to 235 nm. The ICD peak can be accredited to the orientation of transition moments of the **NDI** core perpendicular to the long axis of the DNA double helix. This negative ICD signals in the **NDI** absorption region further confirms the threading intercalation. The shift in the peak resulting from the helicity is an indication of the change in the conformation of DNA double helix upon binding with **4.2**. With addition of

histone to this **4.2**-DNA hybrid, not only the intensity of the ICD signal diminished significantly, the peaks generated from the π–π stacking and helicity returned back to their original positions and intensities. These results suggests the dissociation of **4.2** from its DNA bound state while histone binds to the DNA.

To get further mechanistic detail about the process, a solution of 10 μg mL^{-1} solution of **4.2** was titrated with DNA and the zeta potential (ζ) of the system was monitored. As shown in **Figure 4.12**, the ζ value of **4.2** decreases with increase in concentration of DNA and reaches a saturation value of +7.1 mV. Electrostatic interaction between the positive charges of **4.2** and the phosphates of the surface of DNA decreases the overall charge of the system. Upon titrating the solution with histone, the ζ value enhanced and followed a reverse path to get a final saturation value of +22.4 mV indicating dislodging of the **4.2** molecules not only from the intercalated position but from the surface bound state as well. Another evidence of displacement of **4.2** from DNA by histone was obtained from gel-electrophoresis. As can be seen in **Figure 4.12**, the intensity of the **4.2**-DNA hybrid is much lower than that of free DNA. Notably, the histone treated **4.2**-DNA hybrid is equally intense like histone-DNA and this is significantly higher than that of **4.2**-DNA hybrid. The enhancement of intensity of the **4.2**-DNA band by treatment with histone clearly establish the fact that **4.2** is displaced from its DNA bound state histone. Based on these observations, the sensing process can be summarized pictorially as shown in Scheme 4.1. **4.2** binds with DNA through threading intercalation and consequently loses its emission property. Histone, having a stronger binding affinity toward DNA, displaces **4.2** from DNA. The displacement of **4.2** leads to a situation where it remains in non-aggregated state and thus the emission returns back to the original intensity.

4.3 Conclusion

In conclusion, a series of **NDI** derivatives have been prepared and their DNA binding abilities were evaluated. While cationic derivatives efficiently bind both as intercalator as well as act as groove binder, the anionic species failed to show any affinity toward DNA. The optimal positive charges for strongest binding was found to be two on each sides of **NDI** (in case of **4.2**). Strongest threading intercalation was observed for **4.2** and binding with DNA leads to a significant (97%) loss of its emission. This fluorescence quenching of **4.2** upon binding with DNA is used for quantitative detection of histone. Upon binding with histone, **4.2** molecules are released from their DNA bound state which allows them to regain their emission (95%). The sensor, a hybrid of **4.2** and DNA, was found to be highly selective toward histone and the detection limit calculated to be the lowest reported so far.

4.4 Experimental sections

4.4.1 General Information and Materials

All chemicals and reagents used were obtained from Sigma-Aldrich (USA) and used without further purification. All solvents were procured from Merck, India and Spectrochem, India. DNA from calf thymus (1 mg of DNA is equivalent to 20 A260 Units; Lot no. 105K7025V) was purchased from Sigma-Aldrich (USA). To prepare samples, Milli-Q water with a conductivity of less than 2 $\mu S \cdot cm^{-1}$ was used. ^{1}H NMR, ^{13}C NMR were recorded on a Bruker Ascend 600 MHz (Bruker, Coventry, UK) and referenced to deuterated solvents. ESI-MS was performed with a Q-tof-Micro Quadrupole mass spectrophotometer (Micromass). UV/Vis spectra was recorded with a PerkinElmer Lambda 750 spectrometer. Fluorescence measurements were performed with a Cary Eclipse spectrophotometer (Agilent). Unless otherwise mentioned, all experiments were carried out at room temperature.

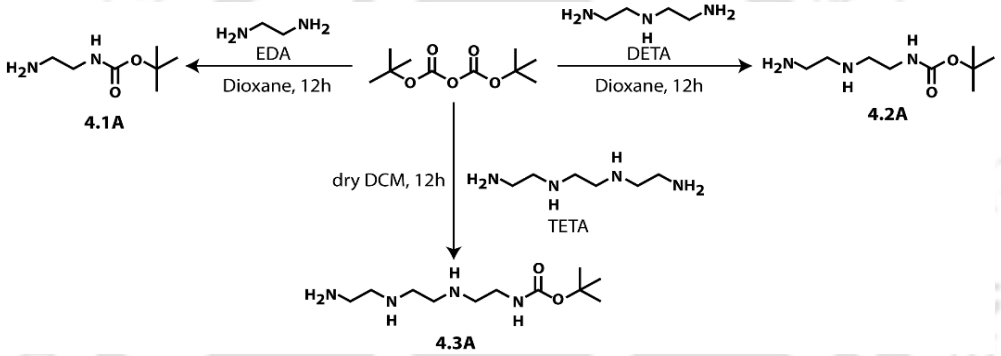

Scheme 4.2. Synthetic scheme for **4.1A**, **4.2A** and **4.3A**.

4.4.2 Synthesis and Characterization of Compounds

Synthesis of 4.1A: To a stirred and cooled solution of EDA (5g, 0.083 mol) in DCM (65 mL) was added di-tert-butyl dicarbonate (1.82g, 0.0083mol) in DCM (45 mL) dropwise for 1h. After stirring at room temperature for 24h, the solvent was removed under reduced pressure. The crude product was dissolved in saturated $NaHCO_3$ (20 mL) solution and was extracted with DCM for 3 times. The organic phase was dried over Na_2SO_4, filtered and the filtrate was concentrated under reduced pressure to give the desired product as a colourless oil. Yield: 60 %. ^{1}H NMR (400 MHz, $CDCl_3$): δ 4.88 (s, 1H), 3.17 (q, J = 5.9 Hz, 2H), 2.79 (t, J = 5.9 Hz, 2H), 1.43 (s, 9H). ESI-MS (m/z): calculated, 160.1212 for $C_7H_{16}N_2O_2$; found, 161.1284 for $[M+H]^+$.

Synthesis of 4.2A: DETA (2.55g, 0.025 mol) was taken in 5 mL of dioxane. To it di-tertbutyl dicarbonate (0.59g, 0.0027mol) in 5 mL dioxane was added dropwise over a period of 15 mins. The mixture was stirred for 22 h in salt-ice bath. The solvent was evaporated in vacuo and 5 mL of water was added to the reaction mixture and the mixture was extracted with DCM for four times.The

organic layer was separated, dried over anhydrous Na_2SO_4 and evaporated to get the desired product as a yellowish liquid. Yield: 58%. ^{1}H NMR (400 MHz, $CDCl_3$) δ 5.11 (s, 1H), 3.15 (t, *J* = 6.0 Hz, 2H), 2.76 – 2.72 (m, 2H), 2.67 (t, *J* = 5.9 Hz, 2H), 2.61 (m, 2H), 1.38 (s, 9H). ESI-MS (m/z): calculated, 203.1634 for $C_9H_{21}N_3O_2$; found, 204.1702 for $[M+H]^+$.

Synthesis of 4.3A: TETA (1.46 g, 10 mmol) was dissolved in 10 mL of dry DCM and cooled to 0°C. A solution of di-tertbutyl dicarbonate (1.96 g, 9 mmol) in 10 mL dry DCM was added dropwise over 1 h. The mixture was stirred at room temperature for 12 h. After removal of the solvent under reduced pressure, the remaining yellow oil was dissolved in ethyl acetate and washed with 0.5 N NaOH. The aqueous phase was diluted with brine and extracted with ethyl acetate. The combined organic phases were dried over $MgSO_4$ and the solvent was removed under reduced pressure. The product was purified by flash chromatography on SiO_2. Yield: 72%. ^{1}H NMR (600 MHz, $CDCl_3$): *δ* 5.05 (s, 1H), 3.26-3.38 (m, 2H), 3.20-3.22 (m, 2H), 2.71-2.79 (m, 4H), 2.40-2.46 (m, 4H), 1.44 (s, 9H) ppm. ESI-MS (*m/z*): calculated, 246.2056 for $C_{11}H_{26}N_4O_2$; found, 247.2323 for $[M+H]^+$.

Synthesis of compound 4.1B, 4.2B, 4.3B: All the compounds were synthesized using simialar synthetic protocol. Naphthalene-1, 4, 5, 8-tetracarboxylic dianhydride (1 mmol) and **4.1A** or **4.2A** or **4.3A** (4.8 mmol) were refluxed in THF (5 mL) for 18 h. The reaction mixture was allowed to cool and then poured into chloroform (10 mL). The precipitate formed was removed by filtration and the solvents were removed under reduced pressure. The residue was dissolved in methanol (5 mL) and poured into water (40 mL). The product was obtained as a reddish brown solid.

Compound 4.1B: Yield 60%. ^{1}H NMR (600 MHz, $CDCl_3$): δ 8.71 (s, 4H), 4.97 (s, 2H), 4.35 (s, 4H), 3.54 (s, 4H), 1.20 (s, 18H), ppm. ESI-MS (*m/z*): calculated, 552.2220 for $C_{28}H_{32}N_4O_8$; found, 553.2291 for $[M+H]^+$ and 227.1182 for $[M+2H]^{2+}$.

Compound 4.2B: Yield: 54%. ^{1}H NMR (600 MHz, $CDCl_3$): *δ* 8.77 (s, 4H), 4.97 (s, 2H), 4.32 (t, *J* = 6.3 Hz, 4H), 3.19-3.21(m, 4H), 3.01 (t, *J* = 6.3 Hz, 4H), 2.81 (t, *J* = 5.8 Hz, 2H), 1.42 (s, 18H) ppm. ESI-MS (*m/z*): calculated, 638.3064 for $C_{32}H_{42}N_6O_8$; found, 639.3134 for $[M+H]^+$ and 320.1602 for $[M+2H]^{2+}$.

Compound 4.3B: Yield: 35%. ^{1}H NMR (600 MHz, $CDCl_3$) *δ* 8.75 (s, 4H), 5.01 (s, 2H), 4.27-4.35 (m, 4H), 3.17-3.40 (m, 4H), 2.93-3.04 (m, 4H), 2.41-2.80 (m, 8H), 2.27-2.31 (m, 4H), 1.42 (s, 18H), ppm. ESI-MS (*m/z*): calculated 724.3908 for $C_{36}H_{52}N_8O_8$; found, 777.4316 for $[M + H + 2\ C_2H_2]^+$.

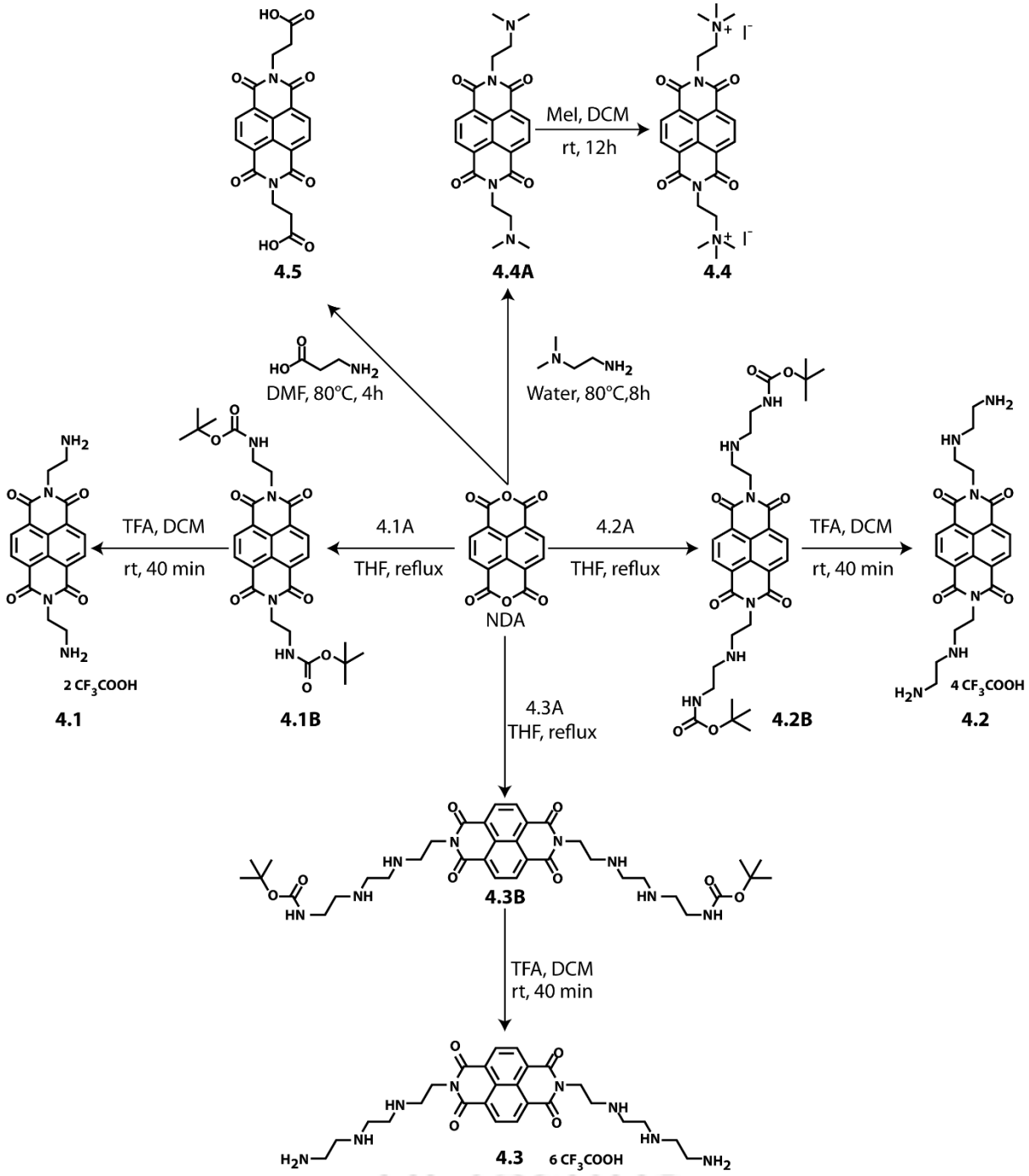

Scheme 4.3. Synthetic pathways for **4.1-4.5**.

Synthesis of NDI conjugates (**4.1-4.3**): Boc protected naphthalene diimide (**4.1B** or **4.2B** or **4.3B**) was dissolved in trifluoroacetic acid (TFA, 5 mL) and stirred for 40 min. Methanol was added to the mixture and solvents were removed under reduced pressure to obtain a pale brown solid. This solid was dissolved in methanol (30 mL) and poured into cold diethyl ether. The precipitate formed was collected and dried under reduced pressure to get a pale pink solid.

Compound 4.1: Yield: 95%. ^{1}H NMR (600 MHz, D_2O): δ 8.64 (s, 4H), 4.52 (t, J = 6.0 Hz, 4H), 3.45 (t, J = 6.0 Hz, 4H), ppm; ESI-MS (*m/z*): calculated, 352.1172 for $C_{18}H_{16}N_4O_4$; found, 353.1257 for $[M+H]^+$ and 177.0671 for $[M+2H]^{2+}$.

Compound 4.2: Yield: 87%. ^{1}H NMR (400 MHz, D_2O) δ 8.72 (s, 4H), 4.53 (t, J = 5.7 Hz, 4H), 3.53 (t, J = 5.7 Hz, 4H), 3.43 (t, J = 5.7 Hz, 4H), 3.33 (t, J = 6.9 Hz, 4H), ppm^{13}C NMR (150 MHz, D_2O): δ 35.53, 37.29, 44.71, 46.88, 126.56, 126.83, 134.50, 165.05 ppm. ESI-MS (*m/z*): calculated, 438.2016 for $C_{22}H_{26}N_6O_4$; found, 439.2220 for $[M+H]^+$ and 220.1183 for $[M+2H]^{2+}$.

Compound 4.3: Yield: 75%. ^{1}H NMR (600 MHz, D_2O): δ 8.73 (s, 4H), 3.54-3.59 (m, 10H), 3.26-3.29 (m, 8H), 2.79-2.83 (m, 6H), ppm; ESI-MS (m/z): calculated, 524.3860 for $C_{26}H_{36}N_8O_4$; found, 577. 3420 for $[M + H + 2\ C_2H_2]^+$.

Synthesis of compound 4.4A: Compound **4.4A** was synthesized by condensation of 1, 4, 6, 8-tetracarboxilic dianhydride (2.68 g, 10 mmol) and *N*, *N*-dimethylethylenediamine (4.4 mL, 40 mmol) in aqueous solution. The suspension was heated at 80 °C for 8 h. The precipitate was filtered and washed with acetone. Yield: 86%. ^{1}H NMR (600 MHz, $CDCl_3$): δ8.75 (s, 4H), 4.35 (t, J = 6.8 Hz, 4H), 2.67 (t, J = 6.8 Hz, 4H), 2.34 (s, 12H), ppm. ESI-MS (*m/z*): calculated, 408.1798 for $C_{22}H_{24}N_4O_4$; found, 409.1975 for $[M+H]^+$ and 205.1028 for $[M+2H]^{2+}$.

Synthesis of compound 4.4: Compound **4.4A** (50 mg, 0.122 mmol) and iodomethane (76.2 μL, 1.22 mmol) were added to DCM (5 mL), and the mixture was stirred for 12h. The reaction mixture was centrifuged and the precipitate was washed with DCM. The resulting yellow solid was dried under vacuum. Yield: 90%. ^{1}H NMR (600 MHz, D_2O): δ 8.82 (s, 4H), 4.71 (t, J = 7.7 Hz, 4H), 3.75 (t, J = 7.6 Hz, 4H), 3.35 (s, 18H), ppm; ^{13}C NMR (150 MHz, DMSO-d_6): δ 33.76, 52.56, 61.89, 126.21, 126.72, 130.92, 164.05 ppm. ESI-MS (*m/z*): calculated, 219.1128 for $C_{24}H_{30}N_4O_4^{2+}$; found, 219.1020 for $[M+2H]^{2+}$.

Synthesis of compound 4.5: A suspension of 1, 4, 5, 8-naphthalenetetracarboxylic dianhydride (1 g, 3.73 mmol) and 3-amino propionic acid (0.80 g, 9.00 mmol) in DMF was heated at 80°C for 4 h. Upon cooling to room temperature, the mixture was poured into water (50 mL). The resulting solid was filtered, washed with water and acetone to give the desired compound as a pink powder. Yield: 78%. The characterization data of 5 was in accordance with the reported ones. ^{1}H NMR (600 MHz, DMSO-d_6): 8.65 (s, 4H), 4.27 (t, J = 7.6 Hz, 4H), 2.63 (t, J = 7.6 Hz, 4H), ppm. ESI-MS (*m/z*): calculated, 411.08 for $C_{20}H_{14}N_2O_8$; found, 411.07 for $[M+H]^+$.

4.4.3 Method

Sample preparation: A super-stock solution of **NDI** derivatives (**4.1-4.4**) were prepared maintaining the concentration of 1 mg mL^{-1} in a 10 mL of volumetric flask using mili-Q water while in case of **4.5**, $NaHCO_3$ buffer (10 mM, pH 9) was used for solubility issue. These stock solutions were diluted to the concentrations required for the experiments.

Preparation of DNA solution: To a 2 mL volumetric flask, 2 mg of DNA was dissolved in phosphate buffer (10 mM, pH 7.4) and the solution was divided in smaller portions and kept at 4 °C. All DNA related experiments were performed by taking appropriate aliquot from these super-stock solutions and diluting it accordingly. The concentration of DNA was determined spectrophotometrically by measuring absorbance at 260 nm, 25 °C using molar extinction coefficient ε_{260} = 13,200 bp $cm^{-1}M^{-1}$ (base pair). However, it is worth mentioning that the concentration of DNA was considered in micro-molarity only in case of dye displacement and ITC measurements while for all other experiments, μg mL^{-1} is considered.

Circular dichroism spectroscopy (CD): Circular dichroism (CD) spectra were recorded on a J-1500 CD (JASCO, U.S.A.) instrument at room temperature. The data were collected at 1 nm intervals with 1 nm band width. All measurements were done in 0.2 cm path length cuvette with 400 mL sample volume. Each CD profile is an average of 3 scans of the same sample collected at a scan speed 100 nm min^{-1}, with a proper baseline correction from buffer. Scans were performed over 200–450 nm.

Thermal denaturation: The absorption (260 nm) of DNA was monitored in the absence or presence of **NDI** derivatives over 25-90 °C. DNA (50 μg mL^{-1}) and **NDI** derivatives (15 μg mL^{-1}) were mixed, and absorption values were measured at 260 nm. The variable temperature mode was used.

Isothermal titration calorimetry (ITC): The binding constant, stoichiometry and thermodynamic parameters for the binding with DNA were determined by isothermal titration calorimetry using Nano-ITC instrument from MicroCal. For every experiment, the temperature was fixed at 298 K. The first data point was omitted from the data set for curve fitting. All solutions were prepared in buffer (10 mM phosphate, pH 7.4) and degassed prior to titration. Heats of dilution were checked by titration of the **NDI** derivatives into a buffer solution and subtracted from the normalized enthalpies. The data were fitted to a theoretical titration curve by one set of sites binding model using a software supplied by Microcal.

Dye displacement study: Stock solutions of EtBr and DAPI were prepared by dissolving a weighed amount of EtBr and DAPI in milli- Q water to attain a concentration of 1 mg mL^{-1}. All experiments involving EtBr and DAPI were performed by taking appropriate aliquots from this super-stock and diluting it accordingly. In a typical experiment, a mixture of the dye and DNA solution (10 μM dye and 10 μM DNA) was titrated with **NDI** solution (1-30 μM) and the emission was monitored by exciting at the respective excitation wavelengths of the dye used. In case of DAPI, control experiments showed no overlap of the emission in the concentration range of 1-30 μM of **NDI**-derivative and 10 μM DAPI. For Stern-Volmer constant calculation, values from the linear part are taken into account (1-6 μM of **NDI**-derivative).

Gel Electrophoresis: Agarose gel electrophoresis (0.8 wt%) was performed in 1× TAE buffer at E = 60 V/cm for 30 min. DNA, **4.2**-DNA, **4.2**-DNA-Histone, DNA-Histone were run on this agarose gel stained with ethidium bromide and photographed upon irradiation with UV light.

Zeta Potential: The zeta potential of the samples were measured at 298 K on a Zetasizer Nano ZS90 from Malvern using a 632.8 nm He-Ne laser. Prior to measurements, the samples were filtered through appropriate filters to remove dust particles if any.

Detection Limit: Detection limits were calculated from the fluorescence titration data. The emission spectra of **4.2**-DNA was measured 10 times, and the standard deviation of blank measurement was determined. To achieve the slope, the fluorescence emission at 412 nm was plotted as a function of the concentration of histone. The detection limits were obtained using the following equation (3.4),

Detection limit = $3\sigma/k$

Where σ is the standard deviation of blank measurement, and k is the slope between the fluorescence emission intensity versus [Histone].

Chapter 5

Picric Acid Detection at Femtogram Level by a Short Peptide Gelator

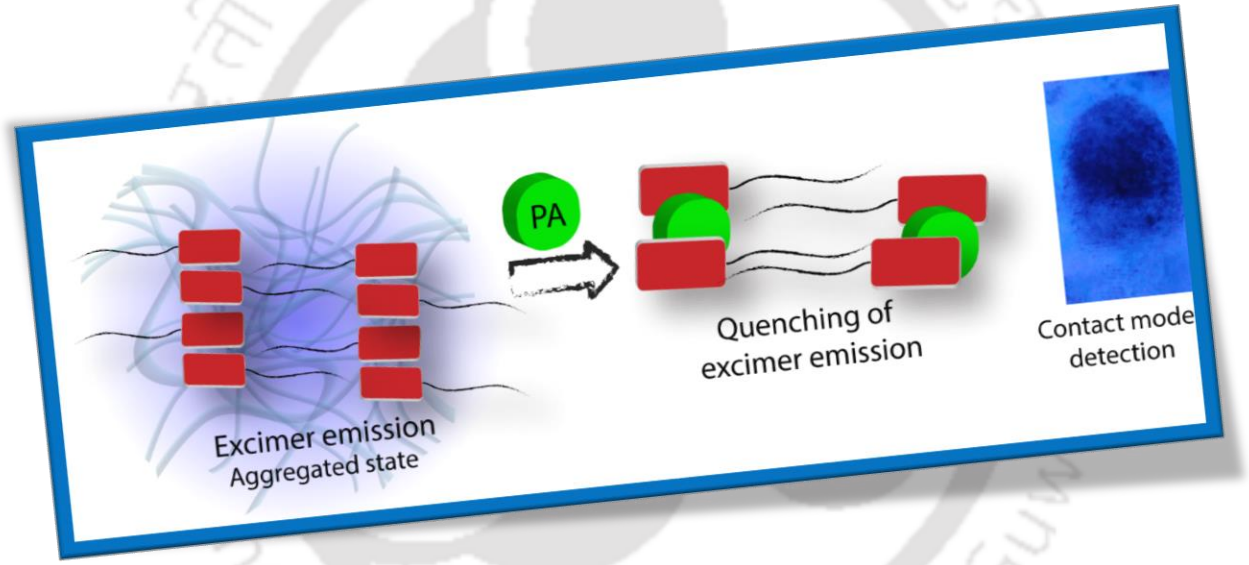

5.1 Introduction

Picric acid (PA) is a strong organic aromatic acid and like many polynitrated aromatic compounds, it also possesses powerful explosive property.[230-232] The explosive power of PA is even greater than trinitrotoluene (TNT) and are found in various explosive formulations. Moreover, exposure to PA leads to severe adverse effects on human health. PA is irritant to skin and eye, causes damage to respiratory organs, liver, spleen and affects the immune system.[233] The biodegradation products of PA are also mutagenic and carcinogenic and the high water solubility of PA allows it to easily contaminate ground water and soil.[234] Above all, the present day scenario regarding the worldwide terrorist activities demands a convenient, efficient and selective sensor for PA. Even though a large number of sensors are reported, a simple and practical approach to the detection of explosives like PA at a scale as low as femtogram (10^{-15} g) still remains a challenge.

Wide range of methods including colorimetry,[235] SERS,[236] X-ray diffraction,[237] surface plasmon resonance,[238] mass spectrometry,[239] electrochemistry[240-241] *etc.* have been utilized for sensing of PA. However, these techniques are not in commonplace as they require expensive instruments as well as complicated and time consuming experimental procedures. Fluorescence based chemo-sensors are an attractive alternative and provides high sensitivity, low cost and can be used without the requirement of any sophisticated instruments.[242] Fluorescence based explosive-sensors predominantly work on fluorescence quenching methods.[243-244] In principle, electron transfer from excited fluorophore to the acceptor analyte results in a decrease in the emission which can be quantitatively monitored. In this regard, molecular self-assembly of fluorophores is an attractive approach. Self-assembled nano-fibers of fluorophore conjugates exhibit properties which are different from those of their constituent molecules.

In this chapter, we have reported a small fluorescent peptide (**5.1**, **Scheme 5.1**) based gel. The gelator molecule is capable of selectively detect PA in solution phase as well as in gel state with high sensitivity (in ppt level). A convenient paper based contact mode technique is developed which detects PA at a record femtogram scale in contact mode.

5.2 Results and Discussion

The peptide was rationally designed by incorporating the aggregating ability of the well-known self-assembling peptide sequence "PhePhe",[245] hydrophobic and π-stacking unit of pyrene and hydrophilic character of lysine. Pyrene also serves the role of the emissive unit of the molecule. The incorporation of pyrene also serves the aim to use the peptide-gelator for sensing of PA as interaction of fused aromatic rings and PA is documented in

literature.[100, 246] The peptide **5.1** was synthesized using standard solid phase peptide synthesis technique employing Fmoc-chemistry. After a thorough screening of different combinations of solvents, it was found that 1:1 mixture of water and acetonitrile (ACN) could be immobilized by **5.1** to form self-supporting gel with minimum gelation concentration (MGC) of 21.85 mM.

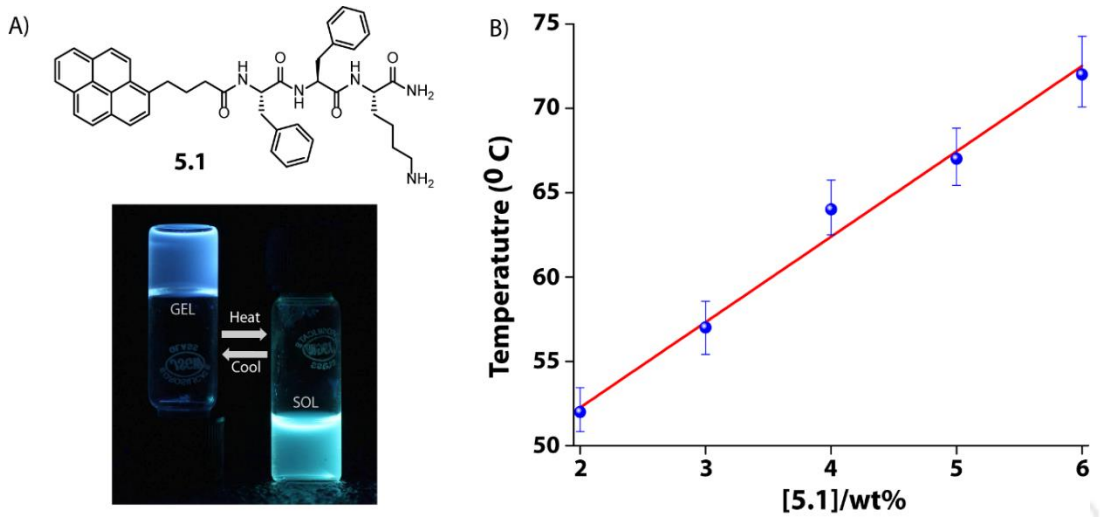

Figure 5.1 A) Chemical structure of **5.1** (Top) and photograph of a 21.85 mM gel of **5.1** in 1:1 Water-ACN under UV light showing the reversible gel-sol transition upon heating/cooling and changes in the emission color when illuminated with UV-light (Below), B) dependence of T_g on the concentration of the gelator.

The cyan colored emission of the solution changes to blue upon gelation (**Figure 5.1**). Gel to sol transition temperature of the gel was found to be 51 °C which showed a linear increase with the concentration of gelator (**Figure 5.1**).[247] Room temperature rheology (**Figure 5.2**) showed the gel character as the storage modulus (G′) was found to be considerably higher than the loss modulus (G″) over a range of applied angular frequency. Interestingly, the gel also has the self-healing property as can be seen from **Figure 5.2**.

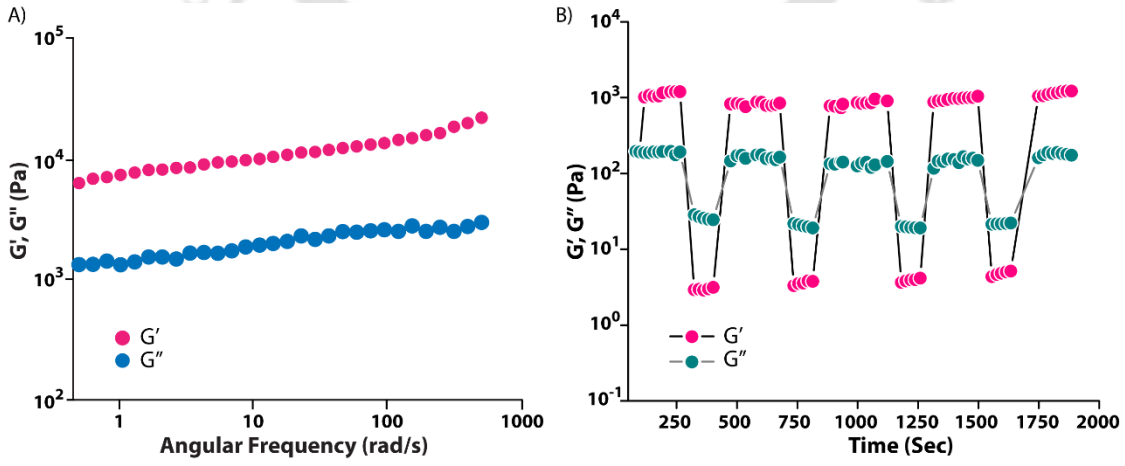

Figure 5.2 A) Changes in storage and loss modulus as a function of shear strain (amplitude sweep at frequency of 1 rad s^{-1}, B) cyclic strain time sweep rheology measurements of **5.1** (21.85 mM) showing the healing behaviour of gel.

A time dependent strain sweep was performed by alternating the applied strains at a fixed angular frequency of 1 rad s^{-1}. At higher strain (γ = 100%), the gel loses its viscoelastic property and interestingly, in every successive step, it regains its initial viscoelastic nature almost completely while coming back to a lower strain (**Figure 5.2B**). Such recovery of the mechanical properties for a gel is termed as self-healing or thixotropic behavior.[248]

Microscopic techniques like FESEM, FETEM and AFM revealed the formation of a tightly knitted fibrous network in the gel state (**Figure 5.3**). Absorption spectra of **5.1** in 1:1 Water-ACN showed three prominent bands at 312, 325, and 341 nm arising from pyrene (**Figure 5.4**). When excited at 337 nm, it resulted in three emission bands at 375, 396, and 417 nm which are typical of pyrene (**Figure 5.4**).

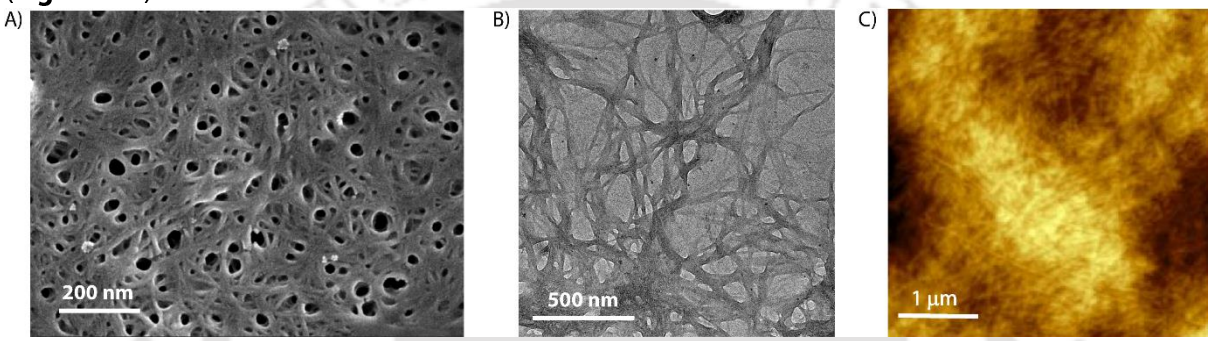

Figure 5.3 A) FESEM, B) FETEM, and C) AFM images of 21.85 mM gel of **5.1** in 1:1 Water-ACN.

^{1}H NMR of **5.1** (1 mM) in CD_3CN with increasing amount of D_2O showed a continuous up-field shift of aromatic protons (**Figure 5.5A**) indicating probable π–π stacking of the aromatic rings in the aggregated state.[181] Importantly, a strong excimer band,[249] centered at 477 nm was observed above 1 mM concentration (**Figure 5.5B**). The appearance of the excimer band also supports the strong π–π stacking of pyrene rings during the self-assembly process.

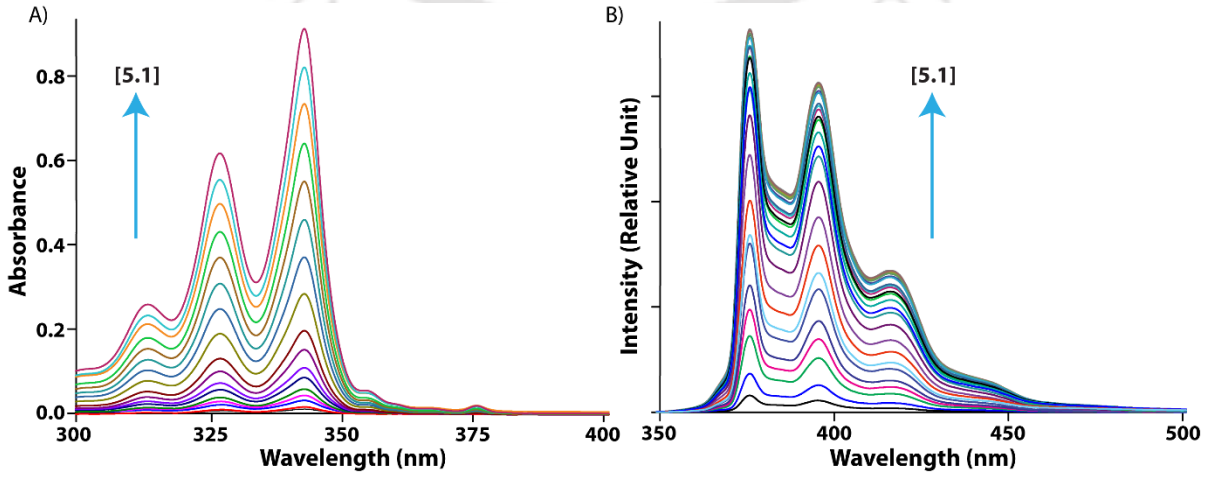

Figure 5.4 Concentration dependent A) absorption, and B) emission spectra of **5.1** in 1:1 Water-ACN measured at room temperature. λ_{ex}= 337 nm.

Solution phase circular dichroism (CD) of **5.1** in this mixed solvent system resulted in interesting features. At very diluted condition (20 μM), a peak appeared at 206 nm which shifted to higher wavelength with increase in concentration (**Figure 5.5C**). At the highest measurable concentration (500 μM), a strong negative signal appeared at 220 nm along with a positive signal at 195 nm demonstrating possible β–sheet formation by the peptide.[250-251] Other negative signals at 243, 286, 340 and 355 nm in the aromatic absorption region suggest the formation of left-handed helical aggregates.[100,180] FTIR of the gel also supports β–sheet formation as two characteristic signals were observed at 1633 and 1671 cm^{-1} (**Figure 5.5D**).[248]

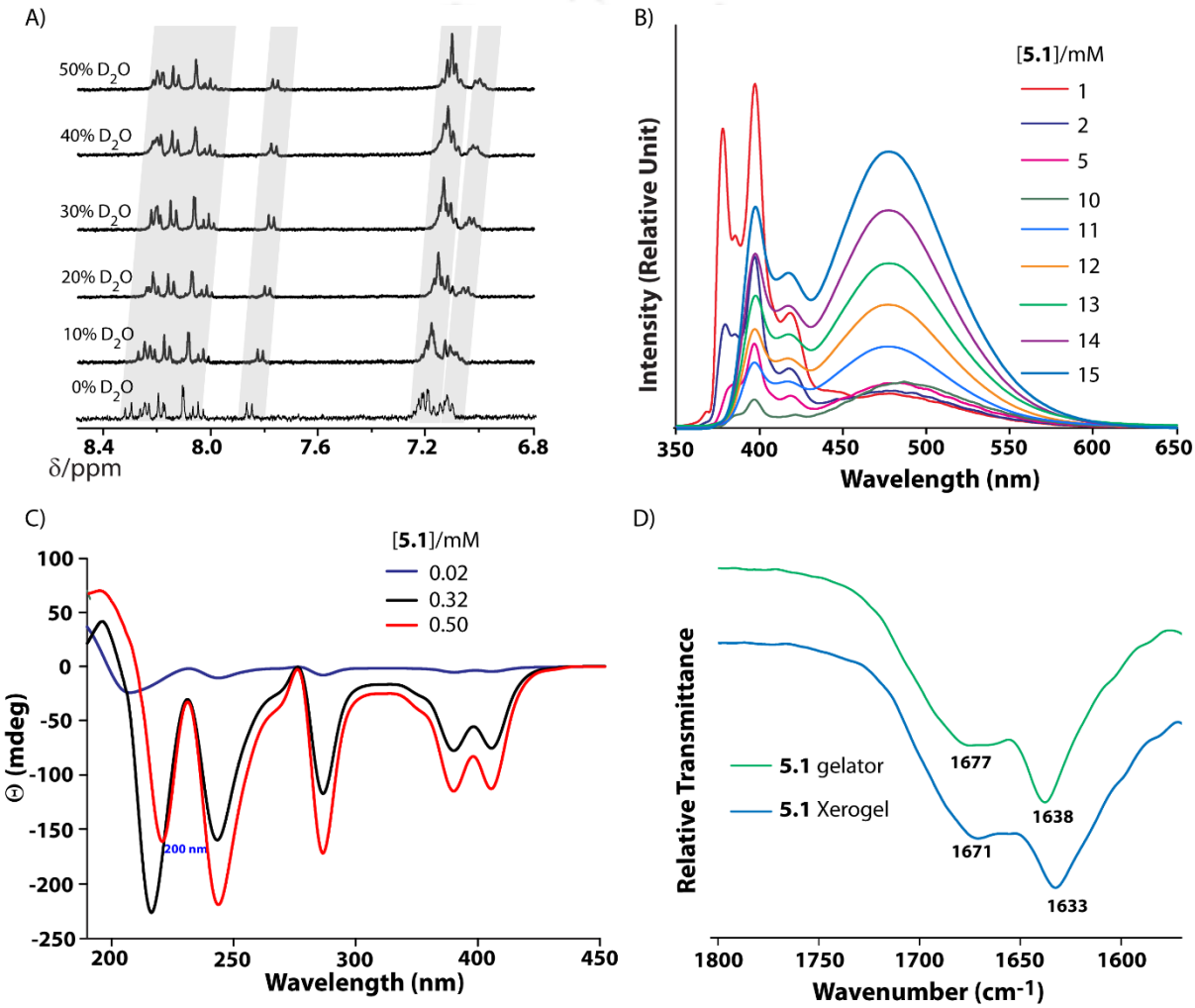

Figure 5.5 A) Aromatic region of ^{1}H NMR spectra of **5.1**(1 mM) in CD_3CN containing different amounts of D_2O. Concentration dependent B) emission (λ_{ex} = 337 nm), and C) CD spectra of **5.1** in 1:1 Water-ACN. D) FTIR spectra of as synthesized **5.1** and the xerogel of **5.1** obtained from a 21.85 mM gel in 1:1 Water-ACN.

All the experimental evidences indicate a possible aggregation of **5.1** where π–π stacking between pyrene rings plays a crucial role and the peptide adopts a β–sheet like structure. The hierarchical self-assembly eventually lead to the formation of fibers which interweave to form the network where solvent molecules are immobilized to form the self-supporting gel.

Solution Phase Detection of PA.

To investigate the ability of the gelator to detect nitroaromatics, first we examined the effect of different aromatic compounds in solution phase. Various compounds including, PA ($C_6H_3N_3O_7$), 2,4-dinitrophenol (DNP, $C_6H_4N_2O_5$), p-nitrophenol (PNP, $C_6H_5NO_3$), phenol (C_6H_6O), 2,4-dinitrotoluene (2,4-DNT, $C_7H_6N_2O_4$), 2,6-dinitrotoluene (2,6-DNT, $C_7H_6N_2O_4$), 4-nitrotoluene (4-NT, $C_7H_7NO_2$), 1,3-dinitrobenzene (1,3-DNB, $C_6H_4N_2O_4$), nitrobenzene (NB, $C_6H_5NO_2$), 4-nitrobenzoic acid (4-NBA, $C_7H_5NO_4$) and benzoic acid (BA, $C_7H_6O_2$) were tested. In the concentration dependent emission spectra of **5.1**, the excimer band appeared only after 1 mM concentration and thus a concentration of 1 μM was safely considered as the monomeric solution of the molecule (**Figure 5.5B**). The emission spectra of a 1 μM **5.1** solution was monitored by exciting it at 337 nm in presence of these analytes (**Figure 5.6A**). Effective fluorescence quenching was observed only in presence of nitrophenol solutions while the other aromatic compounds showed nominal changes. The quenching was observed to be highest for PA (~95%) with ~65% for DNP and 52% for PNP. The effect of nitrophenols on the emission of **5.1** can also be visualized by illuminating the solutions with UV light as can be seen in **Figure 5.6B**.

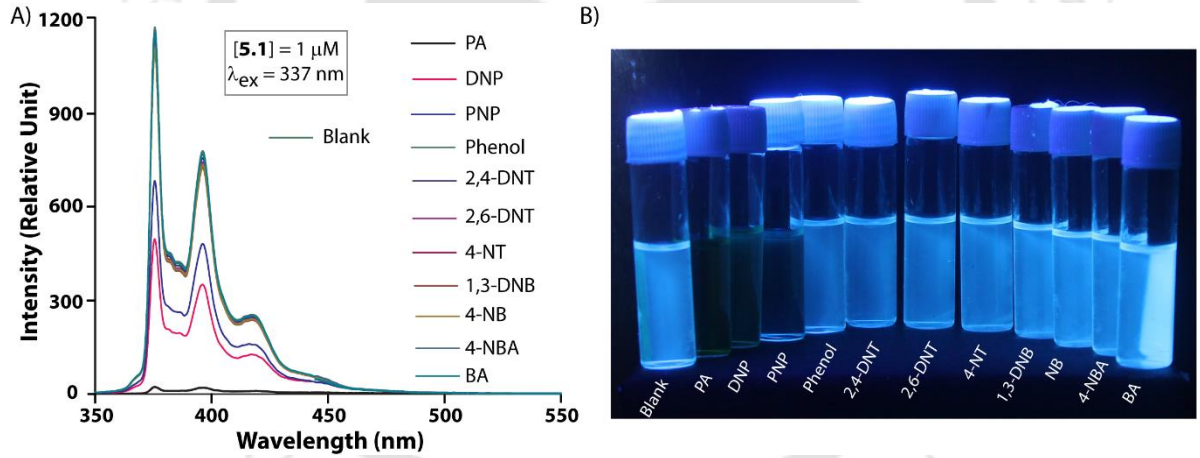

Figure 5.6 A) Emission spectra of **5.1** in 1:1 Water-ACN in presence of different analytes when excited at 337 nm, B) photographs of vials containing 0.1 mM **5.1** in 1:1 Water-ACN in presence of different analytes under UV light.

As only the nitrophenols showed effective quenching amongst all the analytes, fluorescence titration experiments with PA, DNP and PNP were performed. For all three nitrophenols, with increase in concentration of analyte, the emission intensities decreased as can be seen in **Figure 5.7**. The Stern-Volmer (SV) plots were linear at lower concentrations and subsequently deviated from linearity at higher concentrations (**Figure 5.7D**). The nonlinearity of the SV plot can be attributed to self-absorption, a combination of both static and dynamic quenching and an energy transfer process between the nitrophenols and pyrene of **5.1**.[246] At lower concentration of PA (up to 10 equivalence), the K_{SV} was calculated to be 3.94×10^4 M^{-1}. Similarly, the calculated K_{SV} values were

obtained as 2.63 × 10^4 and 9.73 × 10^3 M^{-1} respectively for DNP and PNP (**Figure 5.7**). Comparative studies also suggest that compound **5.1** is highly selective towards PA (**Figure 5.8).**

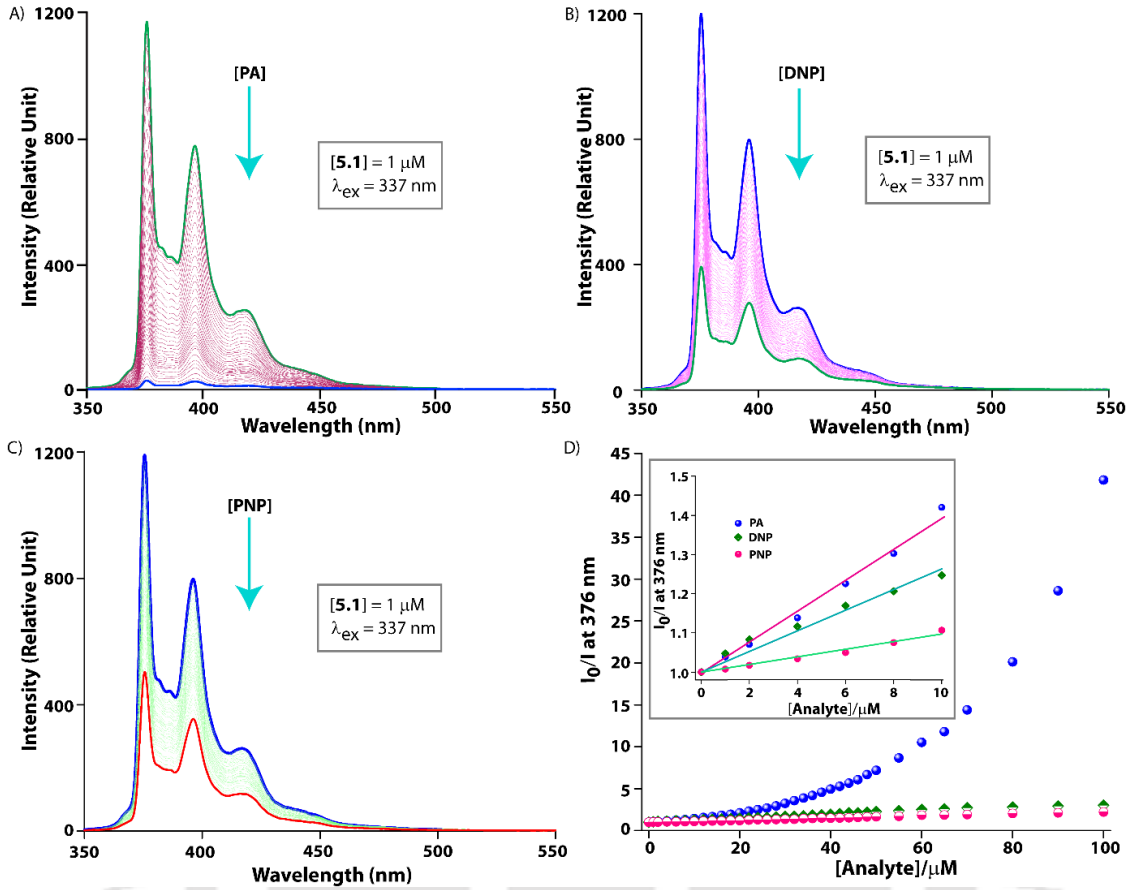

Figure 5.7. Emission spectra of 1 μM **5.1** in 1:1 Water-ACN with increasing amounts of A) PA, B) DNP, and C) PNP. D) Plots of I_0/I vs concentration of PA/DNP/PNP when 1 μM solutions of **5.1** in 1:1 Water-ACN were titrated with these analytes separately at room temperature. Inset: Stern-Volmer plots for PA, DNP and PNP for up to 10 equivalents as obtained from (D).

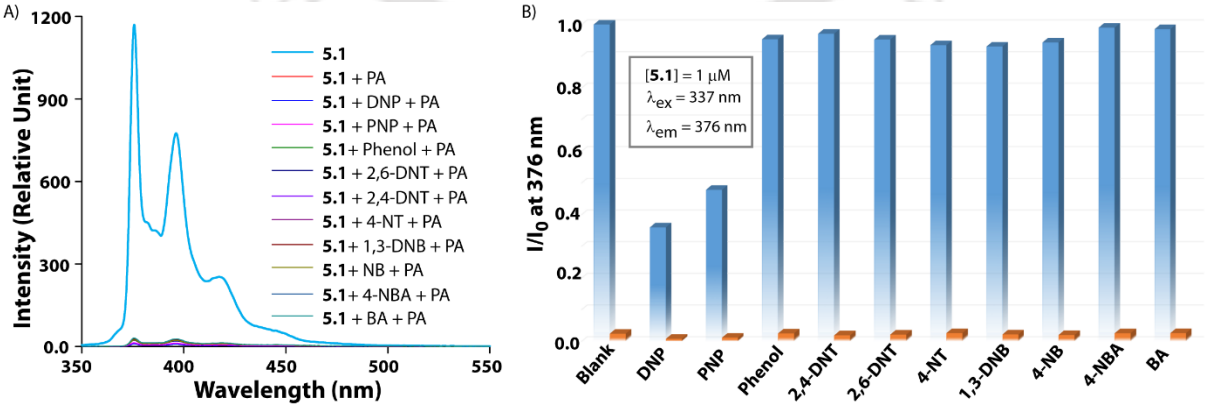

Figure 5.8 A) Comparative study, and B) bar diagram for the interference of different analytes toward detection of PA by **5.1** in 1:1 Water-ACN. Blue bars represent the addition of different analytes to **5.1** and orange bars represent the subsequent addition of PA to these solutions. All experiments were performed at room temperature.

Gel Phase Detection of PA.

Encouraged by the solution phase selective detection of PA, we wanted to evaluate the possibility of sensing PA in gel state. For this purpose, a multiwell PA sensing gel plate was prepared. In a typical process, 200 μL portions of freshly prepared a 21.85 mM **5.1** (1:1 Water-ACN) solution was added to the wells of a 96-well plate and incubated for 30 mins to form gels. The gels showed blue emission when irradiated with UV light (**Figure 5.9A**). Interestingly, the emission spectra of the hydrogel showed predominantly the presence of excimer band of pyrene centered at 477 nm (**Figure 5.9B**). On top of the gels, 30 μL of analyte solutions (1 mM) were added and the plate was incubated at room temperature with constant shaking at 100 rpm for 10 mins. Fluorescence was measured using a multi-well plate reader. The images of the gels in presence and absence of the analytes are shown in **Figure 5.9A**. As expected, the wells containing nitrophenols showed significant quenching in emission while the other gels did not show any noticeable change. The quenching efficiencies were quantified and plotted against each analyte (**Figure 5.9C**). Similar to solution phase, PA showed highest quenching (95.4%).

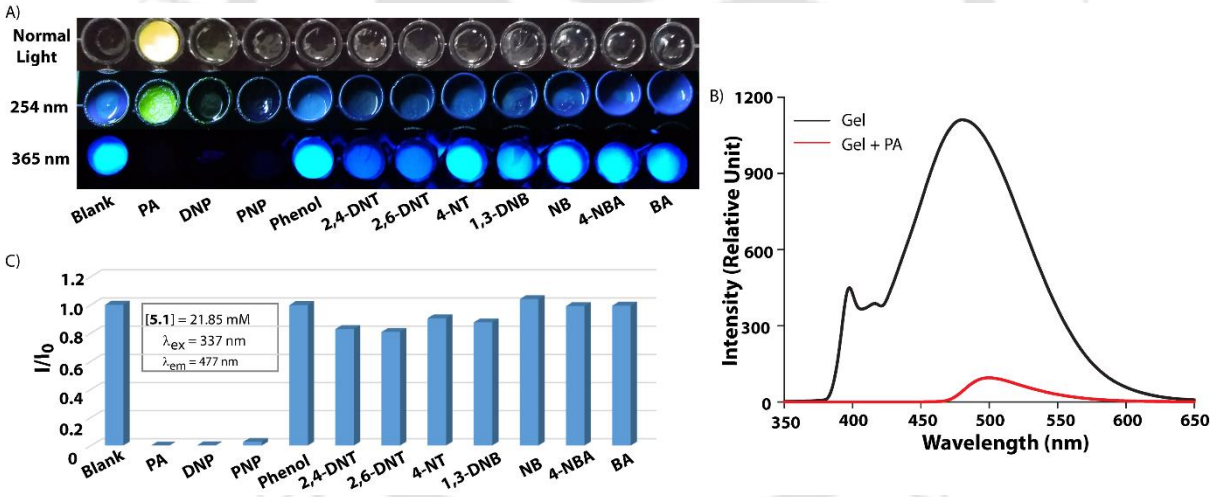

Figure 5.9 A) Photographs of **5.1** gel-loaded wells of a multiwell plate in presence or absence of different analytes under different lights, B) emission spectra of a gel sample in before and after treatment with PA solution (λ_{ex} = 337 nm), and C) the extent of quenching of the 477 nm band in the emission spectra of the gel samples in presence of different analyte solutions. All experiments were performed at room temperature.

When similar experiments were performed with varying concentrations of PA (**Figure 5.10**), below 10^{-7} M concentration, only a small decrease in the emission was monitored. However, at 10^{-7} M, the emission was quenched by 47% and above this concentration, no noticeable emission could be measured. Thus, in the gel phase, the detection limit is determined as 10^{-7} M (22.91 ppb). In presence of PA, the observed decrease in the emission was due to the quenching of the excimer emission as can be seen from **Figure 5.9B**. It is to be noted that the solution phase detection of PA entirely relied on the quenching of monomeric emission. Detection of an analyte using both monomeric and

dimeric emission at two different physical states of a molecule is an interesting phenomenon and are not common in literature.

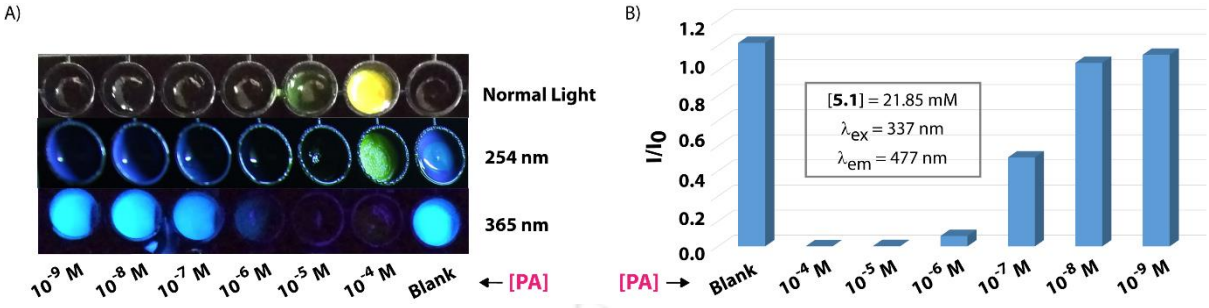

Figure 5.10 A) Photographs of **5.1** gel-loaded wells of a multiwell plate after treatment with solutions of different concentrations of PA under different lights, B) extent of quenching of the emission at 477 nm for samples in (A). All experiments were performed at room temperature

Paper Based Detection of PA

Contamination of human body, clothing or other materials by explosives can happen during preparation of explosive devices or an explosion. In such situations, contact mode detection of residual contamination is the ideal case. In order to prepare a gel coated test-strip, a 21.85 mM gel was heated above its T_g to prepare the sol. Pieces of filter papers were dipped into this solution for 30 s and then removed and air-dried to get the gel coated test strips.[244] The coating of the gel on filter paper surface was confirmed from strikingly different morphology compared to the un-coated filter paper (**Figure 5.11**). Apart from very long fibers (>100 μm) of cellulose, no other features could be found for the un-coated filter papers. However, fibrous network of the gel is clearly visible on the gel coated filter papers. The emission spectra recorded for the gel coated filter paper showed only a broad peak centered at ~444 nm (**Figure 5.11C**).[249] The fine structure of pyrene emission was completely lost and only the excimer peak was observed. Interestingly, a control strip prepared from a 21.85 mM solution in DMF resulted in predominantly the signature signals of pyrene monomer. Appearance of only excimer peak in the gel-coated test strips can be attributed to the formation of fibers during the gelation process of **5.1** as seen in the gel state.

The contact mode detection of PA was tested by placing few crystals of PA on a test strip for 5s. Black spots were seen at those positions when exposed to UV light (**Figure 5.11D**). Similar results were obtained for DNP and PNP while the other analytes failed to create such spots. Further, a human thumb was rubbed with PA (caution: to avoid any direct contact, use glove) and then all visible particles were brushed off. The thumb was pressed on the test strip for 5s and the test strip was exposed to UV light where the thumb impression was clearly visible from the quenching of the emission of **5.1** (**Figure 5.11E**). A control experiment without PA showed no such changes in the

test strip. These experiments and the images illustrate the usefulness of the on-site contact mode detection of PA on a specimen.

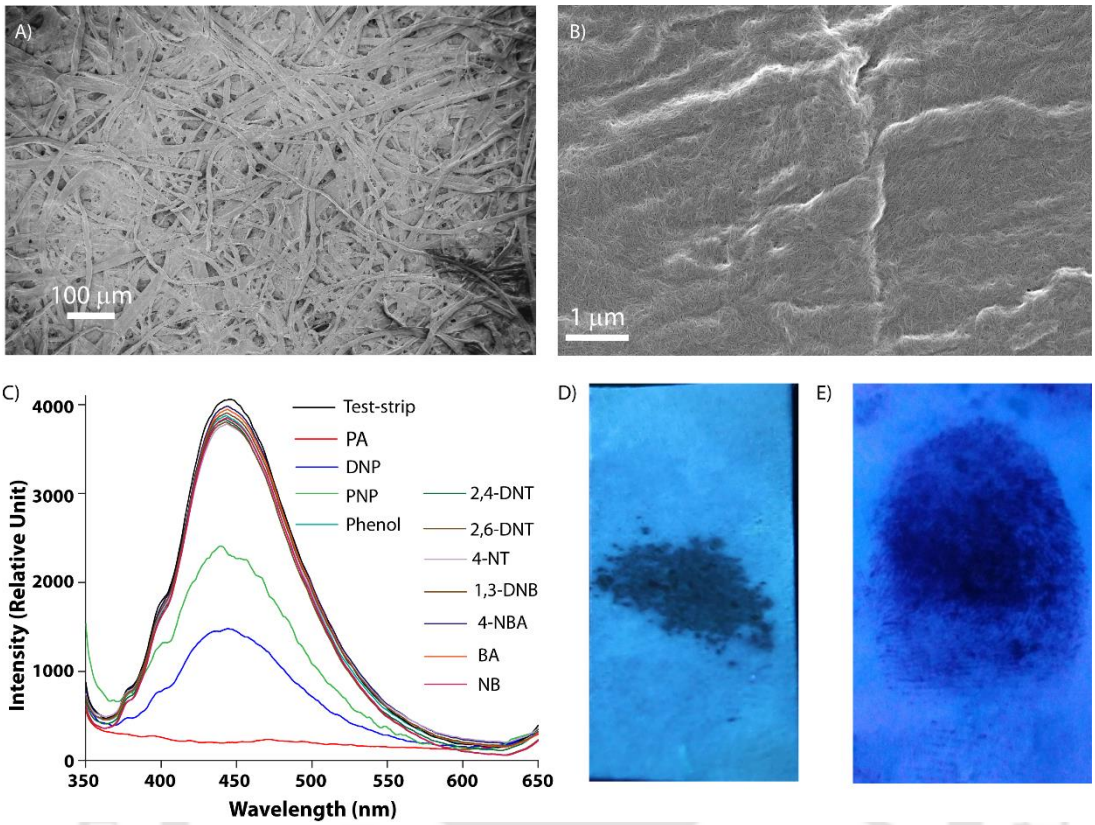

Figure 5.11 FESEM images of A) filter paper, B) **5.1** gel-coated filter paper (test strip), C) emission spectra of the test strips in presence of different analyte solutions. D), and E) photographs of **5.1** gel-coated test strips under different experimental conditions. D) PA crystals on top, and E) thumb impression after rubbing with PA crystals. All photographs were taken under 365 nm UV irradiation.

To quantify the detection efficiency as well as selectivity of these test strips, 10 μL of aqueous solutions (with 0.5% ACN) of all the analytes were drop casted on specific positions in a way that the overall spot area remain ~ 0.2 cm^2. All tests were performed in triplicate to avoid any experimental error. The visual response of different analytes at 1 mM concentration by contact mode detection on these test strips is shown in **Figure 5.12**. Quenching of **5.1** excimer emission in presence of different analytes were recorded at 444 nm and is shown in **Figure 5.11**. It is clear that even in the contact mode detection, the system showed specificity toward the nitrophenols and can detect PA selectively (**Figure 5.12B**). When the concentration of PA was varied, the minimum amount of PA detectable by the naked eye was as low as 10 μL of 1×10^{-12} M and thus the detection limit can be considered as 0.229 ppt. The quenching in emission could be visually detected to the level of 2.29×10^{-15} g using these test strips. From these data, the detection limit of PA was calculated as ~11.45 fg cm^{-2} which is amongst the lowest reported detection limits for PA (**Table 5.1**).[236, 252]

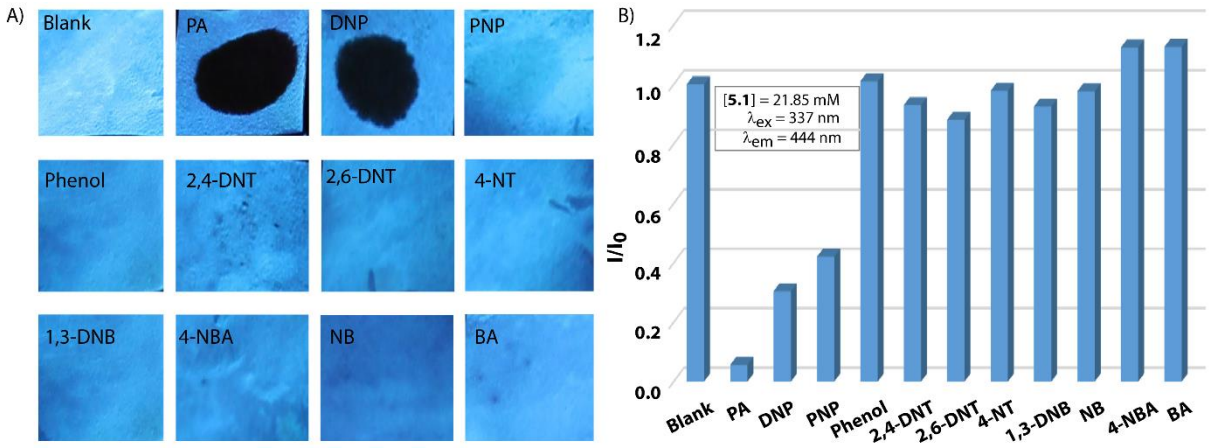

Figure 5.12 A) Photographs of the fluorescence quenching of **5.1** gel-coated test strips by different analytes on contact mode (10 µL solutions with a spot area of ~0.2 cm^2) under 365 nm UV illumination, B) extent of quenching of the emission at 444 nm of the **5.1** gel-coated test strips from (A). All experiments performed at room temperature solutions.

One of the challenging task in PA sensing material is to detect PA in vapour phase owing to its very low vapour pressure (7.4×10^{-7} mm Hg at 25 °C).[232] The sensing performance of the test strips were further tested using saturated vapor of PA. **Figure 5.13** shows the time-dependent fluorescence emission spectra of a test strip exposed to saturated vapours of PA with excitation at λ_{ex} = 337 nm. The fluorescence intensity of the test strip decreases significantly, showing ~ 75% quenching at 444 nm within 30 mins. Considering negligible vapor pressure of PA, this can be regarded as a good response time. The detection limit is thus in the ppb - ppt level for the vapor phase detection.

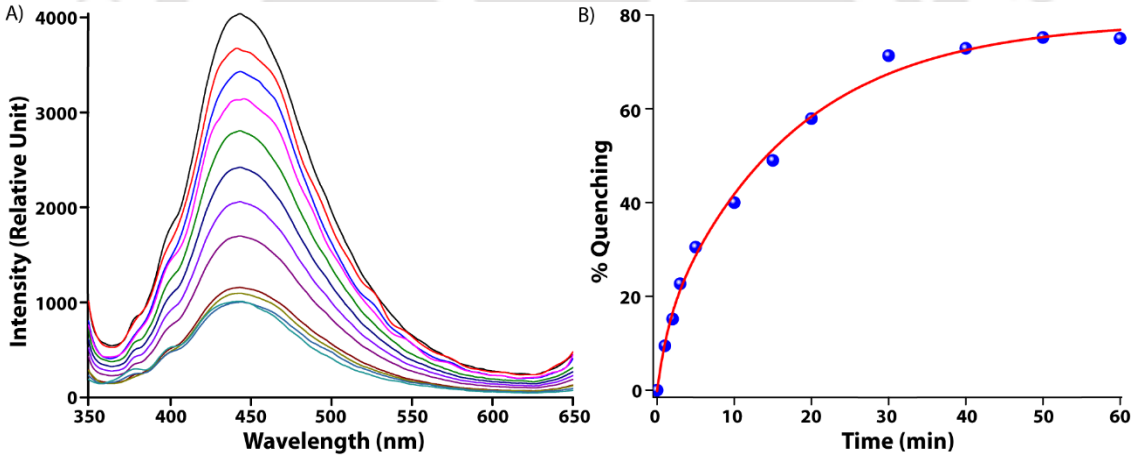

Figure 5.13 A) Time-dependent emission spectra of a **5.1** gel-coated test strip upon exposure to saturated vapours of PA, B) fluorescence quenching of the test strip as a function of time.

Contamination of soil and water by nitrophenols after any military operations is highly possible. Water contamination by PA above ~ 20 ppm level could be dangerous as it is highly toxic and carcinogenic in nature. Detection of PA in ground water at an extremely low level is thus important. We did try our test strip for this purpose following similar procedure as above. Solutions of PA (prepared in local ground water from tube well) at different concentrations of PA were spotted on the test strips and visually detected through the quenching of the emission (**Figure 5.14**). It was

observed that the lowest amount of PA in the ground water can be detected by naked eye is 2.29×10^{-15} g. For comparison amongst different fluorogenic sensors reported in literature and **5.1**, a table containing the detection limits is provided at **Table 5.1**.

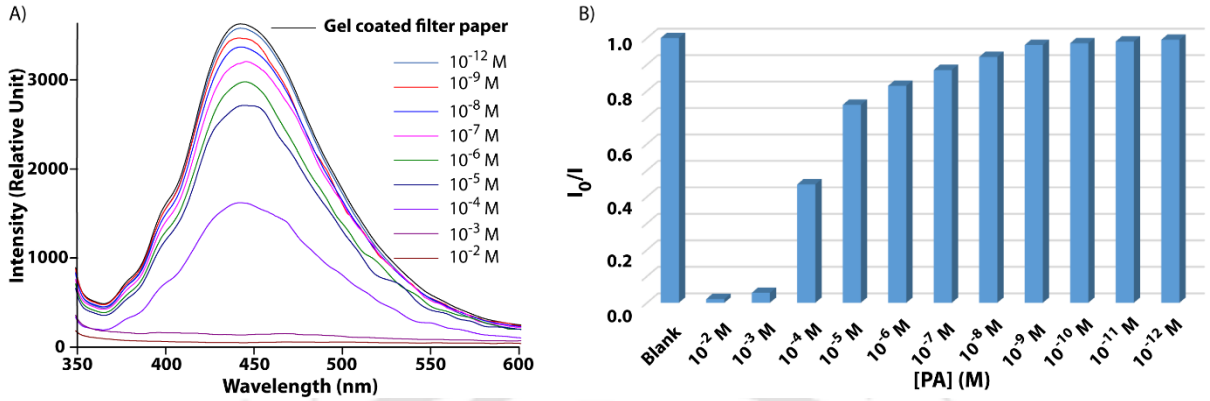

Figure 5.14 A) Emission spectra of the fluorescence quenching of **5.1** gel-coated test strips by different amount of PA in ground water, B) extent of quenching of fluorescence at 444 nm of test strips with added amount of PA in ground water (10 µL).

Mechanism of PA Sensing.

The solution phase detection of PA was carried out at a probe concentration where the molecules were in non-aggregated state. At this monomeric state, the presence of PA presumably formed a complex with pyrene of **5.1** and decreased the emission of the system.[29] The high K_{SV} value at a lower concentration range describes a static quenching process. Moreover, NMR study of **5.1** showed prominent upfield shift of all aromatic protons in presence of PA (**Figure 5.15A**). The spectral changes could be attributed to a possible complex formation between these two molecules.[29] The complexation was further confirmed from the appearance of a **5.1**-PA mass in the ESI MS spectrum of the solution (**Figure 5.15B**). To understand the excited-state behavior of the **5.1** in presence of PA, the fluorescence lifetime decay profiles before and after addition of PA were recorded (**Figure 5.16**). The lifetime decreased from 58.4 ns to 43.1 ns supporting the complex formation.

In the aggregated state (gel or gel-coated test strips), the sensing relies entirely on the quenching of the excimer emission. At higher concentration of **5.1**, the molecules self-assemble to form the fibrous network. As mentioned before, the self-assembly occurs through strong π–π stacking of pyrene units of the gelator. The PA molecules presumably breaks the stacking through complexation with the pyrene rings as in case of the solution phase. This, consequently results in to the drop in intensity of excimer emission. Fluorescence life time measurements of gel state and gel-coated test strip in presence and absence of PA describes a sharp fall (35.8 to 15.4 ns (for gel), and 6.99 to 0.98 ns (for test strip)) in the fluorescence life time of the excimer (**Figure 5.16**).

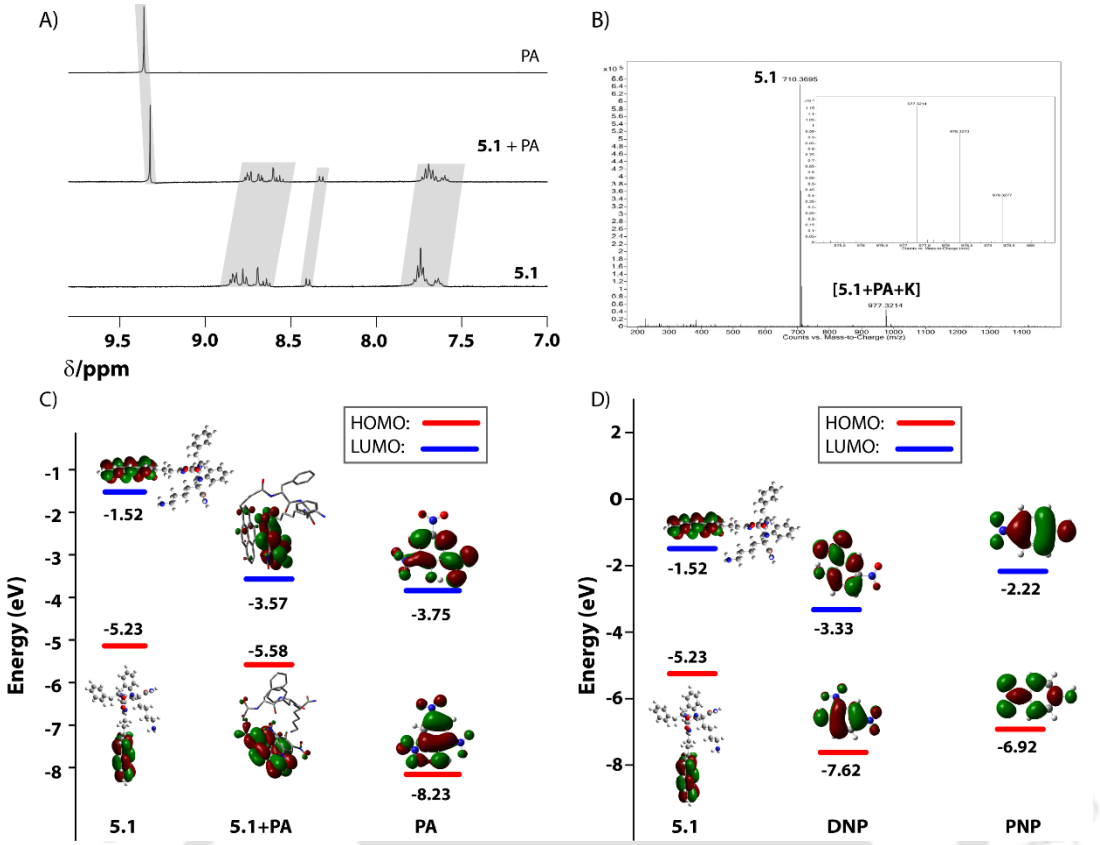

Figure 5.15 A) ^{1}H NMR of **5.1**, PA and a 1:1 mixture of **5.1** and PA in 1:1 D_2O-CD_3CN, B) mass spectrum of a solution of **5.1** in 1:1 Water-ACN in presence of PA showing the mass of the **5.1**-PA complex, C) relative energy levels HOMO and LUMO of **5.1**, PA and **5.1**-PA complex, and D) relative energy levels HOMO and LUMO of **5.1**, DNP and PNP.

In order to further investigate the structural changes what may happen during the PA sensing process in monomeric as well as aggregated states, energy-minimized structures were obtained by density functional theory (DFT) calculations at the B3LYP/6-31G (d,p) level using the Gaussian 9.0 software. As can be seen from **Figure 5.15**, the smaller HOMO (**5.1**)-LUMO (PA) energy difference (1.31 eV) compared to that of HOMO-LUMO (**5.1**) (3.71 eV) favors the complex formation between these two molecules. Similar calculations with DNP and PNP (**Figure 5.15**) explains the preferential binding for PA over the other two compounds as the HOMO (**5.1**)-LUMO (PA/DNP/PNP) was found to be smallest in case of PA. In aggregated state, the energy minimized structure showed preference for face to face stacking of the pyrene rings of molecules from the opposite sides as shown in **Figure 5.16D**. This arrangement also explains the observed β-sheet formation in gel state. Based on this structure, the aggregation can be pictorially explained as in **Figure 5.17**. While the binding energy for dimerization of **5.1** was calculated as -12.59 kcal mol^{-1}, the same for **5.1**-PA complex was -28.65 kcal mol^{-1}. The much lower binding energy of **5.1**-PA presumably allows the PA molecules to enter between pyrene stacks in the aggregated state and this in turn explain the observed quenching of emission (**Figure 5.17**).

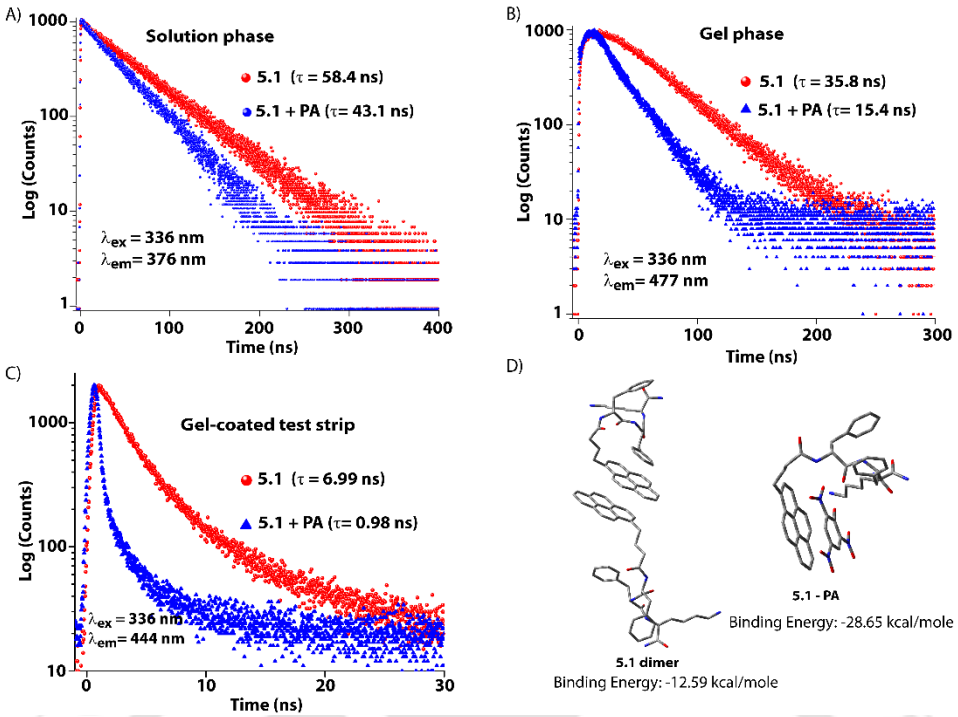

Figure 5.16 A) Lifetime decay profiles of **5.1** A) solution, B) gel, and C) test-strip before and after addition of PA at room temperature, and D) energy minimized structures and calculated binding energies of **5.1** dimer and **5.1**-PA complex.

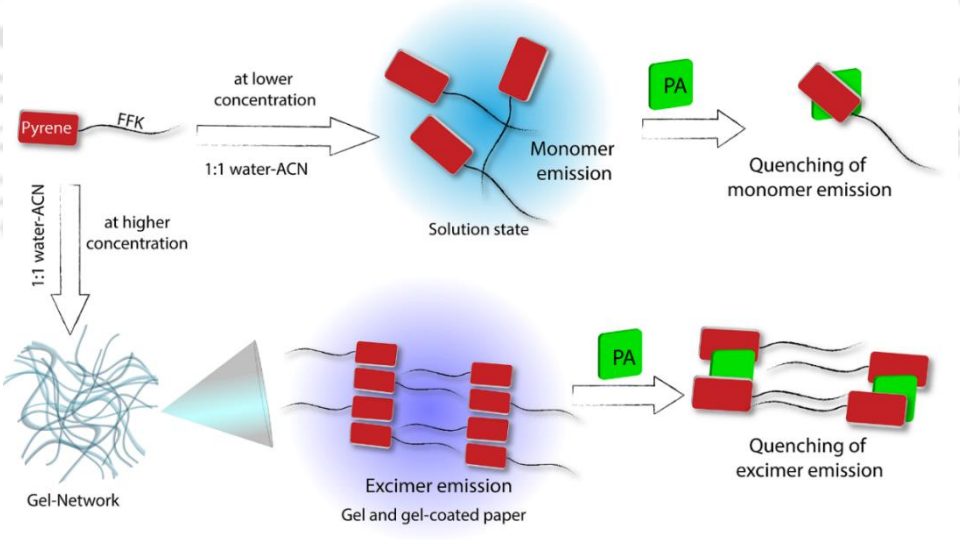

Figure 5.17 Graphical presentation of the aggregation of **5.1** and PA detection mechanism in solution, gel-coated state.

5.3 Conclusion

In summary, a small peptide based gelator, **5.1** and it's efficient and selective sensing of PA in sol, gel and paper based system is reported. The peptide forms self-supporting gel in 1:1 Water-ACN. Strong π–π stacking between pyrene rings along with β-sheet formation by the peptide sequence are the key forces behind the gelation. In solution phase, the detection of PA is achieved via interaction of the pyrene unit and PA molecules which significantly quenches the monomeric emission of pyrene. A multi-well plate based platform is developed where the detection of PA could

be done using the gel. The detection limit in this case is 22.91 ppb. A paper based test strip is created where contact-mode detection of PA is possible for solid PA as well as extremely diluted solutions of the analyte. Moreover, the detection can be achieved for as low as femtogram (2.29×10^{-15} g) level using these test strips. In addition to that, the test strips can detect PA vapors in sub ppb level and are effective for detection of PA contamination in ground water. The detection limits achieved for solution, gel and paper-based system is amongst the lowest reported so far. Importantly, unlike the solution phase, the gel phase or paper-based systems, sensing of PA relies entirely on the excimer quenching. DFT calculation reveals the energetically favorable complex formation between pyrene of **5.1** and PA is behind the quenching in all three states. Overall, the new system is one of the few systems which can be used as a sensor in three different states: sol, gel, and solid. Also the paper based test strips can be used for practical use efficiently.

SL. No.	Material	Medium	Detection Limit
01	Pyrene containing Peptide	Water-ACN (1:1, v/v)	Sol: 115.24 ppt Gel: 22.91×10^3 ppt Test strip: 11.45 fg cm^{-2}
02	Triarylamine-cored dendrimer[253]	THF	224.52 ppt
03	Isophthalic acid derivatives[254]	Water	1.20 X 10^5 ppt
04	Iridium(III) complexes[255]	Water-ACN (9:1, v/v)	3.44 X 10^4 ppt
05	Coordination polymer[256]	Water	2.63 X 10^4 ppt
06	Organic framework[257]	Water	8.20 X 10^5 ppt
07	Nanoparticles[258]	BR buffer (pH 7.0)	5.96 X 10^3 ppt
08	Pyrene–polyethersulfone nanofibers[259]	DMF-THF (4:6, v/v)	5.27 X 10^3 ppt
09	Curcumin Conjugates[260]	Water	3.09 X 10^3 ppt
10	Covalent organic cages[261]	DCM	6.40 X 10^3 ppt
11	Anthracene derivatives[246]	DMSO	3.54 X 10^5 ppt
12	MOF[262]	ACN	Not reported
13	p-phenylenevinylene derivatives[263]	a) Water b) THF	a) 5.04 X 10^3 ppt b) 2.70 X 10^3 ppt
14	Fluoranthene derivatives[252]	Ethanol	2.00 X 10^3 ppt (1.15 fg cm^{-2})
15	Ploysilole[264]	Seawater	6.00 X 10^3 ppt
16	Pyrene based system[136]	THF	0.46 ag
17	Hexa-peri-HexabenzocoroneneBased Chemo-sensors[265]	Water-THF	Attrogram
18	Hexaphenylbenzene derivative + Hg^{2+} [266]	Water-EtOH	~ 2.29 fg cm^{-2}

Table 5.1 A comparative chart of the detection limits for PA with previously reported systems.

5.4 Experimental sections

5.4.1 General Information and Materials: Rink amide MBHA resin and protected amino acids and coupling reagents were purchased from Novabiochem. All other chemicals and reagents were obtained from Sigma-Aldrich (USA). HPLC-grade dimethylformamide (DMF), dichloromethane (DCM), and acetonitrile (ACN) were procured from Spectrochem (India) and Fisher Scientific (India), respectively. To prepare samples, Milli-Q water with a conductivity of less than 2 μScm^{-1} was used. Chromatographic purifications were performed on a Luna 5 μm (C18) column (Phenomenex) using a Dionex Ultimate 3000 HPLC. Standard 10 mm-path quartz cuvettes were used for all spectroscopic measurements. ^{1}H NMR and ^{13}C NMR were recorded with a Bruker Ascend 400 MHz (Bruker, Coventry, UK) spectrometer and referenced to deuterated solvents. ESI-MS were performed with a Q-tof-Micro Quadrupole mass spectrophotometer (Micromass). Absorption and fluorescence spectra were recorded on a Lambda 750 (Perkin Elmer) and a Cary Eclipse (Agilent) spectrophotometers respectively.

5.4.2 Synthesis and Characterization of Compounds

Synthesis of peptide 5.1: The peptide **5.1** was synthesized on Rink amide MBHA resin using standard solid phase peptide synthesis (SPPS) technique and Fmoc-chemistry. Fmoc-Phe-OH, Fmoc-Lys(Boc)-OH and 1-pyrene butyric acid were used as building blocks. In a typical coupling, 3 equiv. of protected amino acid (with respect to the loading of the resin), 3 equiv. of HBTU, and 6 equiv. of DIPEA were taken in 5 mL of DMF (for 0.1 mmol scale with respect to the resin loading) and stirred for 5 minutes prior to addition of the mixture to the resin. The reaction mixture was shaken for 60 min and the resin was washed several times with DMF. Fmoc-deprotection was achieved by treatment of the resin with 20% piperidine (5 mL, 5 minutes, three times) followed by thorough washing of the resin with DMF. The Fmoc-deprotection and coupling steps were repeated until the designed peptide sequence was obtained. Finally, the peptide loaded resin was washed several times with DMF followed by DCM and dried under reduced pressure. The dried resin was then treated with a mixture of 95% trifluoroacetic acid (TFA) in DCM containing 1% triethylsilane (TES) and stirred for 1 h. The resin was finally washed with DCM several times. The cleavage cocktail and the washings were combined and concentrated to a minimum volume on a rotary evaporator. The cleaved peptide was then precipitated from cold dry ether, centrifuged and lyophilized to get the crude peptide. Purification was done in a semi-preparative HPLC using a Luna 5 μm (C18) column (Phenomenex) and an eluent of acetonitrile and water starting at 20% ACN in H_2O reaching at 100% ACN in 8.9 mins) to complete the chromatogram in 20 mins. Yield = 70%. ^{1}H NMR (400 MHz, DMSO-d_6) δ (ppm) = 8.31 – 8.24 (m, 3H), 8.23 – 8.16 (m, 2H), 8.13 (d, J = 2.0 Hz, 1H), 8.12 – 8.07 (m, 2H), 7.99

(d, *J* = 8.2 Hz, 1H), 7.83 (d, *J* = 7.8 Hz, 1H), 7.65 (s, 2H), 7.24 – 7.16 (m, 8H), 7.11 – 7.06 (m, 2H), 4.62 – 4.48 (m, 2H), 4.16 (td, *J* = 8.4, 5.1 Hz, 1H), 3.13 (t, *J* = 7.7 Hz, 2H), 3.06 (dd, J = 14.0, 4.8 Hz, 1H), 2.96 (dd, *J* = 14.0, 4.1 Hz, 1H), 2.85 (dd, *J* = 14.0, 9.0 Hz, 1H), 2.70 (dd, J = 15.8, 5.5 Hz, 3H), 2.17 (t, *J* = 7.2 Hz, 2H), 1.85 (q, *J* = 7.6 Hz, 2H), 1.66 (s, 1H), 1.50 (q, *J* = 7.5 Hz, 3H), 1.35 – 1.21 (m, 2H). ^{13}C NMR (100 MHz, DMSO-d_6) δ (ppm) = 173.23, 172.01, 171.49, 170.63, 137.56, 136.55, 130.89, 130.43, 129.22, 129.10, 128.03, 127.97, 127.52, 127.46, 127.15, 126.51, 126.16, 124.91, 124.79, 123.55, 53.95, 52.08, 37.23, 34.82, 32.06, 31.43, 27.38, 26.64, 22.14. Mass (ESI-MS): *m/z* calcd. for $C_{44}H_{48}N_5O_4$ $[M+H]^+$, 710.37; found 710.39.

5.4.3 Method

Sample preparation: Stock solutions of analytes were prepared in ACN and then diluted to the required concentrations with acetonitrile or Water-ACN mixtures. **Caution!** The nitro aromatic compounds used in this study, especially PA is a very powerful explosives. It must be handled with care and also in very small quantities.

Gel preparation: In a typical experiment, 18 mg of **5.1** was taken in 1 mL of 1:1 mixture of water and acetonitrile in a glass vial. The mixture was sonicated to dissolve the solid completely and then allowed to stand at room temperature without any disturbance. After 30 minutes, a transparent gel was obtained that did not flow downward upon inversion of the glass vial.

Stern-Volmer plots : The quenching behavior was studied by Stern-Volmer equation, $I_0/I = 1+K_{sv}[Q]$, where I_0, I are the fluorescence intensities before and after addition of the quencher, K_{sv} is the Stern-Volmer quenching rate constant and [Q] is the concentration of the quencher.

Circular dichroism (CD): CD spectra of all the samples were recorded on a J-1500 (JASCO, U.S.A.) instrument at room temperature. The data were collected at 1 nm intervals with 2 nm band width. All measurements were done in 0.2 cm path length cuvette with 400 μL sample volume. Each CD profile is an average of 3 scans of the same sample collected at a scan rate 100 nm min^{-1}, with a proper baseline correction from the respective solvents. Scans were performed over 190 to 650 nm.

Determination of sol–gel transition temperature (T_g): T_g was determined using standard ball dropping method. A small steel ball was placed on top of the hydrogel sample (equal volume). The samples were placed in a water bath and the bath was heated at a rate of 0.5 °C/min. The temperature at which the steel ball drops to the bottom was noted as T_g. The experiments were performed in triplicate.

FTIR: KBr pellets were prepared by mixing the samples (as synthesized **5.1** and **5.1** Xerogel) and oven dried KBr. The spectra were recorded on a Nicolet is10 spectrometer. The baseline was subtracted from the obtained absorbance intensity in each case.

Field emission scanning electron microscope (FESEM): For **5.1** gel, a small portion of the gel was casted on a silicon wafer and air-dried for 1 day before the experiment. FESEM images were taken on a Gemini SEM 300 (Sigma Zeiss) instrument.

Field emission transmission electron microscope (FETEM): 5 μL of **5.1** gel was casted on carbon coated copper grid (300 mesh Cu grid with thick carbon film from Pacific Grid Tech, USA) and allowed to air dry for 2 minutes and then the excess sample was bloated with a tissue paper. The grid was then air dried for 1 day. FETEM images were taken in JEOL 2100F microscopes.

Atomic force microsope (AFM): A small portion of the **5.1** gel was casted on a silicon wafer and air-dried for 1 day before the experiment. AFM images were taken on Oxford Cypher microscope.

Rheology: The viscoelastic properties of the **5.1** gel were characterized using rheometer (Anton-Paar MCR 102) equipped with a 20 mm parallel plate measuring system at 25 °C. A strain sweep test was performed first to identify the linear viscoelastic region (LVR) over a range from 0.1 to 100 % strain at a fixed oscillatory frequency of 1 rad/s. The LVR can be defined as where strain has no impact upon G′ and G″. Further, the mechanical strength of the gel was determined from oscillatory test *i.e.*, frequency sweep, which was carried out under an appropriate strain (γ = 0.1 %) selected from the LVR with the frequency ranging from 0.1 to 100 rad s^{-1} at 25 °C.

Lifetime Measurements: Fluorescence lifetimes measurements were carried out with time-correlated single-photon counting (TCSPC) spectrophotometer (Edinburgh FSP920). The samples were excited at 336 nm using a pulsed diode laser (full width at half maximum (FWHM) of 568 ps). An aqueous solution of Ludox was used to measure the instrument response function (IRF). The fluorescence decays were analyzed by re-convolution method using the FAST software provided by Edinburgh Instruments.

Multiwell experiments: A 21.85 mM **5.1** solution was prepared in 1:1 Water-ACN and 200 μL portions of the solution were added to different wells of a 96 multiwell plate and the solution was incubated at room temperature for 30 mins to form gels in the wells. On top of the gels, 30 μL of analyte solutions were added and the plate was incubated at room temperature with constant shaking at 100 rpm for 10 mins. The readings were recorded in a Tecan infinite M1000 multimode microplate reader (TECAN USA) using a filter pair with excitation at 337 nm and emission at 477 nm.

Preparation of test strips: Gel samples of **5.1** (21.85 mM in 1:1 Water-ACN) were heated to 55 °C to melt the gel into sol. Filter paper strips (5 cm × 2 cm) were then dipped into the sol for 30 s, allowed to come to room temperature and finally the solvents were removed under reduced pressure at room temperature. The gel-coated filter papers were then cut into smaller pieces to get the test strips and used for the detection of explosives.

Contact mode visual detection of PA: Aqueous samples were prepared by dissolving PA in ACN-water (0.5:9.5) mixture. The explosive solutions were spotted onto the test strips at the desired concentration level using a glass micro syringe. A solvent blank was spotted near to the spot of each explosive. In order to ensure consistent analysis, all depositions were prepared from a 10 µL volume, thereby producing a spot of ~0.2 cm^2 area (diameter ~0.5 cm). After solvent evaporation, the filter paper was illuminated with 365 nm UV light. The dark spots were identified by an independent observer, and each set of experiments was repeated three times for consistency. The detection limits were calculated from the lowest concentration of the explosive that enabled an independent observer to detect the quenching visually.

Vapor-Phase Detection: The vapor phase detection was done by monitoring the fluorescence spectra of **5.1** gel coated test-strips before and after exposure to equilibrated vapors of PA. Saturated vapors of PA generated by keeping PA in a sealed tube for three days to ensure that the equilibrated vapor pressure is reached. The test strips were then kept in these tubes for a specific time period and the fluorescence spectra of the exposed test-strips were recorded immediately after taking out from the sealed tube without any delay.

Quantitative detection of PA by test strips: The required analyte solutions of various concentrations ($1 \times 10^{-12} - 1 \times 10^{-3}$ M) were added to each strip, and the solvents were allowed to evaporate. The film was placed in such a way that the excitation beam falls on the spot where PA is added. Emission was collected by a front face technique using a film sample holder. Emission of a blank sample was monitored by the addition of solvent alone.

Detection of PA in ground water: A stock solution (1×10^{-2} M) was prepared by weighing appropriate amounts (2.3 mg/mL) of the compound and dissolving in collected ground water sample. This solution was diluted to different concentrations and used as the test samples. The test samples (10 µL) were spotted to the test strips, and the fluorescence quenching was measured with the help of fluorimeter. The minimum detection level of PA was qualitatively determined by measuring the fluorescence quenching (%) using the front face technique.

Detection Limit: Detection limits were calculated using the same protocol described in the previous chapters.

Density functional theory (DFT): The M06 family of functions were chosen over other conventional DFT functions as they are proven to be more accurate toward geometries and energy calculations for a variety of dispersion dominated systems like DNA base pair stacks. HOMO and LUMO orbital energies of the **5.1**, PA and the complex **5.1**-PA were obtained using the density functional theory (DFT) at the B3LYP/6-31G(d,p) accuracy level using the Gaussian 09 package of programs.

NMR, Mass Spectra, and Chromatogram of the Synthesized Compounds

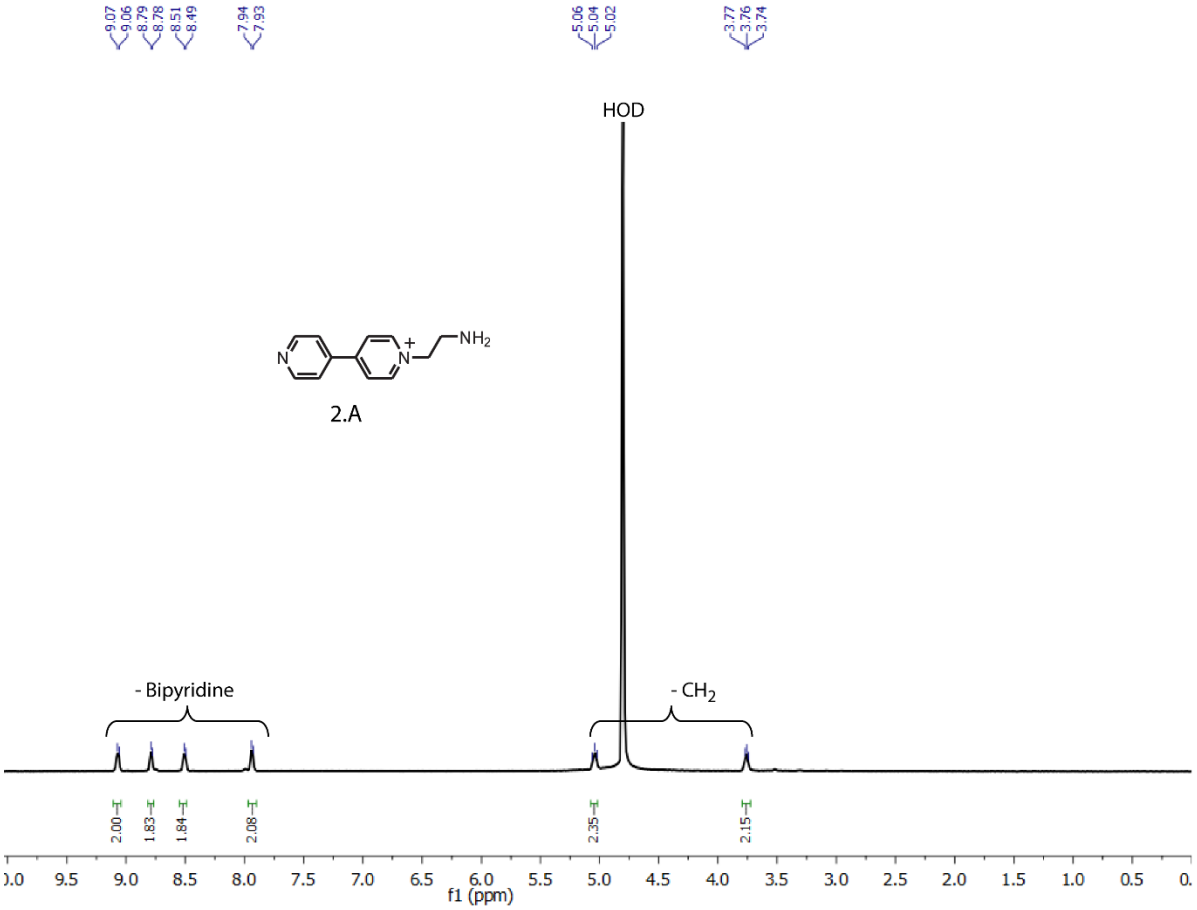

Figure1 ^{1}H NMR spectrum of **2.A**.

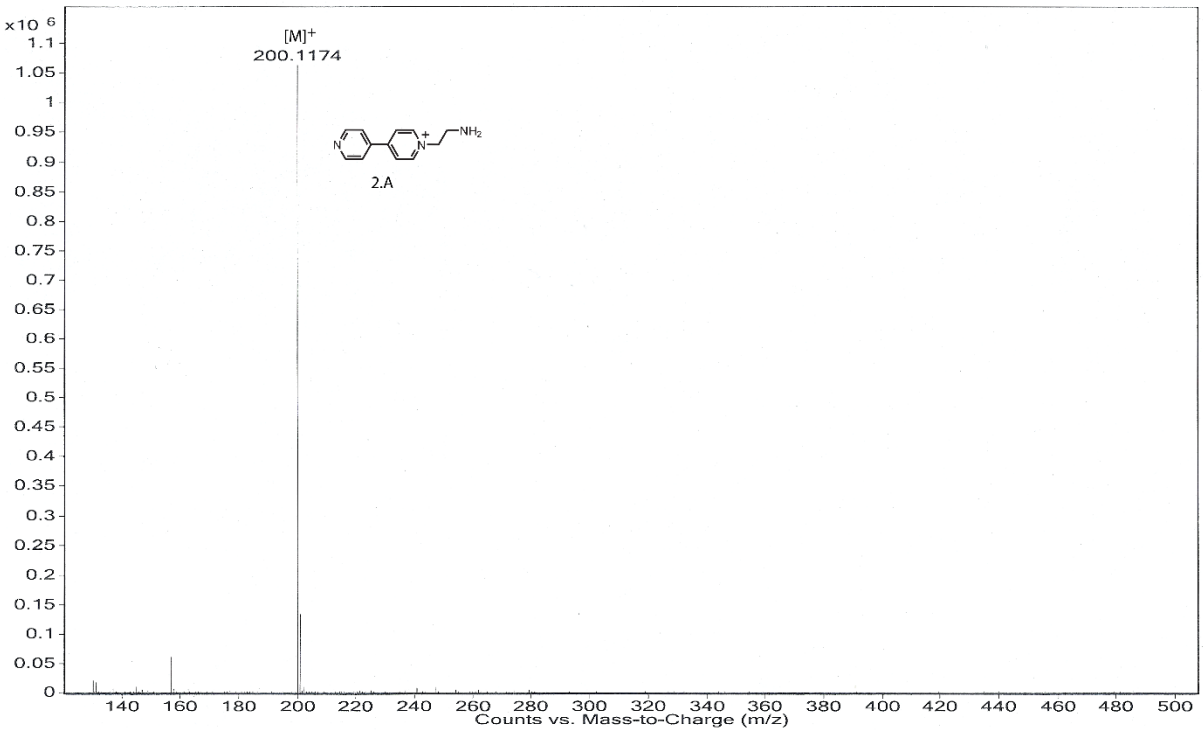

Figure 2 ESI-Ms spectrum of **2.A**.

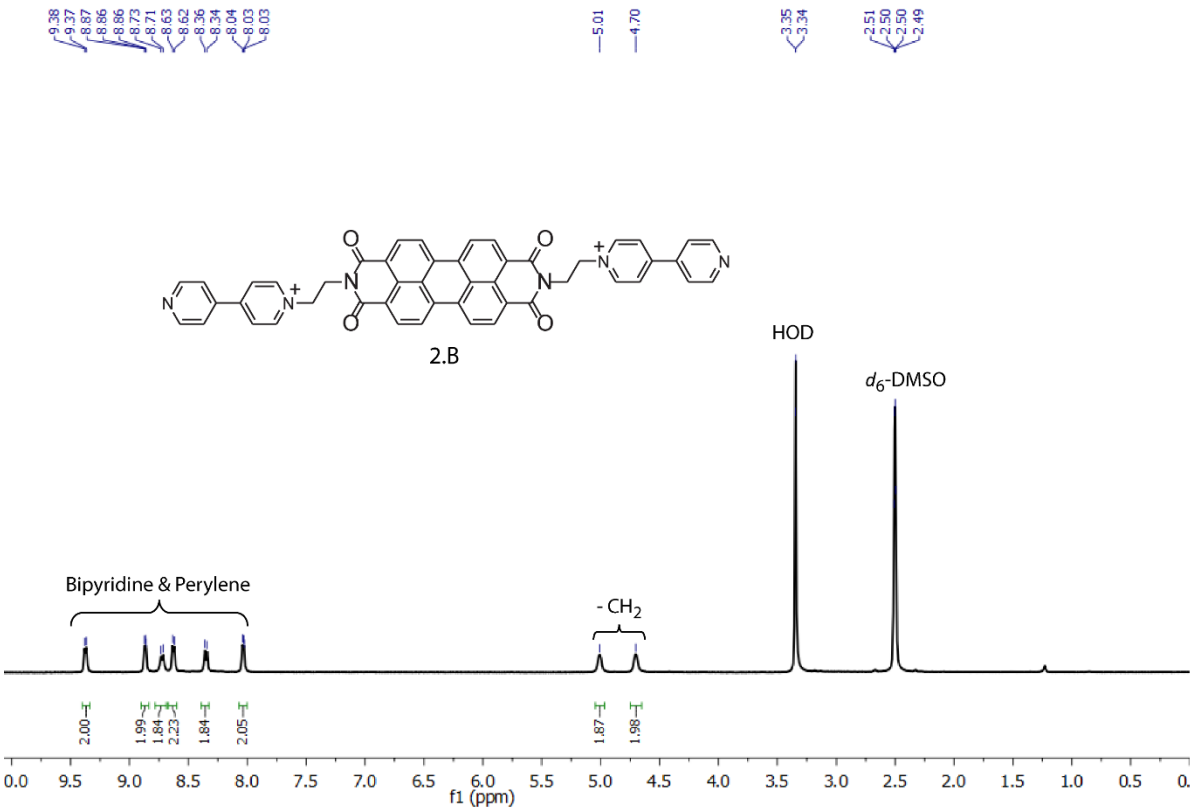

Figure 3 ^{1}H NMR spectrum of **2.B**.

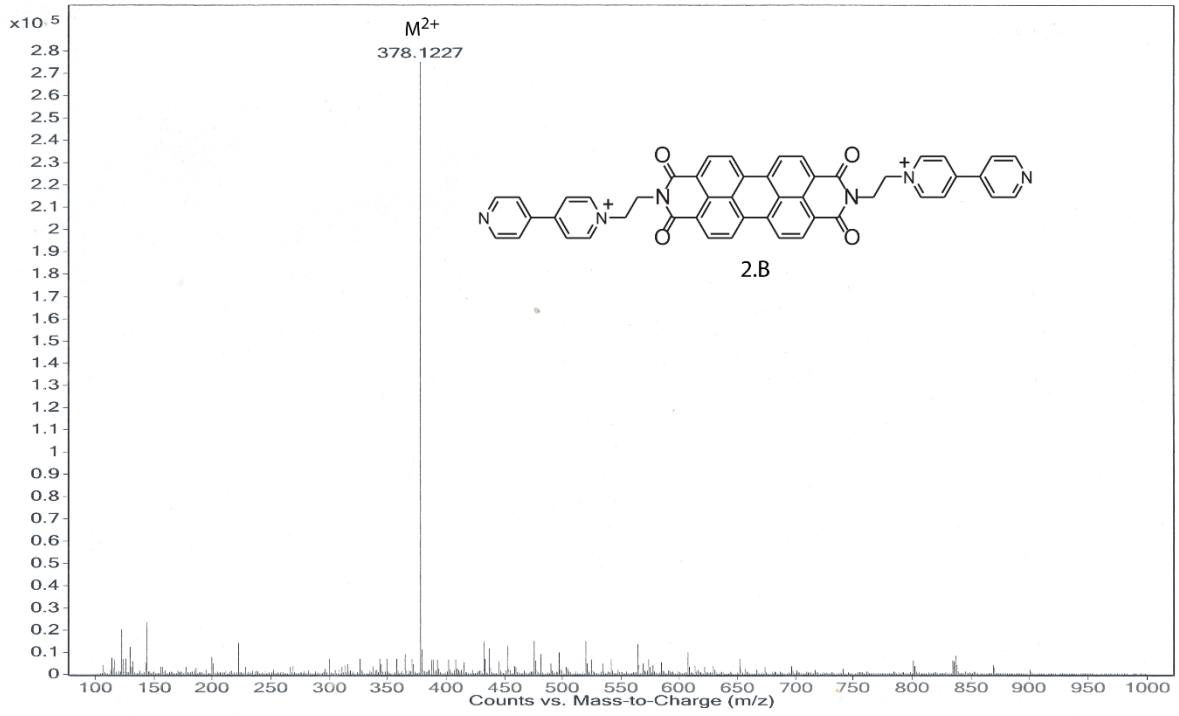

Figure 4 ESI-Ms spectrum of **2.B**.

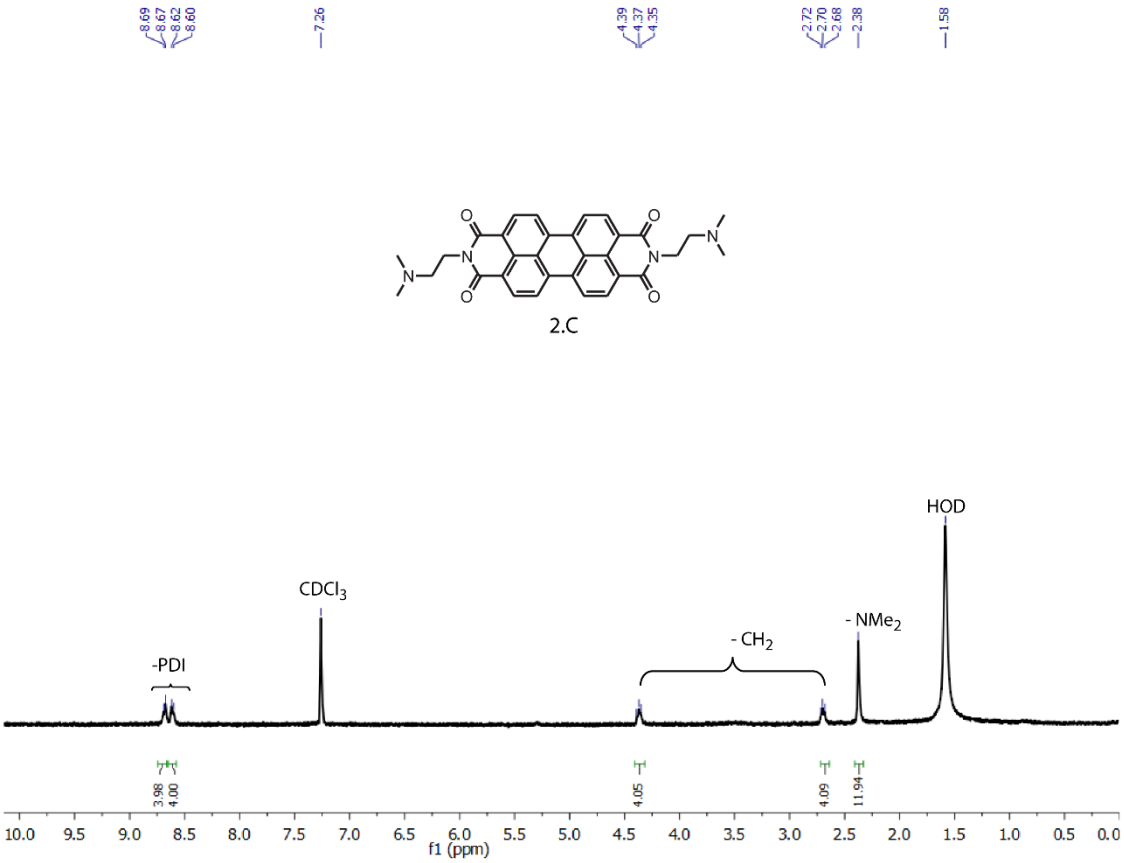

Figure 5 ^{1}H NMR spectrum of **2.C**.

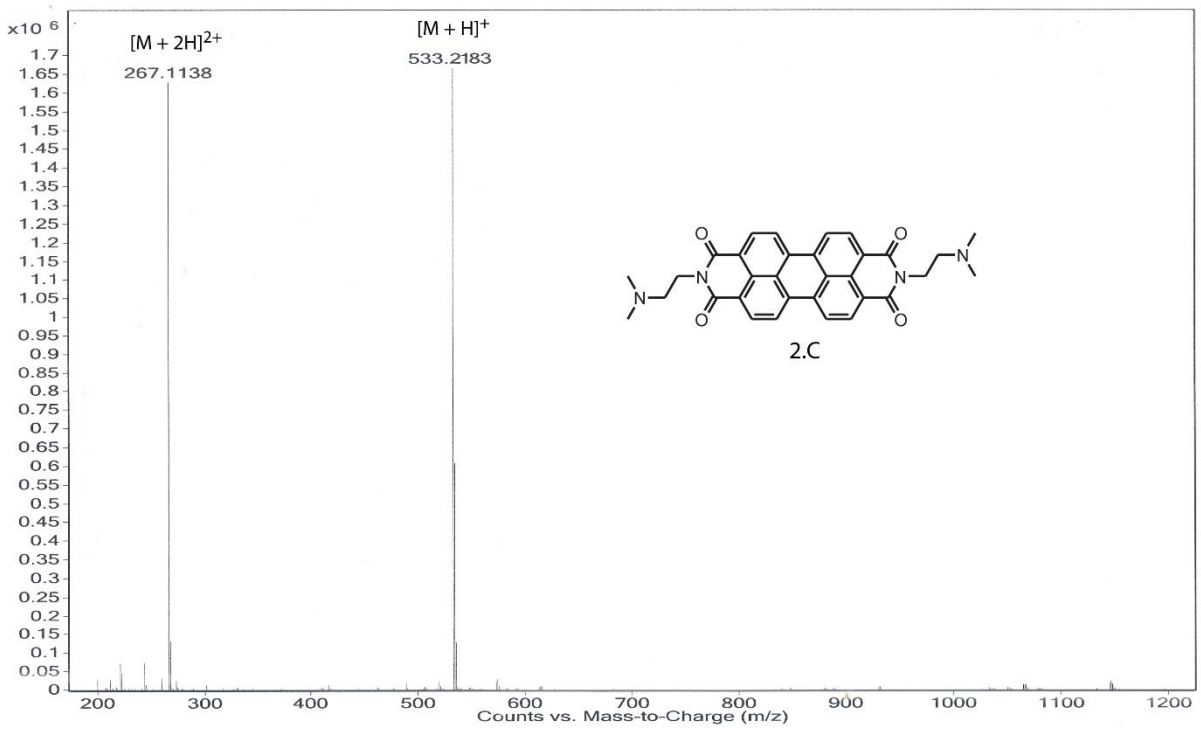

Figure 6 ESI-Ms spectrum of **2.C**.

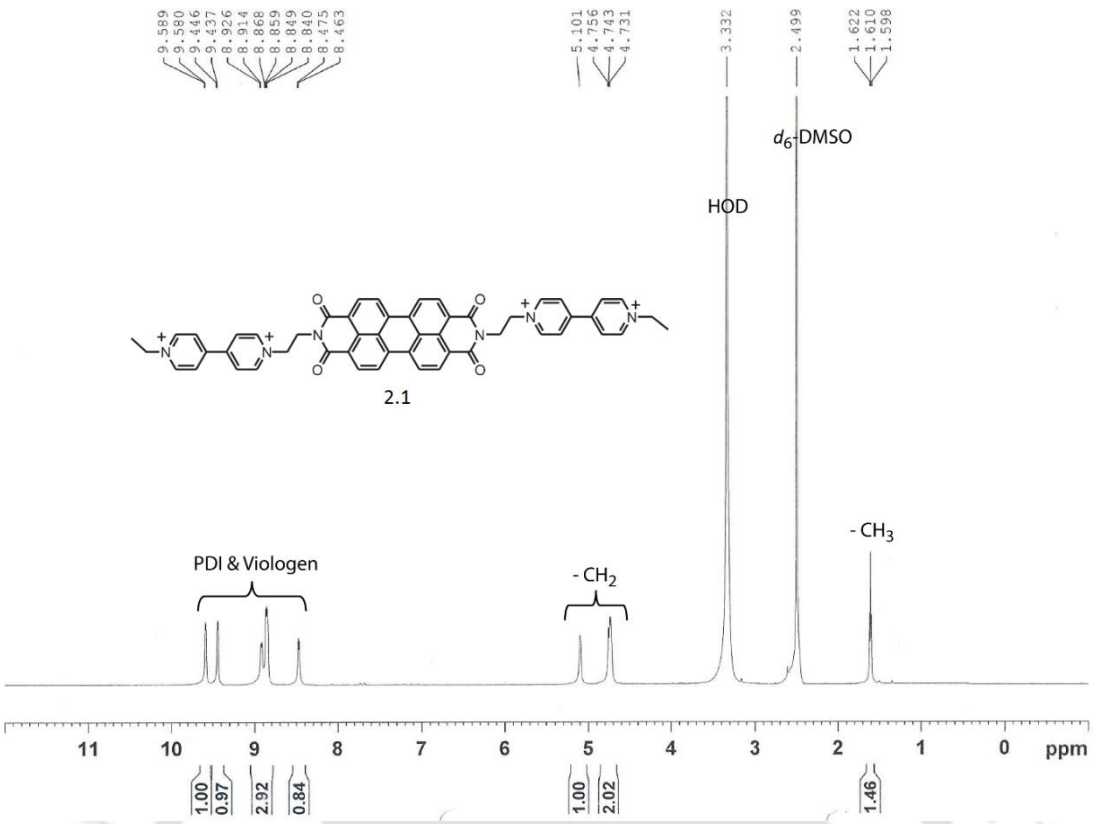

Figure 7 ^{1}H NMR spectrum of **2.1**.

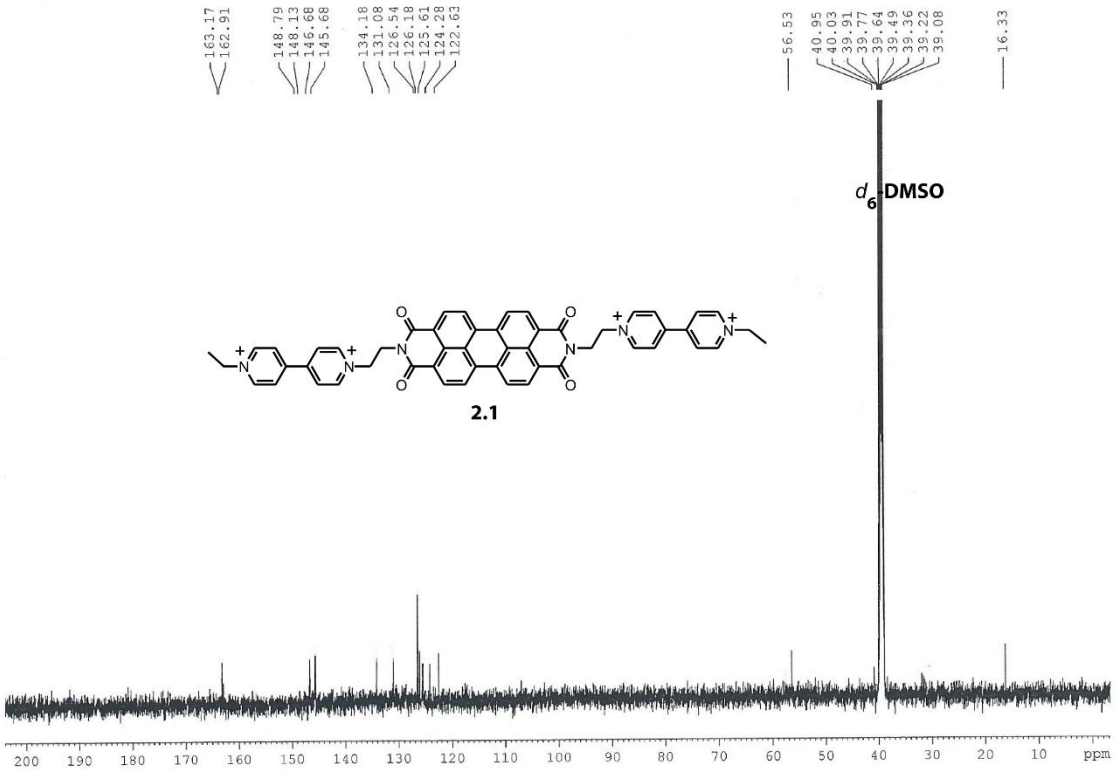

Figure 8 ^{13}C NMR spectrum of Compound **2.1**.

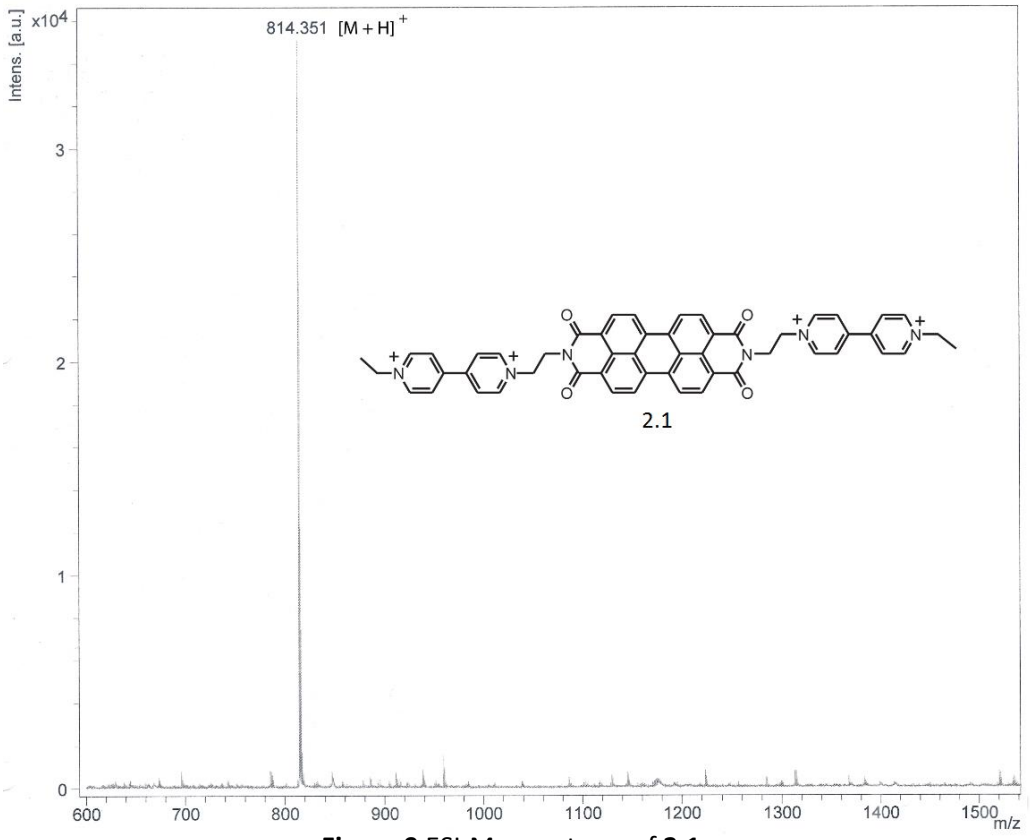

Figure 9 ESI-Ms spectrum of **2.1**.

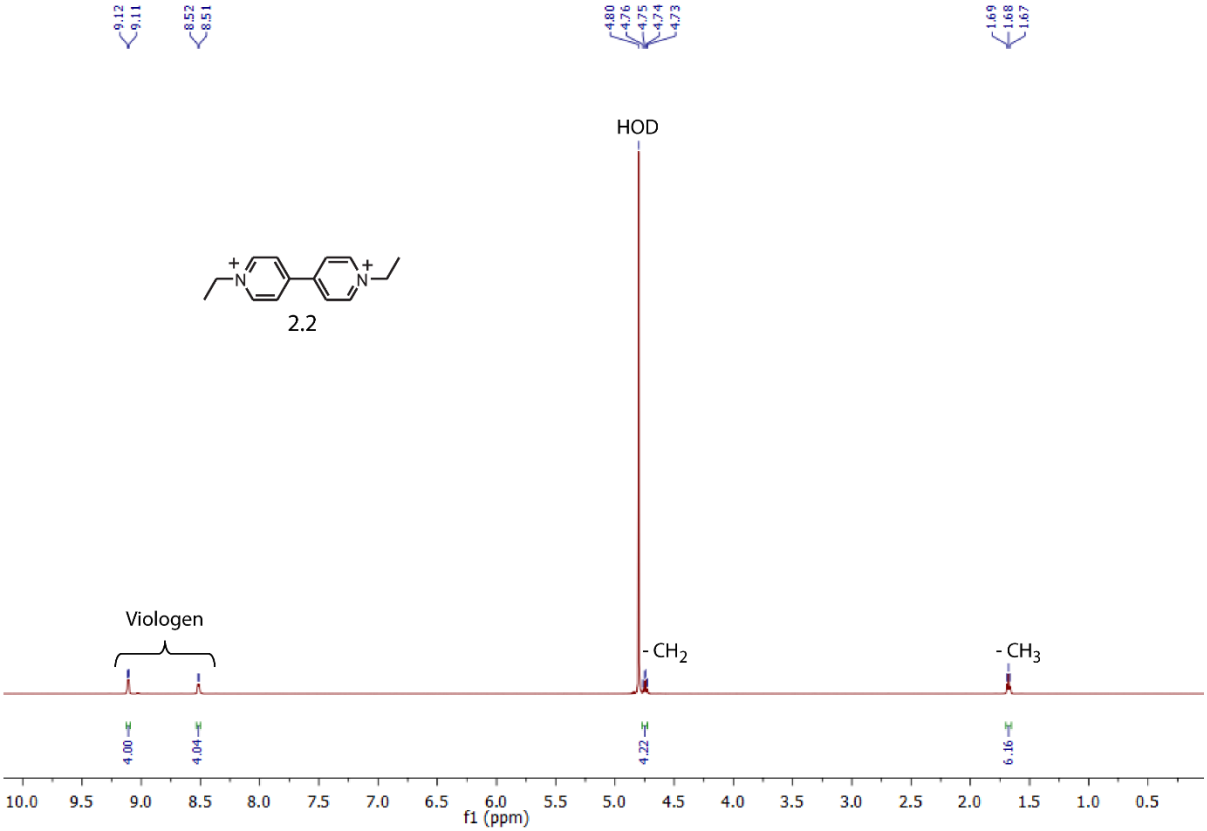

Figure 10 ^{1}H NMR spectrum of **2.2**.

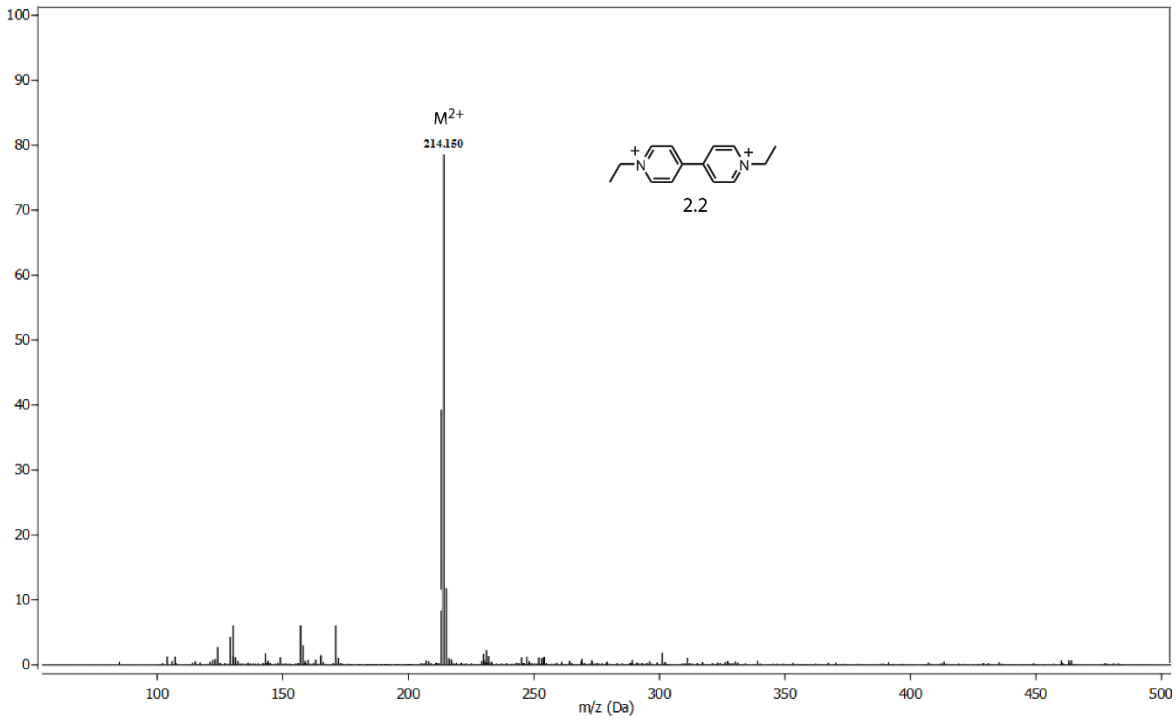

Figure 11 ESI-Ms spectrum of **2.2**.

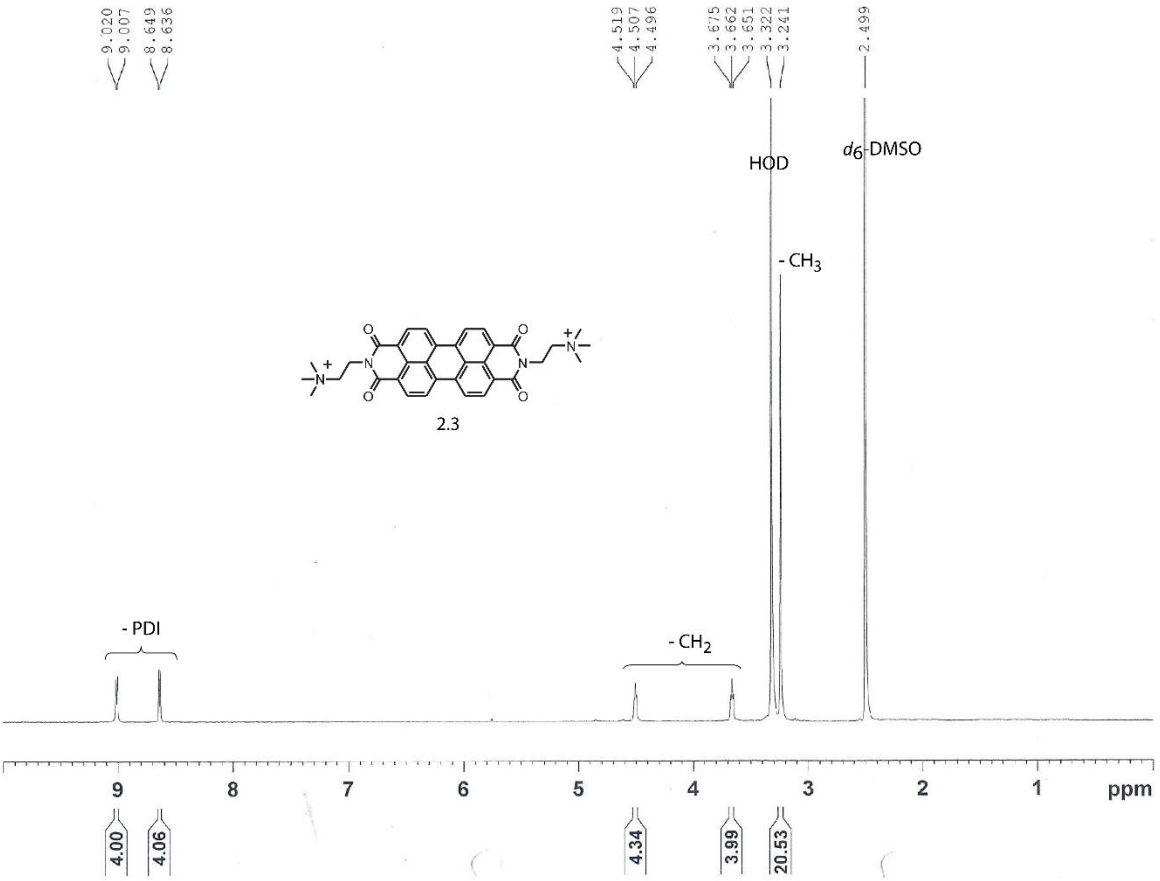

Figure 12 ^{1}H NMR spectrum of **2.3**.

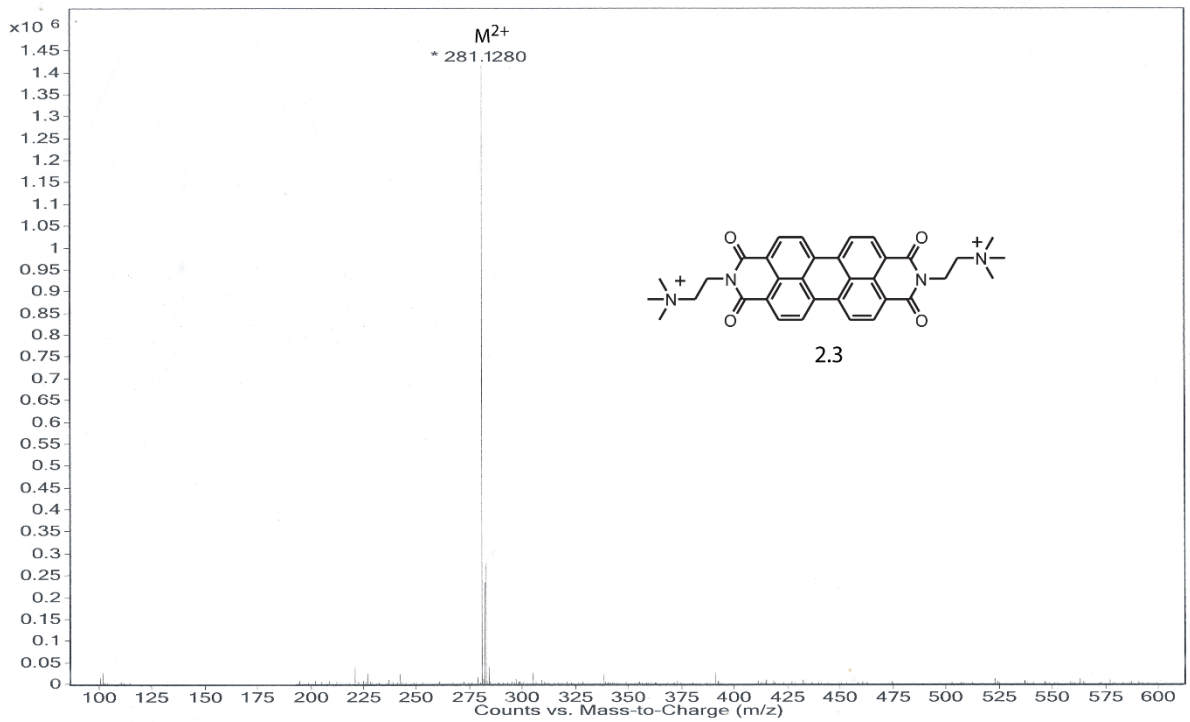

2.3

Figure 13 ESI-Ms spectrum of **2.3**.

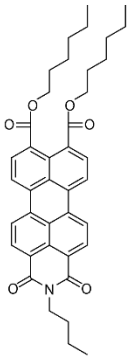

3.A

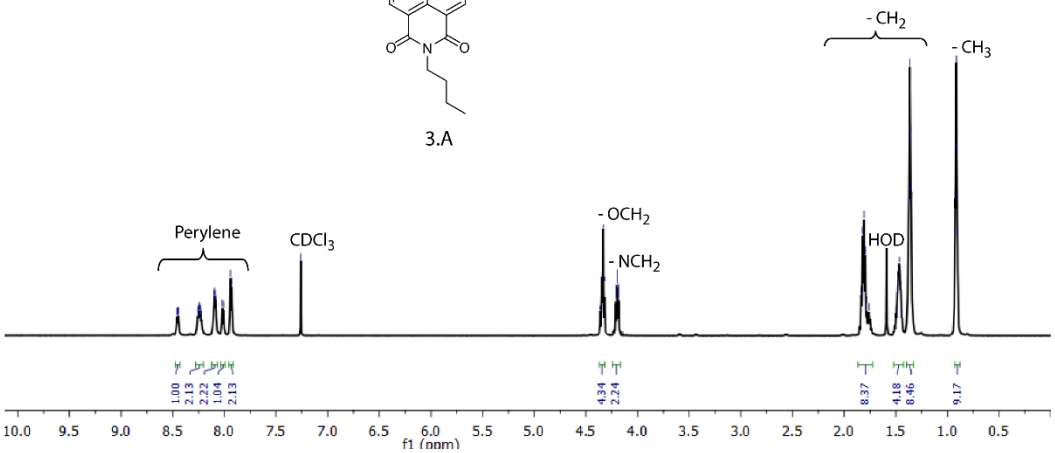

Figure 14 ^{1}H NMR spectrum of **3.A**.

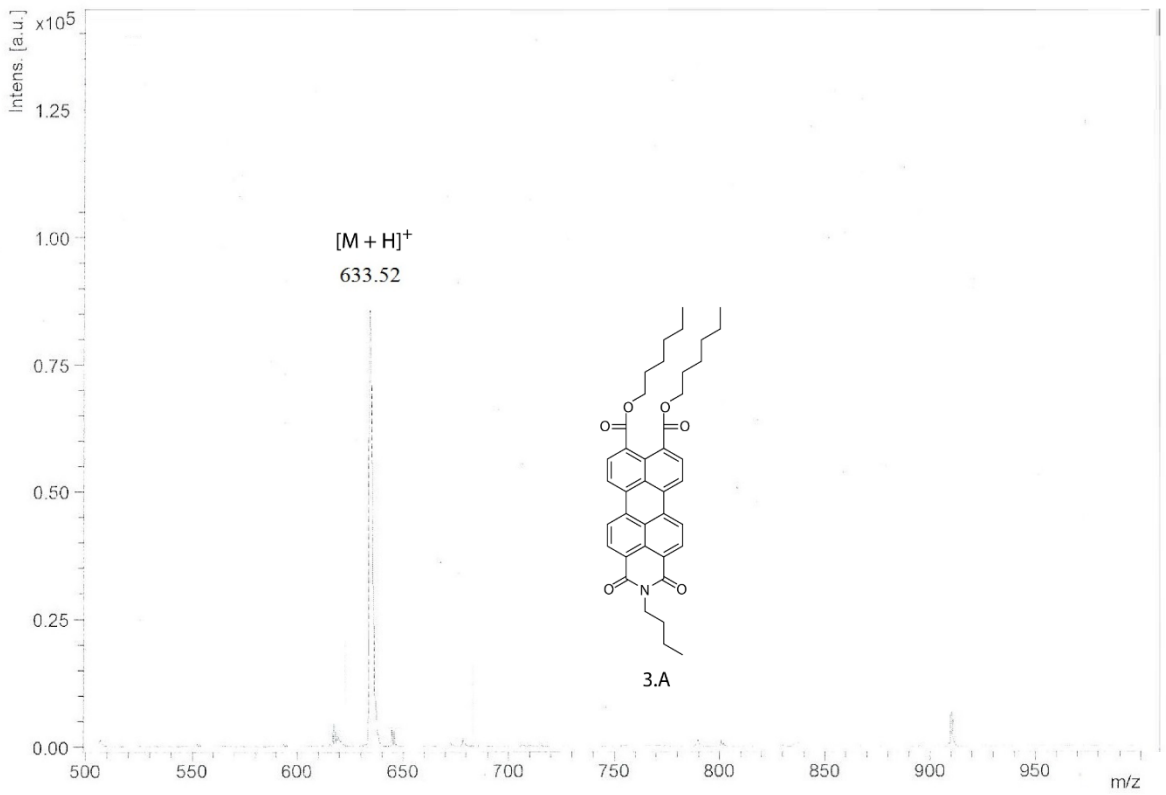

Figure 15 ESI-Ms spectrum of **3.A**.

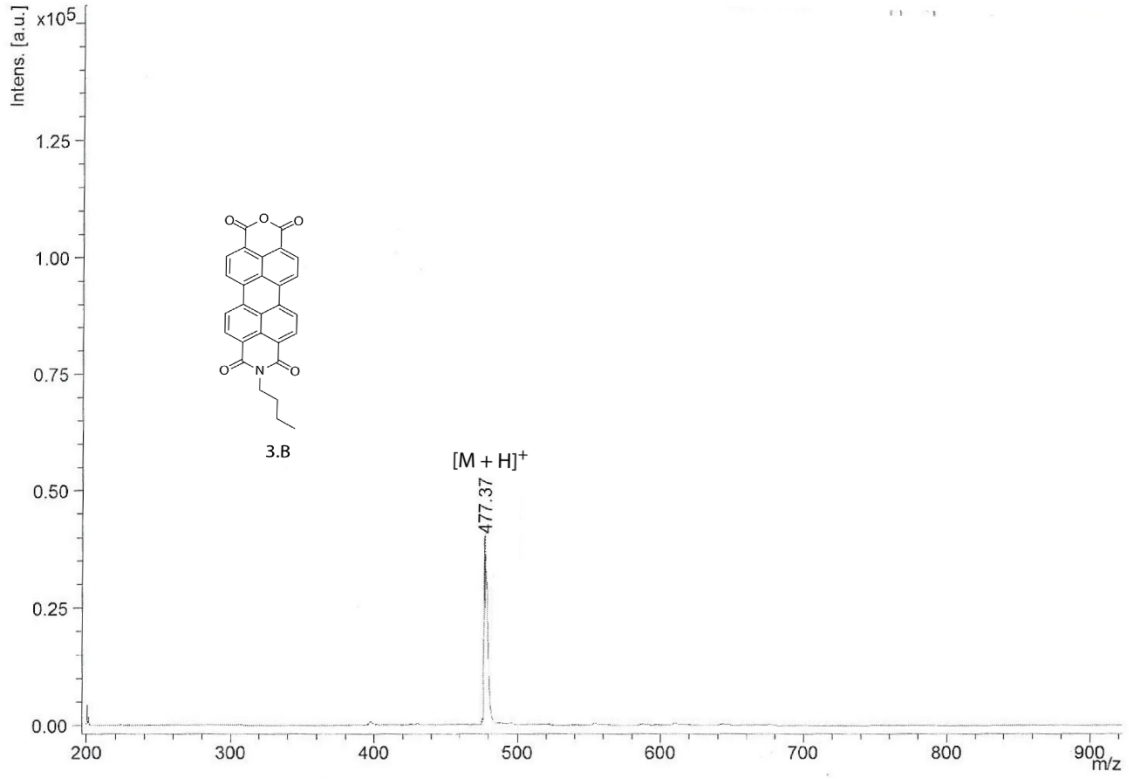

Figure 16 ESI-Ms spectrum of **3.B**.

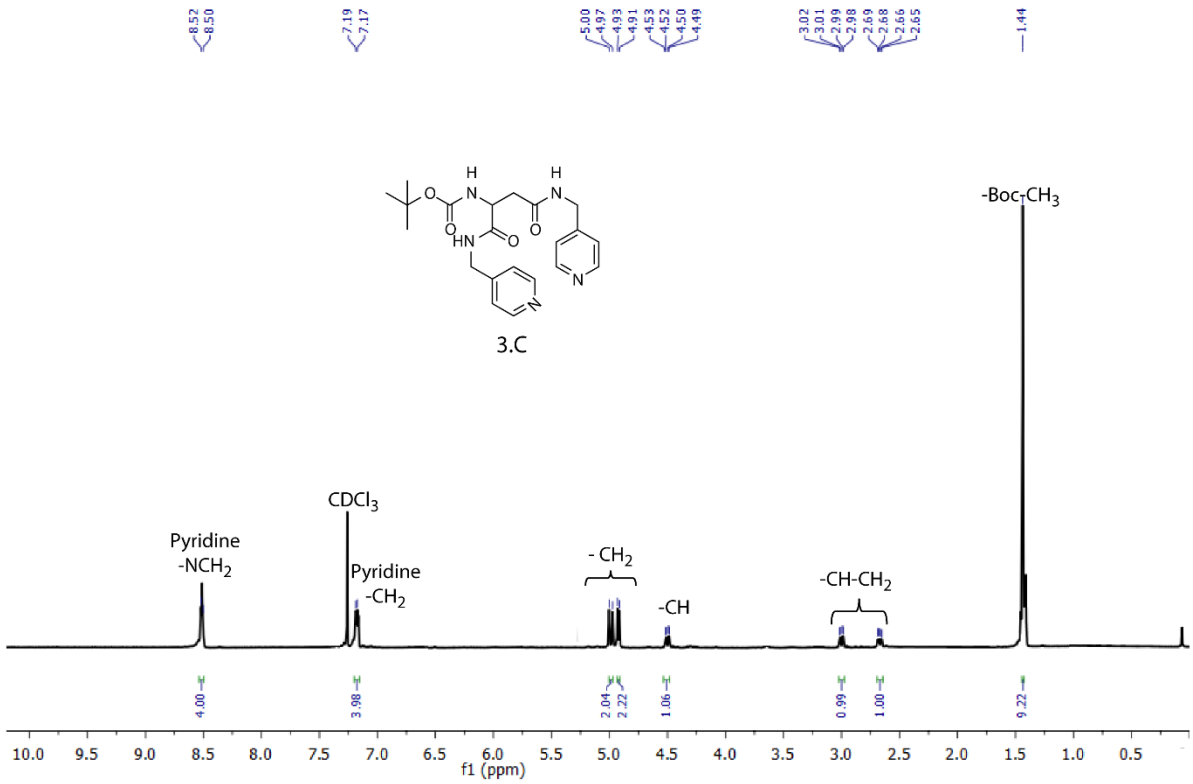

Figure 17 ^{1}H NMR spectrum of **3.C**.

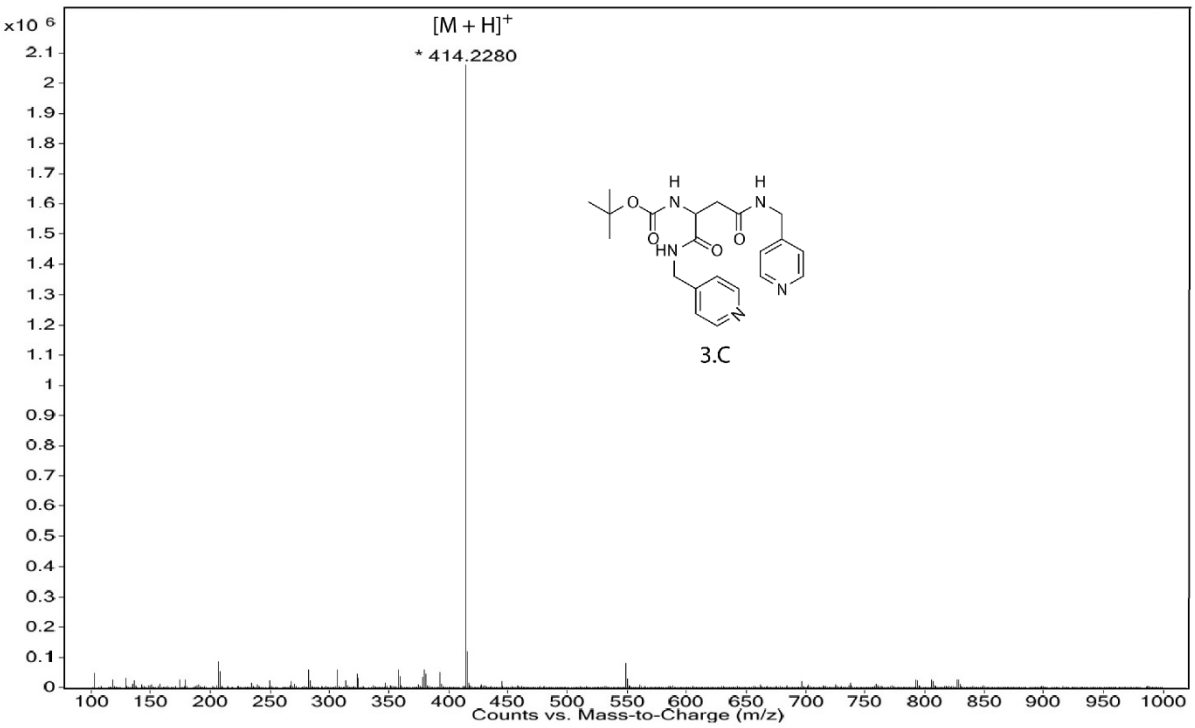

Figure 18 ESI-MS spectrum of **3.C**.

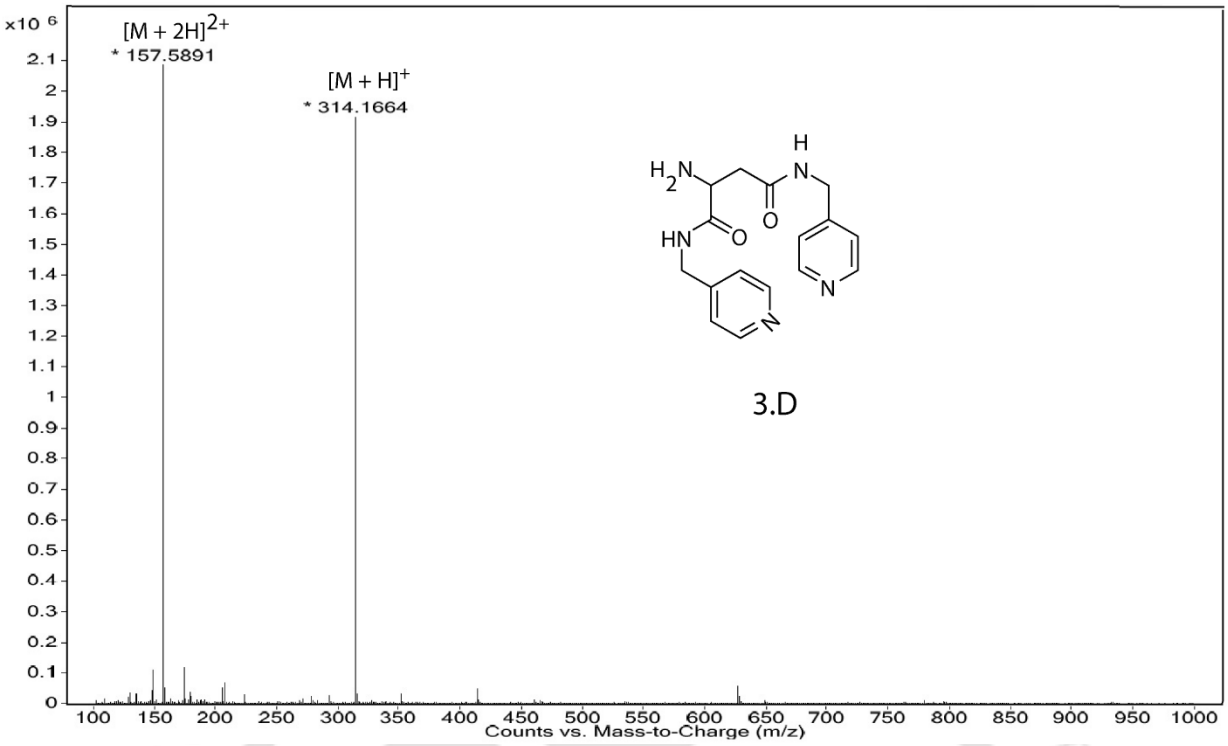

Figure 19 ESI-Ms spectrum of **3.D**.

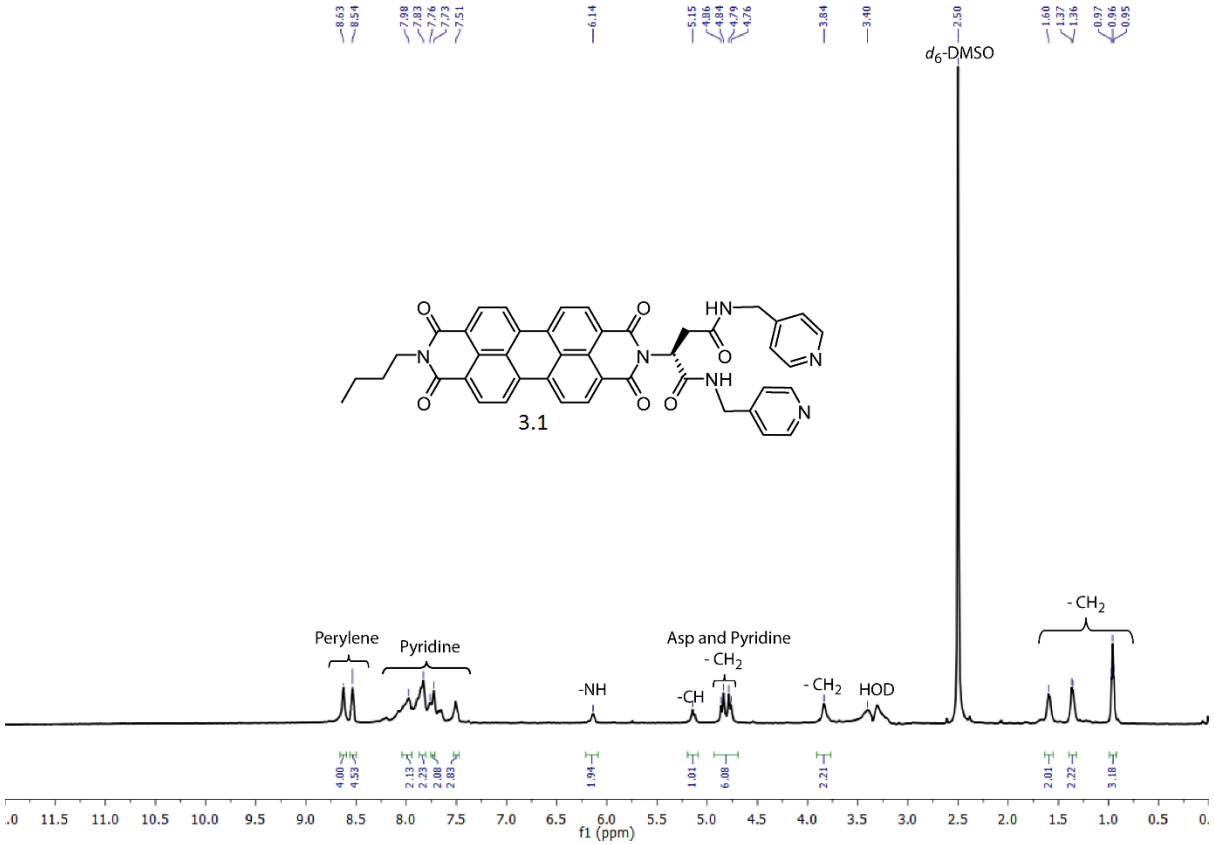

Figure 20 ^{1}H NMR spectrum of **3.1**.

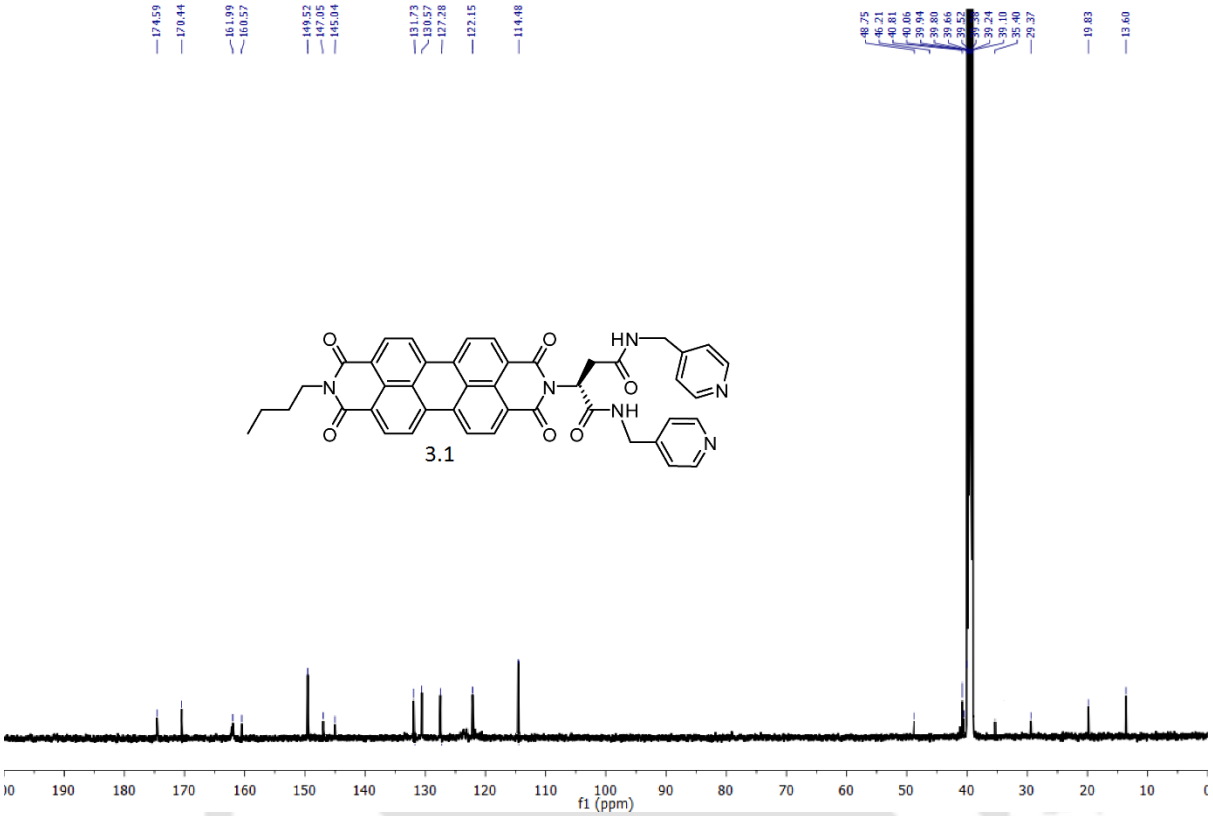

Figure 21 ESI-Ms spectrum of **3.1**.

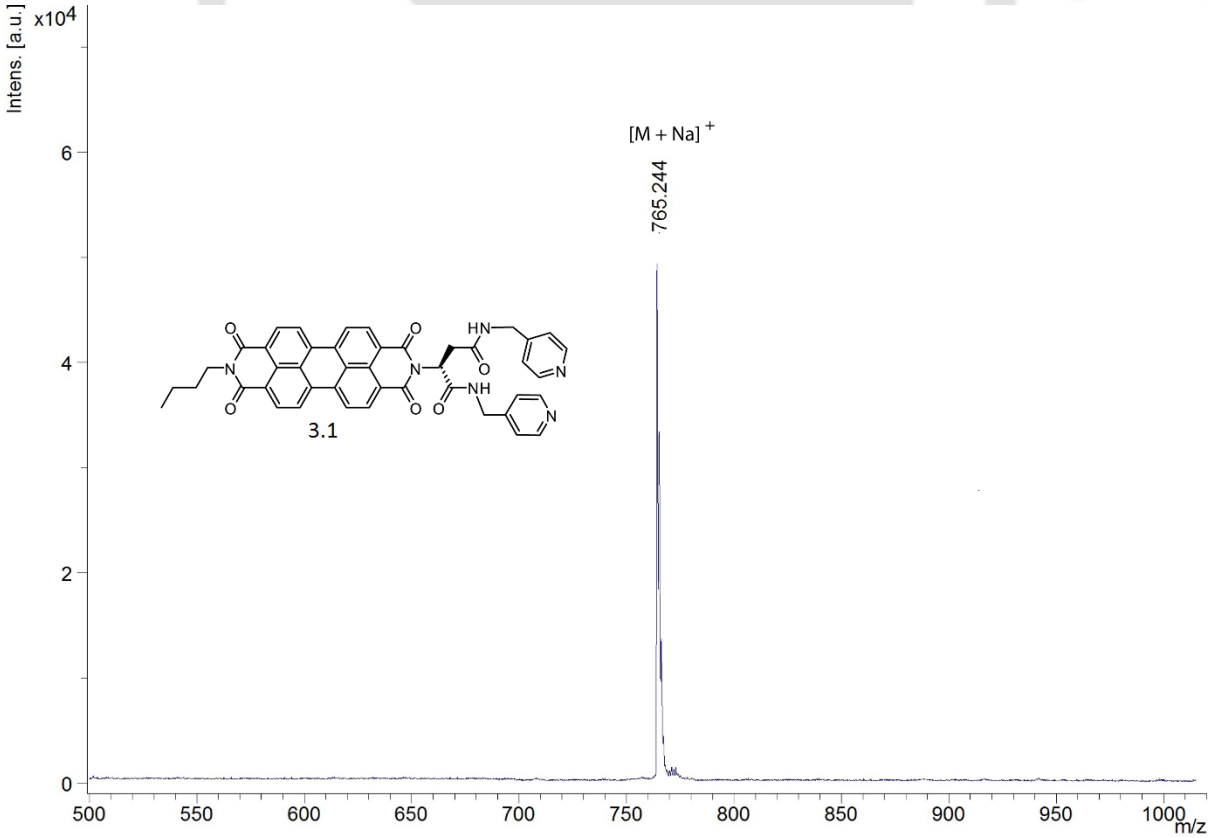

Figure 22 ESI-Ms spectrum of **3.1**.

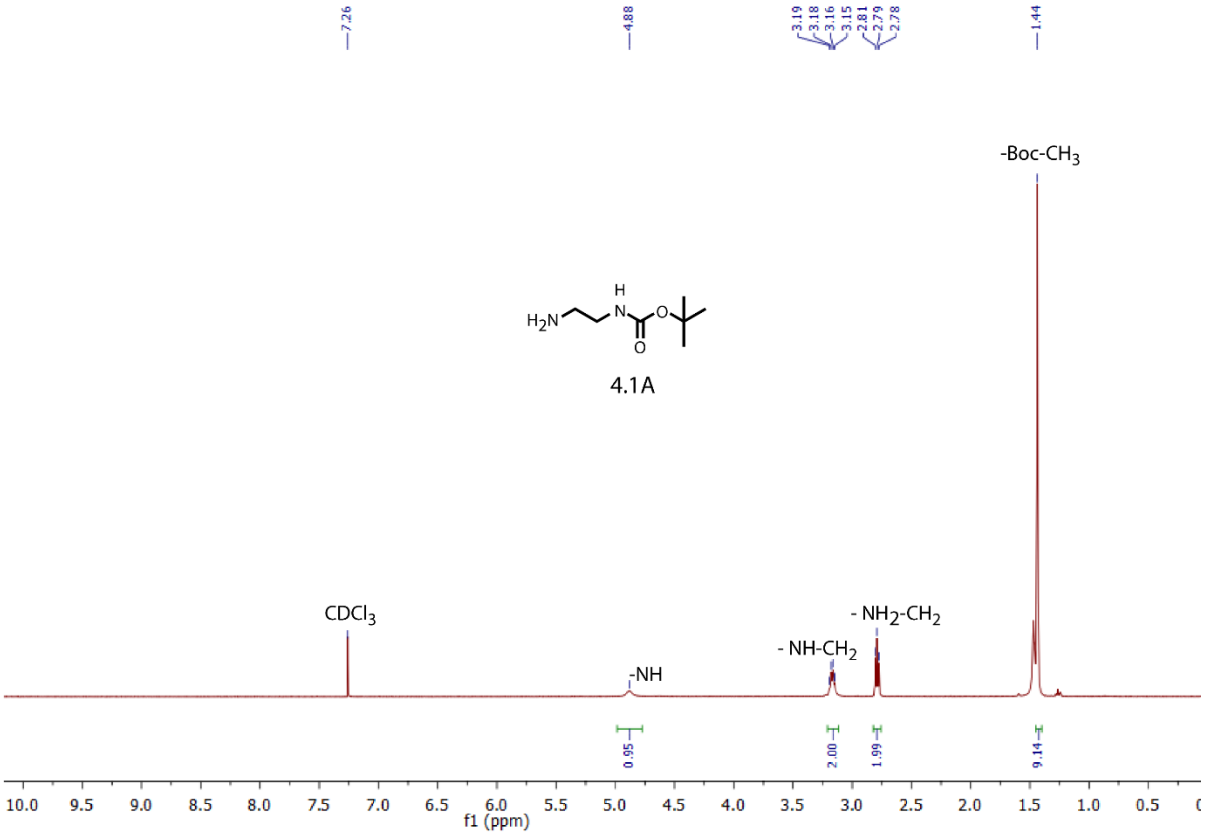

Figure 23 ^{1}H NMR spectrum of **4.1A**.

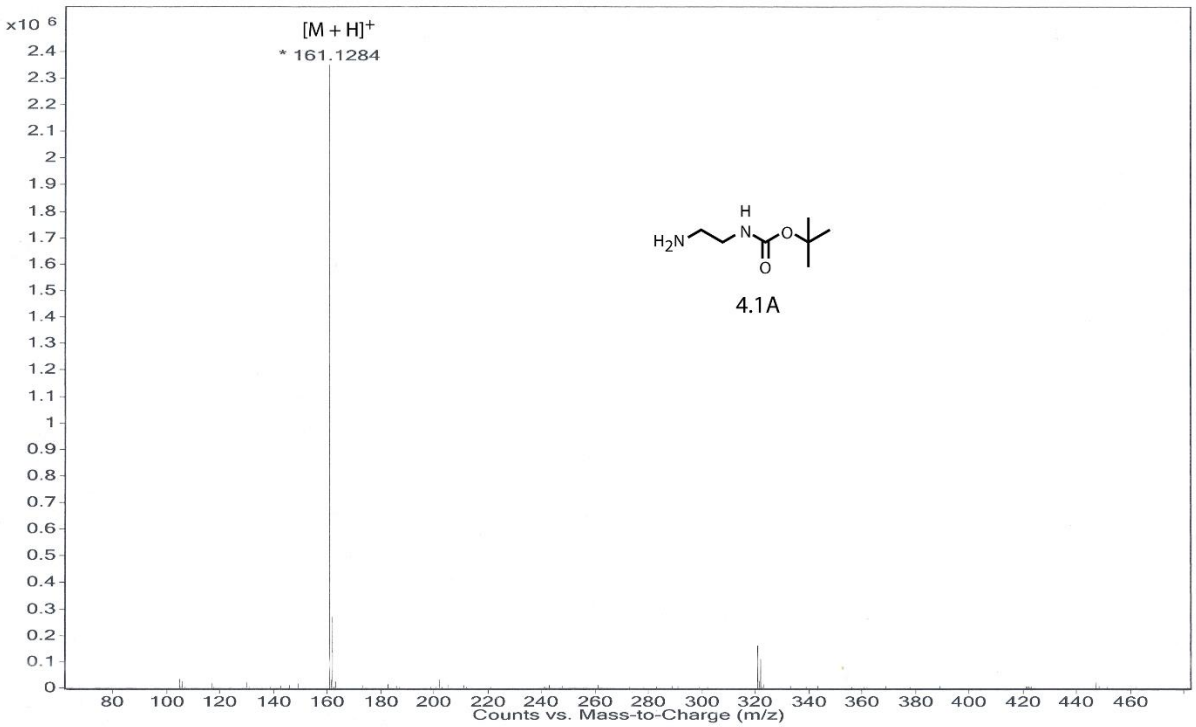

Figure 24 ESI-Ms spectrum of **4.1A**.

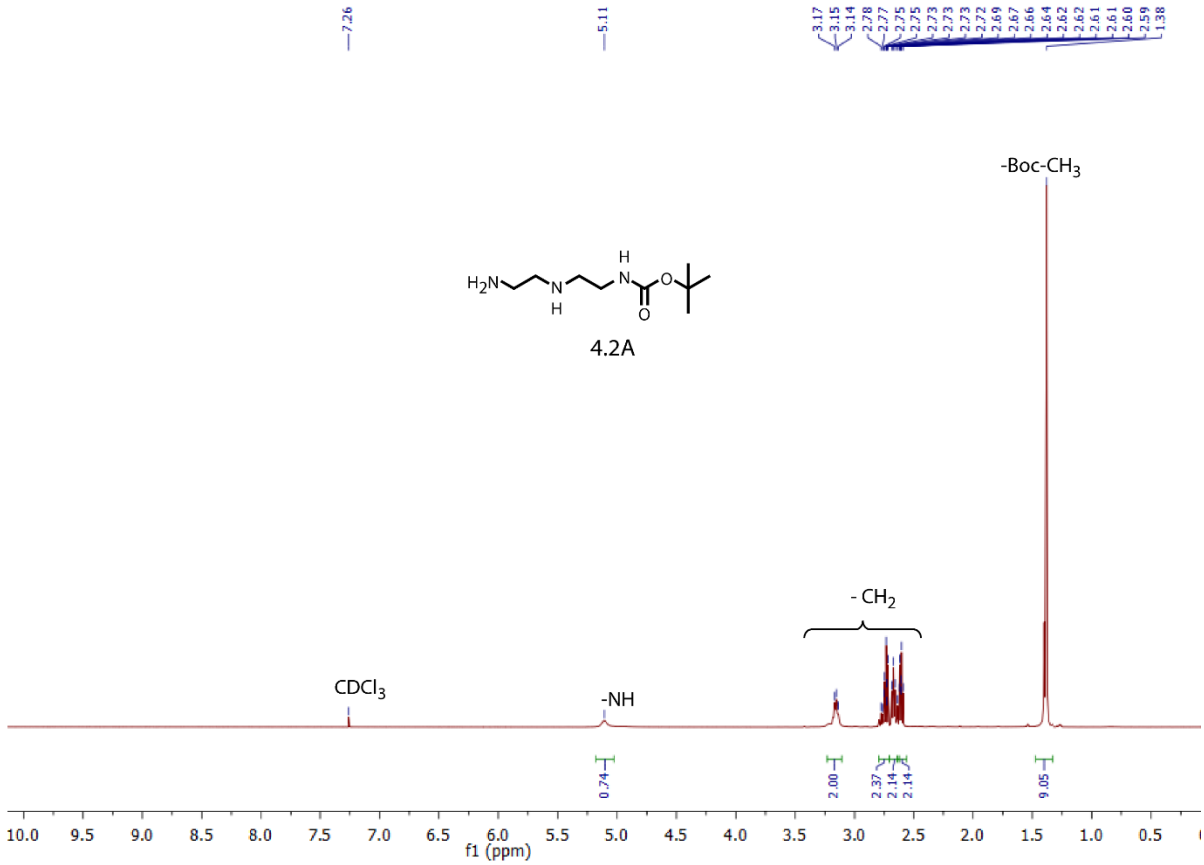

Figure 25 ^{1}H NMR spectrum of **4.2A**.

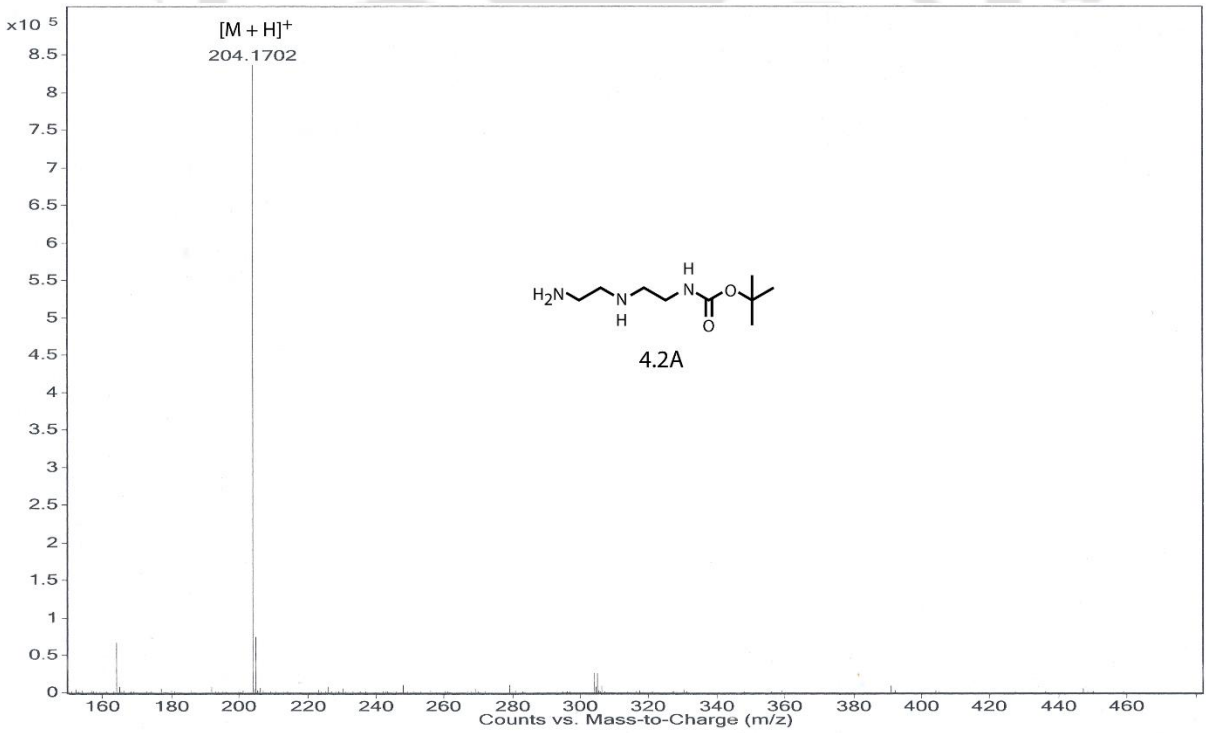

Figure 26 ESI-Ms spectrum of **4.2A**.

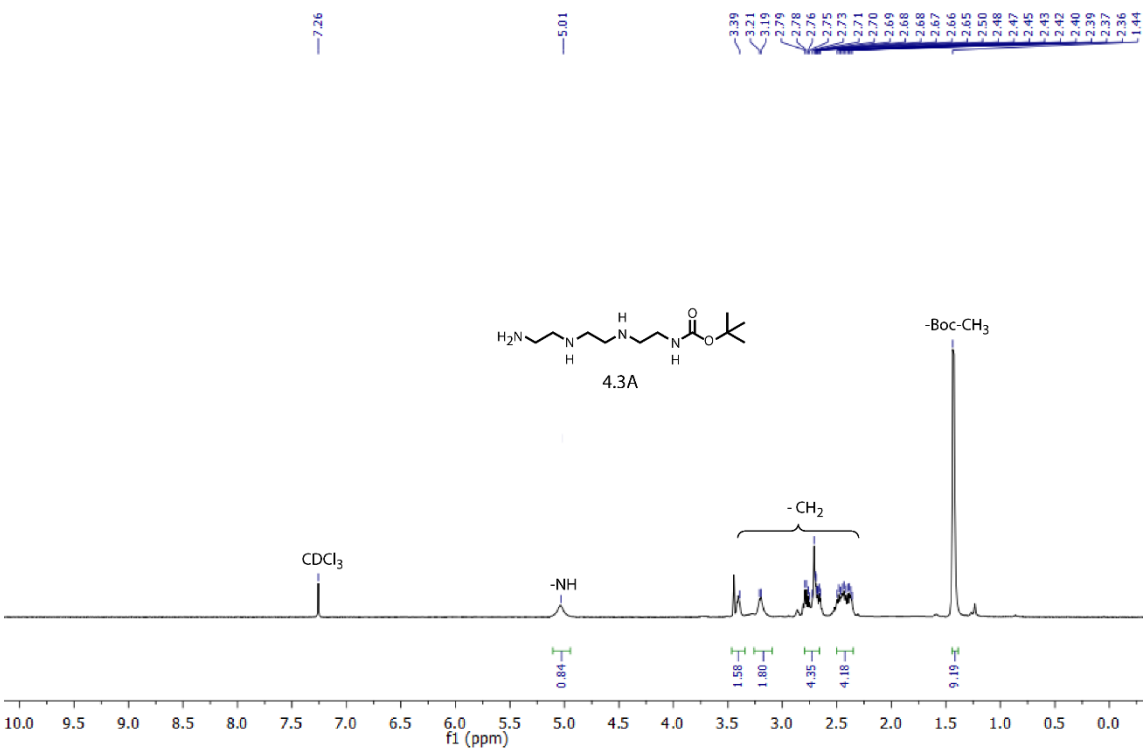

Figure 27 ^{1}H NMR spectrum of **4.3A**.

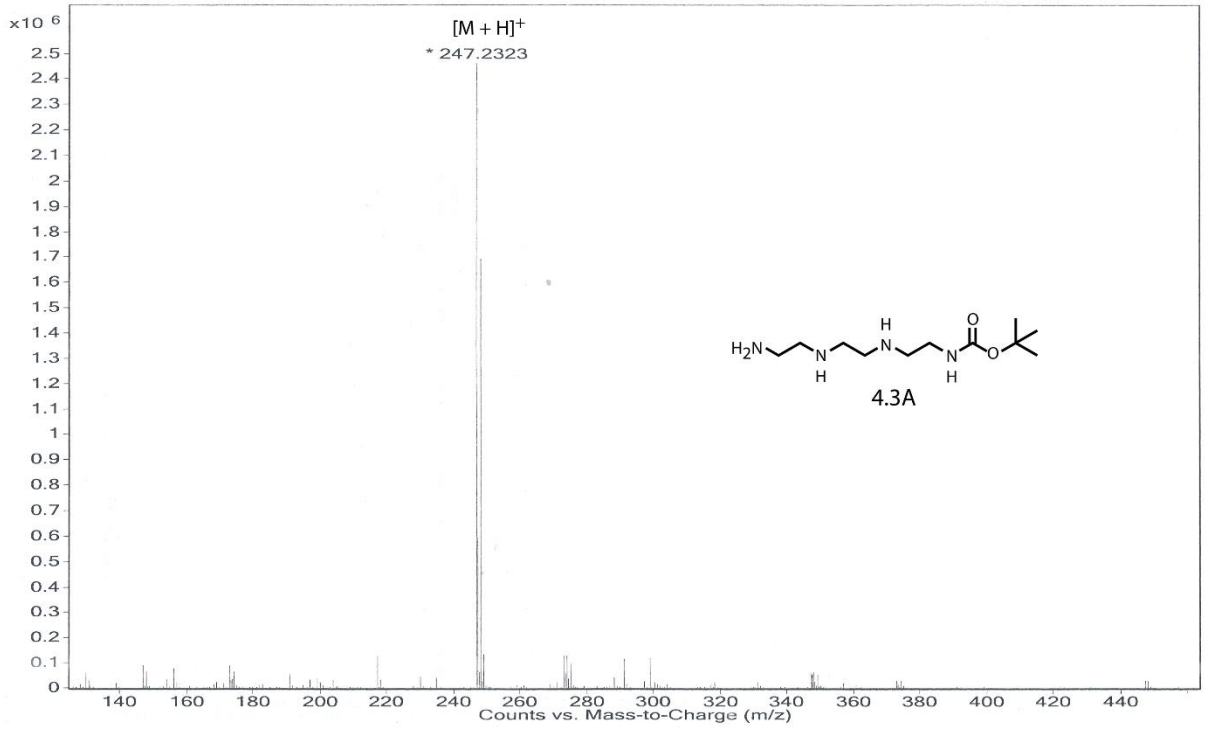

Figure 28 ESI-Ms spectrum of **4.3A**.

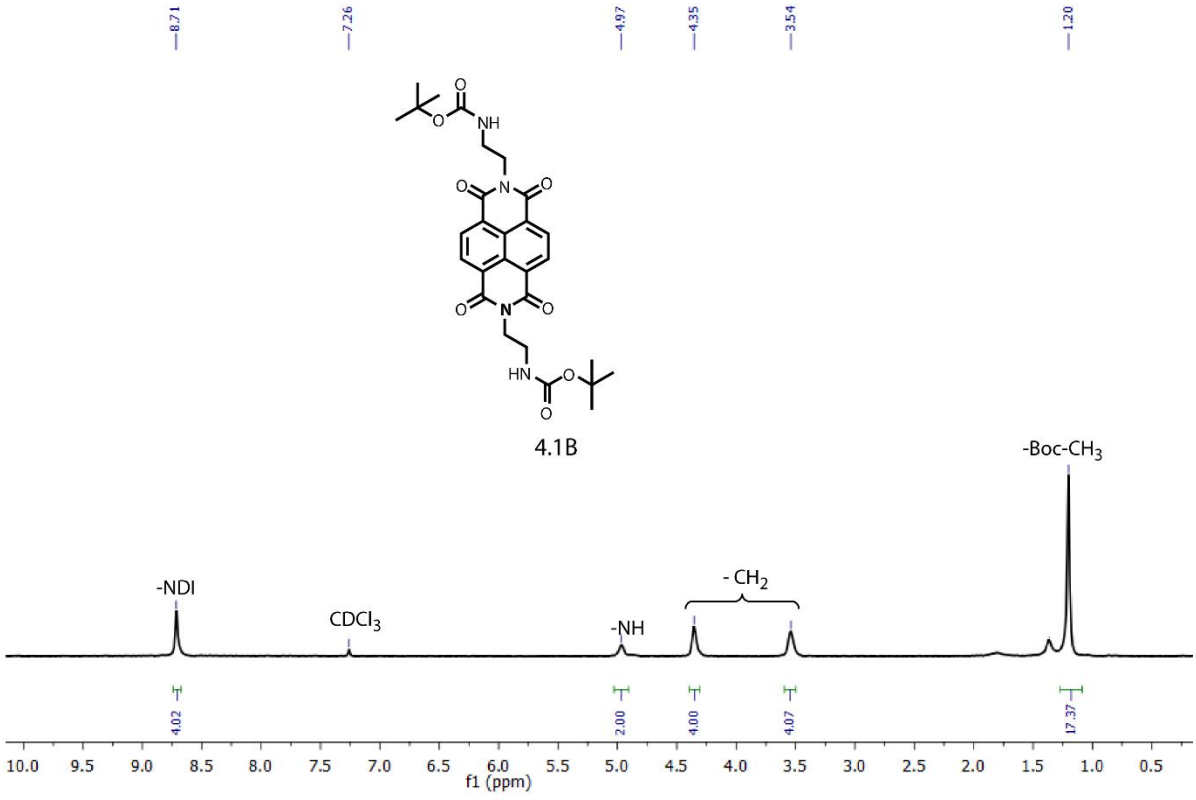

Figure 29 ^{1}H NMR spectrum of **4.1B**.

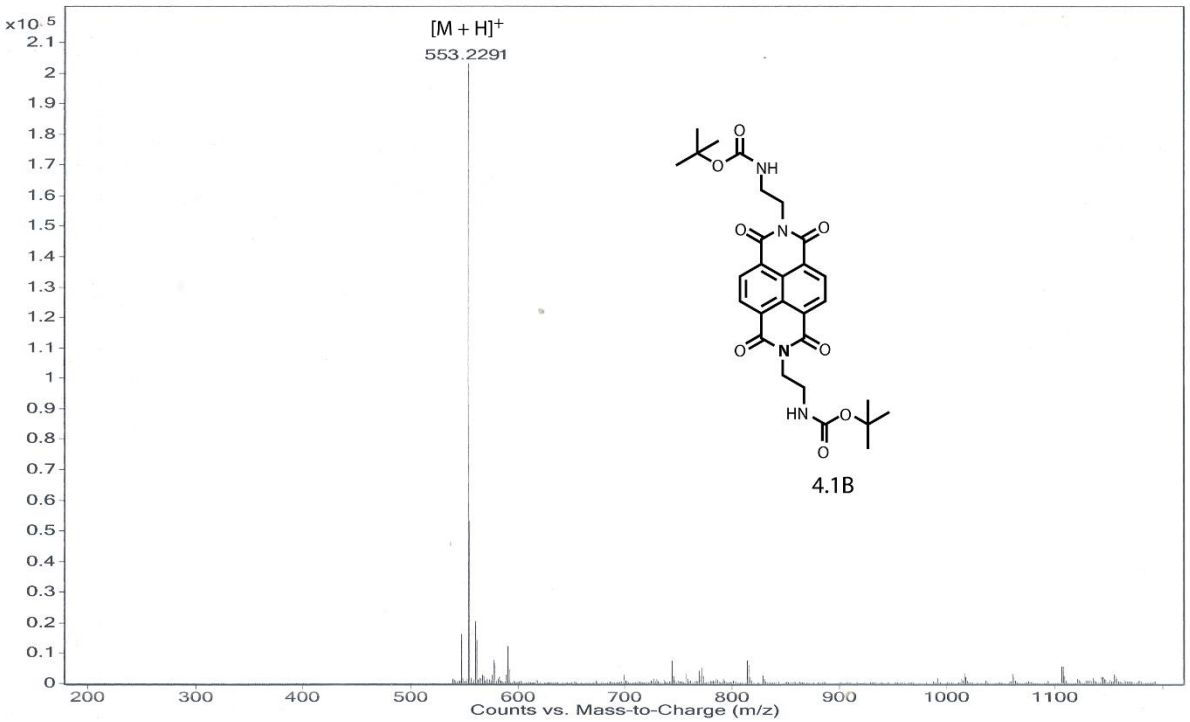

Figure 30 ESI-Ms spectrum of **4.1B**.

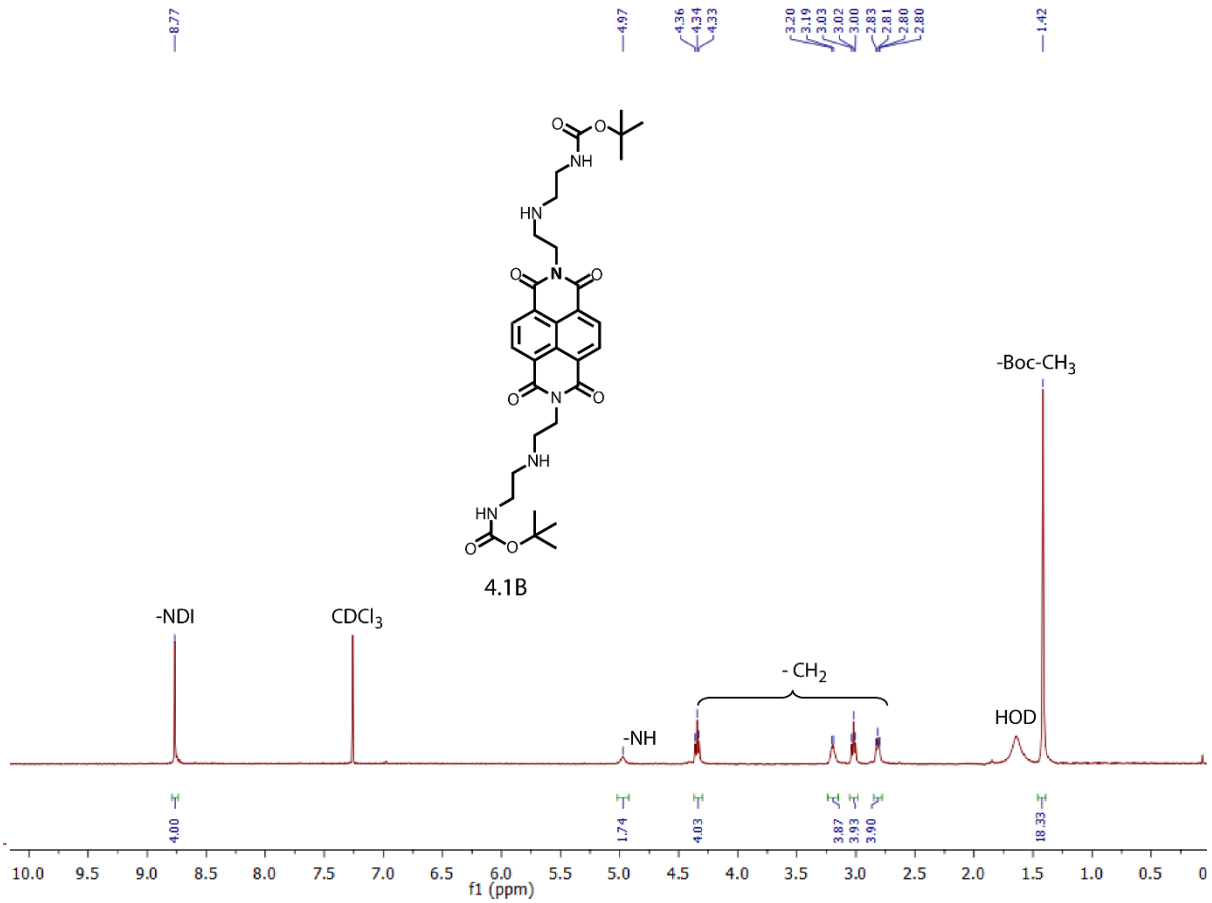

Figure 31 ^{1}H NMR spectrum of **4.2B**.

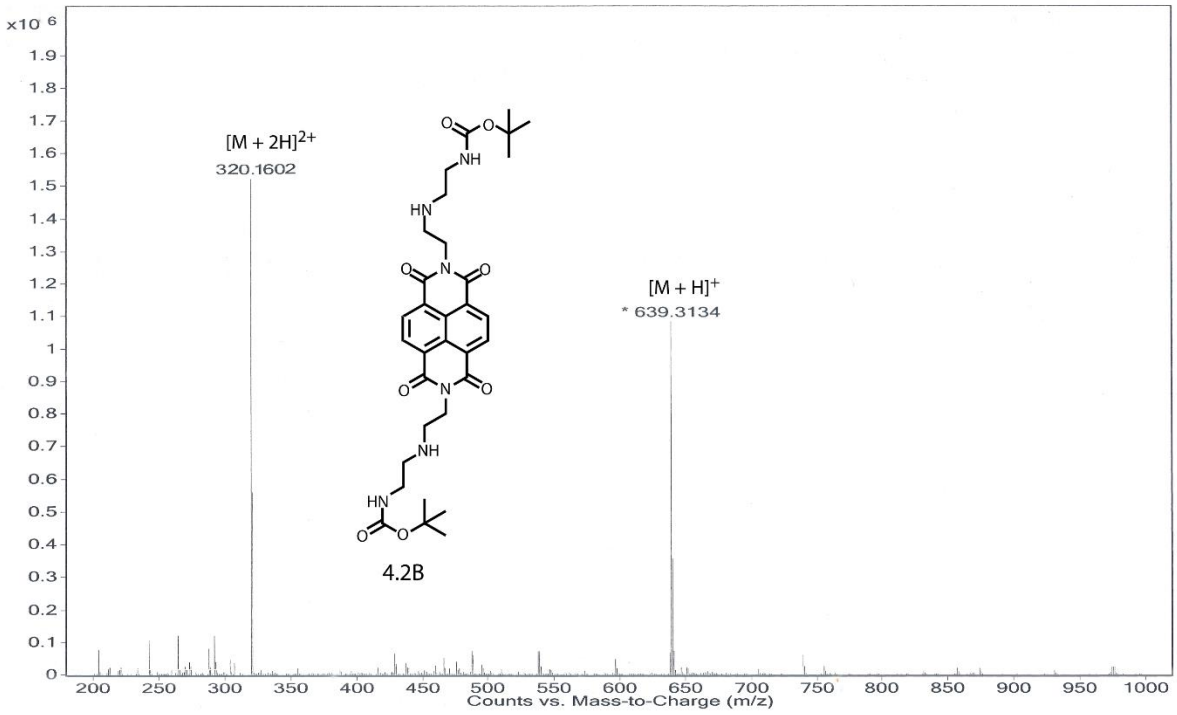

Figure 32 ESI-Ms spectrum of **4.2B**.

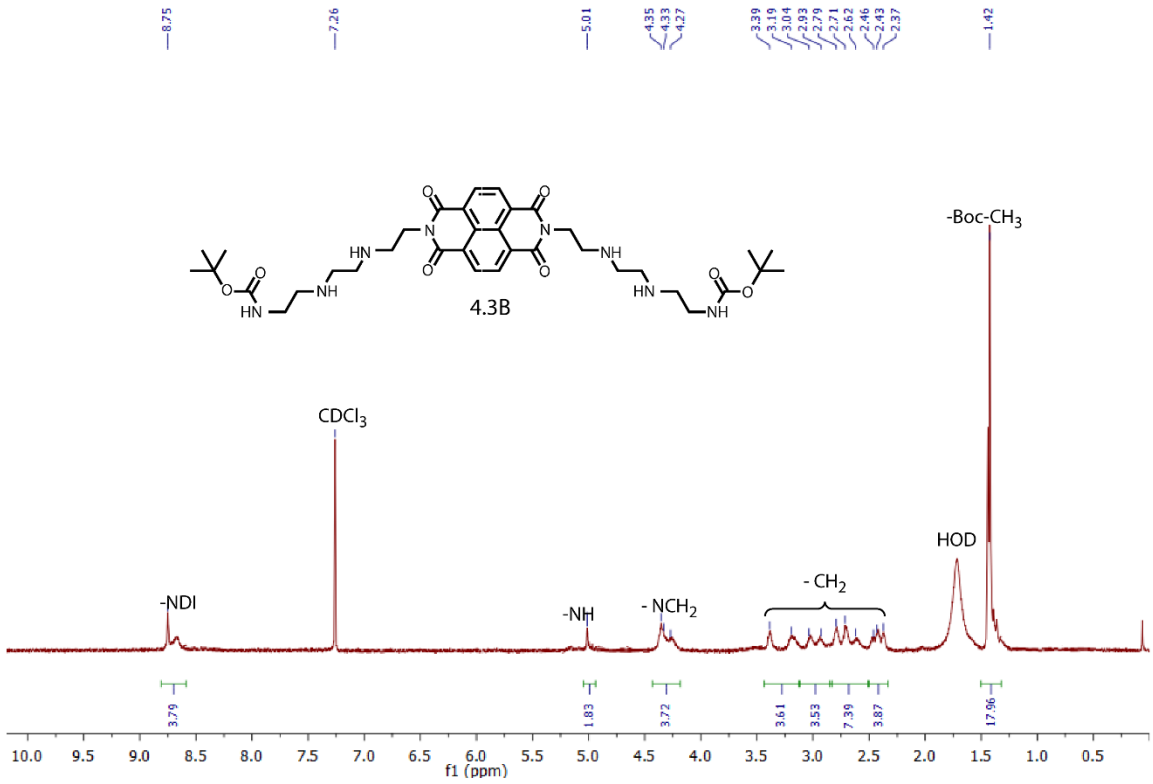

Figure 33 ^{1}H NMR spectrum of **4.3B**.

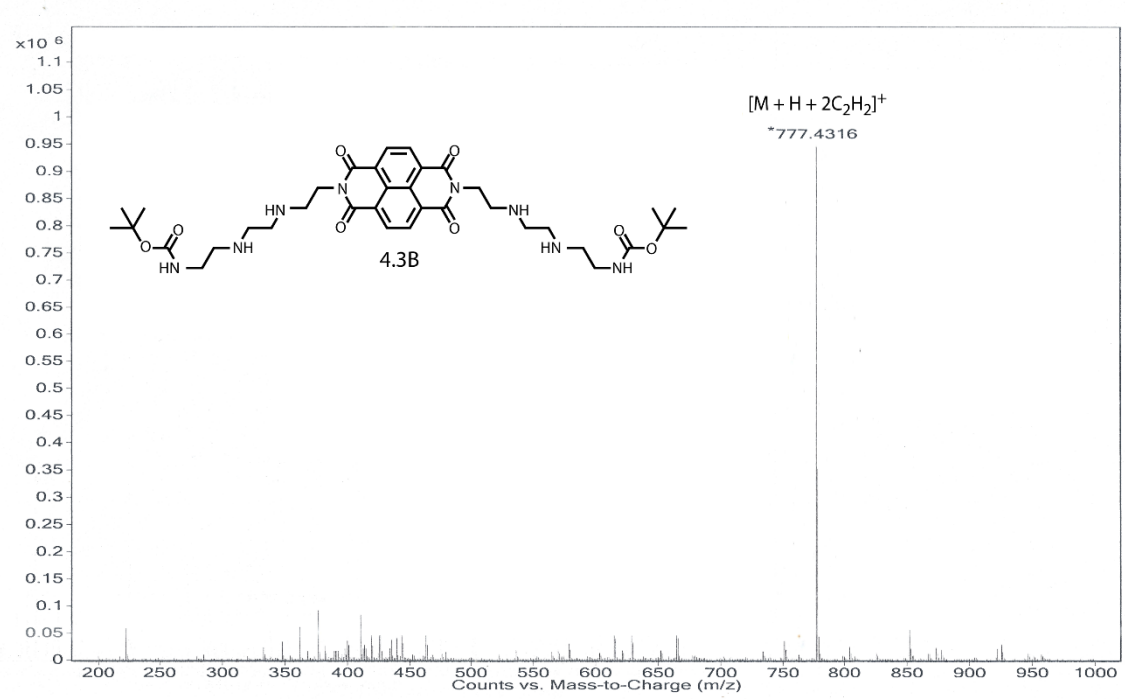

Figure 34 ESI-Ms spectrum of **4.3B**.

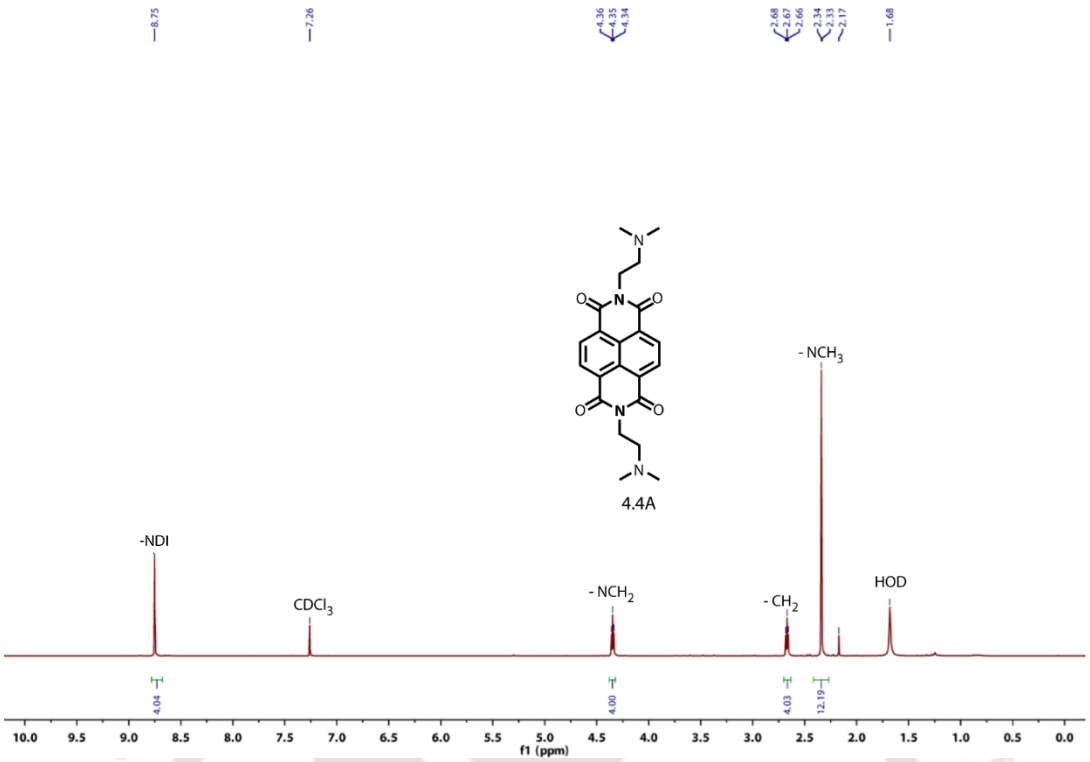

Figure 35 ^{1}H NMR spectrum of **4.4A**.

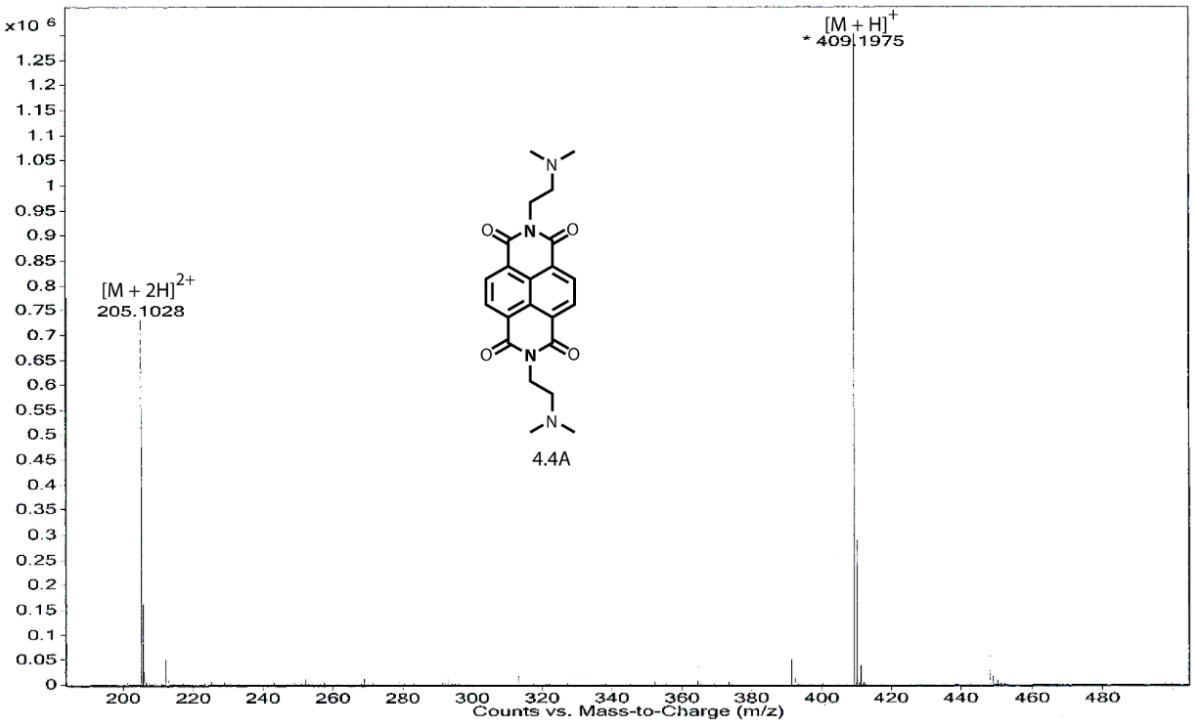

Figure 36 ESI-Ms spectrum of **4.4A**.

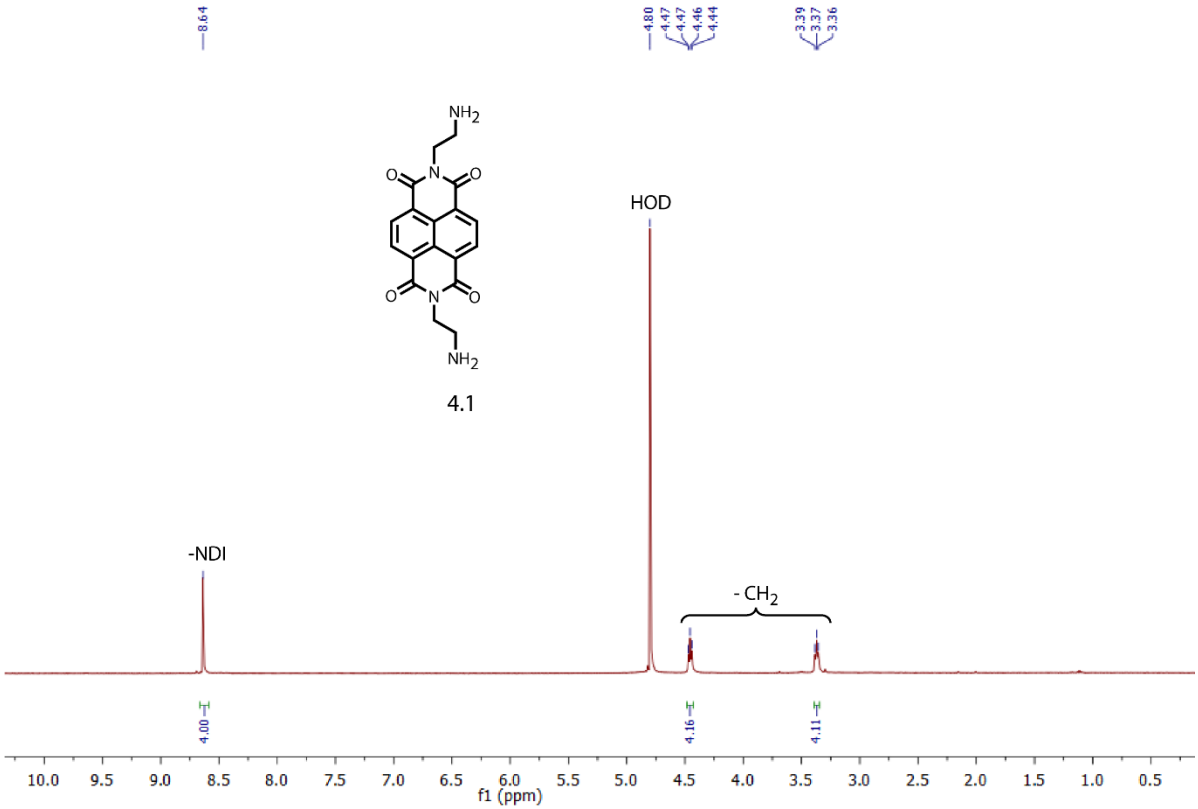

Figure 37 ^{1}H NMR spectrum of **4.1**.

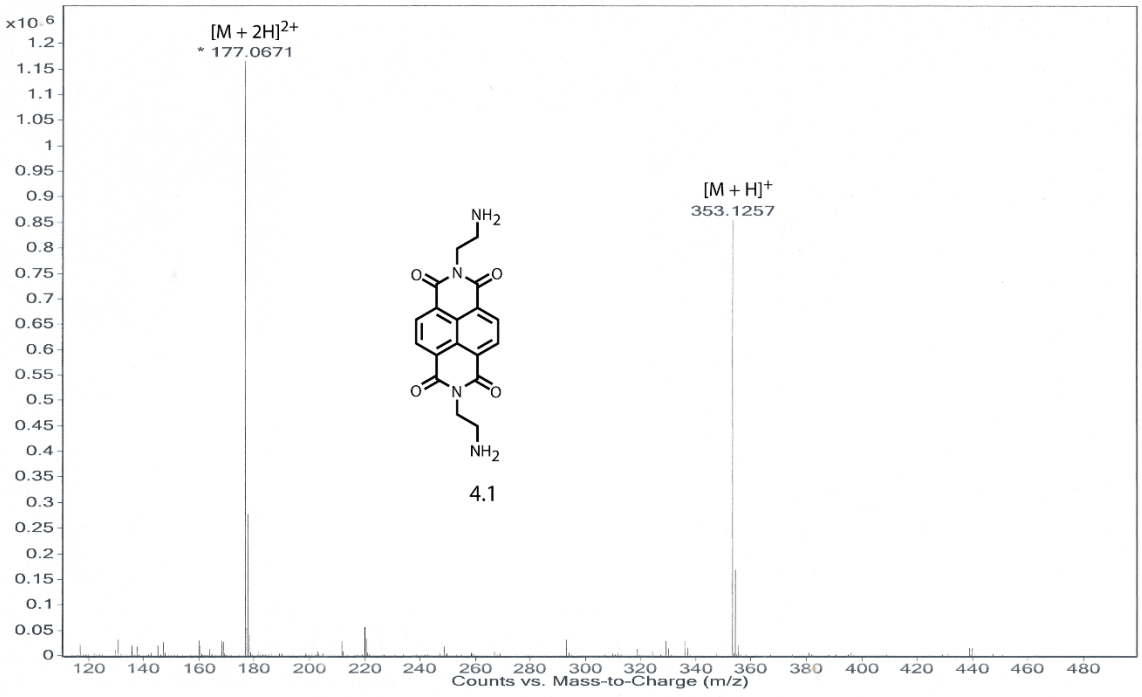

Figure 38 ESI-Ms spectrum of **4.1**.

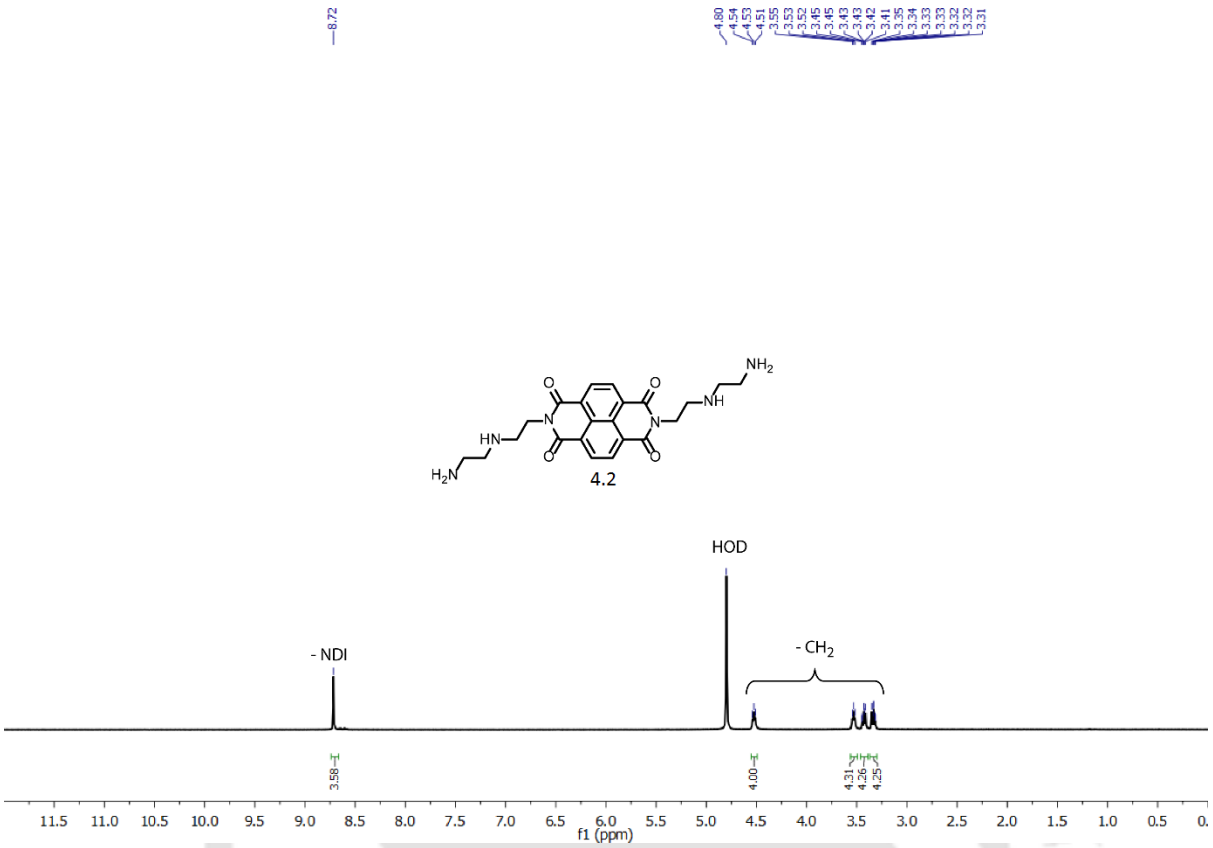

Figure 39 ^{1}H NMR spectrum of **4.2**.

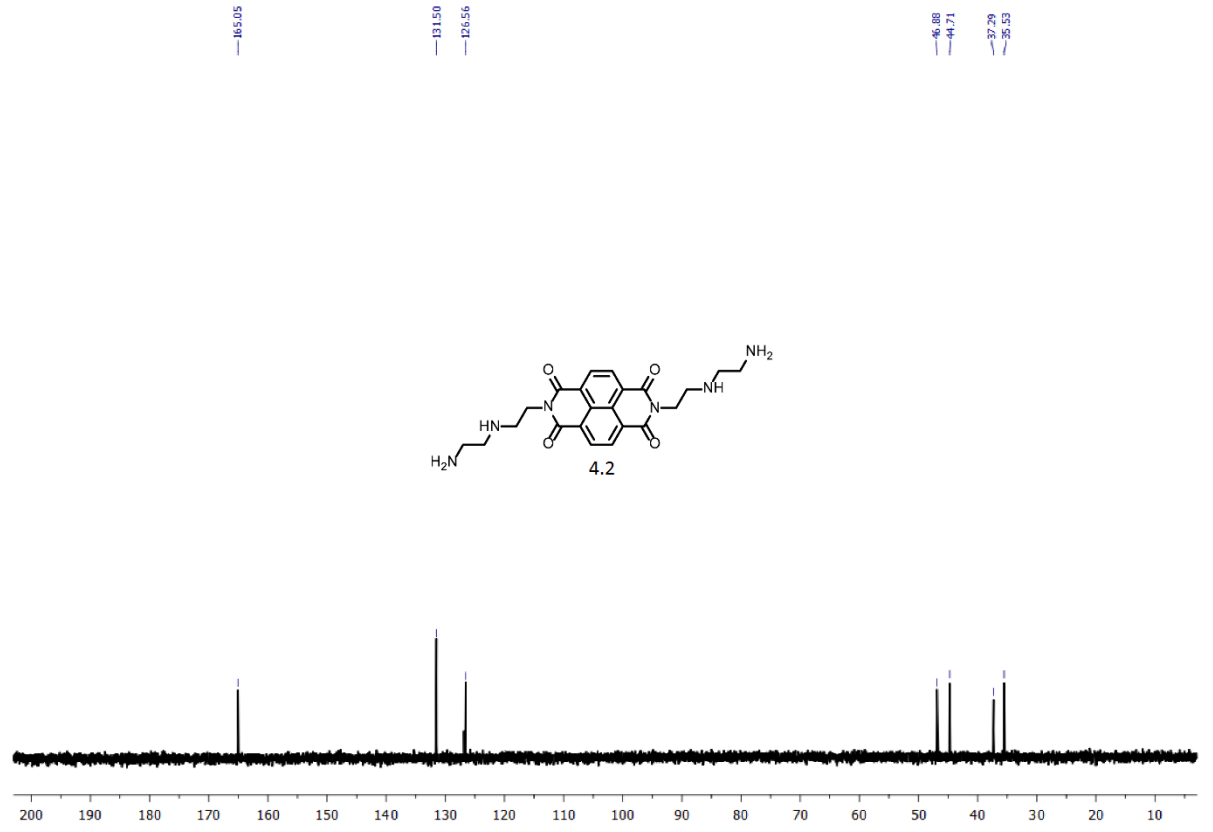

Figure 40 ESI-Ms spectrum of **4.2**.

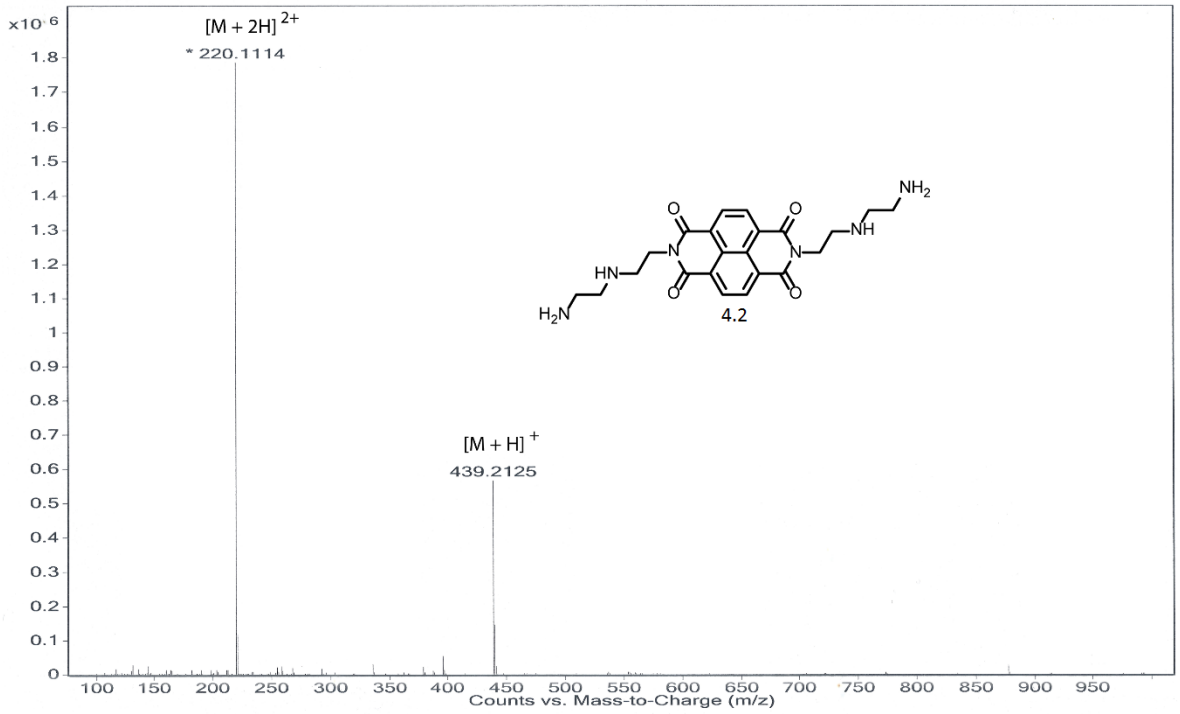

Figure 41 ESI-Ms spectrum of **4.2**.

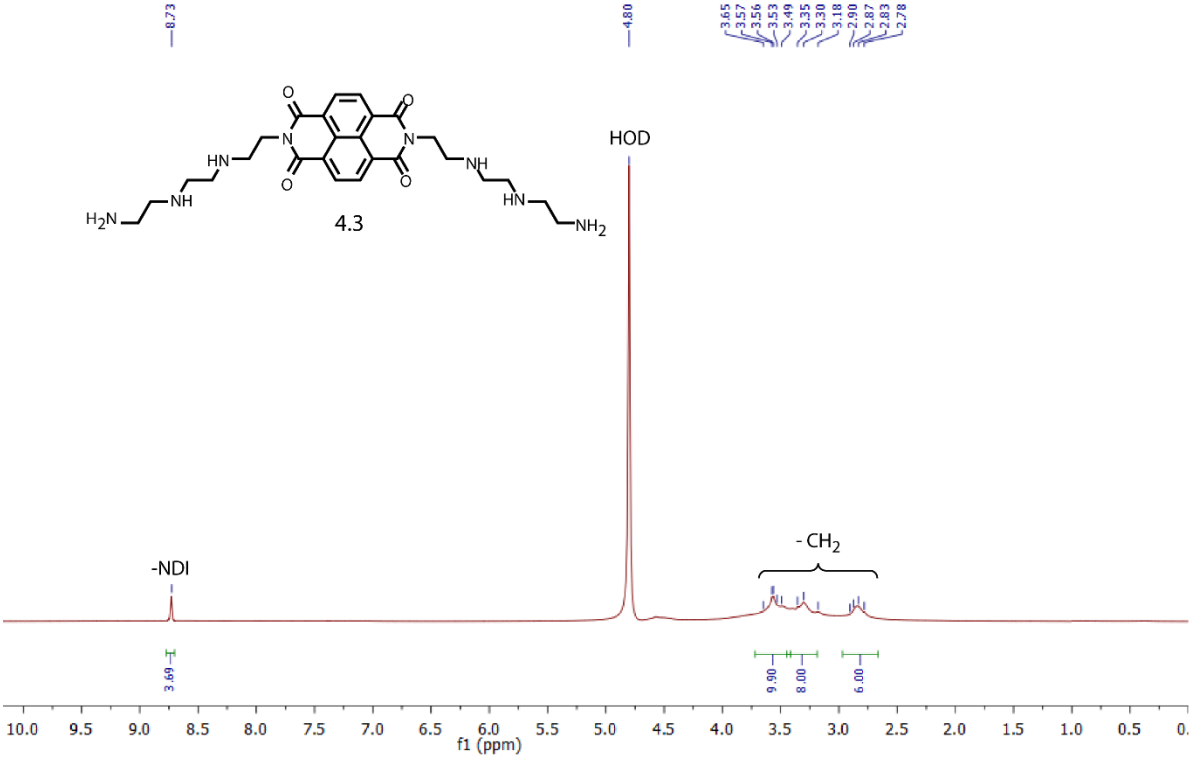

Figure 42 ^{1}H NMR spectrum of **4.3**.

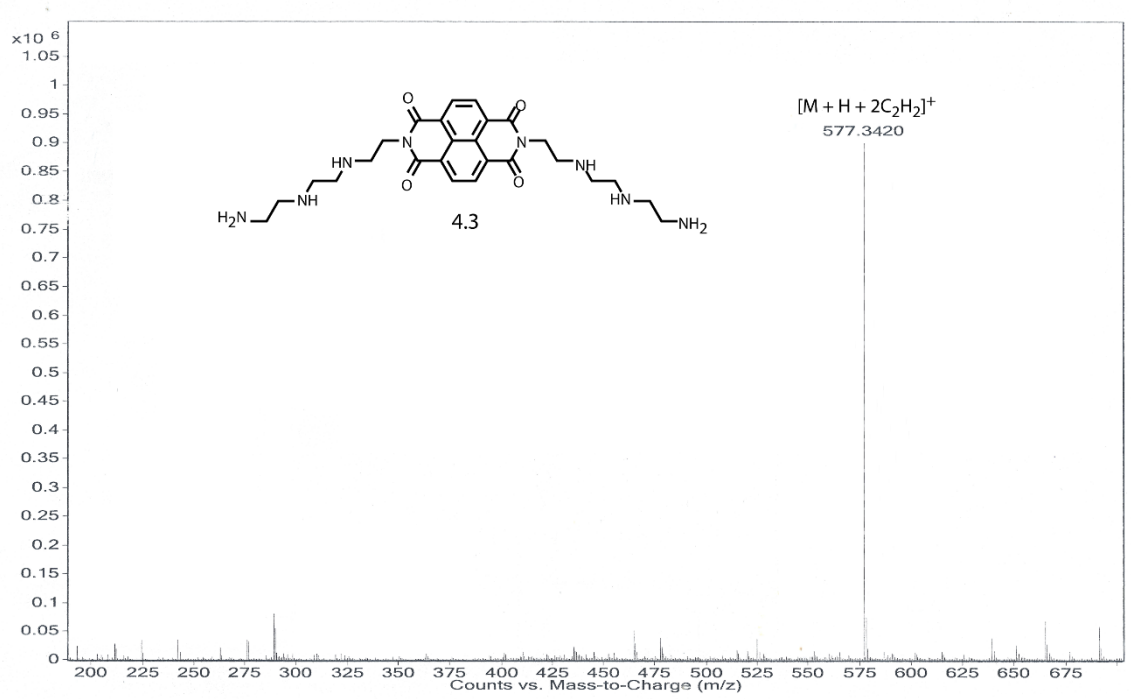

Figure 43 ESI-Ms spectrum of **4.3**.

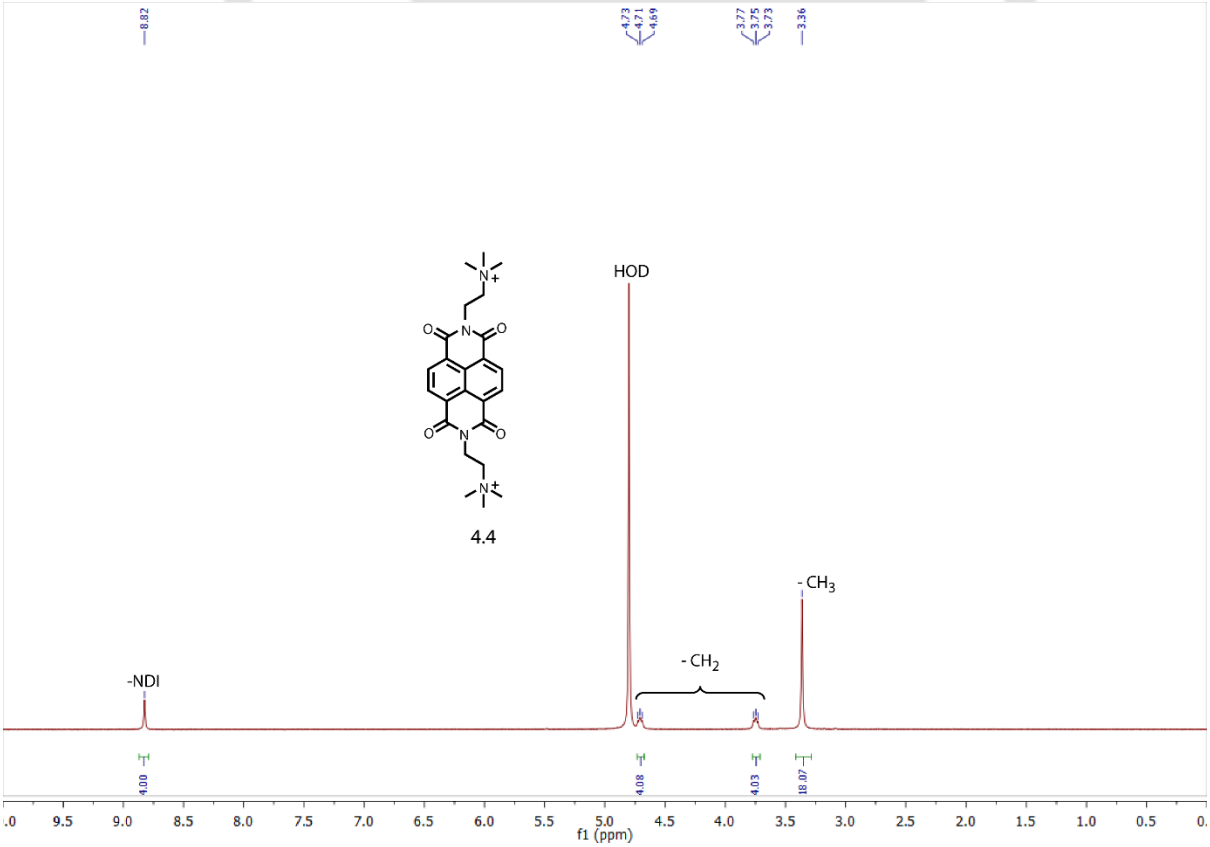

Figure 44 ^{1}H NMR spectrum of **4.4**.

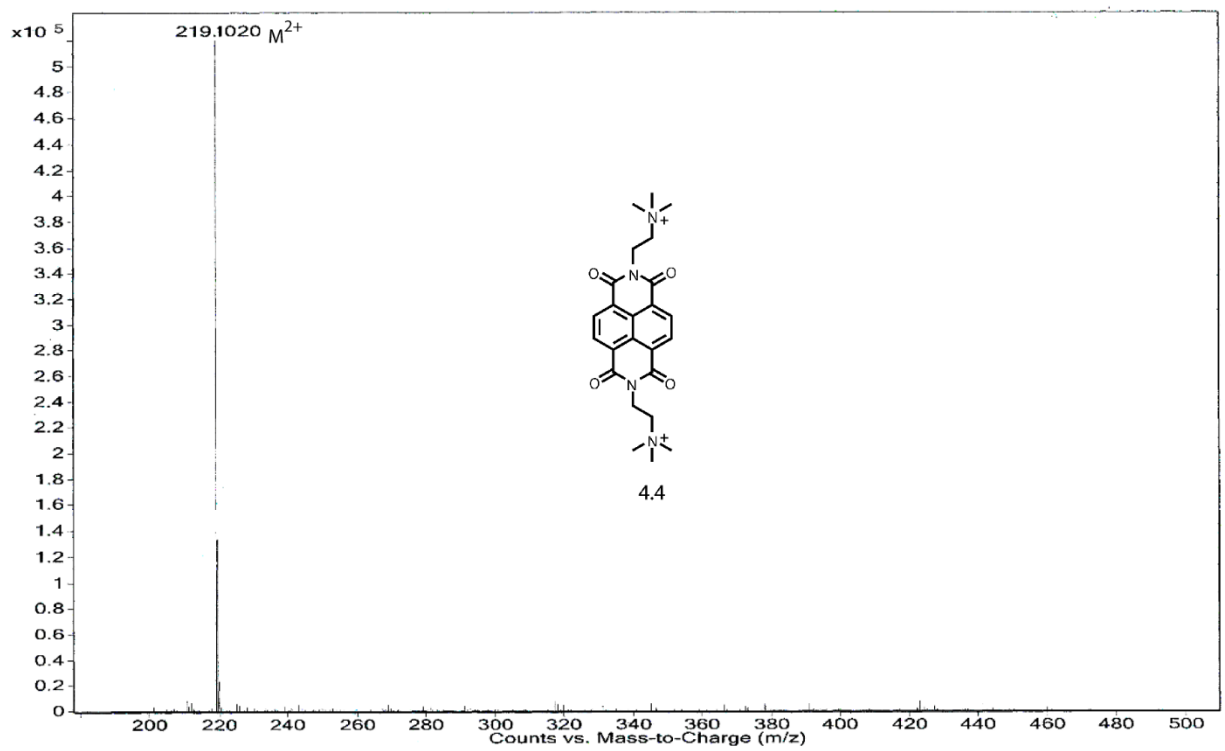

Figure 45 ESI-Ms spectrum of **4.4**.

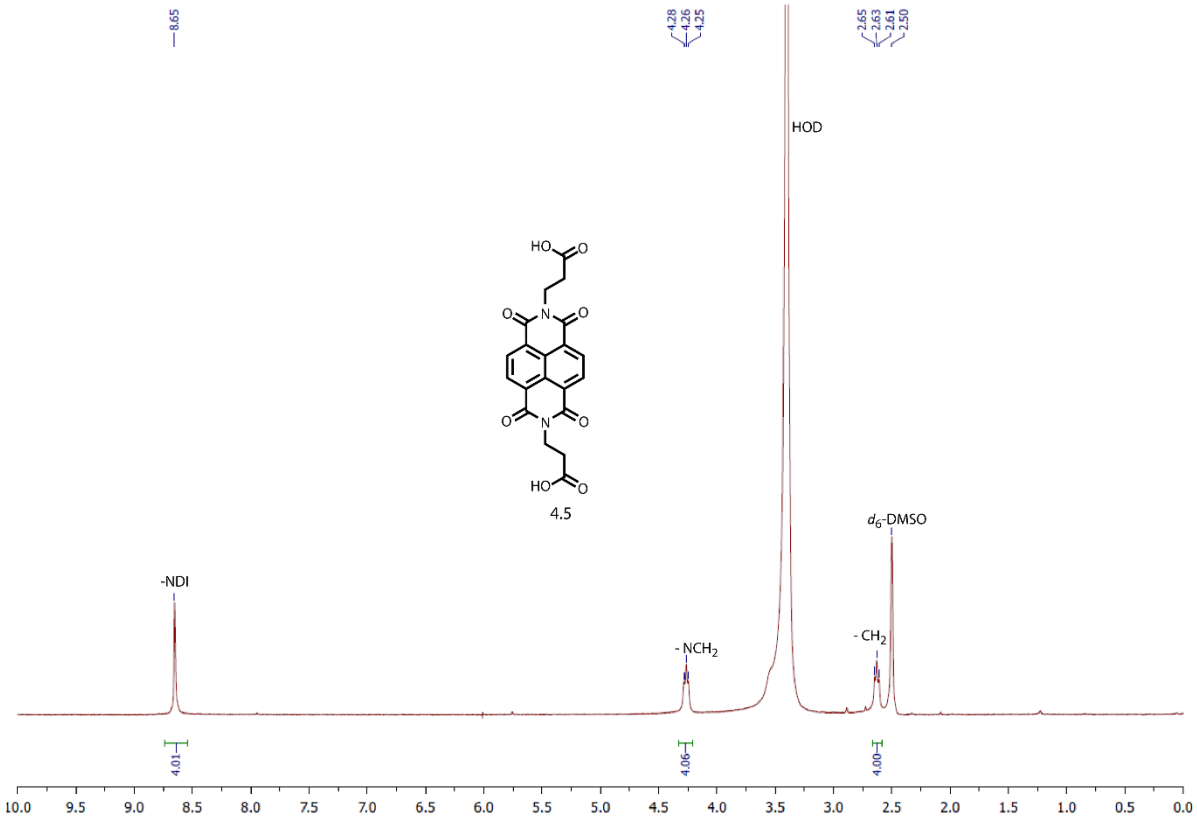

Figure 46 ^{1}H NMR spectrum of **4.5**.

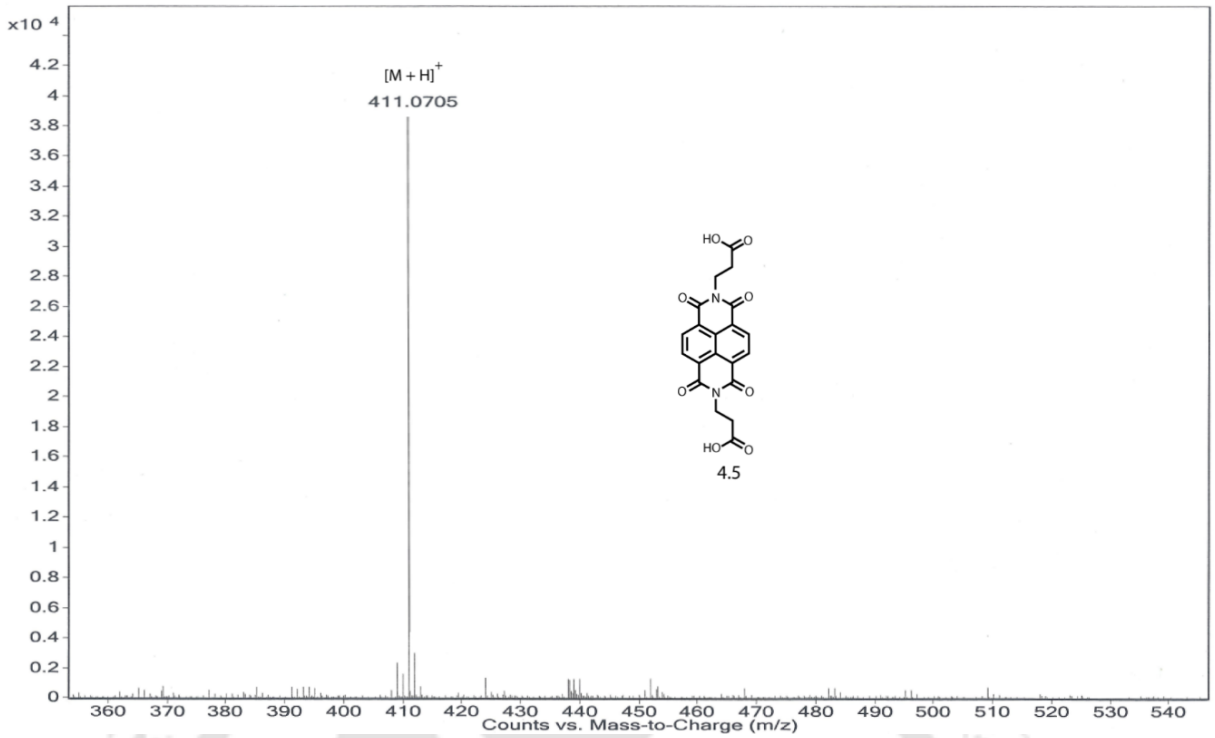

Figure 47 ESI-Ms spectrum of **4.5**.

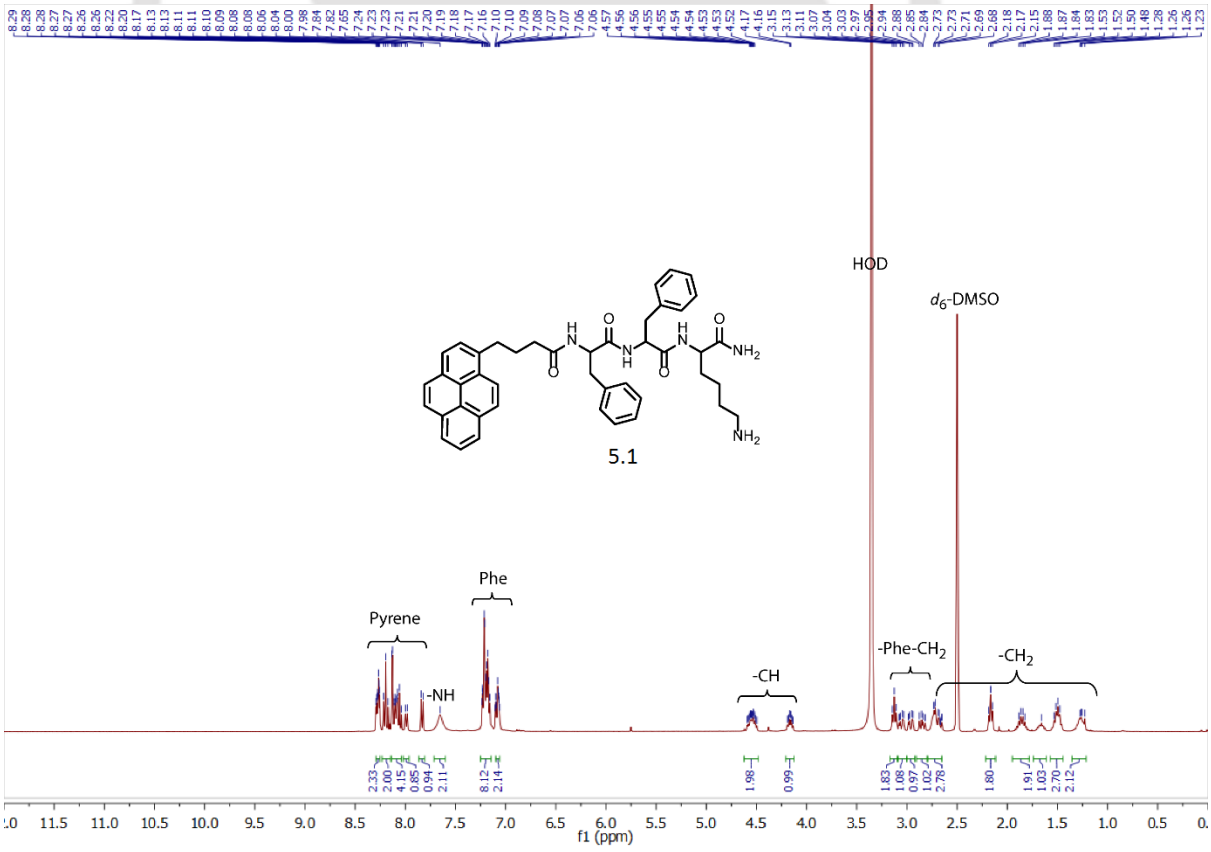

Figure 48 ^{1}H NMR spectrum of **5.1**.

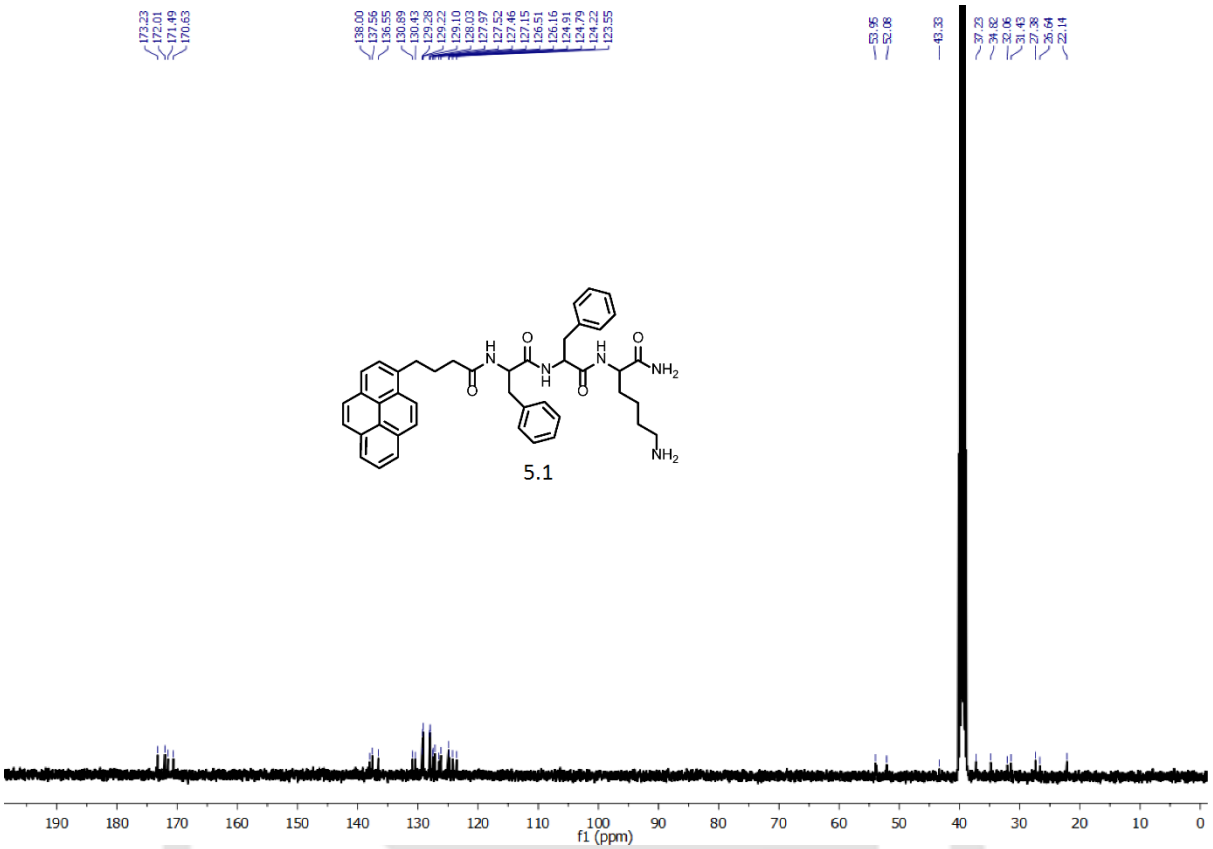

Figure 49 ^{13}C NMR spectrum of **5.1**.

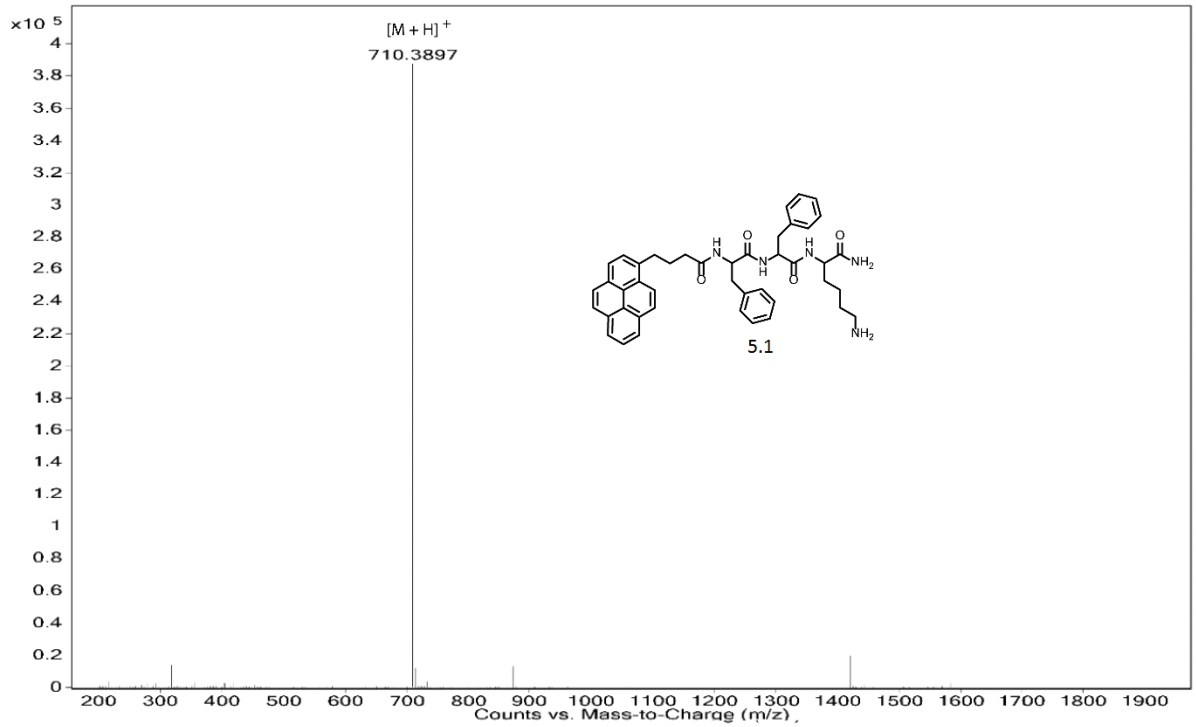

Figure 50 ESI-Ms spectrum of **5.1**.

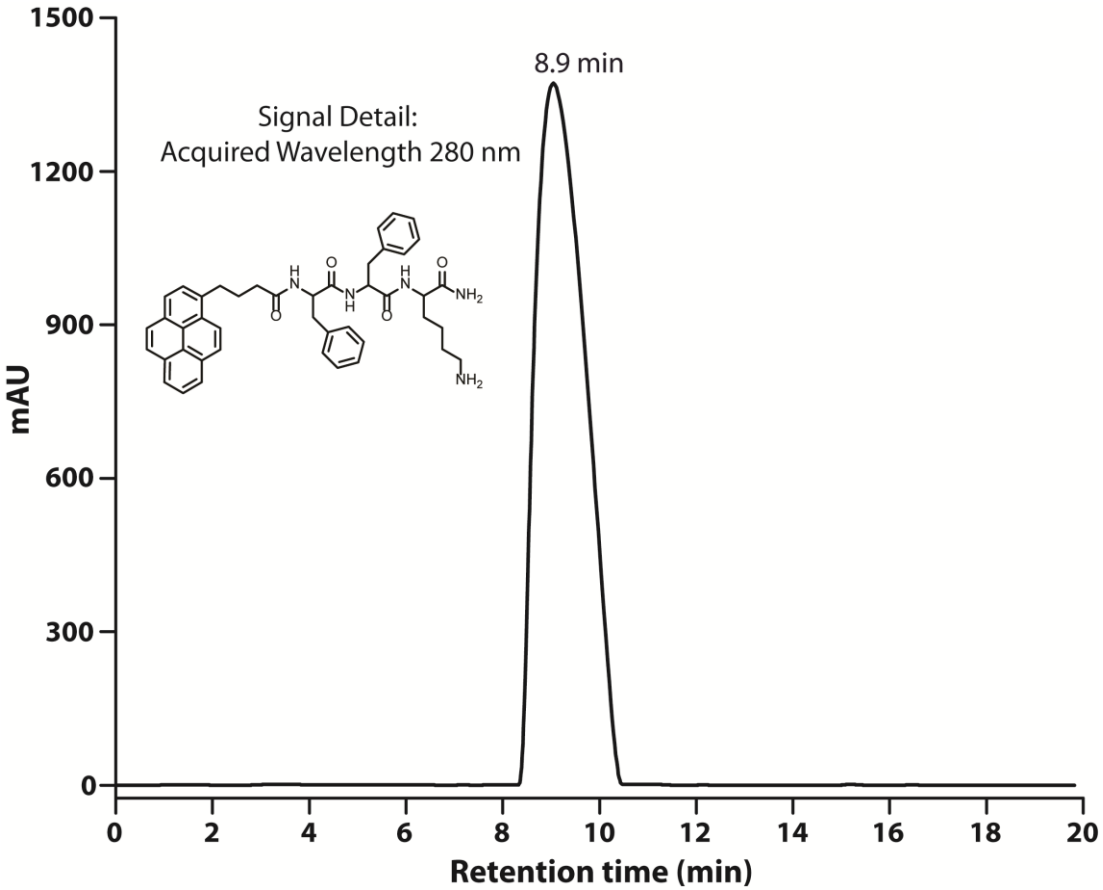

Figure 51 HPLC chromatogram of **5.1**.

References

1. Zhou, X.; Lee, S.; Xu, Z.; Yoon, J. Recent Progress on the Development of Chemosensors for Gases. *Chem. Rev.* **2015**, *115*, 7944−8000.
2. Sun, W.; Guo, S.; Hu, C.; Fan, J.; Peng, X. Recent Development of Chemosensors Based on Cyanine Platforms. *Chem. Rev.* **2016**, *116*, 7768−7817.
3. Chen, X.; Pradhan, T.; Wang, F.; Kim, J.-S.; Yoon, J. Fluorescent Chemosensors Based on Spiroring-Opening of Xanthenes and Related Derivatives. *Chem. Rev.* **2012**, *112*, 1910–1956.
4. Zhou, Y.; Xu, Z.; Yoon, J. Fluorescent and colorimetric chemosensors for detection of nucleotides, FAD and NADH: highlighted research during 2004–2010. *Chem. Soc. Rev.* **2011**, *40*, 2222–2235.
5. Lodeiro, C.; Capelo, J. L.; Mejuto, J. C.; Oliveira, E.; Santos, H. M.; Pedras, B.; Nun˜ez, C. Light and Colour as Analytical Detection Tools: A Journey into the Periodic Table Using Polyamines to Bio-Inspired Systems as Chemosensors. *Chem. Soc. Rev.* **2010**, *39*, 2948–2976.
6. Mancin, F.; Rampazzo, E.; Tecilla, P.; Tonellato, U. Self-Assembled Fluorescent Chemosensors. *Chem. Eur. J.* **2006**, *12*, 1844 – 1854.
7. Thirupathi, P.; Park, J.–Y.; Neupane, L. N.; Kishore, M. Y. L. N.; Lee, K.–H. Pyrene Excimer-Based Peptidyl Chemosensors for the Sensitive Detection of Low Levels of Heparin in 100% Aqueous Solutions and Serum Samples. *ACS Appl. Mater. Interfaces* **2015**, *7*, 14243−14253.
8. Bencini, A.; Berni, E.; Bianchi, A.; Fornasari, P.; Giorgi, C.; Lima, J. C.; Lodeiro, C.; Melo, M. J.; Melo, J. S.; Parola, A. J.; Pina, F.; Pinac, J.; Valtancolia, B. A fluorescent chemosensor for Zn (II). Exciplex formation in solution and the solid state. *Dalton Trans.* **2004,** 2180-2187**.**
9. Wang, L.; Yang, L.; Cao, D. Application of Aggregation-Induced Emission (AIE) Systems in Sensing and Bioimaging. *Current Organic Chemistry* **2014** *18*, DOI: 10.2174/1385272819666140407214006.
10. Hong, Y. Aggregation-induced emission—fluorophores and applications. *Methods Appl. Fluoresc.* **2016**, *4*, 022003.
11. Wu, J.; Kwon, B.; Liu, W.; Anslyn, E. V.; Wang, P.; Kim, J.-S. Chromogenic/Fluorogenic Ensemble Chemosensing Systems. *Chem. Rev.* **2015**, *115*, 7893−7943.
12. Más-Montoya, M.; Janssen, R. A. J. The Effect of H- and J-Aggregation on the Photophysical and Photovoltaic Properties of Small Thiophene–Pyridine–DPP Molecules for Bulk-Heterojunction Solar Cells. *Adv. Funct. Mater.* **2017**, *27*, 1605779.
13. Würthner, F; Kaiser T. E.; Saha-Möller C. R. J-aggregates: from serendipitous discovery to supramolecular engineering of functional dye materials. *Angew. Chem. Int. Ed.* **2011**, *50*, 3376 – 3410.
14. Kumar, S.; Shukla, J.; Kumar, Y.; Mukhopadhyay, P. Electron-poor arylenediimides. *Org. Chem. Front.* **2018**, *5*, 2254–2276.
15. Würthner, F. Perylene bisimide dyes as versatile building blocks for functional supramolecular architectures. *Chem. Commun.* **2004**, *14,* 1564−1579.
16. Rybtchinski, B.; Sinks, L. E.; Wasielewski, M. R. Combining Light-Harvesting and Charge Separation in a Self-Assembled Artificial Photosynthetic System Based on Perylenediimide Chromophores. *J. Am. Chem. Soc.* **2004**, *126*, 12268−12269.
17. Zhang, X.; Rehm, S.; Safont-Sempere, M. M.; Würthner, F. Vesicular perylene dye nanocapsules as supramolecular fluorescent pH sensor systems. *Nat. Chem.* **2009**, *1*, 623−629.
18. Wasielewski, M. R. Self-Assembly Strategies for Integrating Light Photosynthetic Systems. *Acc. Chem. Res.* **2009**, *42*, 1910−1921.

19. Eakins, G. L.; Gallaher, J. K.; Keyzers, R. A.; Falber, A.; Webb, J. E. A.; Laos, A.; Tidhar, Y.; Weissman, H.; Rybtchinski, B.; Thordarson, P.; Hodgkiss, J. M. Thermodynamic Factors Impacting the Peptide-Driven Self-Assembly of Perylene Diimide Nanofibers. *J. Phys. Chem. B* **2014**, *118*, 8642−8651.
20. Krieg, E.; Weissman, H.; Shimoni, E.; Ustinov, A. B. O.; Rybtchinski, B. *J. Am. Chem. Soc.* **2014**, *136*, 9443−9452.
21. Krieg, E.; Bastings, M. M. C.; Besenius, P.; Rybtchinski, B. Supramolecular Polymers in Aqueous Media. *Chem. Rev.* **2016**, *116*, 2414−2477.
22. Anthony, J. E.; Facchetti, A.; Heeney, M.; Marder, S. R.; Zhan, X. n-Type Organic Semiconductors in Organic Electronics. *Adv. Mater.* **2010**, *22*, 3876−3892.
23. Zhan, X.; Facchetti, A.; Barlow, S.; Marks, T. J.; Ratner, M. A.; Wasielewski, M. R.; Marder, S. R. Rylene and Related Diimides for Organic Electronics. *Adv. Mater.* **2011**, *23*, 268−284.
24. Facchetti, A. π-Conjugated Polymers for Organic Electronics and Photovoltaic Cell Applications. *Chem. Mater.* **2011**, *23*, 733−758.
25. Huang, C.; Barlow, S.; Marder, S. R. Perylene-3,4,9,10-Tetracarboxylic Acid Diimides: Synthesis, Physical Properties, and Use in Organic Electronics. *J. Org. Chem.* **2011**, *76*, 2386−2407.
26. Kobaisi, M. A.; Bhosale, S. V.; Latham, K.; Raynor, A. M.; Bhosale, S. V. Functional Naphthalene Diimides: Synthesis, Properties, and Applications. *Chem. Rev.* **2016**, *116*, 11685-11796.
27. Suraru, S.-L.; Wurthner, F. Strategies for the Synthesis of Functional Naphthalene Diimides. *Angew. Chem. Int. Ed.* **2014**, *53*, 7428-7448.
28. Szumilo, M. M.; Gann, E. H.; McNeill, C. R.; Lemaur, V.; Oliver, Y.; Thomsen, L.; Vaynzof, Y., Sommer, M.; Sirringhaus, H. Structure Influence on Charge Transport in Naphthalenediimide–Thiophene Copolymers. *Chem. Mater.* **2014**, *26*, 6796-6804.
29. Wurthner, F.; Saha-Moller, C. R.; Fimmel, B.; Ogi, S.; Leowanawat, P.; Schmidt, D. Perylene Bisimide Dye Assemblies as Archetype Functional Supramolecular Materials. *Chem. Rev.* **2016**, *116*, 962-1052.
30. Li, C.; Wonneberger, H. Perylene Imides for Organic Photovoltaics: Yesterday, Today, and Tomorrow. *Adv. Mater.* **2012**, *24*, 613-636.
31. Ghule, N. V.; La, D. D.; Bhosale, R. S.; Kobaisi, M. A.; Raynor, A. M.; Bhosale, S. V.; Bhosale, S. V.; Effect of Amide Hydrogen Bonding Interaction on Supramolecular Self-Assembly of Naphthalene Diimide Amphiphiles with Aggregation Induced Emission. *Chemistry Open* **2016**, *5*, 157 – 163.
32. Zollinger, H. Color chemistry: syntheses, properties, and applications of organic dyes and pigments. John Wiley & Sons; 2003.
33. Herbst, W.; Hunger K. Industrial Organic Pigments, Production, Properties, Applications 2nd.
34. Langhals H. Cyclic carboxylic imide structures as structure elements of high stability. Novel developments in perylene dye chemistry. H*eterocycles* **1995**, *1,477*-500.
35. Schlettwein, D.; Wöhrle, D.; Karmann, E.; Melville, U.; Novel Synthetic Routes to Carbon-Nitrogen Thin Films. *Chem. Mater.* **1994**, *6*, 3–6.
36. Katz, H. E.; Bao, Z.; Gilat, S. L. Synthetic Chemistry for Ultrapure, Processable, and High-Mobility Organic Transistor Semiconductors. *Acc. Chem. Res.* **2001**, *34*, 359–369.
37. Dimitrakopoulos, C. D.; Malenfant, P. R. L. Organic Thin Film Transistors for Large Area Electronics. *Adv. Mater.* **2002**, *14*, 99–117.
38. Gvishi, R.; Reisfeld, R. Spectroscopy and laser action of the "red perylimide dye" in various solvents. *Chem. Phys. Lett.* **1993**, *213*, 338–344.

39. Dwivedi, A. K.; Pandeeswar, M.; Govindaraju, T. Assembly modulation of PDI derivative as a supramolecular fluorescence switching probe for detection of cationic surfactant and metal ions in aqueous media. *ACS Appl. Mater. Interfaces* **2014**, *6*, 21369–21379.
40. Mais, S.; Tittel, J.; Basché, T.; Bräuchle, C. Terrylenediimide: A Novel Fluorophore for Single-Molecule Spectroscopy and Microscopy from 1.4 K to Room Temperature. *J. Phys. Chem. A* **1997**, *101*, 8435–8440.
41. Han, J. J.; Wang, W.; Li, A. D. Q. Folding and Unfolding of Chromophoric Foldamers Show Unusual Colorful Single Molecule Spectral Dynamics. *J. Am. Chem. Soc.* **2006**, *128*, 672–673.
42. Malenfant, P. R. L.; Dimitrakopoulos, C. D.; Gelorme, J. D.; Kosbar, L. L.; Graham, T. O.; Curioni, A. ; Andreoni, W. N-type organic thin-film transistor with high field-effect mobility based on a N,N′-dialkyl-3,4,9,10-perylene tetracarboxylic diimide derivative. *Appl. Phys. Lett.* **2002**, *80*, 2517–2519.
43. Tang, C. W. Two-layer organic photovoltaic cell. *Appl. Phys. Lett.* **1986**, *48*, 183–185.
44. Wöhrle, D.; Meissner, D. Organic solar cells. *Adv. Mater.* **1991**, 3, 129-138.
45. Schmidt-Mende, L.; Fechtenkötter, A.; Müllen, K.; Moons, E.; Friend, R. H.; MacKenzie, J. D. Self-organized discotic liquid crystals for high-efficiency organic photovoltaics. *Science* **2001**, *293*, 1119-1122.
46. Wang, B.; Yu, C. Fluorescence turn-on detection of a protein through the reduced aggregation of a perylene probe. *Angew. Chem. Int. Ed.* **2010**, *49*, 1485 –1488.
47. Zhang, Z.; Zhang, X.; Zhan, C.; Lu, Z.; Ding, X.; He, S.; Yao, J. The leverage effect of the relative strength of molecular solvophobicity vs. solvophilicity on fine-tuning nanomorphologies of perylene diimide bolaamphiphiles. *Soft Matter* **2013**, *9*, 3089-3097.
48. Kim, S.; Shim, N.; Lee, H.; Moon, B. Synthesis of a perylenediimide-viologen dyad (PDI-2V) and its electrochromism in a layer-by-layer self-assembled multilayer film with PEDOT: PSS. *J. Mater. Chem.* **2012**, *22*, 13558-13563.
49. Echue, G.; Lloyd-Jones, G. C.; Faul, C. F. J. Chiral Perylene Diimides: Building Blocks for Ionic Self-Assembly. *Chem. Eur. J.* **2015**, *21*, 5118 – 5128.
50. Chen, Z.; Stepanenko, V.; Dehm, V.; Prins, P.; Siebbeles, L. D. A. ; Seibt, J. ; Marquetand, P.; Engel, V.; Wurthner, F. Photoluminescence and Conductivity of Self-Assembled π–π Stacks of Perylene Bisimide Dyes. *Chem. Eur. J.* **2007**, *13*, 436 – 449.
51. Ghosh, S.; Li, X.Q.; Stepanenko, V.; Wurthner, F. Control of H- and J-Type π Stacking by Peripheral Alkyl Chains and Self-Sorting Phenomena in Perylene Bisimide Homo- and Heteroaggregates. *Chem. Eur. J.* **2008**, *14*, 11343 – 11357.
52. Islam, M. R.; SundararaJan, P. R. Self-assembly of a set of hydrophilic–solvophobic–hydrophobic coil–rod–coil molecules based on perylene diimide. *Phys. Chem. Chem. Phys.* **2013**, *15*, 21058-21069.
53. Cotlet, M.; Hofkens, J.; Maus, M.; Mark, T. G.; Auweraer, V. d.; Michiels, J.; Dirix, G.; Guyse, M. V.; Antonie, J. V.; Frans, J. W. G. V.; Schryver, C. D. Excited-State Dynamics in the Enhanced Green Fluorescent Protein Mutant Probed by Picosecond Time-Resolved Single Photon Counting Spectroscopy. *J. Phys. Chem. B* **2001**, *105*, 4999-5006.
54. Clark, A. E.; Qin, C.; Li, A. D.Q. Beyond Exciton Theory: A Time-Dependent DFT and Franck–Condon Study of Perylene Diimide and Its Chromophoric Dimer. *J. Am. Chem. Soc.* **2007**, *129*, 7586–7595.
55. Wang, W.; Han, J. J.; Wang, L.; Li, L.; Shaw, W. J.; Li, A. D. Q. Dynamic π–π Stacked Molecular Assemblies Emit from Green to Red Colors. *Nano Letters* **2003**, *3*, 455–458.
56. Heek, T.; Wurthner, F.; Haag, R. Synthesis and Optical Properties of Water-Soluble Polyglycerol-Dendronized Rylene Bisimide Dyes. *Chem. Eur. J.* **2013**, *19*, 10911 – 10921.

57. Chen, Y.; Feng, Y.; Gao, J.; Bouvet, M. Self-assembled aggregates of amphiphilic perylene diimide-based semiconductor molecules: effect of morphology on conductivity. *Journal of Colloid and Interface Science* **2012**, *368*,387-394.
58. Lee, H. N.; Xu, Z.; Kim, S. K.; Swamy, K.M.; Kim, Y.; Kim, S.-J.; Yoon, J. Pyrophosphate-selective fluorescent chemosensor at physiological pH: formation of a unique excimer upon addition of pyrophosphate. *J. Am. Chem. Soc.* **2007**, *129*, 3828–3829.
59. Lu, X.; Zhu, W.; Xie, Y.; Li, X.; Gao, Y.; Li, F.; Tian, H.Near-IR Core-Substituted Naphthalenediimide Fluorescent Chemosensors for Zinc Ions: Ligand Effects on PET and ICT Channels. *Chem. Eur. J.* **2010**, *16*, 8355 – 8364.
60. Kumar, M.; Jonnalagadda, N.; George, S. J. Molecular Recognition Driven Self-Assembly and Chiral Induction in Naphthalene Diimide Amphiphiles. *Chem. Commun.* **2012**, *48*, 10948– 10950.
61. Pandeeswar, M.; GovindaraJu, T. Green-fluorescent naphthalene diimide: conducting layered hierarchical 2D nanosheets and reversible probe for detection of aromatic solvents. *RSC Adv.* **2013**, *3*, 11459-11462.
62. Pal, S.; Hatai, J.; Samanta, M.; Shaurya, A.; Bandyopadhyay, S. A Highly Selective chemodosimeter for Fast Detection and Intracellular Imaging of Hg2+ Ions Based on a Dithiocarbamate- Isothiocyanate Conversion in Aqueous Ethanol. *Org. Biomol. Chem.* **2014**, *12*, 1072–1078.
63. Bobe, S. R.; Bhosale, R. S.; Goskulwad, S. P.; Puyad, A. L.; Bhosale, S. V.; Bhosale, S. V. A highly selective colorimetric Cys sensor based on core-substituted naphthalene diimides. *RSC Advances.* **2015**, *5*, 100697-100701.
64. Ghule, N. V.; Bhosale, R. S.; Puyad, A. L.; Bhosale, S. V.; Bhosale, S. V. Naphthalenediimide amphiphile based colorimetric probe for recognition of Cu^{2+} and Fe^{3+} ions. *Sensors and Actuators B* **2013**, *182*,439-445.
65. Lin, Q.; Mao, P.- P.; Liu, L.; Liu, J.; Zhang, Y.- M.; Yao, H.; Wei, T. -B. A novel water soluble chemosensor based on carboxyl functionalized NDI derivatives for selective detection and facile removal of mercury (II). *RSC Advances* **2017**, *7*, 11206-11210.
66. LiWei, Y.; Li, Y.; JingBo, L.; JingSong, Y. A new perylene diimide-based colorimetric and fluorescent sensor for selective detection of Cu^{2+} cation. *Science in China Series B: Chemistry* **2009**, *52*, 518-522.
67. Ruan, Y.-B.; Li, A.-F.; Zhao, J.-S.; Shena, J.-S.; Jiang, Y.-B. Specific Hg^{2+}-mediated perylene bisimide aggregation for highly sensitive detection of cysteine. *Chem. Commun.* **2010**, *46*, 4938-4940.
68. Yan, L.; Ye, Z.; Peng, C.; Zhang, S. A new perylene diimide-based fluorescent chemosensor for selective detection of ATP in aqueous solution. *Tetrahedron* **2012**, *68*, 2725-2727.
69. Feng, X.; An, Y.; Yao, Z.; Li, C.; G. A Turn-on fluorescent sensor for pyrophosphate based on the disassembly of Cu^{2+}-mediated perylene diimide aggregates. *ACS Appl. Mater. Interfaces*, **2012**, *4*, 614–618.
70. K. Liu, Y. Yao, Y. Kang, Y. Liu, Y. Han, Y. Wang, Z. Li, X. Zhang, A supramolecular approach to fabricate highly emissive smart materials *Sci. Rep.* **2013**, *3*, 2372.
71. Liu, X.; Zhang, N.; Zhou, J.; Chang, T.; Fang, C.; Shangguan, D. A turn-on fluorescent sensor for zinc and cadmium ions based on perylene tetracarboxylic diimide. *Analyst.* **2013**,*138*, 901-906.
72. Malkondu, S.; Erdemir, S. A novel perylene-bisimide dye as "turn on" fluorescent sensor for Hg^{2+} ion found in DMF/H2O. *Dyes and Pigments* **2015,** *113*, 763-769.
73. Weißenstein, A.; Würthner, F. Metal ion ehaviou self-assembly of crown ether functionalized perylene bisimide dyes. *Chem. Commun.* **2015**, *51*, 3415—3418.
74. Liu, K.; Xu, Z.; Yin, M.; Yang, W.; He, B.; Wei, W.; Shen, J. A multifunctional perylenediimide derivative (DTPDI) can be used as a recyclable specific Hg^{2+} ion sensor and an efficient DNA delivery carrier. *J. Mater. Chem. B* **2014**, *2*, 2093-2096.
75. Sukul, P. K.; Santra, D. C.; Singh, P. K.; Maji, S. K.; Malik, S. Water soluble perylene bisimide and its turn off on fluorescence are used to detect cysteine and homocysteine. *New J. Chem.* **2015**, *39*, 5084-5087.

76. Grisci, G.; Mróz, W.; Catellani, M.; Kozma, E.; Galeotti, F. Off-On Fluorescence Response of a Cysteine–based Perylene Diimide for Mercury Detection in Water. *ChemistrySelect* **2016,** *1*, 3033-3037.
77. Kowser, Z.; Jin, C.-C.; Jiang, X.; Rahman, S.; Georghiou, P. E.; Ni, X.-L.; Zeng, X.; Redshawd, C.; Yamato, T. Fluorescent turn-on sensors based on pyrene-containing Schiff base derivatives for Cu2þ recognition: spectroscopic and DFT computational studies. *Tetrahedron* **2016**, *72*, 4575-4581.
78. Padghan, S. D.; Bhosale, R. S.; Bhosale, S. V.; Antolasic, F.; Kobaisi, M. A.; Bhosale, S. V. Pyrene-Phosphonate Conjugate: Aggregation-Induced Enhanced Emission, and Selective Fe3+ Ions Sensing Properties. *Molecules* **2017**, *22*, 1417.
79. Ferreira, P. M. T.; Monteiro, L. S.; Pereira, G.; Castanheira, E. M. S.; Frost, C. G. Synthesis of Fluorescent Alanines by a Rhodium-Catalysed Conjugate Addition of Arylboronic Acids to Dehydroalanine Derivatives. *Eur. J. Org. Chem.* **2013**, 550–556.
80. Zhang, Y.; He, B.; Liu, J.; Hu, S.; Pan, L.; Zhao, Z.; Tang, B. Z. Aggregation-induced emission and the working mechanism of 1-benzoyl and 1-benzyl pyrene derivatives. *Phys. Chem. Chem. Phys.***2018**, *20*, 9922-9929.
81. Bains, G.; Patel, A. B.; Narayanaswami, V. Pyrene: A Probe to Study Protein Conformation and Conformational Changes. *Molecules* **2011**, *16*, 7909-7935.
82. Zhou, Y.; Zhu, C.-Y.; Gao, X.-S.; You, X.-Y. Yao, C. Hg^{2+}-Selective Ratiometric and "Off–On" Chemosensor Based on the Azadiene–Pyrene Derivative. *Org. Lett.* **2010**, *12*, 2566-2569.
83. Zhang, R.; Tang, D.; Lu, P.; Yang, X.; Liao, D.; Zhang, Y.; Zhang, M.; Yu, C.; Yam, V. W. W. Nucleic Acid-Induced Aggregation and Pyrene Excimer Formation. *Org. Lett.* **2009**, *11*, 4302-4305.
84. Yu, C.; Yam, V. W. – W. Glucose sensing via polyanion formation and induced pyrene excimer emission. *Chem. Commun.* **2009**, 1347-1349.
85. Yang, Y.; Gou, X.; Blecha, J.; Cao, H. A highly selective pyrene based fluorescent sensor toward Hg2+ detection. *Tet. Lett.* **2010**, *51*, 3422-3425.
86. Hou, C.; Xiong, Y.; Fu, N.; Jacquot, C. C.; Squier, T. C.; Cao, H. Turn-on ratiometric fluorescent sensor for Pb2+ detection. *Tet. Lett.* **2011**, *52*, 2692–2696.
87. Kar, C.; Adhikari, M. D.; Ramesh, A.; Das, G. Selective sensing and efficient separation of Hg2+ from aqueous medium with a pyrene based amphiphilic ligand. *RSC Adv.* **2012**, *2*, 9201-9206.
88. Wu, J.; Zou, Y.; Li, C.; Sicking, W.; Piantanida, I.; Yi, T.; Schmuck, C. A Molecular Peptide Beacon for the Ratiometric Sensing of Nucleic Acids. *J. Am. Chem. Soc.* **2012**, *134*, 1958–1961.
89. Wu, J.; Zou, Y.; Li, C.; Sicking, W.; Piantanida, I.; Yi, T.; Schmuck, C. A Molecular Peptide Beacon for the Ratiometric Sensing of Nucleic Acids. *J. Am. Chem. Soc.* **2012**, *134*, 1958–1961.
90. Amendola, V.; Bergamaschi, G.; Boiocchi, M.; Fabbrizzi, L.; Mosca, L. The Interaction of Fluoride with Fluorogenic Ureas: An ON1–OFF–ON2 Response. *J. Am. Chem. Soc.* **2013**, *135*, 6345–6355.
91. Ghosh, A.; Sengupta, A.; Chattopadhyay, A.; Das, D. Lysine triggered ratiometric conversion of dynamic to static excimer of a pyrene derivative: aggregation-induced emission, nanomolar detection and human breast cancer cell (MCF7) imaging. *Chem. Commun.*, **2015**, *51*, 11455-11458.
92. Mosca, L.; Behzad, S. K.; Anzenbacher Jr. P. Small-Molecule Turn-On Fluorescent Probes for RDX. *J. Am. Chem. Soc.* **2015**, *137*, 7967–7969.
93. Gong, W.; Wang, S.; Wei, Y.; Ding, L.; Fang, Y. A pyrene-based fluorescent sensor for ratiometric detection of heparin and its complex with heparin for reversed ratiometric detection of protamine in aqueous solution. *Spectrochimica Acta Part A: Molecular and Biomolecular Spectroscopy* **2017**,*170*, 198–205.

94. Zhao, M.; Zhou, X.; Tang, J.; Deng, Z.; Xu, X.; Chen, Z.; Li, X.; Yang, L.; Ma, L.-J. Pyrene excimer-based fluorescent sensor for detection and removal of Fe3 + and Pb2 + from aqueous solutions. *Spectrochimica Acta Part A: Molecular and Biomolecular Spectroscopy* **2017**,*173*, 235-240.
95. Padghan, S. D.; Puyad, A. L.; Bhosale, R. S.; Bhosale, S. V.; Bhosale, S. V. A pyrene based fluorescent turn-on chemosensor: aggregation-induced emission enhancement and application towards Fe3+ and Fe2+ recognition. *Photochem. Photobiol. Sci.* **2017**, *16*, 1591-1595.
96. Liu, L.-N.; Tao, H.; Chen, G.; Chen, Y.; Cao, Q.-Y. An amphiphilic pyrene-based probe for multiple channel sensing of mercury ions. *Journal of Luminescence* **2018**, *203*,189–194.
97. Dasgupta, A.; Mondal, J. H.; Das, D. Peptide hydrogels. *RSC Adv.* **2013**, *3*, 9117-9149.
98. Thirupathi, P.; Lee, K.-H. A new peptidyl fluorescent chemosensors for the selective detection of mercury ions based on tetrapeptide. *Bioorg. Med. Chem.* **2013**, *21*, 7964–7970.
99. Thirupathi, P.; Neupane, L. N.; Lee, K.-H. Fluorescent peptide-based sensors for the ratiometric detection of nanomolar concentration of heparin in aqueous solutions and in serum. *Analytica Chimica Acta* **2015**, 873, 88–98.
100. Madhu, C.; Roy, B.; Makam, P.; Govindaraju, T. Bicomponent β-sheet assembly of dipeptide fluorophores of opposite polarity and sensitive detection of nitro-explosives. *Chem. Commun.* **2018**, *54*, 2280—2283.
101. Tomar, K.; Kaur, G.; Verma, S.; Ramanathan, G. A self-assembled tetrapeptide that acts as a "turn-on" fluorescent sensor for Hg^{2+} ion. *Tet. Lett.* **2018**, *59*, 3653-3656.
102. Wan, J.; Duan, W.; Chen, K.; Tao, Y.; Dang, J.; Zeng, K.; Ge, Y.; Wu, J.; Liu, D. Selective and sensitive detection of Zn (II) ion using a simple peptide-based sensor. *Sensors and Actuators B* **2018**, *255*, 49–56.
103. Preti, G.; Labows, J. N.; Kostelc, J. G.; Aldinger, S.; Daniele, R. Analysis of lung air from patients with bronchogenic carcinoma and controls using gas chromatography-mass spectrometry. *Journal of Chromatography B: Biomedical Sciences and Applications* **1988**, *432*, 1-11.
104. Che, Y.; Zang, L. Enhanced fluorescence sensing of amine vapor based on ultrathin nanofibers. *Chem. Commun.* **2009**, 5106–5108.
105. Jiang, B. - P.; Guo, D. - S.; Liu, Y. Self-Assembly of Amphiphilic Perylene–Cyclodextrin Conjugate and Vapor Sensing for Organic Amines. *J. Org. Chem.* **2010**, 75, 7258-7264.
106. Peng, H; Ding, L.; Liu, T.; Chen, X.; Li, L.; Yin, S.; Fang, Y. An Ultrasensitive Fluorescent Sensing Nanofilm for Organic Amines Based on Cholesterol-Modified Perylene Bisimide. *Chem. Asian J.* **2012**, *7*, 1576-1582.
107. Yue, E.; Ma, X.; Zhang, Y.; Zhang, Y.; Duan, R.; Ji, H.; Li , J.; Che, Y.; Zhao, J. Fluorescent bilayer nanocoils assembled from an asymmetric perylene diimide molecule with ultrasensitivity for amine vapors. *Chem. Commun.* **2014**, *50*, 13596—13599.
108. Sriramulu, D.; Valiyaveettil, S. Perylene derivatives as a fluorescent probe for sensing of amines in solution. *Dyes and Pigments* **2016**, *134*, 306-314.
109. Hu, Y.; Ma, X.; Zhang, Y.; Che, Y.; Zhao, J. Detection of amines with fluorescent nanotubes: applications in the assessment of meat spoilage. *ACS Sens.* **2016**, *1*, 22–25.
110. Hu, Y.; Zhou, Z.; Zhao, F.; Liu, X.; Gong, Y.; Xiong, W.; Sillanpää, M. Fingerprint Detection and Differentiation of Gas-phase Amines Using a Fluorescent Sensor Array Assembled from Asymmetric Perylene Diimides. *Scientific reports* **2018**, *8*, 10277.
111. Balamurugan, R.; Liu, J. - H.; Liu, B.-T. A review of recent developments in fluorescent sensors for the selective detection of palladium ions. *Coord. Chem. Rev.* **2018**, *376*, 196–224.
112. Zhang, L.; Wang, Y.; Yu, J.; Zhang, G.; Cai, X.; Wu, Y. Wang L. A colorimetric and fluorescent sensor based on PBIs for palladium detection. *Tet. Lett.* **2013**, *54*, 4019–4022.

113. Jiang, J.; Jiang, H.; Liu, W.; Tang, X.; Zhou, X.; Liu, W.; Liu, R. A Colorimetric and Ratiometric Fluorescent Probe for Palladium. *Org. Lett.* **2011**, *13*, 4922-4925.

114. Wang, H.-X.; Lang, Y.-H.; Wang, H.-X.; Lou, J.-J.; Guo, H.-M.; Li, X.-Y. Perylene diimide based 'turn-on 'fluorescence sensor for detection of Pd^{2+} in mixed aqueous media. *Tetrahedron* **2014**, *70*, 1997-2002.

115. Nie, H.; Geng, J.; Jing, J.; Li, Y.; Yang, W.; Zhang, X. Triphenylphosphine-assisted highly sensitive fluorescent chemosensor for ratiometric detection of palladium in solution and living cells. *RSC Adv.* **2015**, *5*, 97121-97126.

116. Singh, P.; Mittal, L. S.; Vanita, V.; Kumar, K.; Walia, A.; Bhargava, G.; Kumar, S. Self-assembled vesicle and rod-like aggregates of functionalized perylene diimide: reaction-based near-IR intracellular fluorescent probe for selective detection of palladium. *J. Mater. Chem. B* **2016**, *4*, 3750—3759.

117. Kumar, K.; Bhargava, G.; Kumar, S.; Singh, P. Controllable supramolecular self-assemblies (rods–wires–spheres) and ICT/PET based perylene probes for palladium detection in solution and the solid state. *New J. Chem.* **2018**, *42*, 1010—1020.

118. Ebaston, T. M.; Balamurugan, G.; Velmathi, S. A fluorogenic and chromogenic dual sensor for the detection of cyanide and copper(II) in water samples and living cells. *Anal. Methods* **2016**, *8*, 6909-6915.

119. Matsubara, K.; Akane, A.; Masada, C.; Shiono, H. "First pass phenomenon" of inhaled gas in the fire victims. *Forensic Sci. Int.* **1990**, *46*, 203–208.

120. Singh, P.; Mittal, L. S.; Kumar, S.; Bhargava, G.; Kumar, S. Perylene Diimide Appended with 8-Hydroxyquinoline for Ratiometric Detection of Cu^{2+} Ions and Metal Displacement Driven "Turn on" Cyanide Sensing. *J Fluoresc* **2014**, *24*, 909–915.

121. Kumar, A.; Kim, H.-S. A pyrenesulfonyl-imidazolium derivative as a selective cyanide ion sensor in aqueous media. *New J. Chem.* **2015**, *39*, 2935—2942.

122. Lim, B.; Lee, J. A peptoid-based fluorescent sensor for cyanide detection. *Molecules* **2016**, *21*, 339.

123. Ebaston, T. M.; Balamurugan, G.; Velmathi, S. A fluorogenic and chromogenic dual sensor for the detection of cyanide and copper(II) in water samples and living cells. *Anal. Methods* **2016**, *8*, 6909-6915.

124. Lin, Q.; Liu, L.; Zheng, F.; Mao, P.- P.; Liu, J.; Zhang, Y.-M.; Yao, H.; Wei, T.-B. A benzimidazole functionalized NDI derivative for recyclable fluorescent detection of cyanide in water. *RSC Adv.* **2017**, *7*, 38458–38462.

125. Singh, P.; Mittal, L. S.; Kumar, S.; Bhargava, G.; Kumar, S. Perylene diimide-based organic π-motif for differentiating CN^- and F^- ions by electron-transfer and desilylation mechanisms: applications to complex logic circuits. *New J. Chem.* **2017**, *41*, 10281—10290.

126. Maiti S, Das K, Das PK. Label-free fluorimetric detection of histone using quaternized carbon dot–DNA nanobiohybrid. *Chem. Commun.* **2013**, *49*, 8851—8853.

127. Hayashida, O.; Uchiyama, M. Rotaxane-type resorcinarene tetramers as histone-sensing fluorescent receptors. *Org. Biomol. Chem.* **2008**, *6*, 3166–3170.

128. Sun, P.; Lu, X.; Fan, Q.; Zhang, Z.; Song, W.; Li, B.; Huang, L.; Peng, J.; Huang, W. Water-Soluble Iridium(III)-Containing Conjugated Polyelectrolytes with Weakened Energy Transfer Properties for Multicolor Protein Sensing Applications. *Macromolecules* **2011**, *44*, 8763–8770.

129. Shao, N.; Zhang, K.; Chen, Y.; He, X.; Zhang, Y. Preparation and characterization of DNA aptamer based spin column for enrichment and separation of histones. *Chem. Commun.* **2012**, *48*, 6684–6686.

130. Dhara, K.; Hori, Y.; Baba, R.; Kikuchi, K. A fluorescent probe for detection of histone deacetylase activity based on aggregation-induced emission. *Chem. Commun.* **2012**, *48*, 11534–11536.

131. Yu, C.; Wu, Y.; Zeng, F.; Li, X.; Shi, J.; Wu, S. Hyperbranched polyester-based fluorescent probe for histone deacetylase via aggregation-induced emission. *Biomacromolecules* **2013**, *14*, 4507–4514.

132. Minoshima, M.; Matsumoto, T.; Kikuchi, K. Development of a fluorogenic probe based on a DNA staining dye for continuous monitoring of the histone deacetylase reaction. *Anal. Chem.* **2014**, *86*, 7925−7930.
133. Lian, J.; Liu, Q.; Jin, Y.; Li, B. Histone–DNA interaction: an effective approach to improve the fluorescence intensity and stability of DNA-templated Cu nanoclusters. *Chem. Commun.* **2017**, *53*, 12568—12571.
134. Kumar, A.; Chae, P. S. Aggregation induced emission enhancement behavior of conformationally rigid pyreneamide-based probe for ultra-trace detection of picric acid (PA). *Dyes and Pigments* **2018**, *156*, 307–317.
135. Liu, T.; Ding, L.; Zhao, K.; Wang, W.; Fang, Y. Single-layer assembly of pyrene end-capped terthiophene and its sensing performances to nitroaromatic explosives. *J. Mater. Chem.* **2012**, *22*, 1069–1077.
136. Chopra, R.; Kaur, P.; Singh, K. Pyene-based chemosensor detects picric acid upto attogram level through aggregation enhanced excimer emission. *Analytica Chimica Acta* **2015**, *864*, 55–63.
137. Shyamal, M; Maity, S.; Mazumdar, P.; Sahoo, G. P.; Maity, R.; Misra, A. Synthesis of an efficient Pyrene based AIE active functional material for selective sensing of 2, 4, 6-trinitrophenol. *Journal of Photochemistry and Photobiology A: Chemistry* **2017**, *342*, 1–14.
138. Liang, H.; Yao, Z.; Ge, W.; Qiao, Y.; Zhang, L.; Cao, Z.; Wu, H.- C. Selective and sensitive detection of picric acid based on a water-soluble fluorescent probe. *RSC Adv.* **2016**, *6*, 38328-38331.
139. Turhan, H.; Tukenmez, E.; Karagoz, B.; Bicak, N. Highly fluorescent sensing of nitroaromatic explosives in aqueous media using pyrene-linked PBEMA microspheres. *Talanta* **2018**, *179*, 107–114.
140. Kachwal, V.; Alam, P.; Yadav, H. R.; Pasha, S. S.; Choudhury, A. R.; Laskar, I. R. Simple ratiometric push–pull with an 'aggregation induced enhanced emission'active pyrene derivative: a multifunctional and highly sensitive fluorescent sensor. *New J. Chem.* **2018**, *42*, 1133—1140.
141. Wang, L. K.; Hung, Y.-T.; Lo, H. H.; Yapojakis, C. Handbook of Industrial and Hazardous Wastes Treatment, 2nd Ed; CRC Press, 2004.
142. Busca, G. Bases and basic materials in chemical and environmental processes. Liquid versus solid basicity. *Chem. Rev.* **2010**, *110*, 2217–2249.
143. Guo, X.; Facchetti, A.; Marks, T. J. Imide- and amide-functionalized polymer semiconductors. *Chem. Rev.* **2014**, *114*, 8943-9021.
144. Chen, S.; Slattum, P.; Wang, C.; Zang, L. Self-assembly of perylene imide molecules into 1D nanostructures: methods, morphologies, and applications. *Chem. Rev.* **2015**, *115*, 11967-11998.
145. Kulkarni, C.; Bejagam, K. K.; Senanayak, S. P.; Narayan, K. S.; Balasubramanian, S.; George, S. J. Dipole-moment-driven cooperative supramolecular polymerization. *J. Am. Chem. Soc.* **2015**, *137*, 3924-3932.
146. Wu, H.; Xue, L.; Shi, Y.; Chen, Y.; Li, X. Organogels based on J- and H-type aggregates of amphiphilic perylenetetracarboxylic diimides. *Langmuir* **2011**, *27*, 3074-3082.
147. Zhao, H.-M.; Pfister, J.; Settels, V.; Renz, M.; Kaupp, M.; Dehm, V. C.; Wurthner, F.; Fink, R. F.; Engels, B. Understanding ground- and excited-state properties of perylene tetracarboxylic acid bisimide crystals by means of quantum chemical computations. *J. Am. Chem. Soc.* **2009**, *131*, 15660 – 15668.
148. Li, Y.; Zheng, H.; Li, Y.; Wang, S.; Wu, Z.; Liu, P.; Gao, Z.; Liu H.; Zhu, D. Photonic logic gates based on control of FRET by a solvatochromic perylene bisimide. *J. Org. Chem.* **2007**, *72*, 2878–2885.
149. Chang, C.-W.; Tsai, H.-Y.; Chen, K.-Y. Green Perylene bisimide dyes: Synthesis, photophysical and electrochemical properties. *Materials*, **2014**, *7*, 5488-5506.
150. Shi, W.; Xing, F.; Bai, Y-L.; Hu, M.; Zhao, Y.; Li, M-X.; Zhu, S. High Sensitivity Viologen for a Facile and Versatile Sensor of Base and Solvent Polarity in Solution and Solid State in Air Atmosphere. *ACS Appl. Mater. Interfaces* **2015**, *7*, 14493-14500.

151. Wang, Y.; Xu, S.; Gao, F.; Chen, Q.; Ni B.; Ma, Y. Fast naked-eye detection of amines with viologen derivatives. *Supramol. Chem.* **2013**, *25*, 344–348.

152. Hoffman, M. Z.; Prasad, D. R.; Jonesll, G.; Malba, V. Formation of Photoactive Charge-Transfer Complexes between Methylviologen and Sacrificial Electron Donors. EDTA and Triethanolamine. *J. Am. Chem. Soc.* **1983**, *105*, 6360–6362.

153. Mondal, J. H.; Ahmed, S.; Ghosh T.; Das, D. Reversible deformation–formation of a multistimuli responsive vesicle by a supramolecular peptide amphiphile. *Soft Matter* **2015**, *11*, 4912-4920.

154. Kiriya, D.; Tosun, M.; Zhao, P.; Kang J. S.; Javey, A. Air-Stable Surface Charge Transfer Doping of MoS_2 by Benzyl Viologen. *J. Am. Chem. Soc.* **2014**, *136*, 7853–7856.

155. Jeon, W. S.; Kim, H-J.; Leeb C.; Kim, K. Control of the stoichiometry in host–guest complexation by redox chemistry of guests: Inclusion of methylviologen in cucurbit[8]uril. *Chem. Commun.* **2002**, 1828-1829.

156. Mortimer, R. J. Organic electrochromic materials. *Electrochim. Acta.* **1999**, *44*, 2971−2981.

157. Ahmed, S.; Singha, N.; Pramanik, B.; Mondal, J. H.; Das, D. Redox controlled reversible transformation of a supramolecular alternating copolymer to radical cation containing homo-polymer. *Polym. Chem.* **2016**, *7*, 4393–4401.

158. Datar, A.; Balakrishnan, K.; Zang, L. One-dimensional self-assembly of a water soluble perylene diimide molecule by pH triggered hydrogelation. *Chem. Commun.* **2013**, *49*, 6894 – 6896.

159. Heck, *R. F.* Palladium Reagents in Organic Syntheses, Academic Press, New York, **1985**.

160. Chinchilla, R.; Na´Jera, C. The Sonogashira Reaction: A Booming Methodology in Synthetic Organic Chemistry. *Chem. Rev.* **2007**, *107*, 874-922.

161. International Programme on Chemical Safety. Palladium; environmental Health Criteria Series 226, World Health Organization, Geneva, **2002**.

162. Wataha, J. C.; Hanks, C. T. Biological effects of palladium and risk of using palladium in dental casting alloys. *J. Oral Rehabil.* **1996**, *23*, 309-320.

163. Liu, T. Z.; Daniel T.Y.; Chiu, K.-J.; Tsai, A. Stern, Palladium exacerbates hydroxyl radical mediated DNA damage. *Free Radic. Biol. Med.* **1997**, 23, 155-161.

164. Spikes. J. D.; Hodgson, C. F. Enzyme inhibition by palladium. *Biochem. Biophys. Res. Commun.* **1969**, 35, 420-422.

165. Carey, J. S.; Laffan, D.; Thomson, C.; Williams, M. T. Analysis of the reactions used for the preparation of drug candidate molecules. *Org. Biomol. Chem.* **2006**, *4*, 2337-2347.

166. Garrett, C. E.; Prasad, K. The Art of Meeting Palladium Specifications in Active Pharmaceutical Ingredients Produced by Pd-Catalyzed Reactions. *Adv. Synth. Catal.* **2004**, *346*, 889-900.

167. Cox, M. M.; Nelson, D. L.; Lehniger Principles of Biochemistry, third ed., W. H. Freeman and Company, New York, **2008**, 668-676.

168. Luthy, R. G.; Bruce, S. G. Kinetics of Reaction of Cyanide and Reduced Sulfur Species in Aqueous Solution, *Environ. Sci. Technol.* **1979**, *13*, 1481-1487.

169. Wild, S. R.; Rudd, T.; Neller, A. Fate and effects of cyanide during wastewater treatment processes, *Sci. Total Environ.* **1994**, *156, 93*–107.

170. Liu, B.; Bao, Y.; Du, F.; Wang, H.; Tian, J.; Bai , R. Synthesis and characterization of a fluorescent polymer containing 2,6-bis(2-thienyl)pyridine moieties as a highly efficient sensor for Pd^{2+} detection, *Chem.Commun.* **2011**, *47*, 1731–1733.

171. Liu, W.; Jiang, J.; Chen, C.; Tang, X.; Shi, J.; Zhang, P.; Zhang, K.; Li, Z.; Dou, W.; Yang, L.; Liu, W. Water-Soluble Colorimetric and Ratiometric Fluorescent Probe for Selective Imaging of Palladium Species in Living Cells, *Inorg. Chem.* **2014**, *53*, 12590−12594.

172. Liu, F.; Du, J.; Xu, M.; Sun, G. A Highly Sensitive Fluorescent Sensor for Palladium and Direct Imaging of Its Ecotoxicity in Living Model Organisms. *Chem. Asian J.* **2016**, *11*, 43 – 48.
173. Kumar, R.; Sandhu, S.; Hundal, G.; Singh, P.; Walia, A.; Vanita, V.; Kumar, S. A catalytic chemodosimetric approach for detection of nanomolar cyanide ions in water, blood serum and live cell imaging.*Org. Biomol. Chem.* **2015**, *13*, 11129-11139.
174. Kumar, S.; Singh, P.; Hundal, G.; Hundal, M. S.; Kumar, S. A chemodosimeter for ratiometric detection of cyanide in aqueous media and human blood serum. *Chem. Commun.* **2013**, *49*, 2667-2669.
175. Shi, B.; Zhang, P.; Wei, T.; Yao, H.; Lin, Q.; Zhang, Y. Highly selective fluorescent sensing for CN^- in water: utilization of the supramolecular self-assembly. *Chem. Commun.* **2013**, *49*, 7812-7814.
176. Ma, J.; Dasgupta, P. K. Recent developments in cyanide detection: a review. *Anal. Chim. Acta* **2010**, *673*, 117-125.
177. Ekmekci, Z.; Yilmaz, M. D.; Akkaya, E. U. *Org. Lett.* **2008**, *10*, 461-464.
178. Badugu, R.; Lakowicz, J. R.; Geddes, C. D. Enhanced Fluorescence Cyanide Detection at Physiologically Lethal Levels: Reduced ICT-Based Signal Transduction *J. Am. Chem. Soc.* **2005**, *127*, 3635-3641.
179. Pramanik, B.; Mondal, J. H.; Singha, N.; Ahmed, S.; Mohanty, J.; Das, D. A Viologen-Perylenediimide Conjugate as an Efficient Base Sensor with Solvatochromic Property, *ChemPhysChem* **2017**, *18*, 245 – 252.
180. Ahmed, S.; Pramanik, B.; Sankar, K. N. A.; Srivastava, A.; Singha, N.; Dowari, P.; Srivastava, A.; Mohanta, K.; Debnath, A.; Das, D. Solvent Assisted Tuning of Morphology of a Peptide-Perylenediimide Conjugate: Helical Fibers to Nano-Rings and their Differential Semiconductivity. *Sci. Rep.* **2017,** *7*, 9485.
181. Singha, N.; Gupta, P.; Pramanik, B.; Ahmed, S.; Dasgupta, A.; Ukil, A.; Das, D. Hydrogelation of a Naphthalene Diimide Appended Peptide Amphiphile and Its Application in Cell Imaging and Intracellular pH Sensing. *Biomacromolecules* **2017,** *18*, 3630-3641.
182. Ye, Y.; Zheng, Y.; Ji, C.; Shen, J.; Yin, M. Self-Assembly and Disassembly of Amphiphilic Zwitterionic Perylenediimide Vesicles for Cell Membrane Imaging. *ACS Appl. Mater. Interfaces* **2017**, *9*, 4534-4539.
183. Hariharan, P. S.; Pitchaimani, J.; Madhu, V.; Anthony, S. P. Perylene Diimide Based Fluorescent Dyes for Selective Sensing of Nitroaromatic Compounds: Selective Sensing in Aqueous Medium Across Wide pH Range. *Journal of Fluorescence* **2016**, *26*, 395-401.
184. Pramanik, B.; Ahmed, S.; Roy, R.; Das, B. K.; Singha, N.; Das, D. A DNA-NDI Hybrid to Efficiently Detect Histone in Parts per Trillion (ppt) Level. *ChemistrySelect* **2017**, *2*, 8911-8916.
185. Wang, W.; Wang, L.; Palmer, B. J.; Exarhos, G. J.; Li, A. D. Q. Cyclization and Catenation Directed by Molecular Self-Assembly. *J. Am. Chem. Soc.* **2006**,*128*, 11150- 11159.
186. Echue, G.; HamLey, I.; Jones, G. C. L.; Faul, C. F. J. *Langmuir* **2016**, *32*, 9023-9032.
187. Harvey, P. D.; Reber, C. Distortions in square-planar palladium(II) halides: a nonempirical molecular orbital model study, *Can. J. Chem.* **1999**, *77*, 16-23.
188. Benesi, H. A.; Hildebrand, J. H. A Spectrophotometric Investigation of the Interaction of Iodine with Aromatic Hydrocarbons. *J. Am. Chem. Soc.* **1949**, *71*, 2703-2707.
189. Fu, Y.; Jiang, X-J.; Zhu, Y-Y.; Zhou, B.-J.; Zang, S-Q.; Tang, M-S.; Zhang, H-Y.; Mak, T. C. W. A new fluorescent probe for Al^{3+} based on rhodamine 6G and its application to bioimaging. Dalton Trans. **2014**, *43*, 12624-12632.
190. Tang, L.; Zhou, P.; Zhong, K.; Hou, S. Fluorescence relay enhancement sequential recognition of Cu^{2+} and CN^- by a new quinazoline derivative. *Sensors and Actuators B* **2013**, *182*,439-445.
191. Ho, T.-L. Hard soft acids bases (HSAB) principle and organic chemistry, *Chem. Rev.* **1975**, *75*, 1-20.
192. Hibble, S. J.; Chippindale, A. M.; Bilbè, E.J.; Marelli, E.; Harris, P. J. F.; Hannon, A. C. Structures of $Pd(CN)_2$ and $Pt(CN)_2$: Intrinsically Nanocrystalline Materials? *Inorg. Chem.* **2011**, *50*, 104-113.

193. Harrington, J. M.; Jones S. B.; Hancock, R. D. Determination of formation constants for complexes of very high stability: logb4 for the $[Pd(CN)_4]^{2-}$ ion. *Inorg. Chim. Acta* ***2005***, 358, 4473-4480.

194. Guidelines for drinking-water quality, Vol. 2.Health criteria and other supporting information. 2nd ed., World Health Organization, Geneva, 1996.

195. Kumar, P.; Kumar, V.; Gupta, R. Selective fluorescent turn-off sensing of Pd2+ ion: applications as paper strips, polystyrene films, and in cell imaging. *RSC Adv.* **2017**, *7*, 7734–7741.

196. Huoa, F.; Zhanga, Y.; Kangc, J.; Chaoa, J.; Zhanga, Y.; Yin, C. A novel alkyne compound as a Pd(II) fluorescent probe in aqueous medium and its bioimaging. *Sensors and Actuators B* **2017**, *243*, 429–434.

197. Keum, D.; Kim, S.; Kim, Y. A fluorescence turn-on sensor for the detection of palladium ions that operates through in situ generation of palladium nanoparticles. *Chem. Commun.* **2014**, *50*, 1268—1270.

198. Li, J.-P.; Wang, H.-X.; Wang, H.-X.; Xie, M.-S.; Qu, G.-R.; Niu, H.-Y.; Guo, H.-M. Push–Pull-Type Purine Nucleoside-Based Fluorescent Sensors for the Selective Detection of Pd2+ in Aqueous Buffer. *Eur. J. Org. Chem.* **2014**, 2225–2230.

199. Li, H.; Fan, J.; Hu, M.; Cheng, G.; Zhou, D.; Wu, T.; Song, F.; Sun, S.; Duan, C.; Peng, X. Highly Sensitive and Fast-Responsive Fluorescent Chemosensor for Palladium: Reversible Sensing and Visible Recovery. *Chem. Eur. J.* **2012**, *18*, 12242 – 12250.

200. Chena, C.; Zhaoa, D.; Huc, T.; Suna, J.; Yanga, X. Highly fluorescent nitrogen and sulfur co-doped graphene quantum dots for an inner filter effect-based cyanide sensor. *Sensors and Actuators B* **2017**, *241*, 779–788.

201. Salariyaa, K.; Umar, A.; Mehtaa, K. Rapidly synthesized polyethylene glycol coated cadmium sulphide (CdS) nanoparticles as potential scaffold for highly sensitive and selective lethal cyanide ion sensor. *Sensors and Actuators B* **2017**, *241*, 276–284.

202. Chen, X.; Wang, H.; Li, J.; Hu, W.; Li, M.-J Colorimetric and luminescent bifunctional iridium (III) complexes for the sensitive recognition of cyanide ions. *Spectrochimica Acta Part A: Mol. Biomol. Spectroscopy* **2017**, *173*, 904–909.

203. Shojaeifard, Z.; Hemmateenejad, B.; Shamsipur, M. Efficient On–Off Ratiometric Fluorescence Probe for Cyanide Ion Based on Perturbation of the Interaction between Gold Nanoclusters and a Copper(II)-Phthalocyanine Complex. *ACS Appl. Mater.* Interfaces **2016**, *8*, 15177−15186.

204. Kaushik, R.; Ghosh, A.; Singh, A.; Gupta, P.; Mittal, A.; Jose, D. A. Selective Detection of Cyanide in Water and Biological Samples by an Off-the-Shelf Compound. *ACS Sens.* **2016**, *1*, 1265−127.

205. Jung, K. H.; Lee, K.-H. Efficient Ensemble System Based on the Copper Binding Motif for Highly Sensitive and Selective Detection of Cyanide Ions in 100% Aqueous Solutions by Fluorescent and Colorimetric Changes. *Anal. Chem.* **2015**, *87*, 9308−9314.

206. Holaday, M. G. D.; Tarafdar, G.; Adinarayana, B.; Reddy, M. L. P.; Srinivasan, A. Chemodosimetric cyanide sensing in a 5,15-porphodimethene Pd(II) complex. *Chem. Commun.* **2014**, *50*, 10834—10836.

207. Youngson, R. M. Collins Dictionary of Human Biology; HarperCollins: Glasgow, 2006.

208. Cox, M.; Nelson, D. R.; Lehninger, A. L. Lehninger Principles of Biochemistry; W.H. Freeman: San Francisco, 2005.

209. Imai, K.; Ochiai, K. Role of histone modification on transcriptional regulation and HIV-1 gene expression: possible mechanisms of periodontal diseases in AIDS progression. *J. Oral. Sci.* **2011**, *53*, 1-13.

210. Portela, A.; Esteller, M. Epigenetic modifications and human disease. *Nat. Biotechnol.* **2010**, *28*, 1057.

211. Colpitts, T. M.; Barthel, S.; Wang, P.; Fikrig, E. Dengue virus capsid protein binds core histones and inhibits nucleosome formation in human liver cells. *PLoS One* **2011**, *6*, e24365.

212. Hayashida, O.; Uchiyama, M. Cyclophane-based tetra (resorcinarene) as a host for both histone and hydrophobic molecular guests. *Tet. Lett.* **2006**, *47*, 4091–4094.

213. Minaker, S. A.; Daze, K. D.; Ma, M. C. F.; Hof, F. Antibody-Free Reading of the Histone Code Using a Simple Chemical Sensor Array. *J. Am. Chem. Soc.* **2012**, *134*, 11674–11680.
214. Dervan, P. B. Molecular Recognition of DNA by Small Molecules. *Bioorg. Med. Chem.* **2001**, *9*, 2215-2235.
215. Ralph, R. K.; Marshall, B.; Darkin, S. Potentiation of 4'-(9-acridinylamino) methanesulphon-m-anisidine) action by verapamil. *Trends Biochem. Sci.* **1983**, *8*, 212-214.
216. Leung, C. H.; Chan, D. S.; Ma, V. P.; Ma, D. L. DNA-Binding Small Molecules as Inhibitors of Transcription Factors. *Med Res Rev.* **2013**, *33*, 823-846.
217. Banerjee, S.; Veale, E. B.; Phelan, C. M.; Murphy, S. A.; Tocci, G. M.; Gillespie, L. J.; Frimannsson, D. O.; Kelly, J. M.; Gunnlaugsson, T. Recent advances in the development of 1,8-naphthalimide based DNA targeting binders, anticancer and fluorescent cellular imaging agents. *Chem. Soc. Rev.* **2013**, *42*, 1601—1618.
218. Satpathi, S.; Sengupta, A.; Hridya, V. M.; Gavvala, K.; Koninti, R. K.; Roy, B.; Hazra, P. A Green Solvent Induced DNA Package. *Sci. Rep.* **2015**, *5*, 9137.
219. Holman, G. G.; Zewail-Foote, M.; Smith, A. R.; Johnson, K. A.; Iverson, B. L. A Sequence Specific Threading Tetraintercalator with an Extremely Slow Dissociation Rate Constant. *Nat. Chem.* **2011**, *3*, 875–881.
220. Smith, A. R.; Iverson, B. L. Threading Polyintercalators with Extremely Slow Dissociation Rates and Extended DNA Binding Sites. *J. Am. Chem. Soc.* **2013**, *135*, 12783 –12789.
221. Suseela, Y. V.; Das, S.; Pati, S. K.; Govindaraju, T. Imidazolyl-Naphthalenediimide-Based Threading Intercalators of DNA. *ChemBioChem* **2016**, *17*, 2162 –2171.
222. Tanious, F. A.; Yen, S. F.; Wilson, W. D. Kinetic and Equilibrium Analysis of a Threading Intercalation Mode: DNA Sequence and Ion Effects. *Biochemistry* **1991**, *30*, 1813 –1819.
223. Smith, A. R.; Ikkanda, B. A.; Holman, G. G.; Iverson, B. L. Subtle Recognition of 14-Base Pair DNA Sequences via Threading Polyintercalation. *Biochem.* **2012**, *51*, 4445–4452.
224. Guelev, V.; Sorey, S.; Hoffman, D. W.; Iverson, B. L. Changing DNA Grooves – A 1, 4, 5, 8-Naphthalene Tetracarboxylic Diimide Bis-Intercalator with the Linker (β-Ala) 3-Lys in the Minor Groove. *J. Am. Chem. Soc.* **2002**, *124*, 2864-2865.
225. Hong, L.; Schroth, G. P.; Matthews, H. R.; Yau, P.; Bradbury, E. M. Studies of the DNA Binding Properties of Histone H4 Amino Terminus. *J. Biol. Chem.* **1993**, *268*, 305-314.
226. Islam, Md. M.; Fujii, S.; Sato, S.; Okauchi, T.; Takenaka, S. A Selective G-Quadruplex DNA-Stabilizing Ligand Based on a Cyclic Naphthalene Diimide Derivative. *Molecules* **2015**, *20*, 10963-10979.
227. Lokey, R. S.; Kwok, Y.; Guelev, V.; Pursell, C. J.; Hurley, L. H.; Iverson, B. L. A New Class of Polyintercalating Molecules. *J. Am. Chem. Soc.* **1997**, *119*, 7202–7210.
228. Tse, W. C.; Boger, D. L. Fluorescent Intercalator Displacement Assay for Establishing DNA Binding Selectivity and Affinity. *Acc. Chem. Res.* **2004**, *37*, 61–69.
229. Valeur, B. Molecular Fluorescence: Principles and Applications; Wiley: Weinheim, 2002.
230. Young, J. A. Picric Acid. *J. Chem. Educ.* **2008,** *85*, 492.
231. Picric Acid. In *ACS Reagent Chemicals*; American Chemical Society: **2017**; Chapter 4.
232. Östmark, H.; Wallin, S.; Ang, H. G. Vapor Pressure of Explosives: A Critical Review. *Propellants, Explosives, Pyrotechnics* **2012,** *37*, 12-23.
233. Wollin, K. M.; Dieter, H. H. Toxicological Guidelines for Monocyclic Nitro-, Amino- and Aminonitroaromatics, Nitramines, and Nitrate Esters in Drinking Water. *Arch. Environ. Contam. Toxicol.* **2005,** *49*, 18-26.
234. Nipper, M.; Qian, Y.; Carr, R. S.; Miller, K. Degradation of picric acid and 2,6-DNT in marine sediments and waters: the role of microbial activity and ultra-violet exposure. *Chemosphere* **2004,** *56*, 519-530.

235. Vinita; Tiwari, M.; Prakash, R. Colorimetric detection of picric acid using silver nanoparticles modified with 4-amino-3-hydrazino-5-mercapto-1,2,4-triazole. *Appl. Surface Sci.* **2018,** *449*, 174-180.

236. Hakonen, A.; Wang, F.; Andersson, P. O.; Wingfors, H.; Rindzevicius, T.; Schmidt, M. S.; Soma, V. R.; Xu, S.; Li, Y.; Boisen, A.; Wu, H. Hand-Held Femtogram Detection of Hazardous Picric Acid with Hydrophobic Ag Nanopillar SERS Substrates and Mechanism of Elasto-Capillarity. *ACS Sensors* **2017,** *2*, 198-202.

237. Soldate, A. M.; Noyes, R. M. X-Ray Diffraction Patterns for the Identification of Crystalline Constituents of Explosives. *Anal. Chem.* **1947,** *19*, 442−444.

238. Byram, C.; Moram, S. S. B.; Shaik, A. K.; Soma, V. R. Versatile gold based SERS substrates fabricated by ultrafast laser ablation for sensing picric acid and ammonium nitrate. *Chem. Phys. Lett.* **2017**, *685*, 103-107.

239. Talaty, N.; Mulligan, C. C.; Justes, D. R.; Jackson, A. U.; Noll, R. J.; Cooks, R. G. Fabric analysis by ambient mass spectrometry for explosives and drugs. *Analyst* **2008**, *133*, 1532-1540.

240. Forzani, E. S.; Lu, D.; Leright, M. J.; Aguilar, A. D.; Tsow, F.; Iglesias, R. A.; Zhang, Q.; Lu, J.; Li, J.; Tao, N. A Hybrid Electrochemical−Colorimetric Sensing Platform for Detection of Explosives. *J. Am. Chem. Soc.* **2009**, *131*, 1390-1391.

241. Junqueira, J. R. C.; Araujo, W. R. d.; Salles, M. O.; Paixão, T. R. L. C. Flow injection analysis of picric acid explosive using a copper electrode as electrochemical detector. *Talanta* **2013,** *104*, 162-168.

242. Sun, X.; Wang, Y.; Lei, Y. Fluorescence based explosive detection: from mechanisms to sensory materials. *Chem. Soc. Rev.* **2015**, *44*, 8019-8061.

243. Shanmugaraju, S.; Joshi, S. A.; Mukherjee, P. S. Fluorescence and visual sensing of nitroaromatic explosives using electron rich discrete fluorophores. *J. Mat. Chem.* **2011**, *21*, 9130-9138.

244. Kartha, K. K.; Babu, S. S.; Srinivasan, S.; Ajayaghosh, A. Attogram Sensing of Trinitrotoluene with a Self-Assembled Molecular Gelator. *J. Am. Chem. Soc.* **2012**, *134*, 4834-4841.

245. Reches, M.; Gazit, E. Casting Metal Nanowires within Discrete Self-Assembled Peptide Nanotubes. *Science* **2003**, *300*, 625-627.

246. Roy, B.; Bar, A. K.; Gole, B.; Mukherjee, P. S. Fluorescent Tris-Imidazolium Sensors for Picric Acid Explosive. *J. Org. Chem.* **2013**, *78*, 1306-1310.

247. Das, D.; Dasgupta, A.; Roy, S.; Mitra, R. N.; Debnath, S.; Das, P. K. Water Gelation of an Amino Acid-Based Amphiphile. *Chem. Eur. J.* **2006**, *12*, 5068-5074.

248. Pramanik, B.; Ahmed, S.; Singha, N.; Das, B. K.; Dowari, P.; Das, D. Unorthodox Combination of Cation- p and Charge- Transfer Interactions within a Donor Acceptor Pair. *Langmuir* **2018**, *35*,478-488.

249. Gao, Y.; Liu, H.; Zhang, S.; Gu, Q.; Shen, Y.; Ge, Y.; Yang, B. Excimer formation and evolution of excited state properties in discrete dimeric stacking of an anthracene derivative: a computational investigation. *Phys. Chem. Chem. Phys.* **2018**, *20*, 12129-12137.

250. Wei, Y.; Thyparambil, A. A.; Latour, R. A. Protein helical structure determination using CD spectroscopy for solutions with strong background absorbance from 190 to 230nm. *Biochim. Biophys. Acta Protein Proteomics* **2014**, *1844*, 2331-2337.

251. Smith, A. M.; Williams, R. J.; Tang, C.; Coppo, P.; Collins, R. F.; Turner, M. L.; Saiani, A.; Ulijn, R. V. Fmoc-Diphenylalanine Self Assembles to a Hydrogel via a Novel Architecture Based on π–π Interlocked β-Sheets. *Adv. Mater.* **2008**, *20*, 37-41.

252. Venkatramaiah, N.; Kumar, S.; Patil, S. Femtogram Detection of Explosive Nitroaromatics: Fluoranthene-Based Fluorescent Chemosensors. *Chem. Eur. J.* **2012**, *18*, 14745-14751.

253. Mondal, S.; Bairi, P.; Das, S.; Nandi, A. K. Triarylamine-Cored Dendritic Molecular Gel for Efficient Colorometric, Fluorometric, and Impedometeric Detection of Picric Acid. *Chem. Eur. J.* **2018**, *24*, 5591-5600.

254. Das, P.; Mandal, S. K. Understanding the effect of an amino group on the selective and ultrafast detection of TNP in water using fluorescent organic probes. *J. Mater. Chem. C* **2018**, *6*, 3288-3297.

255. Che, W.; Li, G.; Liu, X.; Shao, K.; Zhu, D.; Su, Z.; Bryce, M. R. Selective sensing of 2,4,6- trinitrophenol (TNP) in aqueous media with "aggregation-induced emission enhancement" (AIEE)- active iridium(iii) complexes. *Chem. Commun.* **2018**, *54*, 1730-1733.

256. Shanmugaraju, S.; Dabadie, C.; Byrne, K.; Savyasachi, A. J.; Umadevi, D.; Schmitt, W.; Kitchen, J. A.; Gunnlaugsson, T. A supramolecular Tröger's base derived coordination zinc polymer for fluorescent sensing of phenolic-nitroaromatic explosives in water. *Chem. Sci.* **2017**, *8*, 1535-1546.

257. Zhang, Y.; Zhan, T.-G.; Zhou, T.-Y.; Qi, Q.-Y.; Xu, X.-N.; Zhao, X. Fluorescence enhancement through the formation of a single-layer two-dimensional supramolecular organic framework and its application in highly selective recognition of picric acid. *Chem. Commun.* **2016**, *52*, 7588-7591.

258. Liu, S. G.; Luo, D.; Li, N.; Zhang, W.; Lei, J. L.; Li, N. B.; Luo, H. Q. Water-Soluble Nonconjugated Polymer Nanoparticles with Strong Fluorescence Emission for Selective and Sensitive Detection of Nitro-Explosive Picric Acid in Aqueous Medium. *ACS Appl. Mater. Interfaces* **2016**, *8*, 21700-21709.

259. Sun, X.; Liu, Y.; Shaw, G.; Carrier, A.; Dey, S.; Zhao, J.; Lei, Y. Fundamental Study of Electrospun Pyrene–Polyethersulfone Nanofibers Using Mixed Solvents for Sensitive and Selective Explosives Detection in Aqueous Solution. *ACS Appl. Mater. Interfaces* **2015**, *7*, 13189-13197.

260. Gogoi, B.; Sen Sarma, N. Curcumin–Cysteine and Curcumin–Tryptophan Conjugate as Fluorescence Turn On Sensors for Picric Acid in Aqueous Media. *ACS Appl. Mater. Interfaces* **2015**, *7*, 11195-11202.

261. Acharyya, K.; Mukherjee, P. S. A fluorescent organic cage for picric acid detection. *Chem. Commun.* **2014**, *50*, 15788-15791.

262. Nagarkar, S. S.; Joarder, B.; Chaudhari, A. K.; Mukherjee, S.; Ghosh, S. K. Highly Selective Detection of Nitro Explosives by a Luminescent Metal–Organic Framework. *Angew. Chem. Int. Ed.* **2013**, *52*, 2881-2885.

263. Dey, N.; Samanta, S. K.; Bhattacharya, S. Selective and Efficient Detection of Nitro-Aromatic Explosives in Multiple Media including Water, Micelles, Organogel, and Solid Support. *ACS Appl. Mater. Interfaces* **2013**, *5*, 8394-8400.

264. Sohn, H.; Calhoun, R. M.; Sailor, M. J.; Trogler, W. C. Detection of TNT and Picric Acid on Surfaces and in Seawater by Using Photoluminescent Polysiloles. *Angew. Chem. Int. Ed.* **2001**, *40*, 2104-2105.

265. Vij, V.; Bhalla, V.; Kumar, M. Attogram Detection of Picric Acid by Hexa-peri-HexabenzocoroneneBased Chemosensors by Controlled Aggregation-Induced Emission Enhancement. *ACS Appl. Mater. Interfaces* **2013**, *5*, 5373-5380.

266. Pramanik, S.; Bhalla, V.; Kumar, M. Mercury assisted fluorescent supramolecular assembly of hexaphenylbenzene derivative for femtogram detection of picric acid. *Anal. Chim. Acta* **2013**, *793*, 99-106.

List of Publications

1. **Bapan Pramanik** and Debapratim Das*, A Perylene-peptide Conjugate for Selective Sensing of Picric Acid. (Manuscript Under Preparation)
2. Payel Dowari, **Bapan Pramanik*** and Debapratim Das*, pH and secondary Structure Instructed Aggregation to a Thixotropic Hydrogel by a Peptide Amphiphile. (Manuscript Communicated)
3. Nilotpal Singha, Basab Kanti Das, **Bapan Pramanik**, Saurav Das and Debapratim Das*, Freeze the Dynamacity: Charge Transfer Complexation Assisted Control Over Reaction Pathway. (Manuscript Under Revision)
4. Nilotpal Singha, Samya Neogi, **Bapan Pramanik**, Saurav Das, Antara Dasgupta, Ranjit Ghosh*, Debapratim Das*, Carbon Quantum Dot/Peptide Composite Xerogel Based Sensor: Ultra-fast, Highly Sensitive and Selective toward p-Xylene at Room Temperature. *ACS Appl. Polym. Mater.* **2019**, DOI: 10.1021/acsapm.9b00594.
5. Nilotpal Singha, Arpita Srivastava, **Bapan Pramanik**, Sahnawaz Ahmed, Payel Dowari, Basab Kanti Das, Ananya Debnath*, Debapratim Das*, A water insoluble supramolecular hydrgzogel with unique confinement property. *Chem. Sci.* **2019**, 10, 5920-5928.
6. **Bapan Pramanik***, Nilotpal Singha, Debapratim Das*, Sol, Gel, and Paper Based Detection of Picric Acid at Femtogram Level by a Short Peptide Gelator. *ACS Appl. Polym. Mater.* **2019**, 1, 833–843.
7. **Bapan Pramanik**, Sahnawaz Ahmed, Nilotpal Singha, Basab Kanti Das, Payel Dowari, and Debapratim Das*, Unorthodox Combination of Cation- π and Charge- Transfer Interactions within a Donor Acceptor Pair. *Langmuir*, **2018**, *35*,478-488.
8. Payel Dowari, Shriya Saha, **Bapan Pramanik**, Sahnawaz Ahmed, Nilotpal Singha, Anindita Ukil*, Debapratim Das*, Multiple Cross-Linking of a Small Peptide to Form Size Tuneable Bio-Polymer with Efficient Cell Adhesion and Proliferation Property. *Biomacromolecules*, **2018**, *19*, 3994-4002.
9. Julfikar Hassan Mondal, **Bapan Pramanik**, Meenakshi Shinde, Raman Khurana, Nilotpal Barooah, Achikanath Bhasikuttan, Debapratim Das*, Jyotirmayee Mohanty*, DNA-induced Novel Optical Features of Ethyl Viologen-tethered Perylenediimide Triad. *J. Phys. Chem. C* **2018**, *122*, 18061–18069.
10. Sahnawaz Ahmed, K. N. Amba Sankar, **Bapan Pramanik**, Kallol Mohanta*, Debapratim Das*, Solvent Directed Morphogenesis and Electrical Properties of a Peptide-Perylenediimide Conjugate. *Langmuir* **2018**, *34*, 8355–8364.
11. Subhajit Ghosh, **Bapan Pramanik**, Debapratim Das*, Self-Aggregation of a Naphthalene-monoimide Amphiphile and its Charge-Transfer Complexation Driven Morphogenesis in Water. *ChemNanoMat* **2018**, *4*, 867-873. (**Invited article for the special issue on Supramolecular Nanostructures**)
12. **Bapan Pramanik**, Debapratim Das*, Aggregation Induced Emission or Hydrolysis by Water? The Case of Schiff Bases in Aqueous Organic Solvents. *J. Phys. Chem. C* **2018**, *122*, 3655-3661.
13. Nilotpal Singha, Purnima Gupta, **Bapan Pramanik**, Sahnawaz Ahmed, Antara Dasgupta, Anindita Ukil*, Debapratim Das*, Hydrogelation of a Naphthalene Diimide Appended Peptide Amphiphile and its Application in Cell-Imaging and Intracellular pH Sensing. *Biomacromolecules* **2017**, *18*, 3630-3641. (**Invited article for the special issue on Organized Peptidic Nanostructures as Functional Materials**)
14. **Bapan Pramanik**, Sahnawaz Ahmed, Rupam Roy, Basab Kanti Das, Nilotpal Singha, Debapratim Das*, A DNA-NDI hybrid to efficiently detect histone in parts per trillion (ppt) level. *ChemistrySelect* **2017**, *2*, 8911 - 8916.
15. **Bapan Pramanik**, Sahnawaz Ahmed, Nilotpal Singha, Debapratim Das*, Self-Assembly Assisted Tandem Sensing of Pd^{2+} and CN^- by a Perylenediimide-Peptide Conjugate, *Chemistry Select* **2017**, *2*, 10061-10066.

16. Sahnawaz Ahmed, **Bapan Pramanik**, K. N. Amba Sankar, Abhinav Srivastava, Nilotpal Singha, Payel Dowari, Arpita Srivastava, Kallol Mohanta, Ananya Debnath, Debapratim Das*,Solvent Assisted Tuning of Morphology of a Peptide-Perylenediimide Conjugate: Helical Fibers to Nano-Rings and their Differential Semiconductivity. *Sci. Rep.* **2017**, *7*, 9485.
17. **Bapan Pramanik**, Julfikar Hassan Mondal, Nilotpal Singha, Sahnawaz Ahmed, Jyotirmayee Mohanty, Debapratim Das*, A Viologen-Perylenediimide Conjugate as an Efficient Base Sensor with Solvochromic Property. *ChemPhysChem* **2017**, *18*, 245 -252.
18. Sahnawaz Ahmed, Nilotpal Singha, **Bapan Pramanik**, Julfikar Hassan Mondal, Debapratim Das*, Redox Controlled Reversible Transformation of a Supramolecular Alternating Copolymer to Radical Cation Containing Homo-polymer. *Polymer Chemistry* **2016**, *7*, 4393-4401.